Elastic wave velocities and attenuation under methane hydrate growth in Bentheim sandstone

- Measurements and modelling

Mathias M. Sæther

Thesis for the Degree of Philosophiae Doctor (PhD)
University of Bergen, Norway
2018

UNIVERSITY OF BERGEN

Elastic wave velocities and attenuation under methane hydrate growth in Bentheim sandstone

- Measurements and modelling

Mathias M. Sæther

Thesis for the Degree of Philosophiae Doctor (PhD)
at the University of Bergen

2018

Date of defence: 18.12.2018

Year: 2018

Title: Elastic wave velocities and attenuation under methane hydrate growth in Bentheim sandstone

Name: Mathias M. Sæther

Print: Skipnes Kommunikasjon / University of Bergen

Preface

This work is the result of a 4-year PhD project financed by the University of Bergen, under the supervision of Professor Per Lunde and Associate Professor Geir Ersland at the Department of Physics and Technology. The design and construction of the experimental measurement setup used in this work has been particularly time consuming. I have chosen to write my PhD as a monograph instead of a collection of articles to describe the challenges concerning the measurement setup thoroughly and systematic.

Firstly, I would like to thank my supervisors for this opportunity at the University of Bergen. I greatly appreciate the opportunity you have given me to study the interesting crossover between the fields acoustics, instrumentation and rock physics.

Specially, I would like to thank Stian Almenningen for helping me out in the hydrate laboratory at the University of Bergen. Thank you to Magne Vestrheim for reading through and commenting on my dissertation. Magne Aanes and Espen Storheim also deserve special thanks. Their willingness to discuss and to help me has been vital for this project.

Finally, I want to thank my friends and family for the great support you have given me. And to my beloved wife, Makalani; you are perfect and I can not thank you enough for your patience and understanding during these last years.

Mathias M. Sæther
Bergen, September 1, 2018.

Summary

Due to the potential for using methane hydrates as an energy source, localizing, monitoring and describing hydrate deposit areas are of interest. This has previously been attempted by using acoustic methods and thus information on the relation between the hydrate saturation, S_H, and acoustic properties, such as c_P, c_S (compressional and shear wave velocity, respectively) and α_P (compressional wave attenuation coeffiscient) is needed.

The overall aim of this PhD thesis is to measure and discuss c_P, c_S and the change in α_P ($\Delta\alpha_P$) in ten Bentheim sandstone specimen having different initial water saturations, S_{w0} as a function of S_H, during hydrate growth.

In the literature, laboratory studies typically focus on measuring c_P and c_S in unconsolidated hydrate bearing sediments using the "first arrival of the pulse," which means that the measurement frequency of the elastic wave is not defined. Only a few laboratory studies are found by this author to measure acoustic properties for hydrate bearing sediments for defined frequencies, and only one study is found to report α_P during hydrate growth. Although one study is found on hydrate bearing consolidated sediments, no laboratory studies are found by this author to measure c_P, c_S and the change in α_P for Bentheim sandstone during hydrate growth.

In this work, a pressure cell in which hydrates may grow is modified so that acoustic measurements can be conducted during hydrate growth. Piezoelectric shear-wave (S-wave) and compressional wave (P-wave) transducers are designed and constructed to be used with the solid buffer measurement method and to fit inside the pressure cell. Due to the limited space inside the pressure cell, unwanted acoustic reflections from e.g. sidewalls will affect the measurements. The S-wave transducers transmit both P-waves and S-waves and mode conversion between these may also occur. To measure P-wave or S-waves, short pulses are needed to separate the measurement signal from the other reflected or mode converted signals. To do so, broadbanded transducers are designed with tungsten-epoxy backing and a quarter wave-length front-layer.

The Fourier spectrum method is able to determine the frequency content of the short

measured signals and is thus used as the main signal processing method together with the solid buffer method for both the S-wave transducers and the P-wave transducers. The effect of the unwanted side-wall reflections and diffraction effects are investigated using finite element simulations on plexiglas specimen having approximately the same dimensions as the Bentheim sandstone specimen. The Fourier spectrum method is simulated using the finite element simulations together with Fourier synthesis. c_P, c_S and α_P for plexiglas measured with the solid buffer method are compared with measurements conducted with the immersion measurement method. The deviation found between these measurement methods aid in understanding the importance of determining the effects of sound diffraction and unwanted sidewall reflections.

Four main categories of measurement results are presented: 1) how the absolute c_P and c_S, and the relative values of c_P, c_S and α_P, change with S_H, 2) how the c_P/c_S ratio changes with S_H, 3) how the compressional wave absorption spectrum differs between distinct S_H, and 4) investigate if dispersion of acoustic waves can be detected.

Hydrates can grow inside a sandstone in different ways, affecting the acoustic properties differently. The distribution of water and gas inside the sandstone also affect the acoustic properties. To investigate the relation between c_P, c_S, S_{w0} and S_H, the results are compared with several numerical hydrate growth models. In the first model, hydrates only form in the fluid, thus "floating" around in the pores. In the second model hydrates grow into the sandstone, becoming a part of the dry frame, acting as second type of load-bearing sediment grain. In the third model, hydrates act as cement around grain contacts, thus stiffening the dry frame.

To investigate how the change in α_P may be related to S_H, two more models are used. The first attenuation model is based on modeling the Biot flow and squirting flow inside the sandstone during hydrate growth. These are attenuation mechanisms caused by pressure induced fluid flow. The second attenuation model is based on Waterman and Truell's multiple scattering theory. As the attenuation mechanisms inside a sandstone is very complex, no attempt is done to directly relate α_P, S_{w0} and S_H. However, based on the numerical attenuation models, it is indicated whether pressure induced fluid flow and multiple scattering mechanisms are present in hydrate bearing Bentheim sandstones.

Contents

Chapter 1

Introduction

1.1 Background and motivation

Gas hydrates exist in sediments beneath the ocean-bed, inland seas and in the permafrost [1, 2, 3, 4, 5]. Even when conservative estimates are considered, the consensus is that hydrocarbon gas hydrate resources are vast [1, 2, 3, 4]. The gas hydrates can potentially be used as an energy resource [6, 1, 3]. The ever-growing need for energy and the fact that the CO_2 footprint from natural gas is substantially lower than that of coal [7] makes utilizing of gas hydrates highly relevant.

However, hydrate deposits stretch over vast areas, and are trapped in complex structures consisting of clay and porous geological structures also containing water and pockets of gas [1]. Such hydrate deposits can cause sea-floor instability and submarine landslides [8, 9, 10, 11]. On a localized scale, drilling operations can destabilize hydrate rich sediments, causing sediment collapse, sub-sea landslides, bore failures and potentially be a risk for sub-sea structures [8]. It is also debated whether dissociated methane gas from such sub-sea landslides could reach the atmosphere [12, 13].

Seismic surveys have for many years been important when mapping the geological structures beneath the sea-floor [14, 15]. Also the description and monitoring of hydrate deposit areas must be done using remote methods, such as acoustic methods [16, 1, 2].

Given the more stable nature of CO_2 - containing hydrates, porous rock reservoirs can also potentially be used for safe storage of CO_2. This has been tested by injecting CO_2 into the Utsira formation [17, 18]. Potential leakage and other safety concerns have been studied in detail [19, 20]. Developing this method further requires close and accurate monitoring of fluid flow and hydrate-, water- and gas saturation, during the injection of CO_2 into the formation. Possible monitoring methods are 4-dimensional seismic surveys or acoustic logging in boreholes, which both rely on the use of acoustic waves.

As such, the safe and efficient extraction of methane gas and insertion of CO_2 gas, requires continuous monitoring and detailed understanding of the changing physical properties in the reservoir. Gas hydrate or ice in sediment pores will significantly affect the acoustic parameters such as compressional and shear wave velocities, c_P, c_S, respectively, and compressional and shear wave attenuation coefficients, α_P, α_S, respectively [21, 22]. Detailed knowledge of these changes can be used to detect and monitor gas hydrates in porous rocks remotely [1]. Theoretical models (detailed in chapter 2), such as the Biot model [23], friable sand model [24], the contact cement model [25, 26] or the constant cement model [27, 28], can give further insight into physical and geological properties of hydrate-containing porous rocks. Acoustic parameters are important input parameters in these models. Efficient use and detailed understanding of sonic logs from sediments bearing hydrates, also requires detailed understanding of the different constituent's elastic properties and their interaction [29]. This information can be acquired through experiments in the controlled environment offered in a laboratory and skilled use of numerical models.

Previously, c_P and c_S have been measured in unconsolidated, compressed sand-packs during hydrate growth in the laboratory [22, 21, 30, 31, 32, 33, 34, 35]. Hydrate content have been found by interpreting the measured c_P and c_S with numerical models [26, 24, 22, 21]. Valuable information of hydrate growth patterns has been achieved, i.e whether hydrates form primarily within the pore fluid, hydrates form and grow on individual grains, becoming a part of the frame, or hydrates form and grow at and around grain contacts, becoming part of the frame but also cementing the grains together. There are seemingly very few laboratory studies of the elastic properties of hydrate bearing consolidated sediments; only one laboratory study has been found by this author [35]. One study has also been found using THF-technique (tetrahydrofuran hydrate formation technique) with consolidated Berea sandstone [36] (synthetic hydrates forming at atmospheric conditions). In both consolidated and unconsolidated sediments, there is a clear increase of both c_P and c_S during hydrate growth. However, for sediments having the same hydrate saturation (S_H), this increase is higher for unconsolidated sediments [22, 21, 30, 31, 32, 33, 34, 35]. This indicates that different elastic properties should be expected for the same amount of methane hydrate depending on whether the reservoir sediment is a consolidated porous rock or unconsolidated sandy sediment. An example of such a consolidated porous rock is Bentheim sandstone, which is relatively homogeneous [37]. To the best of this author's knowledge, no studies of elastic properties in methane hydrate-bearing Bentheim sandstone have been performed.

In laboratory studies of elastic properties in hydrate bearing sediments, both ultrasonic frequencies (>100 kHz) [22, 21, 30, 31, 34, 35] and lower frequencies (<10 kHz) [32, 33] have been used. While ultrasonic frequencies give better resolution and can potentially give better precision and more information than low frequencies, these are not necessarily directly comparable to seismic logs where other dispersion (frequency-dependent sound velocity) and attenuation mechanisms are present [32]. In seismic surveys, the acoustic attenuation in reservoirs containing hydrates have been argued to mostly be due to pressure-induced fluid flow in the reservoir [38, 39, 40]. At low frequencies and high pressures, effects like scattering and frictional sliding are usually considered negligible [41]. Only one laboratory study has been found by this author on the compressional and shear wave attenuation coefficients of hydrate bearing unconsolidated sediments. In this study performed by Nakagawa et al. [33] lower frequencies were used (<10 kHz).

To interpret potentially more detailed and accurate ultrasonic acoustic signals, suitable numerical models must be used. Waite et al. [22] and Winters et al. [21] analyzed hydrate content and growth patterns by interpreting laboratory results with numerical models. In these studies 500 kHz transducers were used, but no attenuation spectra or dispersion mechanisms were considered. Nakagawa et al. [33] used low frequencies (<10 kHz) to measure the c_P and c_S as well as the compressional Q-value (Q_P) and shear wave Q-value (Q_S) in hydrate-bearing sediments. In this study, the Gassman model [42] was used to analyze c_P and c_S but no numerical model was used to investigate the measured Q-values.

There is considerable theoretical knowledge of the different dispersion and attenuation mechanisms in porous rocks [41, 43, 44, 45, 46]. A literature review on the topic is given in sections (Sects.) 1.5 and 1.6. However, none of the laboratory studies on hydrate bearing sediments mentioned above attempted to quantify these mechanisms in a hydrate-bearing porous rock. Allthough one laboratory study was found linking Q_S and Q_P with hydrate content in unconsolidated sediments [33], no studies have been found by this author attempting to relate measured dispersion or attenuation spectrum to hydrate content in hydrate bearing sediments.

Descriptions of experimental measurement setups for measuring acoustic properties in porous rocks during hydrate growth have been given by for example Waite et al. [22] and Hue et al. [35]. However, in these studies, the practical and safety issues of using high voltage sources for weeks in an experiment with methane gas under high pressure have not been addressed. Also, these published studies do not focus on giving insight in the practical challenges of monitoring multi-frequency compressional and shear waves in the confined space inside a pressure cell unattended for weeks. However, acoustic properties of plexiglas specimen have been measured using a measurement setups where unwanted sidewall-reflections may occur [47].

1.2 Objectives

Due to the potential for using methane hydrates as an energy source, localizing, monitoring and describing hydrate deposit areas are of interest. This has previously been attempted by using acoustic methods and thus information on the relation between the hydrate saturation, S_H, and acoustic properties, such as c_P, c_S and α_P is needed.

The overall aim of this PhD thesis is to measure and discuss c_P, c_S and the change in α_P ($\Delta\alpha_P$) in ten Bentheim sandstone specimen having different initial water saturations, S_{w0} as a function of S_H, during hydrate growth.

A pressure-cell setup able to withstand the pressure and temperature required for hydrate formation (83 bar and 4 °C) is to be modified so that acoustic measurements may be conducted inside the cell during hydrate growth. As specific dimensions are required for experimental equipment to fit inside the pressure cell, transmitting and receiving piezoelectric transducers will be designed and constructed. The transducers and the equipment modifying the pressure cell must also be able to withstand the conditions inside the pressure cell during the hydrate growth experiments. Each experiment may last for up to two weeks. A robust Matlab logging algorithm able to log the acoustic signal through the Bentheim sandstone every 15 min for weeks is to be developed. The solid buffer method is to be used to measure c_P, c_S and α_P on hydrate-bearing sandstones inside the pressure cell.

A commonly used signal processing technique to obtain c_P and c_S in hydrate-bearing sediments with the solid buffer method is to use the first arrival of the signal (leading edge or onset of the signal) [22, 21]. However, the accuracy of this technique is debated [48, 49, 50]. As the energy is low during the first half cycle of the signal, any interference in this region may potentially give inaccurate measurements. Mode conversion between S-waves and P-waves is known to occur using the solid buffer method [51]. Especially if using a longer burst, part of of the mode-converted P-wave may interfere with the S-wave, making the P-wave and the S-wave indistinguishable. This source of interference may be minimized by exciting the transmitting transducer with short pulses instead bursts containing several periods. In noisy signals, the very first peak of the signal may also be hard to detect, making measurement methods relying on transit time measurements unreliable. The Fourier spectrum method use short pulses and is not dependent on measuring transit times directly. Therefore, the Fourier spectrum signal processing technique is to be used together with the solid buffer method for measurements on the

Bentheim sandstones inside the pressure cell.

Because of the limited space inside the pressure cell, unwanted acoustic reflections from e.g sidewalls and interference between shear waves and compressional waves will affect acoustic measurements, even when short pulses are used. The degree of this interference and as such the validity of results is to be investigated by measuring c_P, c_S and α_P and simulating c_P and α_P in plexiglas specimen having the same dimensions as the Bentheim sandstones. Finite element simulations are to be performed with Comsol Multiphysics 4.2 with the use of Fourier synthesis to obtain time-domain signals. Using these simulated time domain signals, c_P and α_P will be calculated using both the Fourier spectrum method and methods relying on direct transit time measurements (basic pulse method). Due to lack of computing power, 3D simulations of shear waves are not feasable. The plexiglas properties c_P, c_S and α_P measured using the solid buffer method will be compared with measured c_P, c_S and α_P using the immersion method. The sound diffraction effects in the plexiglas specimen will be investigated using finite element simulations and established methods to correct for diffraction effects [52, 53, 54] for the solid buffer and immersion method. Some attention will be given to other sources of uncertainty, such as the confining pressure that is exerted on the rocks inside the pressure cell and the force which is applied to the transducers and thus on the porous rock.

To formally address the effect of the unwanted acoustic sidewall reflections and sound diffraction effects, the measurement methods used in this work are to be described with transfer functions.

Ten experiments are to be performed on ten different Bentheim sandstones specimen. Each experiment lasts from one to two weeks. S_{w0} of the different specimen range from 0.48 to 0.95. Higher S_{w0} gives potentially a higher S_H after hydrate growth. One pair of in-house built P-wave transducers and one pair of in-house built S-wave transducers are to be used. The S-wave transducers may transmit both P-waves and S-waves. The absolute c_P and c_S and the change in α_P are to be measured during the ten experiments. At S_H below 0.2, the measured absolute value of α_P is seen to highly vary from sandstone to sandstone. Thus, to be able to compare the ten different experiments, α_P is presented relative to α_P at S_H 0.2.

Four main categories of measurement results are to be presented: 1) how the absolute c_P and c_S, and the relative values of c_P, c_S and α_P, change with S_H, 2) how the c_P/c_S ratio changes with S_H, 3) how the compressional wave absorption spectrum differs between distinct S_H, and 4) investigate if dispersion of acoustic waves can be detected.

The measured c_P and c_S from the hydrate growth experiments are to be compared with several numerical models: Helgerud et al.'s models where hydrates form in the fluid or in the frame [24] and Avseth et al.'s constant cement model [27] are used to model hydrate growth with no loss present. From these models the hydrate growth pattern will be discussed, i.e whether hydrates form primarily within the pore fluid, hydrates form and grow on individual grains, becoming a part of the frame, or hydrates form and grow at and around grain contacts, becoming part of the frame but also cementing the grains together.

Helgerud et al.'s frame building hydrate growth model [24] will be used together with the Biot theory [23], Dvorkin et al.'s squirt flow model [55] and Waterman and Truell's multiple scattering theory [56] to discuss whether loss mechanisms such as scattering or pressure induced fluid flow are present in the hydrate-bearing Bentheim sandstone.

The results will be compared with the results of other laboratory studies on hydrate bearing sediments [22, 21, 30, 31, 32, 33, 34, 35]. A discussion on whether these experimental results are relevant for comparison with data from well-logs [39, 57] will also be given.

1.3 Early laboratory measurement of elastic properties in rocks

One of the first experimental studies of Young's modulus and Poisson's ratio in rocks were reported by Adams and Coker in 1906 [58]. Using a static method they found the elastic moduli by measuring the change of dimensions of rock samples subject to an axial compression. Different measurements of elastic parameters of rocks in the early 20th century gave inconsistent results [59]. It has been noted that different axial pressures were applied on the rocks in the published data which is believed to be the cause of this inconsistency [59].

The accuracy of the static method was questioned by Ide in 1936 [60] because of the large deviations in the reported Young's modulus [59]. Ide was one of the first to find the Young's modulus in rocks by exciting it's first thickness resonance mode with a transducer. One transducer was used as transmitter and one as receiver. The results from this dynamic or resonance method was found to differ compared with the static methods of Zisman [59]. A similar experimental setup was used by Birch in 1938 [61]. In his work he measured both compressional and torsional waves in rocks subject to various temperatures and pressures with the resonance method.

Parallel to measurements of the elastic moduli, the attenuation of sound waves in rocks were investigated. When Kimaball and Lovell [62] presented their work on the compressional wave attenuation coefficient in 1927, it was believed by many researchers that the loss mechanisms in solids were mainly due to viscous effects similar to those in pure water. However, Kimball and Lovell and others [63, 64] concluded that other non-linear attenuation mechanisms, so-called "solid friction" attenuation effects, existed in rocks as well.

The resonance method was found to have its limitations [65]. If the solid buffer method is used, the detected resonance frequency will be the resonance frequency of the whole measurement system. This system consists of the transmitting and receiving transducers, buffers, surrounding medium and the test specimen. The resonance frequency of the test specimen can be found if the effect of the transducers, buffers, sound diffraction and the surrounding medium can be eliminated [65]. The measurement frequency is limited to the frequency corresponding to the detected resonance mode in the test specimen. At high frequencies the attenuation of the acoustic waves might be so high that resonance modes are hard to detect.

As electrical components and circuits improved during and after the second world war, fast-writing oscilloscopes became available to researchers. Now, gated time signals or pulses could be inspected with high precision and numerous studies on the elastic moduli of rocks were published [66, 67, 68, 69, 70]. In these studies, transit times were directly measured from the oscilloscope.

1.4 Acoustic measurement methods

McSkimin categorized and discussed strengths and weaknesses of different acoustic measurement methods for various media ranging from low and high viscosity fluids to rubbers, plastics, wood, rocks and metals [65]. The two main categories of signal processing methods for measuring attenuation and velocities in solids were divided into pulse and resonance techniques. The method referred to as the pulse technique by McSkimmin will in this work be called the basic pulse method. This method relies on measuring the transit time of the pulse for wave velocity measurements and the amplitude of the pulse for attenuation coefficient measurements. McSkimin outlined how measurements with the pulse method using the steady-state portion of the signal can be used to find acoustic wave velocities and attenuation for distinct frequencies [65].

Winkler and Plona [51] developed a signal processing method using Fourier spectroscopy of short pulses to measure the dispersion of c_P in rocks based on the work of of Papadakis et al. [52], and Sachse and Pao [71]. The Fourier spectrum method uses short pulses and might be less prone to unwanted reflections. This method has been widely used to measure the absorption spectrum and dispersion of both compressional and shear waves of various materials [51, 72, 73, 74]. In this work, both the Fourier spectrum method and the basic pulse method have been used. The Fourier spectrum method is the primary signal processing method in this work when measuring c_P, c_S and α_P during hydrate growth.

The basic pulse and the Fourier spectrum method can be used with the immersion [72] or the solid buffer measurement method [51] to measure sound velocity and the absorption coefficient. The solid buffer method is a practical method where the transducers can be clamped on directly to the buffers or specimen. To use the solid buffer method, the buffer-specimen transmission coefficient must be known. To use the immersion method, the fluid-specimen transmission coefficient must be known [65, 72]. If shear wave attenuation coefficients or velocity is to be measured using the immersion method, the specimen needs to be rotated so that shear waves are generated on the specimen surface [53]. Shear polarized piezoelectric transducers have often been used measuring shear waves with the solid buffer method [75]. In this work, the solid buffer method is used inside the pressure cell used for growing hydrates. The immersion method is used as a reference method to investigate the accuracy of the solid buffer method.

Many authors make use of transit time measurements of a pulse when finding wave velocities. This is typically done by taking the first rise of the pulse and correct for time delays in the electronics [66, 67, 68, 69, 70] or using a reference measurement. In measurements where unwanted reflections may occur, the use of the first rise of the signal is a suitable technique. However, the accuracy of technique is debated [48, 49, 50]. For highly attenuating media, Futterman [48] found a logarithmic behavior at the rise of the signal and concludes that the very onset of the signal would be hard to pinpoint. Molyneux et al. [49, 50] also discussed how high frequency components overrepresented at the rise of the signal, make precise time of flight measurements difficult.

In early measurements of wave velocities and attenuation coefficients, diffraction of the sound waves was given little or no attention. As experimental equipment improved and high-precision oscilloscopes became available, diffraction effects could no longer be ignored for precise measurements of acoustic properties. In 1951, Williams published a model for the transducer diffraction effects describing the transducer as a plane circular vibrating piston mounted in a rigid, infinite baffle [76]. Khimunin used Williams' model to define a diffraction correction relative to plane waves [77, 78]. Soon after, this technique was used to correct for diffraction effects in experimental setups [52]. Due to it's relatively simple implementation in results attained from the solid buffer method or the immersion method, the approximate formulation (valid for $ka >> 1$, where k is the wavenumber and a is the radius of the piston) of Rogers and Buren is widely used

[79, 53, 51, 72].

While many authors have used diffraction corrections on compressional wave measurements, fewer authors have used diffraction corrections for shear waves. However, it has been proposed to use the same diffraction correction formalism for a circular shear polarized piezoelectric element as for P-wave transducers when measuring shear waves with the solid buffer method [54] or with the immersion method [53].

The diffraction models based on the circular plane piston are not an exact representation of a real transducer. Instead of using the same diameter on the real transducer and the piston in the diffraction model, the piston has been described with an effective diameter [80, 81, 82]. The effective diameter of the piston is typically defined so that the 3dB angle of the main lobe is the same for the transducer and the piston. Since the 3dB angle is hard to measure in a solid, in this work, the same diameter is used on the piston in the diffraction model as the diameter of the piezoelectric element inside the real piezoelectric transducer.

1.5 Studies on the elastic properties of methane-hydrate bearing sediments

Water and methane gas naturally form hydrates at low temperature and high pressure [5]. To understand seismic data from reservoirs containing porous rocks, hydrates, pockets of natural gas and water, the acoustic properties of all components as well as the interaction between them must be known. The acoustic properties of the individual components in the reservoir or of the individual components of a test specimen in the laboratory is also used in numerical models (see section (Sect.) 1.6).

The porous sandstone used in this work is Bentheim sandstone. This is a porous rock with quartz-content typically 95 % [83]. Quartz, natural gas and water is well described in the literature and acoustic properties of these materials can be found in physics textbooks [84].

The compressional and shear moduli of various forms of pure hydrate have been investigated in laboratory studies and found to be similar to the properties of water-ice [85, 29, 86]. In the laboratory studies, transit time measurements using the first arrival of the signal together with the solid buffer method were used to find the compressional and shear moduli. Pandit et al. [85] used piezoelectric transducers exciting pulses with center frequencies 500 kHz -1 MHz and Helgerud et al. [29] and Waite et al. [86] used transducers with center frequency 1 MHz.

Helgerud et al. measured the shear modulus of water-ice to decrease with increasing uniaxial pressure [29]. The shear modulus of methane hydrate samples were reported to increase with increasing uniaxial pressure [85, 29, 86]. The compressibility was reported to be larger for ice than for the methane hydrate samples [85, 29, 86]. Helgerud et al. reported the accuracy in the measured shear and bulk moduli to be 4% and 6%, respectively.

c_P and c_S are seen to increase for increasing confining pressures in both consolidated sandstones [87, 88] and in unconsolidated sand-packs [31, 26]. Due to this effect, many studies on the absolute value of c_P and c_S are not directly comparable [22, 21, 30, 31, 32, 33, 34, 35]. However, the relative increases in c_P and c_S due to hydrate growth have been of interest when analyzing data from well-logs [39, 57, 89] or in seismic surveys utilizing bottom simulating reflectors (BSR) when searching for gas hydrates beneath the ocean-floor [38].

Winters et al. [21], Winters et al. [30] and Waite et al. [22] presented measured values from the same data-set for c_P during hydrate growth in packed Ottawa sand-specimen. In the measurements, a confining stress of approximately 0.3 Mpa was used (approximately 3 bar). c_P was measured with the solid buffer method using transit time measurements and the first arrival of the signal. A piezoelectric transducer having center-frequency 1 MHz was used to generate the acoustic pulse. One of the specimen, having an S_{w0} of 16 %, reached 20 % S_H, gave a baseline c_P of 1.9 km/s and ending at 3 km/s at maximum S_H. Another of the specimen, having an S_{w0} of 58 %, reached 70 % S_H, gave c_P starting at 1.9 km/s and ending at 4 km/s at full S_H. While c_S was not directly studied, the shear strength was seen to increase with S_H in [21, 30].

Rydzy et al. [31] also measured c_P in an Ottawa sand-pack. The sand-pack specimen was subject to a confining pressure of 1 MPa (approximately 10 bar) during hydrate growth and the S_{w0} is reported to be 27.5 %. An increase in c_P from 700 m/s to 2100 m/s at full hydrate growth is found, however, the degree of S_H is not precisely defined. c_P was measured with the solid buffer method using transit time measurements and the first arrival of the signal. A piezoelectric transducer having center-frequency 100 kHz was used to generate the acoustic pulse.

Hu et al. [35] measured the increase of c_P and c_S in both unconsolidated and consolidated sediments. Details of the mineral content and the confining pressure during hydrate growth is not described. For the measurements conducted on the consolidated sediment, c_P is reported to increase from 4242 m/s at zero S_H to 4643 m/s at S_H approximately 66 %. c_P and c_S was measured with the solid buffer method using transit time measurements and the first arrival of the signal. A piezoelectric transducers having center-frequency 500 kHz was used to generate the acoustic pulse.

For the non-consolidated sediment studied by Hu et al. [35], bender element transducers were used with the solid buffer method. The compressional wave frequency was recorded to be centered around three peaks: 75 kHz, 125 kHz and 140 kHz. The shear wave frequency was recorded to be centered around 35 kHz. c_S was measured with the solid buffer method using transit time measurements and the first arrival of the signal. c_P was found by using the Fourier spectrum method, however, no dispersion plots are presented in the study. c_S was found to increase from approximately 500 m/s at zero S_H to 1700 m/s at 100 % S_H. c_P was found to increase from approximately 1300 m/s at zero S_H to 3700 m/s at 100 % S_H. Hu et al. also recorded the change in c_P and c_S during hydrate dissociation. For both the consolidated sediment and the non-consolidated sediment, the same baseline c_P and c_S were measured after the hydrate dissociation process. However, during the dissociation process, some hysteresis is seen. Starting at maximum S_H, c_P and c_S decrease more rapidly in the hydrate dissociation process than seen in the hydrate formation process.

Zhang et al. [34] measured c_P in several samples of unconsolidated quartz sand where S_{w0} ranged from 15% to 70%. Depending upon S_{w0} and the final S_H, the increase in c_P during hydrate growth range from 1200 m/s to 3000 m/s. c_P was measured with the solid buffer method using transit time measurements and the first arrival of the signal. No precise definition of the measurement frequency is given, however, they are reported to be ranging between 500 kHz and 1 MHz. In the measurements a confining pressure of approximately 5 bar was used.

Using the resonance method, Priest et al. [32] measured c_P and c_S in thirteen different quartz sand-packs. The S_H in these thirteen specimen ranged from 0 to 35 %. The confining pressure was set to 5 bar. c_P and c_S were measured from approximately 1600 m/s and 300 m/s, respectively, at $S_H = 0$. c_P and c_S were measured from approximately 2700 m/s and 1500 m/s, respectively, at $S_H = 35\%$. The frequency used in the resonance method in the study of Priest et al. was reported to be 50-450 Hz.

Nakagawa and Kneafsey used the resonance method when measuring c_P, c_S, α_p and α_S in packed US Silica, F110 sand [33]. They measured c_P to range 700 m/s - 3000 m/s from zero to maximum S_H. c_S was measured to range 500 m/s - 1900 m/s from zero to full S_H. They also measured the compressional and shear wave attenuation coefficients to decrease from 3.7 dB/cm to 0.2 dB/cm and from 3.5 dB/cm to 0.4 dB/cm, respectively. The frequencies used in the resonance method was reported to be 500 Hz to 2.5 kHz.

The studies mentioned above performed by Waite et al. [22], Winters et al. [21] and Winters et al. [30] on hydrate growth in unconsolidated sand also show that the hydrates mainly act as a load-bearing member of the frame [22, 21, 30]. No laboratory studies on methane-hydrate growth in consolidated Bentheim sandstones have been found by this author. Hu et. al [35] reported an increase in c_P from 4240 m/s at baseline condition to 4660 m/s at $S_H = 0.65$ in the consolidated sediment they used in their study. For the same specimen c_S was reported to increase from 2530 m/s to 2725 m/s at full S_H. S_{w0} was given as 40 %. This increase in c_P and c_S reported by Hu et al. [35] will be seen to be much lower than the c_P and c_S measurements conducted in this work for Bentheim sandstones.

The basic pulse method has been widely used for measuring acoustic properties in methane-hydrate bearing sediments in the laboratory [22, 21, 30, 35, 35, 31]. Piezoelectric transducers with center-frequencies 500 kHz [22, 21, 30, 35] and 100 kHz [31] have been used as well as bender elements exciting frequencies <100kHz [35]. In all of these studies the first arrival or the first peak of the acoustic signal has been used to measure the acoustic travel time which means that the actual frequency-content in the measured signal is not precisely defined [49]. The Fourier spectrum method which precisely define the measurement frequency, has been used in earth materials for decades [51, 71]. While the Fourier spectrum method has been mentioned as a possible method for measuring acoustic properties in hydrate-bearing sediments [35], this method has not been used in the most cited laboratory studies on the topic [21, 30, 22].

Many well-established studies using the solid buffer method to measure acoustic properties of rock-specimen in a confined space such as a pressure cell, have not discussed whether unwanted acoustic reflections from sidewalls interfere with the signal [66, 67, 70, 51, 30]. However, even short time signal pulses that are used in the Fourier spectrum method may be affected from side reflections and thus be inseparable and subject to interference in the time domain. Specimen dimensions used in hydrate laboratory studies are e.g. 2.5 cm diameter, 6 cm length [31], 7 cm diameter and 14 cm length [22, 21]. Unwanted acoustic reflections in such specimen might be present in laboratory studies but to the best of this author's knowledge, these issues have not been addressed [22, 21, 30, 31, 32, 33, 34, 35].

Acoustic velocities measured with ultrasound frequencies may not always be directly applicable to data from seismic surveys measured with sonic or seismic frequencies because of acoustic wave velocity dispersion [32]. By using the resonance method, measurement frequencies in the sonic range may be used also in the laboratory [32, 33]. However, since the resonance frequency is shifted due to radiation of sound into transducers and other structures in contact with the specimen, calibration or an analytical expression is needed.

In hydrate bearing unconsolidated sediments, laboratory studies show that c_P increase for increasing S_H. [22, 21, 30, 31, 32, 33, 34, 35]. It has been pointed out that an absolute correlation between S_H and c_P does not exist [34], partly because the hydrates growth pattern may be different under different conditions (the main categories of hydrate growth patterns are discussed above). As an example however, in unconsolidated sandy sediments, c_P is reported to increase from 1300 m/s at baseline conditions to 3700 m/s at $S_H = 1.0$ [35]. For consolidated sediments, less literature have been found by this author. Hu et. al [35] reported an increase in c_P from 4240 m/s at baseline condition to 4660 m/s at $S_H = 0.65$ in the consolidated sediment used in their study. In general, a high S_{w0} will give a high S_H and thus potentially a higher c_P.

Laboratory studies also show that c_S increase for increasing S_H in both unconsolidated [32, 33] and in consolidated sediments [35]. Many of the arguments used for an increasing c_P due to hydrate growth is used for c_S. As an example, in unconsolidated sandy sediments, c_S has been reported to increase from 500 m/s at baseline conditions to 1700 m/s at $S_H = 1.0$ [35].

Nakagawa et al. [33] found a general decrease in α_P and α_S for increasing S_H. From low to maximum S_H a decrease of approximately 3.5 dB/cm was found. An unexpected sudden increase at very low S_H is reported [33].

In the laboratory studies on hydrate-bearing sediments discussed here, different confining pressures, different measurement methods and different sediment-types have been used [22, 21, 30, 31, 32, 33, 34, 35]. Due to this, absolute values of c_P, c_S and α_P measured in this work can not be expected to give same values as found in the listed studies. However, it is interesting to compare the relative change of the parameters c_P, c_S and α_P measured in this work with those presented in previous studies [22, 21, 30, 31, 32, 33, 34, 35].

1.6 Numerical models describing the elastic properties of hydrate-bearing sediments

To evaluate the elastic moduli of sediments partially saturated with water, hydrates and natural gas, numerical models describing the interaction of these phases are needed [90, 91, 92, 26, 24, 93]. These models are typically developed out of a combination of a vast number of simpler models [94, 95, 96, 97, 42, 23, 98, 69, 99, 100, 101, 102, 103, 104, 105, 106].

In the two phase Kuster-Toksöz model [94], the effective bulk modulus and shear moduli are found by summing the displacement-contributions from all inclusions to the incoming field. It is a long wavelength, first order scattering approximation which is also called the average T matrix approximation.

The Voigt upper [96] and Reuss [97] lower bounds are methods that calculates the effective elastic modulus of a composite medium using strain and stress considerations respectively. The Reuss lower bound (sometimes called Wood's formula [99]) is found assuming that the stress is everywhere uniform. The Reuss lower bound is a good representation in the low-frequency limit for a mixture of two incompressible fluids. The upper bound (Voigt) is found assuming that the strain is everywhere uniform and is basically a weighted average of the elastic moduli. The true value of the elastic moduli for a composite medium should lie between the Reuss and the Voigt bounds.

Other bounds where found by Hashin and Strikman 1963 [95] by using potential strain energy considerations. By assuming symmetrically distributed, spherical inclusions, more narrow upper and lower bounds where found compared to the Voigt-Reuss bounds.

Other simple models are the Hill average [100], which is the average between the Reuss and Voigt bounds, and Wyllie's equation [69], which is the weighted average of the travel time through the constituents of the composite medium.

Another effective medium model is the differential effective medium model (DEM) [101, 102, 103]. This method is derived by successively mixing very small fractions of one inclusion material in another host material. The host medium changes gradually during this process into the desired composite material.

Gassman included effects of the fluid in a fluid-saturated porous medium by considering the pore pressures and the stresses between solid grains (inter-granular stresses) as the acoustic wave travels through the medium [42]. The inter-granular stresses in the water-saturated porous medium were modeled by introducing the modulus of the dry frame in addition to the modulus of the fluid and the solid constituents. This frame modulus [107] can be found by independent measurements [108] or by models using e.g Digbys grain stiffness contact theory [109, 110, 104] or models using Hertz-Mindlin contact theory [26]. E.g. Tang et. al. [105] used O'Conell and Budiansky's theory for cracked solids [111, 112, 113] to describe the dry frame in Gassman's or Biot's equations. The Kuster-Toksoz model has also been used to find the dry modulus [114].

Biot's model [23] is arguably the most common way of modeling a fluid-saturated porous rock [39, 115]. Like in Gasmann's equation, Biot used a dry frame modulus to describe inter-granular effects. However, Biot offered a more thorough mathematically framework that is capable of explaining additional effects, such as frequency-dependent fluid-solid interaction. The fluid-solid interaction enters the equations as an additional stiffness and mass term (added mass). The acoustic wave generates a pressure gradient as it propagates through the saturated sandstone. This results in a fluid flow from areas having higher pore pressures. The acoustic energy transferred into fluid momentum generates a secondary wave in the medium, the slow wave [38, 23]. This wave is predicted in the equations and have also been measured experimentally [116].

Several authors have modeled three phased media consisting of two solids and one liquid phase [90, 91, 92, 26, 24, 93]. Using Wylie's time-average model [69], Timur was able to model three-phase consolidated permafrost sediments consisting of rock, frozen water and liquid water [90]. Wylie's equation has also been used with Gassman's equation to model partially frozen media [92].

Zimmermann and King [91] used the Kuster-Toksöz model in two stages to model unconsolidated permafrost. First they computed an effective homogeneous material of the water and ice phases with water as the inclusion material. In the next step, inclusions of solid grains where used in the homogeneous, effective ice-water composition.

A popular way to model hydrate growth has been to use Gasmann or Biot's equations to model fluid effects and a dry frame consisting of solid rock and hydrate [22, 21, 117, 118, 24]. Winters et al. [21] and Waite et al. [22] outlined three different main categories in which hydrates can interact with the fluid-saturated sediment and compared the result with a baseline model where no hydrates were present. They used models developed by Dvorkin et al. [25, 26, 119] and Helgerud et al. [24] to analyze their results.

In the baseline model [26, 119, 24] no hydrates exist. In this model a minimum and maximum value of the dry frame were used. Dvorkin et al. [119] defined the minimum value ("well-sorted end member") by using Hertz-Mindlin contact theory [120] to calculate pressure-dependent elastic moduli at critical porosity. Critical porosity is the porosity of an unconsolidated pack of grains in which grain-to-grain contact exist. The maximum value (second end member) was simply defined as the modulus of the fully consolidated, zero-porosity sandstone, i.e. the moduli of the solid mineral grain. At a given porosity between the critical porosity and zero porosity, the calculated modulus will lie between these two end members. A modified version of the Hashin-Strikman lower bound [95] was used in the baseline model [26, 119, 24] to interpolate between these two end members to find the elastic moduli of the sediment. The model was originally developed for unconsolidated sediments [26, 119, 24], however, it has been argued that the model can also be used for sandstones [121, 28]. Dvorkin et al. [119] and Helgerud et al. [24] used the Gassman equation [42] to calculate the saturation effect after the dry frame was found.

The first main category in which hydrates form in the sandstone is when they form within the pore fluid [22, 21]. When hydrates form in the fluid, hydrate alters only the fluid bulk modulus and density. To model this hydrate growth scheme, Helgerud et al.

[24] used the Reuss average to calculate a new effective fluid modulus. They used this new effective fluid in the baseline model to model the effect of hydrates growing in the fluid.

The second way hydrates can grow in a sandstone is becoming a part of the frame, acting as second type of sediment grain [22, 21]. Based on the S_H, Waite et al. [22] and Winters et al. [21] calculated a new sample porosity and density and used these new values in the baseline model. The dry sand pack moduli in the baseline model were recalculated by replacing the moduli of quartz with the Hill average [100] of the bulk and shear moduli for quartz and hydrate.

The third way hydrates can grow in a sandstone is if hydrate act as cement around grain contacts [22, 21]. A cementation model was proposed by Dvorkin based on Digby's contact theory [25, 26]. Two different cementing configurations for an unconsolidated sand-pack at critical porosity were analyzed. One, in which all the hydrates grow around the grain-contacts, cementing the grains together, and one configuration in which the hydrates grow as a coating layer around the grains, successively cementing the grains together as the coating layer grows [25, 26]. This model is called "contact cement model" [28] and assumes that all solid material in excess of the critical porosity is cementing the sediment in accordance to the cementing configuration.

As for the baseline model, a modified version of the Hashin-Strikman lower bound [95] can also be used with the contact cement model [25] to model sandstones with an arbitrary porosity at a given cementing level [27, 28]. This modified contact cement model is called the "constant cement model." The contact cementing model and the constant cementing model are pressure-independent. Pressure-dependence of the frame modulus can been added in the constant cementing model by implementing both cemented and non-consolidated grain contacts [122].

The elastic properties of the different constituents in addition to the grain stiffness were seen by Dvorkin and others to be main factors for deciding the wave velocities in hydrate bearing sediments [26, 22, 21]. The grain stiffness was affected by pressure and cementation [26, 122]. Inside hydrate-bearing sediments, acoustic energy in water, methane gas, hydrate and rock interact in accordance with parameters describing grain dimensions and geometry, the contact surface between grains, pore geometry and fluid and hydrate distribution. Some of these effects have been analyzed using the models of Dvorkin [25, 26, 119]. A full model of the physical behavior of a sediment like this is a formidable task as all the components of the hydrate bearing sediments may affect the elastic moduli and give rise to dissipation effects and acoustic scattering [123]. Main attenuation mechanisms are discussed and summarized by Johnston, Winkler, Best and

Wuff [87, 41, 124, 125, 126, 127] and are here divided into three categories.

The first attenuation mechanism is pressure induced fluid flow that the acoustic wave generates as it is propagating in the sandstone [23]. Acoustic energy from both the rock and the hydrate is transferred into fluid momentum . This flow is divided into two different types: Global flow (Biot flow) and local flow (squirt flow) [106, 55, 128]. Pressure differences between pores or patches of pores give rise to global flow and pressure differences inside a single pore (by e.g. a crack inside a pore) give rise to squirt flow. Especially if parts of a pore (like a crack) are compliant, locally pressure gradients may occur and squirt flow may be induced [106, 55, 128]. When hydrates form, the permeability inside the rock will change and so will the fluid flow. Pores that previously were compliant, giving pressure gradients, may stiffen or even close due to cementation so that the amount of squirt flow and global flow may be reduced. When the fluid saturates regions of the porous rock (patchy saturation), the induced fluid flow is affected by this as well [129, 130].

The second attenuation mechanism is scattering effects. In general, all heterogeneities in a material will contribute to acoustic scattering. The heterogeneities can be small or large pores, cracks or regions with heterogeneities, such as patchy saturation [41, 126]. Pores and gaps between grains are the smallest heterogeneities. In measurements with seismic or sonic frequencies, attenuation from these are typically neglected [33]. For ultrasonic frequencies however, Rayleigh scattering may be present and might even be the dominating attenuation mechanism [126, 131, 44, 45, 132, 133].

Multiple scattering between heterogeneities is relevant in porous materials and sandstones [134, 56, 135, 136, 43, 137, 138]. Sayers studied scattering in porous materials [135] by calculating the scattering coefficients [139, 140] and using Waterman and Truell multiple scattering theory [56]. Use of scattering coefficients of circular cracks has also been used with Waterman and Truell's multiple scattering theory [56, 43]. Patches of water in patchy saturated sandstones, fluid- or gas-filled cracks and pores may give rise to attenuation due to both fluid flow and multiple scattering. These two effects have been studied simultaneously by calculating the scattering coefficients using both the fast and slow wave when calculating the boundary conditions [136, 134, 43, 137].

A third category of attenuation mechanisms is internal friction. Relaxation mechanisms in pure water, hydrate and quartz grains are not mentioned by Johnston, Winkler, Best or Wuff [87, 41, 124, 125, 126, 127], and are considered to be negligible. However, other internal friction mechanisms, such as friction at grain contacts (frictional sliding) have received some attention [141, 142, 143, 144, 87, 41, 126, 145]. This is a non-linear attenuation mechanism in poorly consolidated sediments, which is dependent on the particle displacement if the particle displacement is large [141, 144, 87]. "Loose" grain contacts slip and thus energy dissipates at the grain contact due to the friction force between grains. As hydrate grow, cementing the grains together, the frictional sliding will diminish.

Leclaire [93] extended Biot's theory [23] to be valid for a porous medium containing two solid phases and one liquid phase (three phase Biot theory). Further improvements of the three-phased Biot theory, like cementation, rock-ice interaction and squirt-flow were provided by Carcione [38] and Guerin [39]. Several authors have used three-phase Biot theory to find the effective elastic properties of hydrate and/or clay bearing porous sandstone [39, 40, 57, 146, 40, 147, 148]. Following the three-phase Biot theory formalism, three different longitudinal waves and two different shear waves exist, one longitudinal and one shear in the two solid phases and one longitudinal in the effective water/gas phase.

The models of Dvorkin et al. [26] and Avset et al. [27] have successfully been used to model c_P and c_S in hydrate bearing sediments. Especially the cementing effect of hydrate on the grain stiffnesses in a hydrate-bearing sediment is well-described. These theories are purely elastic and do not regard attenuation mechanisms when they are used with Gassman's equations.

Biot accounted for the added mass and dissipation due to the internal water-flow. The water-flow Biot considered was flow parallel to the acoustic wave propagation (Biot flow). Local flow (squirt flow) have later been incorporated into the Biot's theory and gives a modified Biot's theory [55, 149]. Scattering from pores, cracks or other heterogeneities have been studied in porous rocks [43] by using the Biot theory [23] together with Waterman and Truell's multiple scattering theory [56]. Stoll propose to use a complex modulus for the solid frame in the Biot theory to account for internal friction between grains in the dry frame [150].

1.7 Outline of thesis

This thesis consists of eight chapters in total. The present introduction chapter presents the motivation, relevant literature and the aim for this PhD thesis.

Chapter 2 gives the theoretical background for this work. The hydrate formation inside the porous rock is briefly described. The diffraction correction used in this work and the wave equations solved within Comsol multiphysics are presented. Theoretical numerical models used to discuss the measurements are detailed.

In Chapter 3 the experimental measurement setups are described. First, the pressure cell is presented. Next, the design and construction of the extra equipment needed for acoustic measurements inside the pressure cell is described. Then, the solid buffer method for used inside the pressure cell, and the immersion method for independent reference measurement are detailed. The basic pulse and Fourier spectrum signal processing methods are descibed with an example of the Fourier spectrum method. Last, the impedance analyzer used for electrical conductance measurements of the piezoelectric transducers is described.

The transducer design and construction of the P-wave and S-wave transducers are presented in Chapter 4. Measurements and finite element simulations of the electrical conductance of the transducers are presented for the critical steps of the transducer design.

The simulation setup for the solid buffer method using finite element simulations and Fourier synthesis is presented in Chapter 5. How to formally address unwanted acoustic sidewall reflections in the simulation setup is detailed.

The accuracy of the solid buffer method used inside the pressure cell is considered in Chapter 6. Several simulations of different versions of the solid buffer method is given. The accuracy and reproducability of measurements conducted on homogeneous plexiglas specimen on porous sandstones are considered.

In Chapter 7, the results from the hydrate experiments are presented. c_P, c_S and α_P in Bentheim sandstone specimen are measured during hydrate growth. The four main categories of measurements listed in the objectives (Sect. 1.2) are presented, discussed and compared with simulation results of the numerical models.

Further work and conclusions are given in Chapter 8.

Chapter 2

Theory

Chapter 2 gives the theoretical background for this work. In Sect. 2.1 the theory behind behind hydrate formation and how the hydrates form in Bentheim sandstone specimen inside the pressure cell is presented. The discrete Fourier transform (DFT) used with the Fourier spectrum method is defined in Sect. 2.2. The diffraction correction used for the solid buffer method and the immersion method used in this work is presented in section 2.3. The wave equations solved with finite element (FE) simulations using Comsol multiphysics are presented in section 2.4. The numerical models used to describe and discuss the hydrate growth inside the Bentheim sandstone are discussed in Sect. 2.5: Helgerud et al.'s hydrate growth models [24] and Avseth et al.'s constant cement model [27] are used to model hydrate growth with no loss present. Helgerud et al.'s frame building hydrate growth model [24] will be used together with the Biot theory [23], Dvorkin et al.'s squirt flow model [55] and Waterman and Truell's multiple scattering theory [56] to discuss some of the dispersion and attenuation mechanisms present in the hydrate-bearing Bentheim sandstone.

2.1 Hydrate formation

2.1.1 Methane hydrate chemistry

Natural gas hydrates consist of Van der Waals bounded water molecules structured as cages around gas molecules called guest molecules. An example of such a cage is shown in Fig. 2.1a) and is built up of twelve pentagonal faces, 5^{12} [151]. This cage is called Pentagonal dodecahedron. "5" is labeling the shape of each face (here, a pentagon). "12" is labeling the number of such faces. Another type of cage is built up from twelve pentagonal faces and two hexagonal faces, $5^{12}6^{2}$. "6" is here labeling the hex and "2" is labeling number of hexes in the cage. Methane hydrates are formed by these two cage types and are called structure 1 type of hydrate, Fig. 2.1b). Structure 2 hydrates and structure H hydrates are not addressed in this work. Usually, every cage in a structure 1 type hydrate contain a guest molecule [151]. This gives a ratio between the number of water and guest molecules in structure 1 hydrate of 5.75, called the hydration number, n_w [152]. However, the average hydration number has been measured to be 5.99 in methane hydrates, which indicates that some of the cages are empty of guest molecules [153].

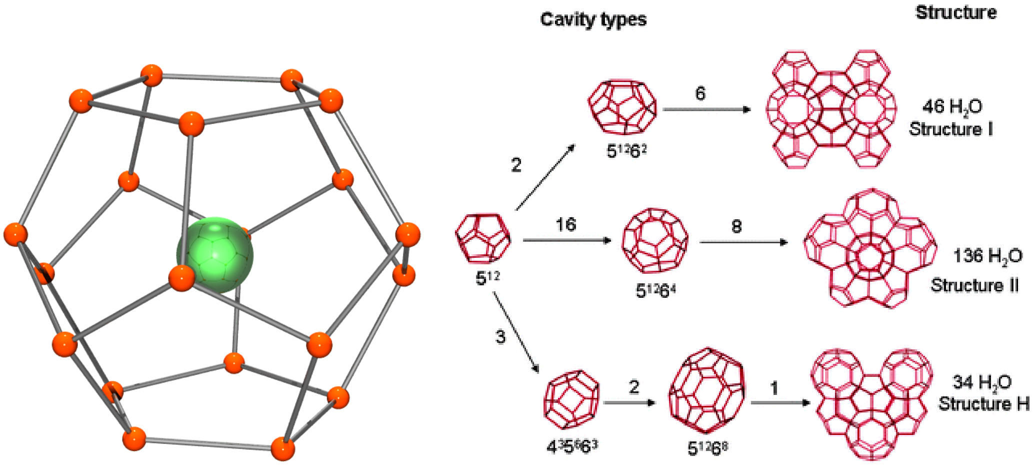

(a) (b)

Figure 2.1: Shows different cages and hydrate structures. The figure is found in the work of Sloan [151]. **a)** Illustration of cage 5^{12} (Pentagonal dodecahedron). **b)** Cages forming different hydrate structures.

2.1.2 Hydrate stability zones

The nature of hydrate formation varies with type of gas filling the cavities in sediments. Both biogenic gas (created by biological activity in sediments) and thermogenic gas (created by geological processes deeper within the earth) can be sources of gas. P-T (pressure - temperature) conditions will define the hydrate stability zones (HZS) (Fig. 2.2 [154]), and the geothermal gradient will govern its depth. For hydrates to form, the surface energy related to creating a new surface needs to be overcome by the thermodynamic driving force. This will happen at temperatures and pressures inside the hydrate stability zones presented in Fig. 2.2. Hydrate formation is a nucleation process in which hydrates form and disperse. The critical mass is the tipping point were the surface energy is less than the thermodynamic driving force and hydrates only form and do not disperse [154].

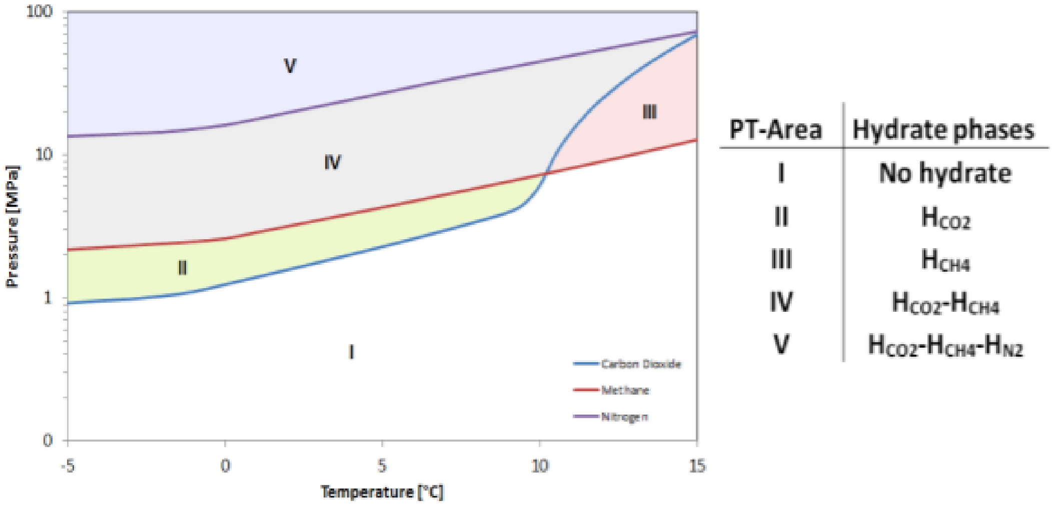

PT-Area	Hydrate phases
I	No hydrate
II	H_{CO2}
III	H_{CH4}
IV	H_{CO2}-H_{CH4}
V	H_{CO2}-H_{CH4}-H_{N2}

Figure 2.2: Hydrate stability zones for methane-hydrates (III,IV,V), CO_2-hydrates (II,IV,V), and nitrogen-hydrates (V) (The figure is found in the work of Husebø [154]).

2.1.3 Methane-hydrate formation in a closed system

If a net volume methane gas, V_{CH4}, is injected into a closed system in which hydrates grow containing a water-saturated Bentheim sandsone, the volume of methane hydrates in the pores would be [152]

$$V_{H_0} = \frac{\frac{V_{CH4}\ \rho_{CH4}^{pump}}{M_{CH4}}\ n_w\ M_w}{\rho_w^{core}}\ 1.26. \tag{2.1}$$

ρ_{CH4}^{pump} is the density of the methane gas injected into the closed system from a pressure pump, ρ_w^{core} is the density of water in the pores.

Because hydrates filling varies somewhat with P-T and some of the cages are believed to be empty, the hydration number, $n_w = 5.99$, is based on experiments in the literature [151]. M_{CH4} and M_w are the molar masses of methane and water, respectively, and 1.26 is the expansion factor of water into methane hydrate.

In this work, the closed system in which hydrate forms, is a pressure cell. The pressure cell and the experimental setup for hydrate growth is presented in Sect. 3.1. As the water expands into hydrate, some of the initial free methane gas will be displaced by the hydrate formation and methane gas will be pushed out of the pressure cell. Thus, the volume, V_{H_0}, calculated from Eq. (2.1) with V_{CH_4} read from the pressure pump log, is too low. Due to the expansion of water the volume of methane gas, V_0^{exp}, that is displaced from the pore volume is [152]

$$V_0^{exp} = \frac{\frac{V_{CH4}\ \rho_{CH4}^{pump}}{M_{CH4}}\ n_w\ M_w}{\rho_w^{core}}\ 0.26. \tag{2.2}$$

This extra volume of methane gas, V_0^{exp}, has also been responsible for forming methane hydrate and the sum $V_{CH4}+V_0^{exp}$ is a more correct value for the total amount of methane gas entering the pressure cell. However, this extra volume that is pushed out of the cell will also have caused some expansion and the same argument can be used all over again. An iteration process can be used to find the total amount of methane entering the pressure cell [152].

$$\begin{aligned} V_{H_{n+1}} &= V_{H_n} + \frac{\frac{V_n^{exp}\ \rho_{CH4}^{core}}{M_{CH4}}\ n_w\ M_w}{\rho_w^{core}}\ 1.26, \\ V_{n+1}^{exp} &= \frac{\frac{V_n^{exp}\ \rho_{CH4}^{core}}{M_{CH4}}\ n_w\ M_w}{\rho_w^{core}}\ 0.26. \end{aligned} \tag{2.3}$$

The iteration process must be continued until the expansion volume, V^{exp}, converges to zero (approximately five steps). The hydrate saturation is found by dividing the hydrate volume, V_{H_n} with the Bentheim sandstone pore volume. Equation 2.3 will be used to calculate S_H in the Bentheim sandstone specimen used in this work.

2.2 Fourier transform

In this work, the Fourier transform is used to analyze frequency components of a time signal. The inverse Fourier transform is used in Fourier synthesis to construct time signals from a known frequency response. The continuous Fourier transform and the continuous inverse Fourier transform are given [155]

$$\begin{aligned} X(\omega) &= \int_{-\infty}^{\infty} x(t)e^{-i\omega t}\ dt, \\ x(t) &= \frac{1}{2\pi}\int_{-\infty}^{\infty} X(\omega)e^{i\omega t}\ d\omega. \end{aligned} \tag{2.4}$$

$X(\omega)$ represents the Fourier transform and $x(t)$ represents the inverse Fourier transform. ω is the angular frequency. The Fourier transform can be discretized in time $t = n\Delta t$ and frequency, $f = l\Delta f$, where Δt is the time interval between two samples in the time domain and Δf is the frequency interval between two points in the frequency domain [155]. l and n are integers.

By using the limits $n \in [0,\ N-1]$ and $\omega = 2\pi k\Delta f = k\frac{2\pi}{N\Delta t}$, gives the DFT and the inverse DFT [155]

$$\begin{aligned} X[l] &= \sum_{n=0}^{N-1} x[n] e^{-i\frac{2\pi k}{N}n}, \\ x[n] &= \frac{1}{N}\sum_{n=0}^{N-1} X[l] e^{i\frac{2\pi k}{N}n}. \end{aligned} \tag{2.5}$$

In this work, the DFT is computed with the fast Fourier transform (FFT) algorithm [155]. The pre-defined FFT algorithm package in Matlab is used in this work [156].

2.3 Diffraction correction

Sound diffraction effects must be corrected for if precise measurements of c_P, c_S, α_P and α_P are to be conducted using the immersion method [53, 72] or the solid buffer method [52, 54, 157]. Based on the diffraction correction model presented by Rogers and Buren [79], diffraction effects are corrected for in this work for the solid buffer method and for the immersion method.

Williams proposed a model to describe the effects of transducer diffraction [76]. The model is exact for a plane circular piston, mounted in a rigid baffle of infinite extent, vibrating with uniform velocity amplitude and phase in an infinite fluid ("baffled piston model"). Khimunin used Williams' expression to define the "diffraction correction," $H^{dif} = \frac{\langle P \rangle}{P^{pl}}$ [77, 78]. $\langle P \rangle$ is the average free-field pressure over a measurement area (with the receiver absent) a distance z from the piston source. $P^{pl} = \rho_w c_w v_0 e^{-ik_w z}$ is the plane wave at the measurement area. $k_w = \omega / c_w$ is the wavenumber in water, c_w is the sound velocity in water and v_0 is the piston particle velocity.

An approximate expression for H^{dif}, valid for $k_w a >> 1$, was found by Rogers and Buren [79]. a is the radius of the piston source and the circular measurement area.

$$\begin{aligned} H^{dif} &= \frac{\langle P \rangle}{P^{pl}} \approx 1 - e^{-i(2\pi/S)}\Big(J_0(2\pi/S) + iJ_1(2\pi/S)\Big), \\ S &= \frac{2\pi z}{k_w a^2}. \end{aligned} \tag{2.6}$$

S is referred to as the Fresnel parameter. J_0 and J_1 are the zeroth and first order Bessel function of the first kind, respectively. The diffraction correction expression of Rogers and Buren, Eq. (2.6) is based upon Williams expression [76] which is developed for wave propagation in a fluid. However, this expression has also been used to correct for diffraction effects in c_P and α_P - measurements in solids [157]. The expression has also been used to correct for diffraction effects in shear wave measurements using the solid buffer method [54] and seemingly for the immersion method [53].

In both the immersion method and in the solid buffer method, two different measurement setups are used: Measurement A without specimen inserted, and measurement B with the specimen inserted into the wave propagation path. In measurement A, Rogers and Buren's expression, Eq. (2.6), can be used directly, where k_w is the wave number of the water (when using the immersion method) or buffers (when using the solid buffer method). By dividing the Fresnel parameter, S, into two terms, one term for the water or buffers and the second term for the specimen, Eq. (2.6) can also be used for measurement B. This way Rogers and Buren's expression has been used to correct for sound diffraction effects in the immersion method [72, 53] in measurement A and B:

$$\begin{aligned} H_A^{dif} &= 1 - e^{-i(2\pi/S_A)}\Big(J_0(2\pi/S_A) + iJ_1(2\pi/S_A)\Big), \qquad S_A = \frac{2\pi D}{k_w a^2}, \\ H_B^{dif} &= 1 - e^{-i(2\pi/S_B)}\Big(J_0(2\pi/S_B) + iJ_1(2\pi/S_B)\Big), \qquad S_B = \frac{2\pi(D-d)}{k_m a^2} + \frac{2\pi d}{k_m a^2}. \end{aligned} \tag{2.7}$$

S_A and S_B are the Fresnel parameters in measurement A and B, respectively. D is the distance between the transducers and d is the specimen thickness. $k_m = k_m^P$ is the compressional wavenumber and $k_m = k_m^S$ is the shear wavenumber for the specimen. Seemingly Wu et al. [53] present Eq. (2.7) to be used for shear wave diffraction correction. Using the immersion method for shear wave measurements, the specimen is tilted to an angle, θ_i [53] (detailed in Fig. 3.16). A note is made here regarding how the tilting of the specimen affects the shear wave propagating distance L inside the specimen (L in Fig. 3.16). However, as will be seen in the plexiglas measurements in Ch. 6, the shear wave diffraction effects of the plexiglas specimen used in this work are negligible using Eq. (2.7).

Green et al. [54] defined the diffraction correction for use in solids in a similar way as Khimunin [77, 78]. The medium in which the elastic waves propagate is defined as a half space. $H^{dif} = \frac{\langle t^z \rangle}{t^{pl}}$ for compressional waves and $H^{dif} = \frac{\langle t^x \rangle}{t^{pl}}$ for shear waves. $\langle t^z \rangle$ is the average traction vector in the z-direction (compressional waves) over the measurement area and $\langle t^x \rangle$ is the average traction vector in the x-direction (shear waves) over the measurement area. A coordinate system is shown in Fig. 2.5. t^{pl} is the shear or compressional plane wave traction vector propagating from the source. In the same way as for the immersion method, the Fresnel parameter is divided into two terms, one term for the buffers and the second term for the specimen. This way Rogers and Buren's expression, Eq. (2.6) has been used to find expressions for diffraction corrections for sound diffraction effects in the solid buffer method [157]:

$$\begin{aligned} H_A^{dif} &= 1 - e^{-i(2\pi/S_A)}\Big(J_0(2\pi/S_A) + iJ_1(2\pi/S_A)\Big), \qquad S_A = \frac{2\pi 2D_b}{k_b a^2}, \\ H_B^{dif} &= 1 - e^{-i(2\pi/S_B)}\Big(J_0(2\pi/S_B) + iJ_1(2\pi/S_B)\Big), \qquad S_B = \frac{2\pi 2D_b}{k_b a^2} + \frac{2\pi d}{k_m a^2}. \end{aligned} \tag{2.8}$$

D_b is the buffer length. $k_b = k_b^z$ is the buffer compressional wave number and $k_b = k_b^x$ is the buffer shear wave number. This expression has been used in this work when measuring c_P, c_S and α_P with the solid buffer method. In the studies using Eqs. (2.7) [72, 53] and (2.8) [54, 157] the validity of the expressions are referred to Rogers and Buren [79], that is $ka >> 1$, where k is the wave number of the medium in which the waves propagate.

2.4 Simulations of electrical conductance and sound waves using Comsol Multiphysics

Comsol Multiphysics version 4.2 has been used to simulate the electrical conductance of the P-wave transducers used in this work as well as the transfer functions defined in section 5.2.1 needed for the solid buffer method simulations. The expressions obtained directly from the Comsol user's guide [158, 159] use bold symbols for vectors ($\boldsymbol{u}$). In the rest of the thesis the vector notation, $\vec{u}$ is used.

Because of the limited space inside the pressure cell, unwanted acoustic reflections from for example sidewalls will affect acoustic measurements. The simulations are used to quantize the impact of the unwanted acoustic reflections on the measured c_P and α_P inside the pressure cell. In this section, the equations solved with Comsol governing the wave propagation in the piezoelectric material, the elastic material and in fluid domains are presented. The finite element simulation models describing material data, elements/wavelength and dimensions are presented in Ch. 5. As of today, the reference manuals for version 4.2 are not accessible on-line without a license.

Piezoelectric elastic domains

In Comsol Multiphysics 4.2, the equation to be solved for the anisotropic, lossy piezoelectric domains are [159]

$$\begin{aligned} -\rho\omega^2\boldsymbol{u} &= \nabla \cdot s + \boldsymbol{F}_v, \\ \nabla \cdot \boldsymbol{D} &= \rho_v, \end{aligned} \tag{2.9}$$

with

$$\begin{aligned} s &= s_0 + C_E : (\epsilon - \epsilon_0) - e^{\mathrm{T}}\boldsymbol{E}, \\ \boldsymbol{D} &= \boldsymbol{D}_r + e(\epsilon - \epsilon_0) - \epsilon_{0,vac}\epsilon_{rS}\boldsymbol{E}, \\ \epsilon &= \frac{1}{2}(\nabla\boldsymbol{u} + (\boldsymbol{u}\nabla)^{\mathrm{T}}). \end{aligned} \tag{2.10}$$

Some of the variables used in Eqs. (2.9) and (2.10) are not easily accessible from the Comsol structural mechanics reference manual [159]. However, from the manual it is clear that ρ is the density of the solid material, ω is the angular frequency, $\boldsymbol{u}$ is the particle displacement vector, ∇ is the del-operator, s is the stress tensor, ϵ is the strain tensor. C is the stiffness tensor relating strain to stress. : is the double-dot tensor multiplication operator [159]. ρ_v is the volume charge density and is zero in this work. $\boldsymbol{D}$ is the electrical displacement field. $\epsilon_{0,vac}$ is the permittivity in vacuum (ϵ is used as both permittivity and as strain). In the reference manual, ϵ_{rS} is defined as "the relative permittivity used on stress-charge form." e is the piezoelectric coefficient tensor. In the reference manual [159], C is defined as the stiffness tensor. C_E is assumed to be the stiffness tensor in the piezoelectric material at constant electric field, $\boldsymbol{E}$. $\boldsymbol{D}_r$ is defined as the remnant electric displacement.

The other symbols used in Eq. (2.12) and (2.13) were not found in the Comsol reference manual [159] by this author. However, $\boldsymbol{F}_v$ is assumed to by body-forces, s_0 and ϵ_0 are assumed to describe the initial stress and strain, respectively. All the terms $\boldsymbol{F}_v$, s_0, ϵ_0 and $\boldsymbol{D}_r$ are assumed to be set to zero by Comsol Multiphysics. To avoid confusion with strain and permittivity in the notation, stress is renamed to τ, strain is renamed to S, giving the equations

$$\begin{aligned}
\rho\frac{\partial^2 u_i}{\partial t^2} &= \tau_{ij,j}, \\
D_{i,i} &= 0, \\
\tau_{ij} &= C^E_{ijkl}S_{kl} - e_{kij}E_k, \\
D_i &= e_{ikl}S_{kl} - \epsilon^S_{ik}E_k,
\end{aligned} \tag{2.11}$$

In the diffraction correction description (Sect. 2.3) and in the system models presented in Ch. 3, x, y and z are used to describe the cartesian coordinates. Due to the heavy notation needed to describe the elastic waves in this section and in Sect. 2.5, Einstein's notation is used instead of x, y and z-coordinates ($x_1 = x$, $x_2 = y$ and $x_3 = z$). In Eq. (2.14), Einstein's summation convention is used and the comma symbol with an index defines the spatial derivative. i, j, k and l are summation indices. τ_{ij}, S_{ij} and u_i are the stress tensor, strain tensor and particle velocity vector, respectively. C^E_{ijkl} is the stiffness tensor at constant electrical field. D_i is the electrical displacement field, ϵ^S_{ik} is the permittivity at constant strain, e_{ikl} is the piezoelectric charge coefficient tensor and E_k is the electrical field. The equation of continuity lies implicit in the derivation of the first equation in Eq. (2.11) [160]. Loss is implemented using complex stiffness tensor. Complex tensors for C^E_{ijkl}, ϵ^S_{ik} and e_{ikl} are defined for the anisotropic lossy elastic piezoelectric domains.

Isotropic, viscoelastic domains

In Comsol Multiphysics 4.2, the equation to be solved for the isotropic, viscoelastic domains are [159]

$$-\rho\omega^2\boldsymbol{u} = \nabla \cdot s + \boldsymbol{F}_v, \tag{2.12}$$

with

$$\begin{aligned} s &= s_0 + C : (\epsilon - \epsilon_0 - \epsilon_{inel}) \\ \epsilon &= \frac{1}{2}(\nabla\boldsymbol{u} + (\boldsymbol{u}\nabla)^{\mathrm{T}}). \end{aligned} \tag{2.13}$$

Eq. (2.12) is the same as in Eq. (2.9). The variables are already defined for the piezoelectric elastic domains above except from ϵ_{inel}, which is assumed to describe inelastic strain components. This parameter is assumed to be set to zero by Comsol Multiphysics. Using the same assumptions as for the piezoelectric elastic domains above the, this can be written

$$\begin{aligned} \rho\frac{\partial^2 u_i}{\partial t^2} &= \tau_{ij,j}, \\ \tau_{ij} &= C_{ijkl}S_{kl}, \\ S_{kl} &= \frac{1}{2}(u_{i,j} + u_{j,i}). \end{aligned} \tag{2.14}$$

For the isotropic viscoelastic materials, the components of the stiffness tensor can be described with two complex Lamé-constants. To calculate the Lamé-constants, a complex c_P and c_S are defined for the isotropic viscoelastic domains.

Fluid domains

In this work, the "linear elastic with attenuation" fluid model in the acoustics fluid module in Comsol Multiphysics 4.2, defines the fluid elements [158]. In this fluid model, no viscosity but a complex compressional velocity (c) is defined for the lossy fluid elements. In Comsol the equation to be solved for the fluid domains are given [158]

$$-\nabla \cdot \frac{1}{\rho_c}(\nabla p - \boldsymbol{q}_d) - \frac{k_{eq}^2 p}{\rho_c} = Q_m, \tag{2.15}$$

with

$$\begin{aligned} p &= p_0 + p', \\ k_{eq}^2 &\equiv (\frac{\omega^2}{c_c})^2, \\ c_c &\equiv c, \\ \rho_c &\equiv \rho. \end{aligned} \tag{2.16}$$

ρ is here the fluid density, p is the total pressure, p_0 the static pressure, p' is the dynamic pressure and c is the compressional wave velocity in the fluid [158]. Q_m is defined as the monopole source term and q_d is defined to be the dipole source term. Both Q_m and q_d are assumed to be set to zero by Comsol in this work. Some of this notation may seem to be unnecessary, however, no effort is done by this author to explain the reason behind the notation and why e.g. the fluid velocity is defined $c_c \equiv c$. By not defining p_0, this is assumed to be set to zero by Comsol. By using the equation of continuity [160], Eq. (2.15) may be written as

$$\frac{1}{c}\frac{\partial^2 p}{\partial t^2} = p_{,ii} \tag{2.17}$$

Boundary conditions

To solve the equations governing the wave propagation in the piezoelectrc domains, the elastic domains and in the fluid domains, appropriate boundary conditions must be applied.

Comsol Multiphysics solves the set of equations 2.14, 2.11 and 2.17 using the finite element method [159, 158]. To solve the wave equation between two media, boundary conditions must be applied. A rigorous definition of these boundary conditions have not been found by this author in the structural or acoustics reference manuals [159, 158].

However, for the solid-solid and solid-fluid interfaces, the displacement and the traction vectors must be continuous through the boundary [160]. The outer boundaries of the solids are in this work oscillating freely. In Comsol Multiphysics reference manual [159] this boundary condition is called "free" and on these boundaries the normal component of the traction vector is zero. On the boundaries outside fluid domains, the boundary is called "hard" [158] and on these boundaries, the normal component of the displacement vector is defined to be zero. Across the electrodes of the piezoelectric element of the transmitting transducer, the electrical potential 1 V is applied in this work. The simulation setup for the Comsol models used in this work are presented in Ch. 5.

2.5 Numerical model to model hydrate growth in Bentheim sandstone

Waite et al. [22] and Winters et al. [21] outlined three main categories in which hydrates may form inside a porous rock or sandy sediment. The first main category is hydrate forming primarily in the pore fluid. For this hydrate-growth scenario the "HFl"-model is used in this work, which is based on Helgerud et al.'s "hydrates in fluid model" [24].

Two versions of the HFl-model is implemented in this work: HFlU-model, where the gas and water are uniformly distributed in the sandstone pores and the HFlP-model where the gas and water are distributed separately in patches. In the HFlP-model, the gas hydrates grow in the water-filled pores.

The second way hydrates can grow in a sandstone is becoming a load-bearing member of the dry frame, acting as second type of sediment grain. For this hydrate-growth scenario the "HFr"-model is used in this work, which is based on Helgerud et al.'s "frame building model" [24]. As for the HFl-model, two versions of the HFr-model is implemented: HFrU-model, where the gas and water are uniformly distributed in the sandstone pores and the HFrP-model where the gas and water are distributed separatley in pathces.

The third way hydrates can grow in a sandstone is if hydrates act as cement around grain contacts, stiffening the dry frame. For this hydrate-growth scenario, Aveth et al.'s "constant cement model" [27] is used. This model is labeled "HC" in this work. As for the HFl-model and the HFr models, two versions of the HC-model is implemented: HCU-model, where the gas and water are uniformly distributed in the sandstone pores and the HCP-model where the gas and water are distributed separately in patches.

All these three models (HFl, HFr and HC) are based upon the work of Dvorkin et al. [25, 26]. A schematic of these models is shown in Fig. 2.3. In the models presented by Helgerud et al. [24] the initial dry frame bulk modulus and the dry frame shear modulus (before hydrate growth) where calculated with yet another model, the Hertz-Mindlin model [120]. In this work, however, fixed dry frame bulk and shear moduli are used so that the models fit the measurements conducted on Bentheim sandstone specimen better. These are the dry frame bulk ($K_{sm,0}$) and shear moduli ($\mu_{sm,0}$) before hydrate growth.

These three models (two versions of each model) are purely elastic, meaning no loss is present. To model and discuss α_P and the dispersion of c_P during hydrate growth, the "BiotHFrU," "BiSqHFrU", "WaTrHFrU" and the "WaTrBiSqHFrU"-models are used. "BiotHFrU" simulates hydrates growing into the frame, includes loss due to global flow and is based on the HFrU-model and the Biot theory [23, 161]. "BiSqHFrU" simulates hydrates growing into the frame, includes loss due to squirting flow and global flow and is based on the HFrU-model and Dvorkin et al's combined squirting flow and global flow theory [55]. In Fig. 2.4 a schematic of squirting flow and Biot flow is shown.

"WaTrHFrU" simulates hydrates growing into the frame, includes multiple scattering effects inside the sandstone and is based on the HFr-model and Waterman and Truell's multiple scattering theory [56]. "WaTrBiSqHFrU" is purely a combination between the BiSqHFrU and the WaTrHFrU-models. The WaTrBiSqHFrU-model include loss-mechanisms due to both scattering and pressure induced fluid flow effects. No schematic of the multiple scattering effect is given here. However, space not occupied by quarz grains or hydrate in Fig. 2.3 A), are treated as spherical scatters of different size in the WaTrBiSqHFrU and the WaTrHFrU-models.

All these seven models are used in Ch. 7 to discuss the experimental results. The models are detailed below. In the hydrate bearing Bentheim sandstone, the contents of water, gas, pure quartz and hydrates are assumed to be given:

$$\phi_w + \phi_g + \phi_H + \phi_q = 1. \tag{2.18}$$

$\phi_q = 0.76$ is the typically quartz volume fraction in Bentheim sandstone [162]. The volume fraction of hydrates, ϕ_H, is defined as an input vector ranging from zero to 0.24. ϕ_g and ϕ_w are the volume fractions of gas and water, respectively. The initial water (ϕ_{w0}) and gas volume fractions are known. Water forms into hydrate and expand by a factor 1.26 (see section 2.1). In this work it is assumed that hydrates expand into gas-regions, pushing some of the methane gas out of the sandstone. This process is assumed to go on until (almost) all the methane gas is pushed out of the sandstone. When the methane gas inside the sandstone is depleted, water will be pushed out of the sandstone. Thus, depending on ϕ_H, two regimes of calculating the volume fractions of water (ϕ_w) and gas (ϕ_g) have been implemented in this work:
When methane gas is available inside the sandstone, $\phi_g > 0$:

$$\begin{aligned} \phi_w &= \phi_{w0} - S_H/1.26\beta, \\ \phi_g &= 1 - \phi_q - \phi_H - \phi_w. \end{aligned} \tag{2.19}$$

β is the porosity. When (almost) all the methane gas is pushed out of the sandstone and $\phi_g \to 0$ in Eq. (2.19), ϕ_w is calculated:

$$\phi_w = 1 - \phi_q - \phi_H - \phi_g. \tag{2.20}$$

The volume fractions ϕ_w, ϕ_q, ϕ_H and ϕ_g are calculated with these equations during the hydrate growth process and used in the following numerical models as input parameters. To the best of this author's knowledge, this way of calculating ϕ_w, ϕ_q, ϕ_H and ϕ_g has not been reported. Important input parameters for the numerical models used in this work are given in Tab. 2.1. These parameters together with a few others defined when the specific model is used give the basis for the numerical models used in this work.

Table 2.1: List of important parameters used in the numerical models.

Parameter	Description
$\phi_q = 0.76$	Volume fraction of quartz
$\rho_w = 1000$ kg/m^3	Density water [55]
$\rho_g = 70$ kg/m^3	Density methane gas at 83 bar [163]
$\rho_q = 2650$ kg/m^3	Density quartz [55]
$\rho_H = 850$ kg/m^3	Density methane hydrate [86]
$K_w = 2.25$ Gpa	Bulk modulus of water [55]
$K_g = 11$ Gpa	Bulk modulus of methane gas at 4°C, 83 bar [163]
$K_q = 38.7$ Gpa	Bulk modulus of quartz [55]
$K_H = 7.7$ Gpa	Bulk modulus of methane hydrate [86]
$\beta_0 = 0.24$	Porosity of Bentheim sandstone before hydrate growth [162]
$\beta_c = 0.40$	Critical porosity of sandpack
$K_{sm,0} = 11$ Gpa	Initial dry frame bulk modulus
$\mu_{sm,0} = 8$ Gpa	Initial dry frame shear modulus
$\mu_q = 39.6$ Gpa	Shear modulus of quartz [55]
$\mu_H = 3.2$ Gpa	Shear modulus of methane hydrate [86]
$\eta_g = 12.9$ µPa s	Viscosity of methane gas at 4°C, 83 bar [163]
$\eta_w = 1.8$ mPa s	Viscosity of water at gas at 4°C [38]
$n_e = 9$	Number of grain contacts per grain [26]
$h = 170$ µm	Diameter of quartz grains [55]
$\kappa_{s0} = 1.1$ D	Permeability in Bentheim sandstone before hydrate growth [83]
$\rho_{12} = -420$ kg/m^3	Fluid-solid mass coupling parameter [55]

As argued in Sec. 1.6, accurate modeling of the elastic wave propagation in a sandstone during hydrate growth is a formidable task. The models presented in this section simplify the complex nature of a sandstone. A thorough analysis on the accuracy of the different models is not performed in this work. However, models based on the same principles as the HFl, HFr and HC - models are widely used to model c_P and c_S in hydrate bearing sediments for both low measurement frequencies (<20 kHz) [164] and for higher measurement frequencies (approximately 500 kHz) [22, 21, 34].

Attempts to model the attenuation in hydrate bearing sediments from well logs have been seen in the literature [39]. No attempt have been found by this author to model attenuation in hydrate bearing sediments in laboratory studies. The BiSqHFrU and the WaTrHFrU models are based on modeling attenuation mechanisms due to pressure induced fluid flow and scattering of elastic waves, respectively, which are attenuation mechanisms known to exist in sandstones [55, 41, 165].

The models are used to qualitatively discuss the measured c_P and c_S and which attenuation mechanisms that might be present in the sandstones used in this work.

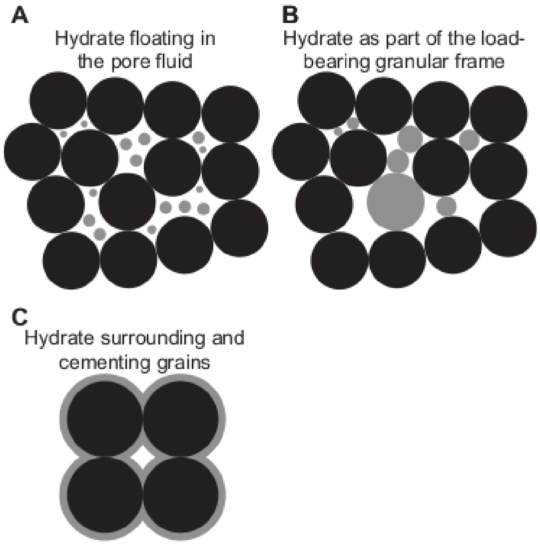

Figure 2.3: A schematic of hydrate growth models [22]. In A, the hydrates from in the pore fluid (HFl). In B, hydrates grow into the frame, acing as a second grain (HFr). In C, hydrates evenly coat grains, cementing them together (HC).

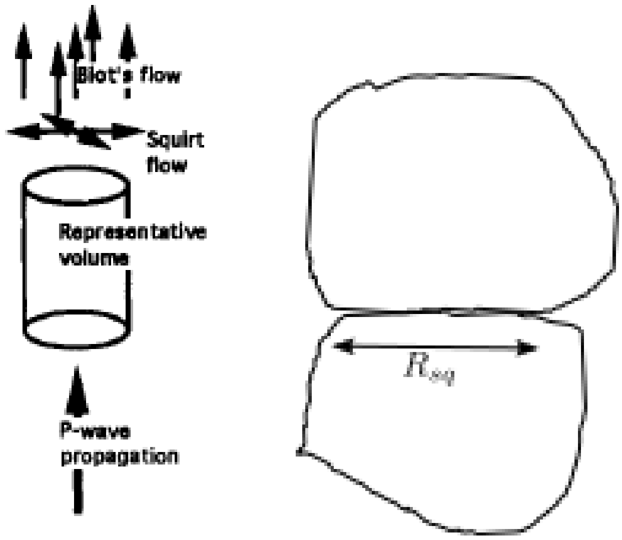

(a) (b)

Figure 2.4: Schematic for the Biot-squirt model [55]. a) An illusttration of the Biot flow and the squirt flow as presented by Dvorkin and Nur [55]. In this work, the ”Representative volume” is described with the HFr-model. The P-wave is attenuated due to the Biot flow and the squirt flow. b) An illustration of the squirting length parameters, R_{sq} used in the models treating squirting flow.

2.5.1 Hydrates only forming in the fluid: HFl-model

In this work, the HFl-model is used to find c_P and c_S (Eq. (2.21)) for the hydrate-bearing Bentheim sandstone when hydrates only form in the fluid (See Fig. 2.3 A)). The effective bulk and shear moduli, K_{eff} and μ_{eff}, respectively, are found based on the Gassman's equation [42]. The hydrates only affect the bulk modulus of the fluid. The model is derived by Helgerud et al. [24]. However, while Helgerud et al. [24] used the Hertz-Mindlin model [120] to calculate the dry frame moduli, $K_{sm,0}$, and $\mu_{sm,0}$ are set to 11 Gpa and 8 Gpa, respectively, so that the models fit the measurements conducted on Bentheim sandstone specimen better.

Like Helgerud et al. [24], two different versions of the HFl-model (HFlU and HFlP) are used in this work. Both use Eq. (2.21), but in his work the effective saturated bulk and shear moduli, K_{eff} and μ_{eff}, respectively, are calculated differently.

$$\begin{aligned} c_S &= \sqrt{\frac{\mu_{eff}}{\rho_{tot}}}, \\ c_P &= \sqrt{\frac{K_{eff} + \mu_{eff}4/3}{\rho_{tot}}}. \end{aligned} \tag{2.21}$$

The total density, ρ_{tot} is defined

$$\rho_{tot} = \phi_w \rho_w + \phi_g \rho_g + \phi_H \rho_h + \phi_q \rho_q. \tag{2.22}$$

ρ_w, ρ_g, ρ_h and ρ_q are the densities of water, gas, hydrate and quartz, respectively. ϕ_w and ϕ_g are calculated with Eqs. 2.19 and 2.20.

The HFlU-model: hydrates growing in the fluid with uniform gas and water distribution

In the first version, hydrates form uniformly only in the pore fluid and an effective fluid bulk modulus, K_f, is calculated using the Reuss average [97], Eq. (2.23).

$$K_f = \Big(\frac{S_w}{K_w} + \frac{S_g}{K_g} + \frac{S_H}{K_H}\Big)^{-1}. \tag{2.23}$$

S_w, S_g, S_H are the water, gas and hydrate saturations, respectively. K_w, K_g, and K_H are the bulk moduli of water, gas and hydrate, respectively. Using K_f as the fluid bulk modulus, the total effective saturated bulk modulus, K_{eff}, is found with the Gassmann's equation (Eq. (2.24)):

$$\begin{aligned} K_{eff} &= K_s \frac{\beta K_{sm} - (1+\beta) K_f K_{sm}/K_s + K_f}{(1-\beta)\beta K_f + \beta K_s - K_f K_{sm}/K_s}, \\ \mu_{eff} &= \mu_{sm}. \end{aligned} \tag{2.24}$$

β is the porosity. Since hydrates are only forming in the pore fluid, the solid bulk modulus is the quartz bulk modulus and the dry frame bulk and shear moduli are equal to $K_{sm,0}$ and $\mu_{sm,0}$, respectively. That is

$$\begin{aligned} K_{sm} &= K_{sm,0}, \\ \mu_{sm} &= \mu_{sm,0}, \\ K_s &= K_q. \end{aligned} \tag{2.25}$$

K_q is the pure quartz bulk modulus. Calculating c_P and c_S with Eq. (2.21) using Eqs. (2.23), (2.24) and (2.25) is in this work called the HFlU-model.

The HFlP-model: hydrates growing in the water with the gas and water distributed in patches

If the hydrates are growing in the water and the gas is separately distributed in patches, Helgerud et al. [24] proposed the following formula for K_{eff} and μ_{eff}:

$$\begin{aligned} \frac{1}{K_{eff} + \frac{4}{3}\mu_{eff}} &= \frac{S_w + S_H}{K_{sat,wH} + \frac{4}{3}\mu_{sat,wH}} + \frac{S_g}{K_{sat,g} + \frac{4}{3}\mu_{sat,g}}, \\ \mu_{eff} &= \mu_{sat,wH} = \mu_{sat,g} = \mu_{sm,0}. \end{aligned} \tag{2.26}$$

$K_{sat,wH}$ and $\mu_{sat,wH}$ are the bulk and shear moduli, respectively of the sediment fully saturated with the hydrate-water fluid mix having bulk modulus $K_{wH} = \left(\frac{S_w}{(S_w+S_H)K_w} + \frac{S_H}{(S_w+S_H)K_H}\right)^{-1}$. $K_{sat,g}$ and $\mu_{sat,g}$ are the bulk and shear moduli, respectively of the sediment fully saturated with the gas having bulk modulus K_g. Because the fluid does not support shear waves, the saturated shear frame modulus is the same as the dry shear modulus, $\mu_{eff} = \mu_{sat,wH} = \mu_{sat,g} = \mu_{sm,0}$.

Gassman's equation, Eq. (2.24) is used to obtain $K_{sat,wH}$ using $K_f = K_{wH}$ and to obtain $K_{sat,g}$ using $K_f = K_g$. As in the HFlU-model, the fluid is not affecting the dry frame bulk or shear modulus and thus Eq. (2.25) is used in the calculations.

Calculating c_P and c_S with Eq. (2.21) using Eq. (2.26) and $\mu_{eff} = \mu_{sm} = \mu_{sm,0}$ is in this work called the HFlP-model.

2.5.2 Hydrates growing in the dry frame, acting as a second grain: HFr-model

To model hydrates growing in a sandstone and become a load-bearing member of the dry frame, acting as second type of sediment grain, the HFr-model is used (See Fig 2.3 B)). The model was derived by Helgerud et al. [24] as in the Hfl-model, $K_{sm,0}$, and

$\mu_{sm,0}$ are set to 11 Gpa and 8 Gpa, respectively, so that the model fit the measurements conducted on Bentheim sandstone specimen better.

In the same way as for the HFl-model, K_{sm} is used with the Gassmann's equation to calculate c_P and c_S. However, the dry frame modulus, K_{sm} is now altered due to hydrate growth. It is described with the modified Hashin-Strikman lower bound model [26], Eq. (2.27).

As for the HFl-model, two different versions of the HFr-model (HFrU and HFrP) are used in this work. Both use Eq. (2.27) but the fluid affects the saturated bulk modulus in the HFrU and HFrP-models differently.

$$K_{sm} = \Big[\frac{\beta/\beta_0}{K_{sm,0} + 4/3\mu_{sm,0}} + \frac{1-\beta/\beta_0}{K_s + 4/3\mu_{sm,0}}\Big]^{-1} - 4/3\mu_{sm,0},$$

$$\mu_{sm} = \Big[\frac{\beta/\beta_0}{\mu_{sm,0} + Z} + \frac{1-\beta/\beta_0}{\mu_s + Z}\Big]^{-1} - Z, \tag{2.27}$$

$$Z = \frac{\mu_{sm,0}}{6}\Big(\frac{9K_{sm,0} + 8\mu_{sm,0}}{K_{sm,0} + 2\mu_{sm,0}}\Big).$$

When hydrate grows, the porosity, β, of the rock will decrease. The modified Hashin-Strikman lower bound model [26] is a heuristic model giving $K_{sm} = K_{sm,0}$ and $\mu_{sm} = \mu_{sm,0}$ at $\beta = \beta_0$. β_0 is the porosity before hydrate growth. $K_{sm,0} = 11$ Gpa and $\mu_{sm,0} = 8$ Gpa are the dry frame bulk and shear moduli, respectively, before hydrate growth. The model gives $K_{sm} = K_s$ and $\mu_{sm} = \mu_s$ at $\beta = 0$. K_s and μ_s are the effective mineral bulk and shear moduli, respectively, calculated with the Hill average [100]:

$$\begin{aligned} K_s &= \frac{1}{2}\Big[\frac{\phi_q}{\phi_q + \phi_H}K_q + \frac{\phi_H}{\phi_q + \phi_H}K_H + \Big(\frac{\phi_q}{\phi_q + \phi_H}\frac{1}{K_q} + \frac{\phi_H}{\phi_q + \phi_H}\frac{1}{K_H}\Big)^{-1}\Big], \\ \mu_s &= \frac{1}{2}\Big[\frac{\phi_q}{\phi_q + \phi_H}\mu_q + \frac{\phi_H}{\phi_q + \phi_H}\mu_H + \Big(\frac{\phi_q}{\phi_q + \phi_H}\frac{1}{\mu_q} + \frac{\phi_H}{\phi_q + \phi_H}\frac{1}{\mu_H}\Big)^{-1}\Big]. \end{aligned} \tag{2.28}$$

μ_q and μ_H are the shear moduli of pure quartz and hydrate, respectively.

The HFrU-model: hydrates growing the frame with uniform fluid and hydrate distrubution

In this version, an effective fluid bulk modulus, K_f, is calculated using the Reuss average [97] of water and gas:

$$K_f = \Big(\frac{S_w}{K_w} + \frac{S_g}{K_g}\Big)^{-1}, \tag{2.29}$$

Using Eqs. (2.21), (2.24), (2.27) and (2.29) to calculate c_P and c_S is in this work called the HFrU-model.

The HFrP-model: hydrates growing the frame with gas and water distributed in patches

If the water and gas are located separately in patches and are not uniformly distributed, Helgerud et al. [24] proposed the following formula for K_{eff} and μ_{eff}:

$$\begin{aligned} \frac{1}{K_{eff}+\frac{4}{3}\mu_{eff}} &= \frac{S_w}{K_{sat,w}+\frac{4}{3}\mu_{sat,w}}+\frac{S_g}{K_{sat,g}+\frac{4}{3}\mu_{sat,g}}, \\ \mu_{eff} &= \mu_{sm}. \end{aligned} \tag{2.30}$$

$K_{sat,w}$ and $\mu_{sat,w}$ are the bulk and shear moduli, respectively, of the sediment fully saturated with water. $K_{sat,g}$ and $\mu_{sat,g}$ are the bulk and shear moduli, respectively of the sediment fully saturated with the gas having bulk modulus K_g. These are calculated with Eq. (2.24) using Eq. (2.27) and (2.28).

Using Eqs. (2.21), (2.30) and $\mu_{eff} = \mu_{sm}$ from Eq. (2.27) to calculate c_P and c_S, is in this work called the HFrP-model.

2.5.3 Hydrates cementing grains: HC-model

A third way hydrates can grow in a sandstone is if hydrates act as cement around grain contacts, stiffening the dry frame. For this hydrate-growth scenario, Avseth et al.'s "constant cement model" is used [27] (see Fig. 2.3 C)). The model is based on Dvorkin et al's cement model [25] which is developed for unconsolidated sand-packs. In this work, this model is labeled the HC-model. As $K_{sm,0}$ and $\mu_{sm,0}$ are not input parameters in this model, no attempt is done to fit this model to the Bentheim sandstone measurements.

There are also two different versions of the HC-model: The HCU-model where the fluid is distributed uniformly in the sandstone and the HCP-model where the water and gas is distributed in seperate patches.

Dvorkin's cementing model [25] is based on Digby's contact theory [104] and how added cement affects the grain-grain contact. The model make use of the concept of critical porosity: the porosity, β_c, of an unconsolidated pack of grains in which grain-grain contact exist. At lower porosities than the critical, the excess material is either located around or away from the grain-grain contacts. In Dvorkin's cementing model, all excess material is located around the grain contacts, thus cementing them together, giving a bulk modulus and shear modulus for the cemented sand-pack

$$\begin{aligned} K_{sm,D} &= \frac{n_e(1-\beta_c)(K_H + 4/3\mu_H)S_n}{6}, \\ \mu_{sm,D} &= \frac{3K_D}{5} + \frac{n_e(1-\beta_c)\mu_H S_\tau}{20}. \end{aligned} \tag{2.31}$$

$n_e \approx 9$ is the number of contact points between the mineral grains [25]. Dvorkin et al. use Digby's contact theory [104] to calculate the normal grain-grain stiffness, S_n, and the tangential grain-grain stiffness, S_τ, between spheres cemented together. A pack of such spheres with $n \approx 9$ number of contacts per grains and with porosity β_c has a dry frame bulk modulus $K_{sm,D}$ and a dry frame shear modulus $\mu_{sm,D}$. The cementing material is hydrate. Dvorkin et al. [25] give approximate expressions for the normal grain-grain stiffness, S_n, and the tangential grain-grain stiffness, S_τ with an error margin less than 1%:

$$\begin{aligned} S_n &= A_n(\Lambda_n)\alpha^2 + B_n(\Lambda_n)\alpha + C_n(\Lambda_n), \\ S_\tau &= A_\tau(\Lambda_\tau, \nu)\alpha^2 + B_\tau(\Lambda_\tau, \nu)\alpha + C_\tau(\Lambda_\tau, \nu), \\ A_n(\Lambda_n) &= -0.024153\Lambda_n^{-1.3646}, \\ B_n(\Lambda_n) &= 0.20405\Lambda_n^{-89008}, \\ C_n(\Lambda_n) &= 0.00024649\Lambda_n^{-1.9846}, \\ A_\tau(\Lambda_\tau, \nu_q) &= -10^{-2} \cdot (2.26\nu_q^2 + 2.07\nu_q + 2.3) \cdot \Lambda_\tau^{0.079\nu_q^2 + 0.1754\nu_q - 1.342}, \\ B_\tau(\Lambda_\tau, \nu_q) &= (0.0573\nu_q^2 + 0.0937\nu_q + 0.202) \cdot \Lambda_\tau^{0.0274\nu_q^2 + 0.0529\nu_q - 0.8765}, \\ C_\tau(\Lambda_\tau, \nu_q) &= 10^{-4} \cdot (9.654\nu_q^2 + 4.945\nu_q + 3.1) \cdot \Lambda_\tau^{0.01867\nu_q^2 + 0.4011\nu_q - 1.8186}, \\ \Lambda_n &= \frac{2\mu_H}{\pi\mu_q}\frac{(1-\nu_q)(1-\nu_H)}{1-2\nu_H}, \\ \Lambda_\tau &= \frac{\mu_H}{\pi\mu_q}, \\ \alpha &= 2\Big[\frac{\beta_c - \beta_D}{3n(1-\beta_c)}\Big]^{0.25}. \end{aligned} \tag{2.32}$$

ν_H is Poisson's ratio of hydrate. ν_q is Poisson's ratio of quartz. α is a parameter describing an evenly distributed cementing layer coating the quartz grains. After the cementing hydrate is added, the porosity is reduced to β_D. For details, refer to the study of Dvorkin et al. [25]. In Dvorkin et al.'s paper [25], other cementation schemes are also presented, giving other values for α.

Avseth et al. [27] combined Dvorkin et al.'s [25] cement model with the modified Hashin-Strikman lower bound (equation 2.27) to model the dry frame of cemented sandstones with a porosity β. In this way of using the modified Hashin-Strikman lower bound, K_{sm} and μ_{sm} are substituted with $K_{sm,D}$ and $\mu_{sm,D}$, respectively. β_0 is substituted with β_b. Now $K_{sm} = K_{sm,D}$ and $\mu_{sm} = \mu_{sm,D}$ at $\beta = \beta_D$, and $K_{sm} = K_s$ and $\mu_{sm} = \mu_s$ at $\beta = 0$.

$$K_{sm} = \Big[\frac{\beta/\beta_D}{K_{sm,D} + 4/3\mu_{sm,D}} + \frac{1-\beta/\beta_D}{K_s + 4/3\mu_{sm,D}}\Big]^{-1} - 4/3\mu_{sm,D},$$

$$\mu_{sm} = \Big[\frac{\beta/\beta_D}{\mu_{sm,D} + Z} + \frac{1-\beta/\beta_D}{\mu_s + Z}\Big]^{-1} - Z, \tag{2.33}$$

$$Z = \frac{\mu_{sm,D}}{6}\Big(\frac{9K_{sm,D} + 8\mu_{sm,D}}{K_{sm,D} + 2\mu_{sm,D}}\Big).$$

K_s and μ_s are given with Eq. (2.28).

The HCU-model: hydrates acting as cement with uniform fluid and hydrate distrubution

In this version, an effective fluid bulk modulus, K_f, is calculated using the Reuss average, Eq. (2.29). Using Eqs. (2.21), (2.24), (2.33) and (2.29) to calculate c_P and c_S is in this work called the HCU-model.

The HCP-model: hydrates acting as cement with gas and water distributed in patches

If the water and gas are located separately in patches and are not uniformly distributed, Helgerud et al's. [24] Eq. (2.30) for calculating K_{eff} and μ_{eff} can be used

In this version, the water and gas are distributed separately in patches. Using Eqs. (2.21) and (2.33) with $\mu_{eff} = \mu_{sm}$ from Eq. (2.33) and K_{eff} fraom Eq. (2.30) to calculate c_P and c_S, is in this work called the HCP-model.

2.5.4 Biot's model during hydrate growth with uniform fluid and hydrate distrubution (BiotHFrU)

In this work the Biot theory [23] is used to discuss the measured developement of attenuation and dispersion curves during hydrate growth. Biot's theory is a framework governing the wave propagation in fluid saturated porous media [23]. Fluid flow induced by the pressure-wave give rise to attenuation of the propagating wave (See Fig 2.4). At static conditions, there are no fluid flow and the Biot model breaks down to the Gassmann equation [42]. In the same way as Gassman's equation 2.24, Biot's model relies on determining the dry frame modulus, K_{sm} and the fluid bulk modulus K_f. In this work K_{sm} and K_f is found in the same way as in the HFrU-model.

The Biot theory only considers fluid flow parallel to the wave propagation direction. This type of fluid flow is called "global flow" or "Biot flow" [55]. Studies have shown that in a porous rock, there may be many compliant cracks [41, 128, 55]. These compliant cracks are very sensitive to the pressure changes induced by the acoustic wave, and fluid will flow in and out of the cracks. This flow is called "local flow" or "squirt flow." Squirt flow is considered in section 2.5.5. In the original Biot model [23], the pores are assumed to be circular tubes where in the fluid flows according to Poiseuille's law. Above a certain frequency, $f_t = \frac{\pi \eta_f}{4h^2 \rho_f}$, where h is the diameter of the tubes, η_f is the fluid viscosity and ρ_f is the fluid density, the Poiseuille flow breaks down. For pores with diameter 150 µ, f_t =62 Hz which is far below the frequencies used in this work. Biot extended his model to be valid for frequencies above f_t by defining a parameter describing the deviation from Poiseuille flow, F. $\eta_f = F\eta_{f0}$, where η_{f0} is the fluid viscosity. η_f is in this work called the dynamic fluid viscosity. The equations describing this factor, F, are given in Eqs (3.16), (3.17) and (3.19) in Biot's second paper in 1956 [161]. There seems to be an inconsistency due to a typing error in Eq. (3.17), and the factor F is not successfully implemented in this work using the equations from Biot's paper. However, a numerical implementation of the factor F is presented by Leclaire [93] and has also been used by others [39, 38]. This numerical implementation is used in this work:

$$\begin{aligned} F(\xi) &= \frac{1}{2} + \frac{1}{12}(2\xi + e^{-0.7178(\xi - 3.2)}) + i\frac{1}{6}, \\ \xi &= \frac{h}{2}\sqrt{\frac{\omega \rho_f}{\eta_{f0}}}. \end{aligned} \tag{2.34}$$

Gei et al. [147] give the effective fluid viscosity, η_{f0}:

$$\eta_{f0} = S_w \eta_w + S_g \eta_g. \tag{2.35}$$

η_w and η_g are the water and gas viscosities, respectively. The fluid flow is governed by the viscosity of the fluid, η_f, and the permeability of the sandstone κ_s. While hydrates grow inside the pores of the sandstone, the permeability is altered substantially [166, 167, 168]. κ_s of the hydrate-bearing sandstone now depends on the hydrate growth pattern, i.e whether hydrates grow on pore walls, or if the hydrates float around in the pore fluid or if hydrates grow in pore throats, plugging the passage of the fluid flow. A precise description of this permeability is complex and empirical models are typically used for different growth patterns [166, 167, 168]. In Eq. (2.36), a simple model for the permeability in a hydrate-bearing porous rock is presented [166]. $\kappa_0 = 1.1$ Darcy is the permeability for Bentheim sandstone without hydrate growth. For $N_{perm} = 2$, this models describes the situation in which hydrates coat the cylindrical walls with a uniform layer. From Eq. (2.36), $N_{perm} = 0$ gives $\kappa_s = \kappa_0$ and the hydrates have no affect on the permeability. At $N_{perm} = 0$, all hydrates are thus assumed to be forming in the pore fluid, not affecting the permeability. For $N_{perm} > 2$, the hydrates are plugging the pores in a more efficient way than when hydrates coat the cylindrical walls with a uniform layer. Thus, when $N_{perm} > 2$, hydrates are growing in the frame, blocking the fluid flow. κ_s is given [166]

$$\kappa_s = \kappa_0(1 - S_H)^{N_{perm}}. \tag{2.36}$$

N_{perm} is a paramter used to fit the model with measurements.

A review of the Biot's theory [23] is given here. Biot developed his theory by considering the motion along the x_1-direction in a cartesian coordinate system. He used the Lagrange equation to obtain the equations of motion in the solid and in the fluid.

$$\begin{aligned} \frac{\partial}{\partial t}\Big(\frac{\partial L}{\partial \dot{u}_1}\Big) - \frac{\partial L}{\partial u_1} &= 0, \\ \frac{\partial}{\partial t}\Big(\frac{\partial L}{\partial \dot{U}_1}\Big) - \frac{\partial L}{\partial U_1} &= 0. \end{aligned} \tag{2.37}$$

$L = T - V$ is the lagrangian where T is the kinetic energy and V is the total potential energy. $\dot{u}_1$ and $\dot{U}_1$ are the time derivative of the particle velocities in the x_1-direction for the solid and the fluid, respectively. The total potential energy can be written as $V = V_l + V_d$ where V_l is the elastic potential energy and V_d is defined by Leclaire [93] as the loss in potential energy due to dissipation. Only the kinetic energy in the Lagrangian is dependent on the particle velocity ($\dot{u}_1$, $\dot{U}_1$) and thus the potential energy cancels out in the first terms in Eq. (2.37). Only the potential energy in the Lagrangian is dependent on the particle displacement (u_1, U_1) and thus the kinetic energy cancels out in the second terms in the equations 2.37. The elastic forces in the solid and the fluid, respectively, are defined q_1 and Q_1. The dissipation forces in x_1-direction for the solid and the fluid are defined f_{1d} and F_{1d}, respectively.

$$\begin{aligned} q_1 &= -\frac{\partial V_l}{\partial u_1}, & f_{1d} &= -\frac{\partial V_d}{\partial u_1} = -\frac{\partial D}{\partial \dot{u}_1}, \\ Q_1 &= -\frac{\partial V_l}{\partial U_1}, & F_{1d} &= -\frac{\partial V_d}{\partial U_1} = -\frac{\partial D}{\partial \dot{U}_1}. \end{aligned} \tag{2.38}$$

D is the dissipation function and is related to the coefficient b as

$$\begin{aligned} D &= \frac{1}{2}b\Big((\dot{u}_1 - \dot{U}_1)^2 + (\dot{u}_2 - \dot{U}_2)^2 + (\dot{u}_3 - \dot{U}_3)^2\Big), \\ b &= \frac{\eta_f \beta^2}{\kappa_s}. \end{aligned} \tag{2.39}$$

Inserting the lagrangian, L into Eq. (2.37) and using the definitions in Eq. (2.38) gives

$$
\begin{aligned}
q_1 &= \frac{\partial}{\partial t}\Big(\frac{\partial T}{\partial \dot{u}_1}\Big) - \frac{\partial D}{\partial \dot{u}_1},\\
Q_1 &= \frac{\partial}{\partial t}\Big(\frac{\partial T}{\partial \dot{U}_1}\Big) - \frac{\partial D}{\partial \dot{U}_1}.
\end{aligned}
\tag{2.40}
$$

To further develop Eq. (2.40), expressions for the kinetic and the potential energy must be obtained. Biot found such expressions [23], inserted them into Eq. (2.40) and obtained the equations of motion

$$
\begin{aligned}
N\nabla^2\vec{u} + \nabla\Big((A+N)\epsilon_s + Q\epsilon_f\Big) &= \frac{\partial^2}{\partial t^2}(\rho_{11}\vec{u} + \rho_{12}\vec{U}) + b\frac{\partial}{\partial t}(\vec{u} - \vec{U}),\\
\nabla\Big(Q\epsilon_s + R\epsilon_f\Big) &= \frac{\partial^2}{\partial t^2}(\rho_{12}\vec{u} + \rho_{22}\vec{U}) - b\frac{\partial}{\partial t}(\vec{u} - \vec{U}).
\end{aligned}
\tag{2.41}
$$

$\vec{u} = u_1\hat{x_1} + u_2\hat{x_2} + u_3\hat{x_3}$ and $\vec{U} = U_1\hat{x_1} + U_2\hat{x_2} + U_3\hat{x_3}$ are the displacement vectors in the solid and the fluid, respectively. $\hat{x_1}$, $\hat{x_2}$ and $\hat{x_3}$ are the unit vectors in direction x_1, x_2 and x_3, respectively. $\epsilon_s = \frac{\partial u_1}{\partial x_1} + \frac{\partial u_2}{\partial x_2} + \frac{\partial u_3}{\partial x_3}$ and $\epsilon_f = \frac{\partial U_1}{\partial x_1} + \frac{\partial U_2}{\partial x_2} + \frac{\partial U_3}{\partial x_3}$ are the solid and fluid dilatations, respectively. $\rho_{11} = (1-\beta)\rho_s - \rho_{12}$ and $\rho_{22} = \beta\rho_f - \rho_{12}$. ρ_{12} is the additional density experienced by the solid due to the motion of the solid into the fluid [23]. ρ_{12} is calculated by several authors by considering the drag force of a spherical solid grain moving through a fluid [169, 93]. In sandstones consisting of quartz-grains, typically $\rho_{12} = -420$ kg/m^3 [55].

The parameters A, N, Q, R are found by looking at the stress/strain-relations and are given in Eq. (2.42). Refer to Biot and Willis [108] for details on the calculation.

$$
\begin{aligned}
N &= \mu_{sm},\\
A &= \frac{\gamma K_{sm} + \beta^2 + (1-2\beta)(1 - K_{sm}/K_s)}{\gamma + 1/K_s - K_{sm}/K_s^2} - \frac{2}{3}\mu_{sm},\\
Q &= \frac{\beta(1 - \beta - K_{sm}/K_s)}{\gamma + 1/K_s - K_{sm}/K_s^2},\\
R &= \frac{\beta^2}{\gamma + 1/K_s - K_{sm}/K_s^2},\\
\gamma &= \beta(1/K_f - 1/K_s).
\end{aligned}
\tag{2.42}
$$

Biot [23] solved Eq. (2.41) by using the constants in Eq. (2.42). In this work, instead of solving Eq. (2.41), Dvorkin and Nur's modified Biot-squirt model is implemented [55] and solved. Dvorkin and Nur's Biot-squirt model is a model of c_P and α_p in fluid-saturated porous rocks considering both the global flow and the squirt flow. The model is used to analyze the measurements of c_P and α_P in chapter 7. In the Biot theory and the Biot-squirt model, the medium is assumed to be statistically isotropic. For this to be valid, the wavelength must be much larger than the pores. By using F_{biot} (defined in Eq. (2.47)), the Dvorkin and Nur's Biot-squirt equations give the same results as the

Biot theory solving Eq. (2.41). Attenuation and dispersion due to scattering of sound waves are discussed in section 2.5.6.

In the following there is a brief review of the Biot-squirt model presented by Dvorkin and Nur's [55]. The x_1-component in Eq. (2.41) is rewritten into Eq. (2.43) [55]:

$$\begin{aligned} (1-\beta)\rho_s \frac{\partial^2 u_1}{\partial t^2} + \beta\rho_f \frac{\partial^2 U_1}{\partial t^2} &= M\frac{\partial^2 u_1}{\partial x_1^2} - \alpha_{biot}\frac{\partial P}{\partial x_1}, \\ \beta\rho_f \frac{\partial^2 U_1}{\partial t^2} - \rho_a\left(\frac{\partial^2 u_1}{\partial t^2} - \frac{\partial^2 U_1}{\partial t^2}\right) - \frac{\eta_f \beta^2}{\kappa_s}\left(\frac{\partial u_1}{\partial t} - \frac{\partial U_1}{\partial t}\right) &= -\beta\frac{\partial P}{\partial x_1}, \end{aligned} \tag{2.43}$$

where P is the pressure and $M = K_{sm} + 4/3\mu_s m$. The rest of the parameters are defined in Eq. (2.47). The equation of mass conservation for one-dimensional fluid flow in the porous rock is

$$\frac{\partial \beta\rho_f}{\partial t} + \frac{\partial(\rho_f \beta(U-u))}{\partial x} = 0. \tag{2.44}$$

By introducing $u = C_1 e^{i(kx-\omega t)}$, $U = C_2 e^{i(kx-\omega t)}$ and $P = P_0 e^{i(kx-\omega t)}$ into Eqs. (2.43)-(2.44), where C_1, C_2 and P_0 are the amplitudes of the waves, a second order equation was found which has two solutions for the wavenumber, k for the compressional wave:

$$\begin{aligned} \frac{k_1^2}{\omega^2} &= -\frac{B}{2A} + \sqrt{\left(\frac{B}{2A}\right)^2 - \frac{C}{A}}, \\ \frac{k_2^2}{\omega^2} &= -\frac{B}{2A} - \sqrt{\left(\frac{B}{2A}\right)^2 - \frac{C}{A}}. \end{aligned} \tag{2.45}$$

From k_1 and k_2, the wavenumber giving the highest $c_P = \omega/k_{1,2}$ is defined as the fast wave, k_{fast}. The other is the slow wave. The parameters A, B, C are defined

$$\begin{aligned} A &= \frac{\beta F_{biot} M}{\rho_2}, \\ B &= \frac{F_{biot}(2\alpha - \beta - \beta\frac{\rho_1}{\rho_2}) - (M + F_{biot}\frac{\alpha^2}{\beta})(1 + \frac{rho_a}{\rho_2} + i\frac{\omega_c}{\omega})}{\rho_2}, \\ C &= \frac{\rho_1}{\rho_2} + (1 + \frac{\rho_1}{\rho_2})(\frac{\rho_a}{\rho_2} + i\frac{\omega_c}{\omega}). \end{aligned} \tag{2.46}$$

The parameters used in Eq. (2.46) are given

$$\begin{aligned}
F_{biot} &= \Big(\frac{1}{\rho_f c_f^2} + \frac{1}{\beta Q_c}\Big)^{-1},\\
M &= K_{sm} + \frac{4}{3}\mu_{sm},\\
\rho_1 &= \beta\rho_s,\\
\rho_2 &= (1-\beta)\rho_s,\\
\alpha_{biot} &= 1 - K_{sm}/K_s,\\
\rho_a &= -\rho_{12},\\
\omega_c &= \frac{\eta_f\beta}{\kappa_s\rho_f},\\
Q_c &= \frac{K_s}{1-\beta-K_{sm}/K_s},
\end{aligned} \tag{2.47}$$

where c_f is the sound velocity in the fluid. The results obtained from Eq. (2.45) does not contain squirt flow as long as the expression for F_{biot} in Eq. (2.47) is used, and is a representation of the Biot theory for compressional waves.

When calculating c_P and α_P using Eqs. (2.45), (2.46) and (2.47) with hydrates growing in the frame with uniform water and gas distribution (Eqs. (2.29), (2.27) and (2.28)) is here called the BiotHFrU-model. c_P is calculated using the real part of the fast wave number, $c_P = Real(\frac{\omega}{k_{fast}})$ and α_P is calculated using the imaginary part of the fast wave number, $\alpha_P = -imag(k_{fast})$.

2.5.5 Biot-squirt model during hydrate growth (BiSqHFrU)

To include squirt flow, Dvorkin and Nur introduced fluid flow in the radial direction in a cylindrical coordinate system (See Fig. 2.4). The equation of mass conservation (Eq. (2.44)) was rewritten using cylindrical coordinates with the global fluid flow in the x_1-direction and the squirt flow in the r-direction in a cylindrical coordinate system.

$$\frac{\partial\beta\rho_f}{\partial t} + \frac{\partial(\rho_f\beta(\dot{U}_1 - \dot{u}_1))}{\partial x} + \nabla^{cyl}(\rho_f\beta\dot{U}_q) = 0. \tag{2.48}$$

∇ is the del-operator in cylindrical coordinates and U_q is the fluid displacement in the $q-$direction seen in Fig. 2.5. As for the Biot-theory, the dot is the time derivative ($\frac{\partial}{\partial t}$). By introducing $u_1 = C_1e^{i(kx_1-\omega t)}$, $U_1 = C_2e^{i(kx_1-\omega t)}$, $U_q = C_3e^{i(kr-\omega t)}$ and $P = P_0e^{i(kx_1-\omega t)}$ into Eqs. (2.43) and (2.48) and assuming that the average pressure in the r-direction is representative for the pressure along the r-axis, a new expression of F_{biot} in Eq. (2.47) was found. F_{sq} is used instead of F_{biot} in Eq. (2.47) [55]:

$$
\begin{aligned}
F_{sq} &= F_{biot}\Big(1 - \frac{2J_1(\lambda R_{sq})}{\lambda R J_0(\lambda R_{sq})}\Big), \\
\lambda &= \sqrt{\frac{\rho_f \omega^2}{F_{biot}}\Big(\frac{\beta + \rho_a/\rho_f}{\beta} + i\frac{\omega_c}{\omega}\Big)}.
\end{aligned}
\tag{2.49}
$$

R_{sq} is a parameter describing the distance of the fluid flow in the r-direction and is called "squirt flow length" (See Fig. 2.4 b)). R_{sq} is typically set to be close to the grain radius of the porous rock [55]. As the model is not consistent with the Gassmann equation at low frequencies [42], the model has been critizied [170]. However, the model has been used widely to account for squirt flow [105, 149, 171] and has also been used in this work.

When calculating α_P using Eqs. (2.45), (2.46) and replacing F_{biot} in Eq. (2.47) with F_{sq} (Eq. 2.49) and letting hydrates grow in the frame with uniform water and gas distribution (Eqs. (2.29), (2.27) and (2.28)) is here called the BiSqHFrU-model. c_P is calculated using the real part of the fast wave number, $c_P = Real(\frac{\omega}{k_{fast}})$ and α_P is calculated using the imaginary part of the fast wave number, $\alpha_P = -imag(k_{fast})$. No attempt has been made to alter the squirting length, R, due to closing pores during hydrate growth. Different values of N_{perm} is used in the model and N_{perm} is defined in chapter 7.

2.5.6 Multiple scattering model during hydrate growth (WaTrHFrU)

Waterman and Truell [56] found a model describing the effective, complex wave number, k, through a medium containing n_0 identical scatterers. The model has been seen to be valid for volume fractions of scatterers below 0.3 [135] and used to find c_P and α_P in porous media [135, 138, 136, 134]. In this work, the total volume of the scatterers (V_{scat}) is approximated by the gas and water volume in the HFr-model (Fig. 2.3 B)). In each simulation, all scatterers are spherical and have the same radius (R_{scat}). The model is used to investigate whether spherical heterogeneities with different effective radii (R_{scat} =100 µm, 500 µm, 700 µm and 1000 µm) inside the Bentheim sandstones might attenuate the acoustic wave.

Hydrates are assumed to grow into the frame in the scattering model used in this work, thus contributing to the effective background medium needed in the multiple scattering model (wavenumber k_0 in Eq. (2.50)). Such an effective background medium has been previously used by for example Ciz et al. [136] togeher with Waterman and Truell's scattering theory. S_{w0} contributes to this effective background medium because it is calclulated with the HFrU-model. When hydrates grow into the frame, the porosity is reduced. The left pore space is described with n_0 spherical inclusions. To avoid confusion, it is worth noting that when $S_{w0} > 0$, the background medium calculated with the HFrU-model medium contains water. However, the inclusions used in the scattering model are only treated as either 100 % water inclusions or cavities (vacuum). In other words S_{w0} used to calculate the background medium is not used to calculated the scatterer properties. In the models using water as scatterers, Eq. (2.58) is used to calculate the scattering coefficients A_n used in Eq. (2.52). In the models using methane gas as scatterers, Eq. (2.60) is used to calculate the scattering coefficients A_n.

As hydrates grow, the volume of the scatterers decrease according to Eq. (2.18). By approximating the pore space not occupied by methane hydrates in Fig. 2.3 B) by spherical inclusions (either water-inclusions or cavities), Waterman and Truell's multiple scattering theory [56] can be used to calculate the effective complex wave number, k, of the porous rock:

$$\left(\frac{k}{k_0}\right)^2 = \left[1 + \frac{2\pi n_0 f(0)}{k_0^2}\right] - \left[\frac{2\pi n_0 f(\pi)}{k_0^2}\right]^2. \tag{2.50}$$

N_0 is related to the total volume fraction of scatterers, V_{scat} and the radius of the scatterers, R_{scat}:

$$n_0 \frac{4}{3}\pi R_{scat}^3 = V_{scat}. \tag{2.51}$$

Different values of R_{scat} will be used when presenting the results in Ch. 7. V_{scat} will decrease with increasing hydrate saturation. $f(0)$, and $f(\pi)$ in Eq. (2.50) are called the forward and backward scattering far-field amplitudes, respectively [56], and are given:

$$\begin{aligned} f(0) &= \frac{1}{ik}\sum_{n=0}^{\infty}(2n+1)A_n, \\ f(\pi) &= \frac{1}{ik}\sum_{n=0}^{\infty}(-1)^n(2n+1)A_n. \end{aligned} \tag{2.52}$$

k_0 is the wave number of the background medium. Refer to Waterman and Truell [56] for details. Two different versions are implemented for the WaTrHFrU-model. One version where inviscid fluid inclusions act as scatterers. In this case A_n is calculated using Eq. (2.58). In the second version, the inclusions are spherical cavities and A_n is calculated with Eq. (2.60). This two versions are not given specific names, they are both referred to as the WaTrHFrU-model. In this simple model, hydrate does not contribute to scattering. When hydrates fill a pore, V_{scat} reduces.

In the WaTrHFrU-model, the HFrU-model is used to calculate the compressional wave velocity of the background medium, c_{HFrU}, to obtain $k_0 = \omega/c_{HFrU}$ (see Sect. 2.5.2). Next $\alpha_P = -imag(k)$ is calculated using Eq. (2.50) and the scattering coefficients, A_n from either Eq. (2.58) or Eq. (2.60).

Scattering coefficients

A_n is the compressional wave scattering coefficient of a single scatterer and is needed in Waterman and Truell's multiple scattering model, Eq. (2.50). The compressional wave scattering coefficients for a spherical inclusion in an elastic medium were investigated by Ying and Truell [139]. A compact way of calculating these scattering coefficients were presented by Mao and Pao [140]. A plane elastic wave may be decomposed into a translational and a rotational part [93]: An non-rotational vector corresponding to translations of matter without shear deformations and a vector without divergence describing rotations without volume change. Here this is done by introducing the non-rotational displacement scalar potential, Φ and the divergence-free displacement vector potential, Ψ. For an elastic isotropic medium, the displacement vector, $\vec{u}$ and the stress tensor $\tilde{T}$ can thus be written [140]:

$$\begin{aligned} \vec{u} =& \nabla^s \Phi + \nabla^s \times (\vec{e}_\Phi \frac{\partial \Psi}{\partial \theta}) \\ \tilde{\tau} =& \lambda(\nabla^s \cdot \vec{u})[I] + 2\mu(\nabla^s \vec{u} + \vec{u}\nabla^s). \end{aligned} \tag{2.53}$$

λ is the Lame's first parameter, $[I]$ is the identity matrix, ∇^s is the del-operator in spherical coordinates, θ is the polar angle shown in Fig. 2.5. $\vec{e}_\phi$ is the unit vector along the azimuth angle, ϕ. λ_1 and λ_2, are the Lame's first parameters outside and inside the scatterer, respectively. ρ_1 and ρ_2 are the densities outside and inside the scatterer, respectively. μ_1 and μ_2 are the shear moduli insisde and outside the scatterer, respectively. r is the distance from origo, O. q is the radial distance. The arrows beneath the figure illustrate the incoming plane wave.

The incident plane compressional wave on a scatterer in spherical coordinates can be described with the two incoming displacement potentials [140]:

$$\begin{aligned} \Phi^i &= \Phi_0 \sum_{n=0}^{\infty} (2n+1) i^n j_n(k_{P1} r) P_n(\cos(\theta)) \\ \Psi^i &= 0 \end{aligned} \tag{2.54}$$

where Φ_0 is the amplitude of the incoming wave, j_n is the spherical Bessel function of the first kind of order n. k_{P1} is the compressional wavenumber in medium 1. P_n is the Legendre polynomial of order n. The reflected wave is given [140]:

$$\begin{aligned} \Phi^r &= \sum_{n=0}^{\infty} A_n h_n(k_{P1} r) P_n(\cos(\theta)), \\ \Psi^r &= \sum_{n=0}^{\infty} B_n h_n(k_{S1} r) P_n(\cos(\theta)) \end{aligned} \tag{2.55}$$

where k_{S1} is the shear wavenumber in medium 1. B_n is the shear wave scattering coefficient. h_n is the spherical Hankel function of first kind, order n. The refracted wave is given [140]:

$$\begin{aligned}\Phi^f &= \sum_{n=0}^{\infty} C_n j_n(k_{P2}r)P_n(\cos(\theta)) \\ \vec{\Psi}^f &= \sum_{n=0}^{\infty} D_n j_n(k_{S2}r)P_n(\cos(\theta))\end{aligned} \tag{2.56}$$

k_{P2} and k_{S2} are the compressional and shear wave numbers, respectively, in the scatterer (medium 2). C_n and D_n are the amplitude coefficients of the shear wave and the compressional wave inside the inclusions.

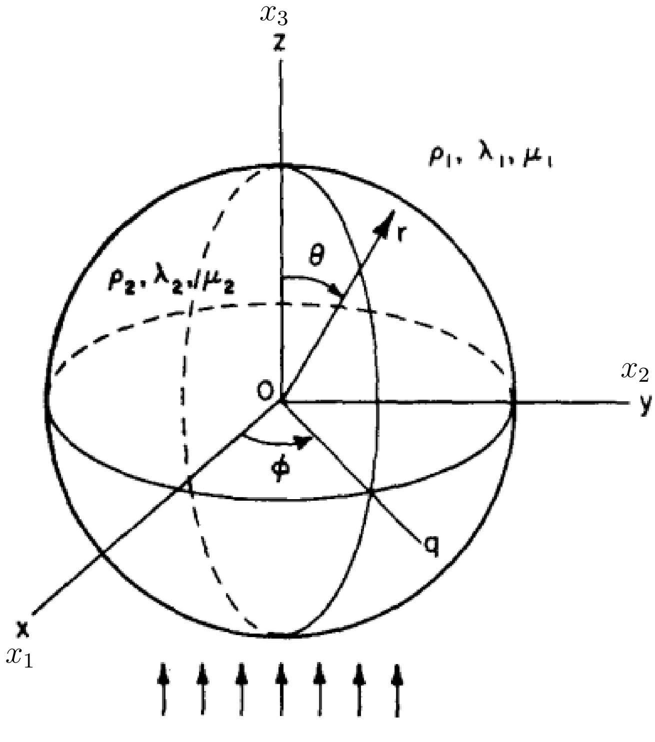

Figure 2.5: Spherical coordinate system with he directions $x_1 = x$, $x_2 = y$ and $x_3 = z$. The other symbols are described in the text above. This figure is found in the work of Pao and Mow [140].

Inviscid fluid inclusions

For spherical inviscid fluid inclusions, continuity in displacement and traction through the boundary gives the following boundary conditions [140]:

$$\begin{aligned} u_r^i + u_r^r &= u_r^f, \\ \tau_{rr}^i + \tau_{rr}^r &= \tau_{rr}^f, \\ \tau_{r\theta}^i + \tau_{r\theta}^r &= 0. \end{aligned} \tag{2.57}$$

u_r^i is the r-component of the incoming displacement-vector. u_r^r is the r-component of the reflected displacement-vector. u_θ^i is the θ-component of the incoming displacement-vector. u_θ^r is the θ-component of the reflected displacement-vector. u_r^f is the r-component of the refracted displacement-vector. u_θ^f is the θ-component of the refracted displacement-vector.

τ_{rr}^i is the rr-component of the incoming stress field. τ_{rr}^r is the rr-component of the reflected stress field. τ_{rr}^f is the rr-component of the refracted stress field. $\tau_{r\theta}^i$ is the $r\theta$-component of the incoming stress field. $\tau_{r\theta}^r$ is the $r\theta$-component of the reflected stress field.

Using the boundary conditions with the equations for displacement and stress, Eq. (2.53) and inserting the potentials from Eqs. (2.54 - 2.56), gives a system of equations

$$\begin{bmatrix} E_{11} & E_{12} & E_{13} \\ E_{31} & E_{32} & E_{33}^f \\ E_{41} & E_{42} & 0 \end{bmatrix} \begin{bmatrix} A_n \\ B_n \\ C_n \end{bmatrix} = \Phi_0 \begin{bmatrix} E_1 \\ E_3 \\ E_4 \end{bmatrix}, \tag{2.58}$$

where all values of E_{ij} (also E_{33}^f) are given by Pao [140]. For Pao's equations to be consistent with Waterman and Truell's, $\Phi_0 = \frac{1}{(2n+1)i^n}$ [56, 140]. From Eq. (2.58) the inviscid fluid single scatterers coefficients, A_n, are calculated.

Cavity inclusions

For spherical cavity inclusions, the boundary conditions are [140]

$$\begin{aligned} \tau_{rr}^i + \tau_{rr}^r &= 0, \\ \tau_{r\theta}^i + \tau_{r\theta}^r &= 0, \end{aligned} \tag{2.59}$$

giving the system of equation

$$\begin{bmatrix} E_{31} & E_{32} \\ E_{41} & E_{42} \end{bmatrix} \begin{bmatrix} A_n \\ B_n \end{bmatrix} = \Phi_0 \begin{bmatrix} E_3 \\ E_4 \end{bmatrix}. \tag{2.60}$$

2.5.7 Combined scattering and Biot-squirt flow model during hydrate growth (WaTrBiSqHFrU)

In this model an attempt to model attenuation mechanisms due to scattering, global flow and squirt flow is made. This is the same model as the WaTrHFrU-model (Sect. 2.5.6), however, instead of using the HFrU-model to obtain the background medium, the BiSqHFrU-model during hydrate growth is used instead. This model is called the WaTrBiSqHFrU-model.

Chapter 3

Measurement methods and experimental setup

In this chapter, the measurement methods and experimental setup for monitoring the acoustic properties (c_P, c_S and α_P) for a porous sandstone during hydrate growth is presented. In Sect. 3.1, the setup for the pressure cell used for growing hydrates, in which acoustic measurements are conducted, will be shown. The pressure cell has been used for years at the hydrate laboratory at the University of Bergen but not not for acoustic measurements.

In this work, equipment for acoustic measurements has been added to the existing experimental setup to conduct acoustic measurements inside the pressure cell. A custom made transducer holder with a custom made electrical feedthrough has been used with the pressure cell. This equipment is presented in Sect. 3.2. The solid buffer method, which is employed inside the pressure cell, is presented in Sect. 3.3. The immersion method has been used as a reference method to compare with the solid buffer method and is described in Sect. 3.4. The immersion method is also used to measure acoustic properties in materials used in the transducer construction and for FE-modeling. Different signal processing techniques for use with the acoustic measurement methods are are presented in Sect. 3.5. An example of the use of the Fourier spectrum method is given. To characterize the electrical conductance of the in-house built transducers, an impedance analyzer has been used and described in Sect. 3.6.

3.1 Pressure cell and experimental setup for hydrate growth

The conditions used for hydrate growth in this work, are pressure 83 bar and temperature 4 °C. As seen in Fig. 2.2 these conditions are inside the methane hydrate stability zone.

These conditions are achieved inside the pressure cell used in this experimental setup (Figs. 3.1 and 3.2).

The experimental equipment used for achieving the methane hydrate conditions can be divided into four main parts: 1) The pressure cell, where the sandstone is placed and hydrates form (number 5 in Fig. 3.1). 2) the gas pressure tank, storing and providing the methane gas to the experiment, Fig. 3.3 a). 3) the pressure regulating pump, which accurately regulates the pressure inside the pressure cell to be 83 bar, Fig. 3.3 b). 4) the cooling system, lowering the temperature in the pressure cell from room temperature to 4 °C (number 11 in Fig. 3.1). The rest of the equipment and the use of it in Fig. 3.1 are described in section 3.3.

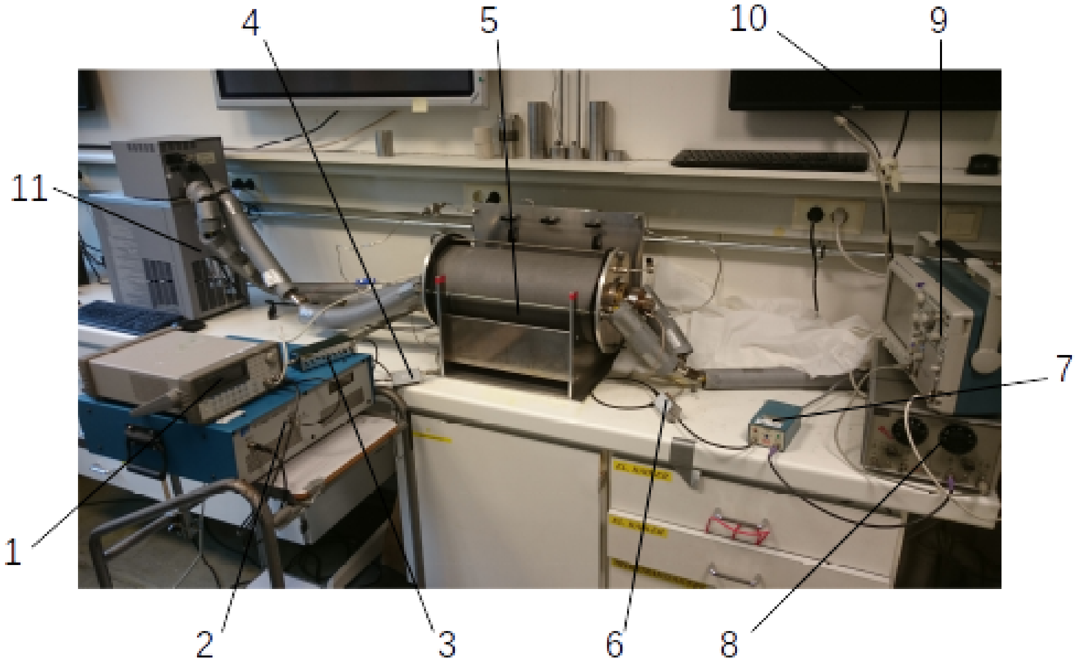

Figure 3.1: Experimental setup for acoustic measurements inside the pressure cell. 1: Signal generator, 2: Power amplifier, 3: Attenuator, 4: Matching filter, 5: Pressure cell, 6: Matching filter, 7: Signal amplifier, 8: HP high pass filter, 9: Oscilloscope, 10: Logging computer, 11: Cooling pump.

Methane gas, which is injected into the pressure cell, is stored on a pressure tank certified for gas pressure up to 200 bar. Through a valve, some of this gas is let into the closed loop system containing the pressure cell and the pressure regulating pump (Fig. 3.2). Inside the pressure regulating pump there is a volume controlled by a piston. When the piston moves, the volume inside the pressure pump and thus the pressure in the closed system changes.

After closing the valve (see Fig. 3.2), the pressure in the closed loop is monitored for about 24 hours to detect any gas leaks out of the pressure cell. Potential leaks are located by spraying thick, liquid soap onto joints, gas inlets, electrical feedthroughs etc. and looking for bubbles. An extensive description of the measurement setup for hydrate formation, without the transducer holders, is given by Almenningen [152].

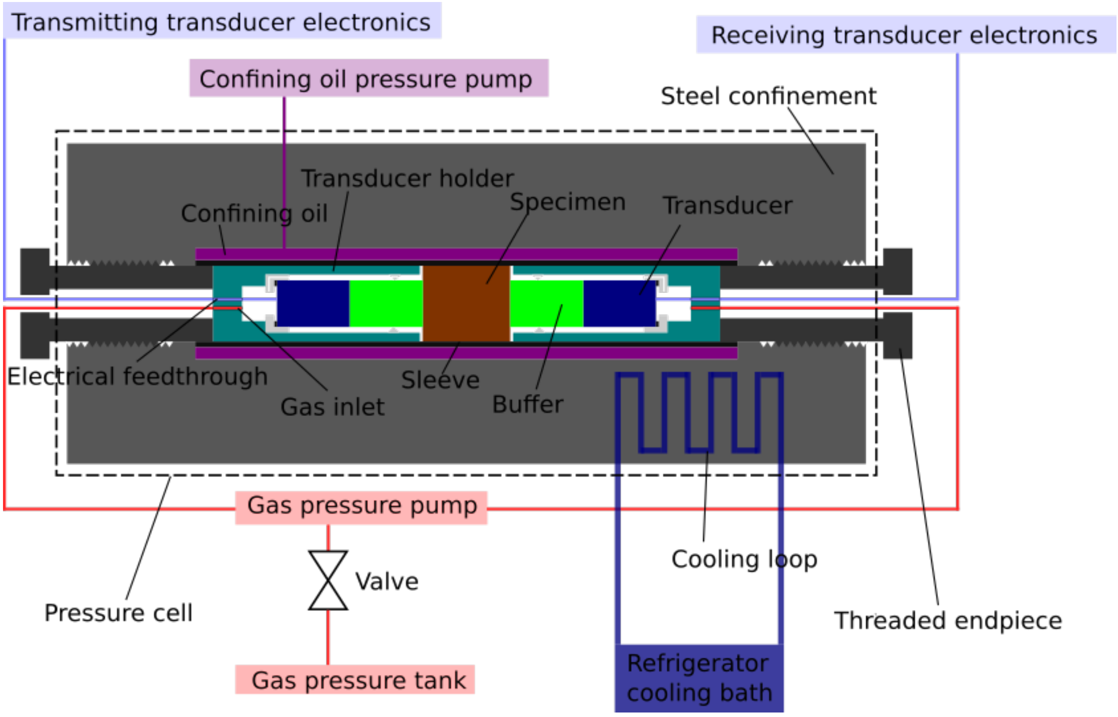

Figure 3.2: Schematic of the main parts of the experimental setup for hydrate growth. Dimensions and more details are shown in Fig. 3.8.

If there are no leakages after 24 hours, the refrigerator pump is turned on, looping water through the pressure cell, cooling the system down to 4 °C, see Fig. 3.2. In this experimental setup, the water looping through the pressure cell was cooled to 1.5 °C to maintain 4 °C in the pressure cell. After several hours, when the temperature in the inner chamber approaches 4 °C, hydrates start to form inside the sandstone specimen. As hydrates form, methane gas is consumed and the methane gas volume inside the pressure regulating pump is logged. The total volume of methane gas, V_H, consumed by hydrate formation can be found by using the iteration scheme in section 2.1.3. The methane hydrate saturation, S_H, in the pore volume, V_{pore} can then be found by

$$S_H = \frac{V_H}{V_{pore}}. \tag{3.1}$$

Since Bentheim sandstones are almost pure quartz (99 % quartz), the pore volume V_{pore} is calculated by first vacuuming and drying the Bentheim specimen, then weighing and measuring the dimensions of the the dry specimen. The volume of the Bentheim specimen, density of pure quartz (2650 kg/m^3) and the mass of the dry Bentheim specimen, the pore volume is found. Similarily to S_H, the initial water saturation (S_{w0}) is found:

$$S_{w0} = \frac{V_{w0}}{V_{pore}}, \tag{3.2}$$

where V_{w0} is the volume of water inside the pores before hydrates start to grow.

The inner chamber of the pressure cell is cylindrical and sealed with a rubber-sleeve open in both ends, see Fig. 3.2. In this inner chamber, the test specimen and the transducer holders with the transmitting and the receiving transducers are placed. Oil under pressure squeezes the sleeve firmly around the specimen, the transducer holders and the threaded end-pieces. This squeezing prevents gas from creeping out, between the rubber sleeve and the transducer holder. The transducer holders are described further in section 3.2.

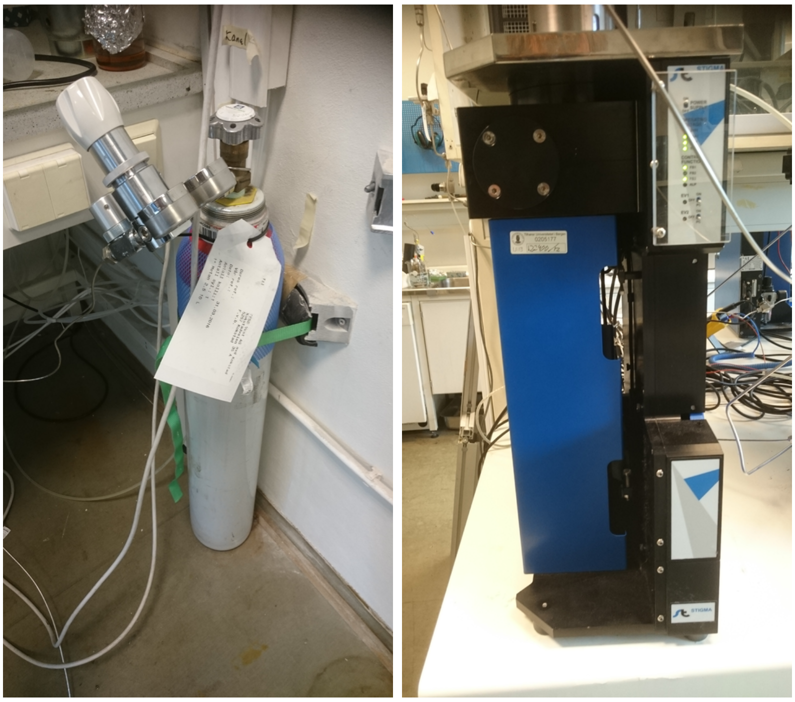
(a) (b)

Figure 3.3: Photographs of **a)** Methane gas on pressure tank (200 bar). **b)** Pressure regulating pump.

The oil to methane gas differential pressure is set to be approximately 30 bar for the cell to be pressure tight, i.e. oil pressure at 110 bar when the methane gas pressure is 83 bar. All components inside the inner chamber must be cylindrical and have a diameter that fits the inner chamber so that the inner sleeve doesn't bulge inwards and tear. The components must also be strong enough to withstand the differential pressure of 30 bar. In Fig. 3.2 there is a small glitch between the transducer-holders and the specimen, leaving the inner sleeve unsupported. For the sleeve to not bulge inwards and tear, such glitches can only be a few millimeter wide. In this setup, these glitches are less than 2 mm. The absolute oil pressure must always be higher than the absolute pressure inside the pressure cell so that the sleeve does not bulge outwards, into the oil chamber.

3.2 Transducer holders and electrical feedthrough

The experimental setup for the pressure cell has been proven pressure tight without the use of acoustic measurement equipment [152]. In this work, however, two new components are introduced and must be proven pressure tight to satisfy the "no-leak" condition of maximum 3ml/24 hours leak rate at the methane hydrate laboratory at the University of Bergen. The transducer holder and the electrical feedthrough are shown in Fig. 3.4 and as a component in the measurement setup in Fig. 3.8. The transducer holders with the electrical feedthrough have two main functions: holding the transducers in a fixed position during acoustic measurements and act as the pressure barrier to the atmospheric conditions outside the pressure cell.

3.2.1 Transducer holders

The transducer holders are acting as the pressure barrier and are aligning the transducers, making reproducible acoustic measurements possible. The transducer holders are turned out of solid pieces of aluminum at the mechanical workshop at the University of Bergen. All turning and use of a lathe in this work, is done on the mechanical workshop. The transducers and the buffers are glued together to have as few loose parts as possible inside the pressure cell (detailed in Ch. 4: transducer design). In Fig. 3.4, the transducer-buffer construction is shown. The holders are designed so that the transducers with the buffers are sticking out approximately 2 mm (exaggerated in Fig. 3.4). The acoustic energy can now by radiated directly into the specimen, as shown in Fig. 3.2.

Inside the transducer-holder, there is a plexiglas ring, and a plexiglas cup made to centralize the transducers. Grooves in the plexiglas cup and the plexiglas ring ensures that gas may pass through. In section 3.3 it is described how a torque wrench is used to apply a net force on the transducer. The rubber ring between the plexiglas cup and the transducer makes sure that the torque exerted on the transducer holder, uniformly transfers to a net force on the transducers.

Behind the plexiglas cups are some room for the cable to bend and adjust, so that e.g an unwanted rotation of the transducer will not twist and damage the cable. The diameter of the transducer holder is the same as the specimen, 50 mm. The sleeve inside the pressure cell will clamp on the transducer holders so that no gas can leak out, along the sides of the transducer holders. The transducer holder shown in Fig. 3.4 is made of a aluminum cylinder having 5 mm thick walls with inner radius 40 mm and open in one end. Threads are drilled in through the base of the aluminum cup, for the gas inlet and for the electrical feedthrough. Swagalock fittings (1/8") have been used for the gas inlet. A conax plug (1/4") is used to seal a custom made electrical feedthrough for transferring electrical power into the pressure cell.

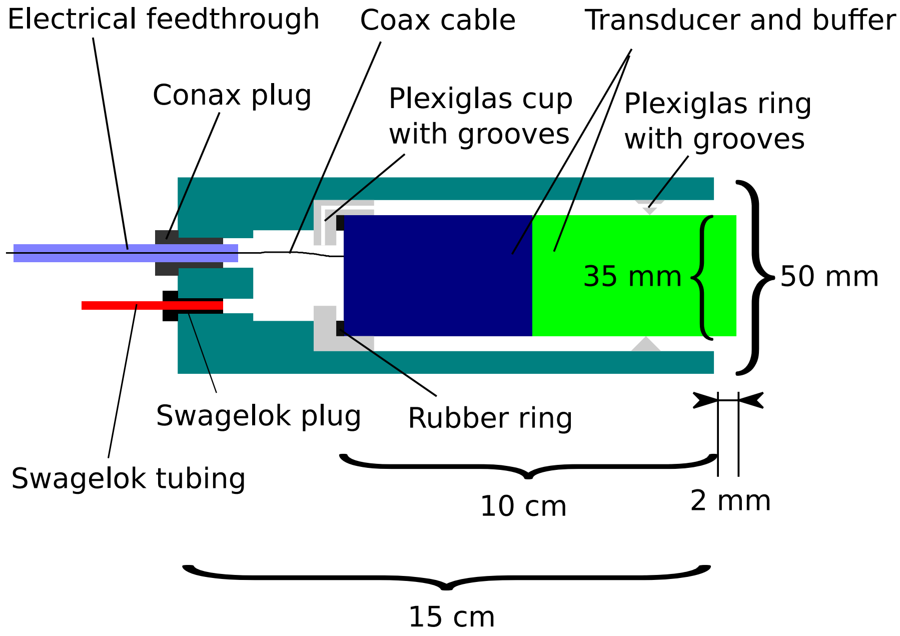

Figure 3.4: Schematics of the transducer holder

3.2.2 Electrical feedthrough

The electrical feedthrough enables transfer of electrical power to the transducer inside the pressure cell, without gas leakage. The signal wire is threaded through a 10 cm long steel pipe. The steel pipe with the wire is then potted with polyurethane so that the steel pipe with the wire is pressure tight, see Fig. 3.5. A PG2 Conax plug is then used to seal the steel pipe, as seen in Fig. 3.4.

Tapered threads are drilled into the transducer holder so that a PG2 Conax plug 1/4" can be screwed into the transducer holder. The steel pipe has 1/4" outer diameter and wall thickness 1.5 mm. The last centimeter at one of the ends is tapered so that the wall thickness is 2 mm at the far end, see Fig. 3.5. A 1 cm long PVC-cylinder with outer diameter equal to the steel pipe inner diameter is machined in the turning-lathe at the mechanical workshop. A 0.5 mm hole for the signal wire is drilled through the center of the PVC cylinder. The PVC-cylinder acts as a plug and is squeezed down through the pipe, down to the tapered end. Now, Solr-Res 01 polyurethane is pressed into the the steel cylinder from the non-tapered end, filling the steel pipe completely. Finally, a 0.5 mm single copper wire is threaded through the steel pipe, from the tapered end, through the hole in the PVC-plug and through the steel pipe. After curing, this is a pressure tight electrical feedthrough where the high pressure side is the non-tapered end. The shield of a coax-cable is glued to the inside of the steel pipe, on the tapered end, with silver paint. The space behind the PVC-plug is then filled with 5 min rapidly drying epoxy from Loctite. Now, the coax-shield is cemented in position and will not come in touch with the single copper wire in the steel pipe. The inner wire of the coax cable is soldered on the single wire in the steel pipe. A small Lemo-connector with outer diameter less than 1/4" is attached to the coax cable. On the transducer side, almost the same procedure is repeated. The transducer cable is 3 cm long. The shield is glued with silver paint and epoxy to the steel pipe on the outside. The inner wire is soldered onto the copper-wire in the steel pipe. Some rapidly drying epoxy is used to make sure the shield and the signal wire are not in contact. The electrical feedthrough now acts as a solid coax cable with an outer steel shield.

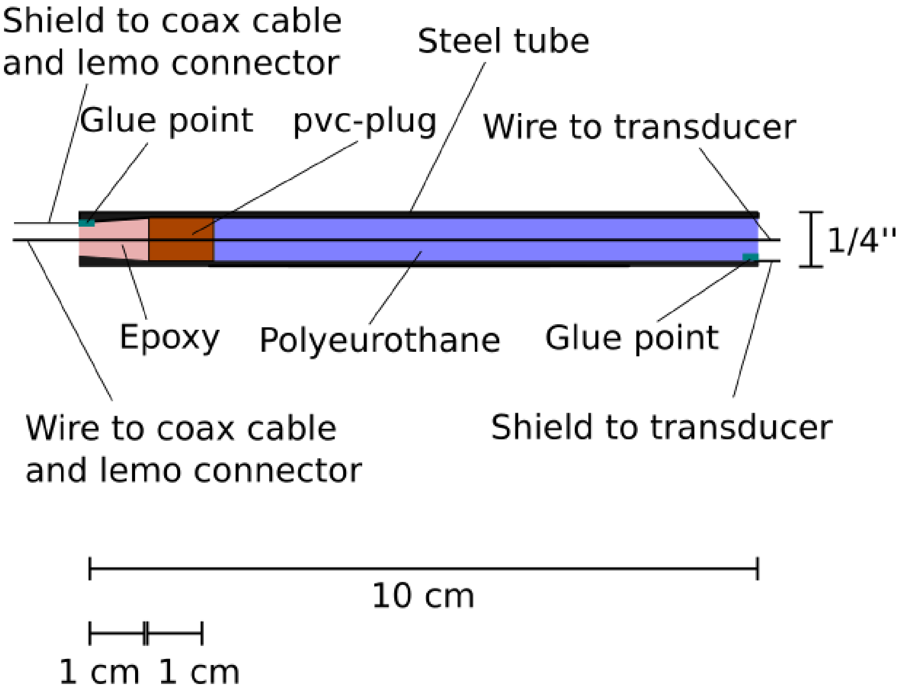

Figure 3.5: Schematics of the electrical feedthrough.

Different potting materials and construction designs of electrical feedthroughs were tested for use with the pressure cell before the design of the electrical feedthrough presented in Fig, 3.5 was found.

3.3 Solid buffer method inside pressure cell

The solid buffer method is widely used for measuring acoustic properties of rocks under pressure [22, 21, 30, 31, 32, 33, 34, 35]. To monitor the changes of acoustic properties in a Bentheim sandstone specimen during methane hydrate growth, the solid buffer method is employed inside the pressure cell at methane hydrate conditions (83 bar, 4 °C). In this work, the acoustic parameters of interest are the compressional wave velocity, the shear wave velocity and the compressional wave attenuation coefficient. The term "wave velocities" is often referring to both the compressional wave velocity and the shear wave velocity.

3.3.1 Experimental setup

In the solid buffer method, two different measurement setups are used: Measurement A without specimen inserted, and measurement B with the specimen inserted into the wave propagation path. The compressional and shear wave velocities and the compressional wave attenuation coefficients for the specimen are found by comparing measurement A and measurement B.

In the measurements, in-house constructed shear-wave and compressional-wave transducers, with center frequencies 460 kHz and 560 kHz, respectively, have been used. Two block diagrams for the different components in the measurement setups for measurement A and measurement B are shown in Fig. 3.6. The only thing separating the diagrams is the specimen inserted in measurement B.

The transmitting transducer is driven by an Agilent 33250A signal generator, connected to an ENI 240L RF power amplifier and a simple impedance matching filter. The power amplifier has a gain of 50 dB. A picture of the measurement setup is shown in Fig. 3.1. In the measurement setup, there is an attenuator which is meant for use if the smallest possible voltage output from the signal generator is too high (number 3 in Fig. 3.1). To ensure that the transducers will not be damaged, the signal from the signal generator never exceeds 100 mV. Still, a too high voltage (below 100 mV) has been seen to give non-linear effects or produce signals larger than the oscilloscope can handle. This is the case for measurement A for the solid buffer method. Even for the lowest possible output signal from the signal generator, 1 mV, a distorted signal is seen on the oscilloscope for measurement A. To avoid this distorted signal in measurement A, the attenuator is attenuating the signal 20 dB. No disortion is seen in measurement A after the 20 dB attenuation.

When the Bentheim sandstone is inserted (measurement B), no distortion is seen by dynamically changing the voltage from the signal generator with the logging script. During measurement B, the attenuator is still present in the measurement setup, however, it is set to give no extra attenuation, i.e attenuation 0 dB. A simple test is performed to investigate whether there is any difference in the phase response of the attenuator at 0 dB and 20 dB. By examining the steady-state portion of different electrical signals having frequencies 250 kHz, 500 kHz and 1 MHz, passing through the attenuator, no time-shift is seen in the signal using the attenuator settings 0 dB, 10 dB, 20 dB, 30 dB, 40 dB and 50 dB. This means that the phase response of the attenuator is the same in measurement A and measurement B.

Maximum power is transmitted from a source to a load (here a transducer) when $Z_s = Z_T^{conj}$, where Z_s is the output impedance of the source and Z_T^{conj} is the complex conjugate of the input impedance of the transducer. The output and input impedances of the signal generator and power amplifier are listed to be 50 Ω [172, 173]. The input and output impedances of the attenuator is assumed to be 50 Ω as well. The input impedances of the transducers have an reactive and resistive part. In this work no attempt is performed to match the resistive part of Z_s (50 Ω) and Z_T. However, an inductor is put in series with the transmitting transducer intending to satisfy $X_s = 0 = \omega L + X_T$, at 500 kHz, where X_s is the output reactance seen from the output ports of the attenuator. L is the inductance of the inductor and X_T is the input reactance of the transducer. The reactance of the transducer, X_T is measured to be approximately 200 Ω at 500 kHz. To satisfy the equation $0 = \omega L + X_T$, L should be 64 µH, however, 33 µH inductors where used. The same impedance-matching principle is used on the receiving side. Now, the output impedance seen at the transducer output ports is matched with the input impedance on the signal amplifier using the same matching principle as described above. In this work, an increase of signal transmission from transducer to transducer of approximately 10 % is seen by using the inductor matching filters.

For the hydrate measurements, a 1 cycle pulse with frequency 500 kHz is used. The burst repetition rate of the signal generator is set to be 50 ms. The amplitude needed for the signal to propagate through the porous sandstone depends heavily on the amount of hydrate present in the sandstone. In the measurements, the amplitude of the signal from the signal generator is initially set to 100 mV. The oscilloscope volts/div-setting is then adjusted to the signal. No distortion is seen in the signal at these settings. By changing the signal generator input voltage from 100 mV to 50 mV, no change in the phase is seen in the recorded signal. However, the amplitude of the signal seen on the oscilloscope is not linearly scaling by changing the signal generator input voltage from 100 mV to 50 mV. From this, it is assumed that non-linear effects are negligible for c_P and c_S-measurements but not negligible for α_P measurements. Signal generator input voltage amplitudes below 50 mV give a weak acoustic signal before hydrate growth, which is hard to record on the oscilloscope. An extensively study of non-linear effects is not conducted in this work. However, during hydrate growth, the attenuation in the specimen is seen to greatly reduce. Now the acoustic signal can be recorded at a much lower signal generator emf. At hydrate saturation 0.2, the signal generator emf is typically reduced to 10 mV. It is assumed that there are no non-linear effects affecting α_P-measurements for S_H higher than 0.2. For hydrate bearing Bentheim sandstones, α_P-measurements are only presented for S_H higher than 0.2.

By having the volts/div setting on the oscilloscope fixed and instead dynamically change the voltage from the signal generator to fit the signal inside the oscilloscope window distortion of the signal is avoided. The signal generator amplitude settings are dynamically changed from 100 mV to 1 mV during the hydrate growth experiment. When the signal amplitude from the signal generator is at the lowest possible value (1 mV), the oscilloscope window settings are changed to acquire the signal.

One measurement series of the acoustic properties of a Bentheim sandstone during hydrate growth may last for up to 10 days. A robust and automatic logging script is thus needed to measure the acoustic signal. A logging script was developed able to change the frequency, number of cycles and the voltage of the input signal, as well as automatically finding a suitable window on the oscilloscope (see appendix A for the logging script). The acquired time and voltage signal is saved in addition to the time of each measurement, and all the input parameters listed above. The signal was logged and saved every 15 min giving approximately 100 saved data files every day.

A too high signal amplitude can damage the equipment and also lead to non-linear effects. Potential electrical shortcuts and damaged electrical equipment due to high voltages are of extra concern in a methane gas laboratory. The Eni power amplifier used is capable of delivering high power, thus it is very important that the maximum limit of 100 mV is never exceeded.

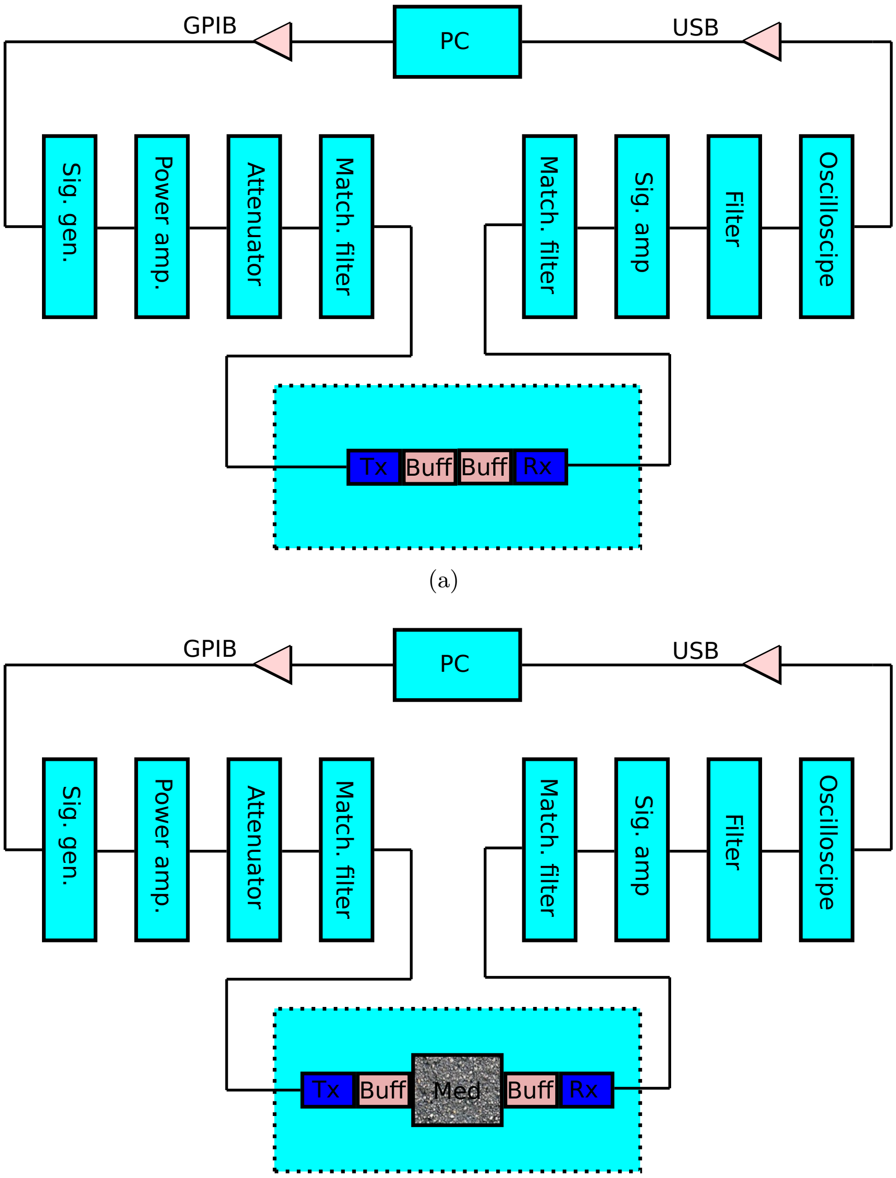

(a)

(b)

Figure 3.6: Schematic overview of the solid buffer method used inside the pressure cell. **a)** Measurement A, **b)** Measurement B.

The receiving transducer is connected to the matching filter and then to a Panametrics Ultrasonic Preamp with gain 60 dB and a HP high-pass filter with cutoff-frequency 200 kHz. Because of the large attenuation coefficient in porous materials, lower frequency components may dominate in the signal. The HP filter is used as a high-pass filter to ensure that the signal frequency is detectable. A Tektronix DPO 3012 oscilloscope acquires the signal by continuously averaging 256 measured signals. The signal acquired by the oscilloscope is triggered externally by the pulse from the signal generator. The script (presented in appendix A) ensures that measurements are taken every 15 min during the test period. The signal generator is controlled by the PC via GPIB communication and the signal is acquired with the oscilloscope via an USB connection.

The acoustic measurement equipment in Fig. 3.1 is also used for measurements on plexiglas at atmospheric pressure. These measurements are conducted to validate the solid buffer method and investigate the effect of unwanted sidewall reflections (presented in Ch. 6). In these measurements the exact same measurement setup is used, apart from that the power amplifier and the attenuator is bypassed. The transmitting transducer is excited with both one cylce pulses and 10 cycles bursts with signal amplitudes 20 mV.

3.3.2 Measurements

As described above, the solid buffer method, transducers and other components have been custom made to fit inside the pressure cell, see fig. 3.8. The available space inside the pressure cell is a tube with inner diameter 50 mm and length 30 cm. Methane gas will be flowing inside the pressure cell and the porous rock needs to have a certain surface exposed to the gas for the gas to efficiently seep into the porous rock. The diameters of the constructed transducers and the buffers must therefore be a little smaller, 35 mm. The design of the transducer with dimensions is presented in Ch. 4.

In an ideal measurement setup for the solid buffer method, the buffers and the specimen would have a much wider diameter to avoid sidewall reflections. This is however not feasible in the current hydrate laboratory at the University of Bergen. The acoustic waves may be reflected from the sidewalls of the buffers and interfere with the direct signal. The effect of these unwanted sidewall-reflections on the measurements have been seen to not be critical compared with other uncertainties in the measurements. Sidewall reflections and uncertainty contributions are discussed in Ch. 6. Acoustic measurements have been conducted on cylindrical Bentheim sandstone specimen, during hydrate growth, having length 4-6 cm and diameter 50 mm. Measurements on plexiglas have also been conducted to quantify the effect of the sidewall reflections. The length of these specimen are 20 mm and 60 mm with diameter 50 mm. The specimen are shown in Fig. 3.7.

To make the acoustic measurements reproducible, the acoustic transmission through the buffer/specimen interfaces must be the same in all measurements. The transducers with buffers have to be pressed together with the same force, or if the specimen is present, the two transducers with buffers must be pressed towards the specimen with the same force in all measurements. As descried in section 3.2.1, this is done using the custom made transducer holders. They are designed so that the transducers are aligned and centralized. A force is exerted on the transducer-holder by applying a torque wrench on the torque key adapter that is attached to the threaded end-pieces, see Fig. 3.8 and fig. 3.9. A flexible rubber-ring inside the transducer-holder ensures that a force exerted on the transducer-holder is uniformly transfered to the transducer. In all measurements, a torque of 10 Nm is used.

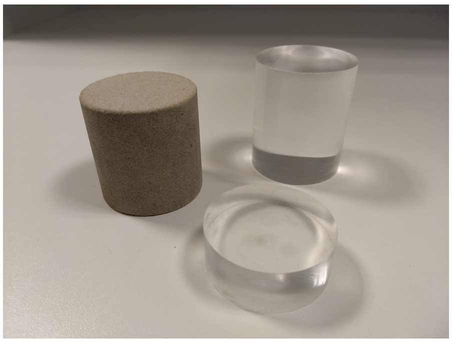

Figure 3.7: Photographs of specimen used in the solid buffer method. The Bentheim sandstone has length 4.8 cm and diameter 50 mm. The plexiglas specimen have lengths 20 mm and 60 mm and diameter 50 mm.

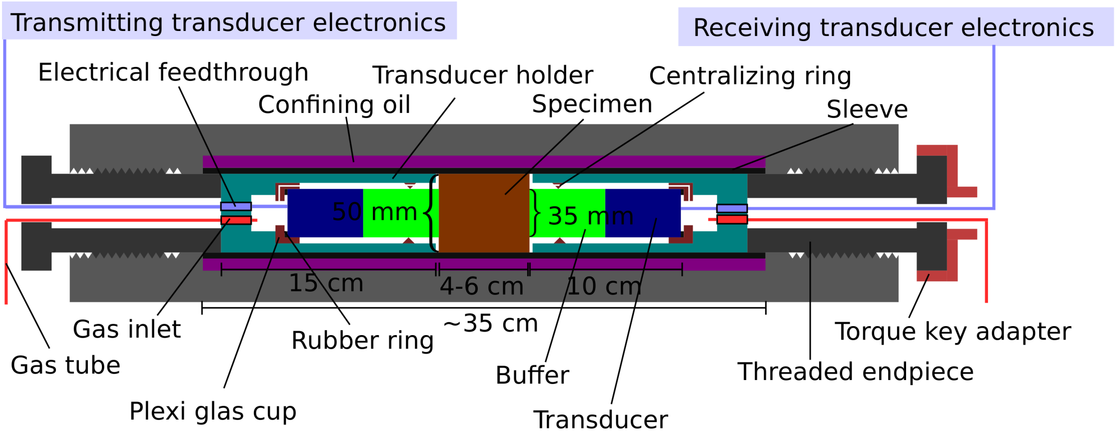

Figure 3.8: Detailed schematic overview of the components inside the pressure cell.

Coupling fluid is applied on the P-wave transducers. On the S-wave transducers, a thin film of polyurethane is covering the surface of the buffers, acting as a coupling layer. A more detailed description of the design of the transducers and the transducer holders is presented in Ch. 4 and in Sect. 3.2, respectively.

Care must be taken when screwing in the end-pieces. The friction between the transducer holder and the end-piece may be so large that the transducer holder also may rotate inside the pressure cell. The signal transmitted from the compressional wave transducers are symmetric and the signal is therefore not affected by the rotation of the transducers. On the contrary, the shear waves from the shear wave transducers are asymmetric by nature and a rotation of the transducers will affect the received signal in both phase and magnitude. The transducer holders may also twist while the the transducer itself stays fixed due to the friction against the specimen. A rotation of the transducer holder while the transducer stays fixed may twist the cable of the transducer so that it eventually snaps. This is further detailed in Ch. 4. Some considerations on the uncertainties of the measurements are given in Ch. 6.

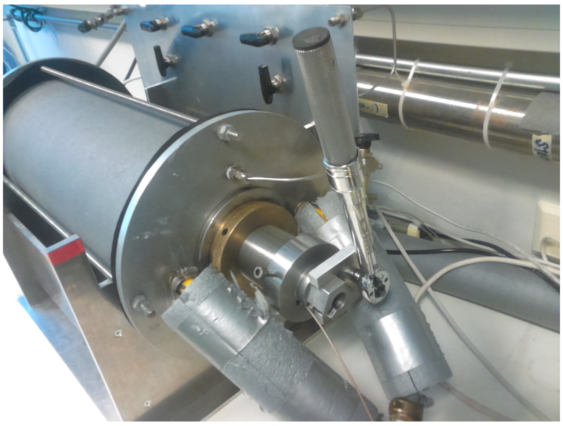

Figure 3.9: Torque wrench used on the torque key adapter attached on the transducer holder.

3.3.3 System model for the solid buffer method

To describe the measurements conducted with the solid buffer method in this work, block diagrams are used. Block diagrams of measurement A and measurement B are shown in Fig. 3.11 a) and b), respectively. Each block may be described with a transfer function, which enables a mathematical description of the measurement system.

Probes generating compressional or shear waves in a solid have previously been modeled with a traction on the surface of the transmitter [174, 175, 176]. Such a transducer description has also been used here. In the system model used to describe the measurements in this chapter, numbered nodes may lead to confusion if x_1 and x_3 where used to describe the directions. Due to this x and z-coordinates are used. In Fig. 3.10, a cartesian coordinate system used for describing the solid buffer method is shown. For compressional waves, the traction vector is pointing in the direction of the receiving transducer, z-direction, and for shear waves, the traction vector is pointing in the x-direction. The y-axis is directed inwards in into the paper, "Tx" and "Rx" are the transmitting and receiving transducers, respectively, "buff" are the buffers and "Med" is the specimen. In the following description, t^z is the traction vector component in the z-direction, t^x is the traction vector component in in the x-direction. To avoid describing two almost identical models for shear wave measurements and compressional wave measurements, * decides whether compressional waves or shear waves are measured. $^* = z$ for compressional wave measurements and $^* = x$ for shear wave measurements.

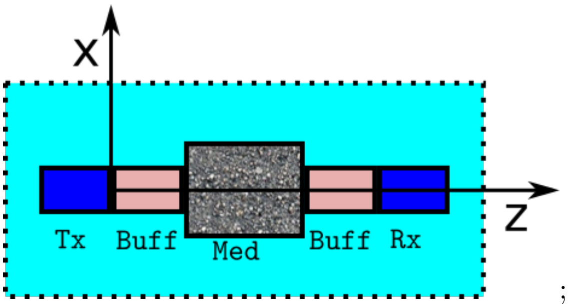

;

Figure 3.10: Shows the coordinate system used for the system model. Here the acoustic transducers with buffers and specimen for measurement B is shown as an illustration.

Schmerr and Song [177], Niklasson et. al. [174], Bostrom et. al. [175] and Eriksson et. al. [176] use system models and transfer functions to describe acoustic wave propagation. None of these studies have addressed unwanted acoustic reflections from e.g. sidewalls as they define the traction in an elastic half-space. The half-space is analogue to the free-field conditions in a fluid. In the solid buffer method used in this work, some unwanted reflections will be present. To the best of this author's knowledge, there are no established system models for quantitatively including such unwanted reflections. In this work, transfer functions including unwanted reflections have been defined so that unwanted reflections can be addressed in a more formal way (Eq. (3.5)). To quantify such reflections, finite element simulations are presented in Ch. 5 and 6.

In Fig. 3.11, system models for measurement A and measurement B, respectively, are shown for the solid buffer method. The different blocks represent the transfer functions of components of the measurement setup shown in Fig. 3.6. In between every block, a node is defined. Either voltage, V, or the on-axis traction vector, t, is defined at each of these nodes, labeled with a number. Here, the "on-axis" is defined by the symmetry-axis of the transducers (along z-axis, x=0 in Fig. 3.10). All variables are in the frequency domain. Each variable is labeled with the node number and A or B, denoting measurement A or measurement B, respectively. r is labeling a variable containing acoustic and electrical reflections from all directions in addition to noise.

For measurement A, the input voltage on the signal generator, transmitting electronics and the transmitting transducer are denoted as $V_{0,A}$, $V_{1,Ar}$ and $V_{2,Ar}$, respectively. The transmitting electronics corresponds to the power amplifier, attenuator and matching filter shown in Fig. 3.6 a). The input voltage is assumed to be the same as the emf of the signal generator. $t^*_{3,A}$ denotes the on-axis $*$-component of the traction vector (z or y-component) at the transmitting transducer's front surface. $t^*_{4,A}$ denotes the on-axis $*$-component of the traction vector at the buffer-buffer interface. That is, between the buffer attached to the transmitting transducer (buffer 1) and the buffer attached to the receiving transducer (buffer 2). $t^*_{5,A}$ denotes the on-axis $*$-component of the traction vector at the receiving transducer's front surface. $V_{6,Ar}$ and $V_{7,Ar}$ denote the input voltage on the receiving electronics and oscilloscope, respectively. The receiving electronics is the matching filter, signal amplifier and filter, shown in Fig. 3.6 a).

For measurement B, the input voltage on the signal generator, transmitting electronics and the transmitting transducer are denoted as $V_{0,B}$, $V_{1,Br}$ and $V_{2,Br}$, respectively. Here, the transmitting electronics corresponds to the power amplifier, attenuator and matching filter shown in Fig. 3.6 b). The input voltage is assumed to be the same as the emf of the signal generator. $t^*_{3,B}$ denotes the on-axis $*$-component of the traction vector (z or x-component) at the transmitting transducer's front surface. $t^*_{4,B}$ denotes the on-axis $*$-component of the traction vector at the buffer-specimen interface on the transmitting side. $t^*_{5,B}$ denotes the on-axis $*$-component of the traction vector at the specimen-buffer interface at the receiving side. $t^*_{6,B}$ denotes the on-axis $*$-component of the traction vector at the receiving transducer's front surface. $V_{7,Br}$ and $V_{8,Br}$ denote the input voltage on the receiving electronics and oscilloscope, respectively. The receiving electronics is the matching filter, signal amplifier and filter, shown in Fig. 3.6 b).

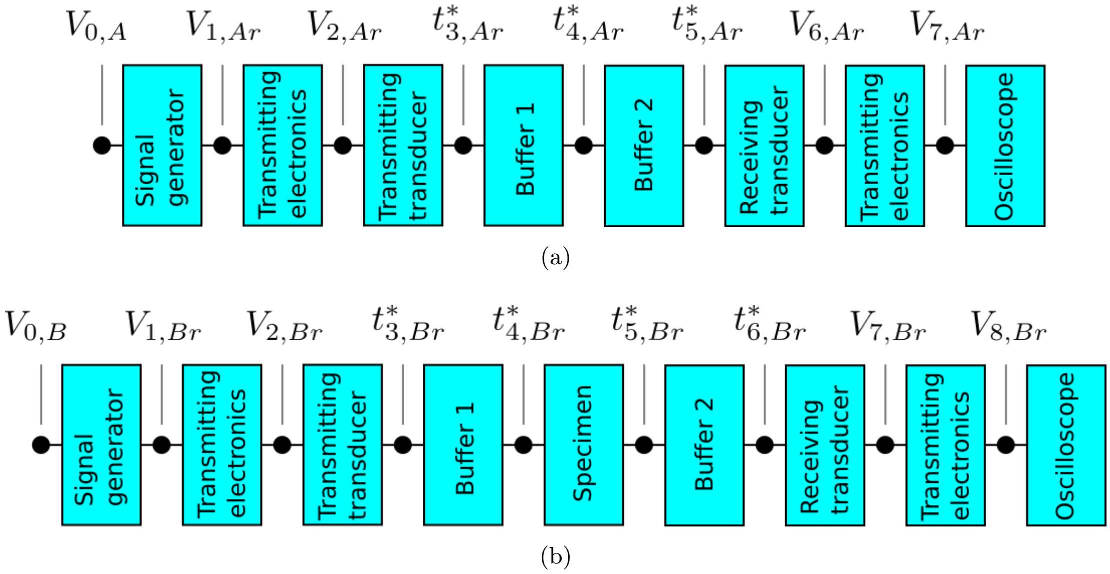

Figure 3.11: System model of the solid buffer method presented as a block diagram. **a)** Measurement A. **b)** Measurement B.

Mathematically, the system model for measurement A and B can be written

$$V_{7,Ar} = V_{0,A}\ \frac{V_{1,Ar}}{V_{0,A}}\ \frac{V_{2,Ar}}{V_{1,Ar}}\ \frac{t^*_{3,Ar}}{V_{2,Ar}}\ \frac{t^*_{4,Ar}}{t^*_{3,Ar}}\ \frac{t^*_{5,Ar}}{t^*_{4,Ar}}\ \frac{V_{6,Ar}}{t^*_{5,Ar}}\ \frac{V_{7,Ar}}{V_{6,Ar}}, \tag{3.3}$$

$$V_{8,Br} = V_{0,B}\ \frac{V_{1,Br}}{V_{0,B}}\ \frac{V_{2,Br}}{V_{1,Br}}\ \frac{t^*_{3,Br}}{V_{2,Br}}\ \frac{t^*_{4,Br}}{t^*_{3,Br}}\ \frac{t^*_{5,Br}}{t^*_{4,Br}}\ \frac{t^*_{6,Br}}{t^*_{5,Br}}\ \frac{V_{7,Br}}{t^*_{6,Br}}\ \frac{V_{8,Br}}{V_{7,Br}}. \tag{3.4}$$

To formally describe the simulations presented in section 5.2.1 - 5.2.2 and link them to the measurements, some transfer functions are useful:

$$\begin{aligned} H^{VV,open}_{26,Ar} &\equiv \frac{V^{open}_{6,Ar}}{V_{2,Ar}}, \qquad & H^{VV,open}_{27,Br} &\equiv \frac{V^{open}_{7,Br}}{V_{2,Br}}. \\ H^{VV,open}_{26,A} &\equiv \frac{V^{open}_{6,A}}{V_{2,A}}, \qquad & H^{VV,open}_{27,B} &\equiv \frac{V^{open}_{7,B}}{V_{2,B}}. \end{aligned} \tag{3.5}$$

"*open*" denotes terminated with an open circuit. $V^{open}_{6,Ar}$ is the voltage across the electrodes of the receiving transducer in measurement A, for open circuit conditions. $V^{open}_{7,Br}$ is the voltage across the electrodes of the receiving transducer in measurement B, for open circuit conditions. When "r" is left out in the expressions, there are no acoustic (or electrical) reflections in the measurement system, in either the x or z-direction. The transfer function in Eq. 3.5 are used in the finite element simulations of the solid buffer method (Sect 5.2).

The system model in Eqs. (3.3) and (3.4) can in principle describe all effects related to wave propagation, such as diffraction effects, acoustic wave reflections, electrical wave reflections, electrical cross-talk and other noise-effects. Such model will be extremely complex and an analytical solution of the variables in the different nodes would be hard to find.

To obtain an expression used for calculating c_P and α_P, the equation for the system model is rewritten using an uniformly vibrating, circular piston mounted in an infinite rigid baffle as the transmitting transducer. $t_3 = t^z_3$ is then the traction in the z-direction across the whole surface of the piston source. A similar approach is used to obtain an expression for c_S. The source is vibrating in the x-direction (see Fig. 3.10) and $t_3 = t^x_3$ is then the traction in the x-direction across the whole surface of source. The wave propagation for both the compressional and shear waves is described with a plane wave description and a diffraction correction term. The diffraction correction term describes the deviation between the plane wave and the average of the traction vector in a half-space across a surface equal to the receiving transducer. The approach of using a plane wave and a diffraction correction term to describe the wave propagation is used in both fluid [72, 53] and in solids [52, 54]. Assuming there are no unwanted reflections in the measurement system, the modified system model for measurement A and B can mathematically be expressed

$$V_{7,A} = V_{0,A} \; \frac{V_{1,A}}{V_{0,A}} \; \frac{V_{2,A}}{V_{1,A}} \; \frac{t^*_{3,A}}{V_{2,A}} \; e^{-ik^*_b D_b} T^*_A e^{-ik^*_b D_b} \; \frac{\langle t^*_{5,A} \rangle}{t^{*,pl}_{5,A}} \; \frac{V_{6,A}}{\langle t^*_{5,A} \rangle} \; \frac{V_{7,A}}{V_{6,A}}, \quad (3.6)$$

$$V_{8,B} = V_{0,B} \; \frac{V_{1,B}}{V_{0,B}} \; \frac{V_{2,B}}{V_{1,B}} \; \frac{t^*_{3,B}}{V_{2,B}} \; e^{-ik^*_b D_b} T^*_{B1} e^{-ik^*_m d} T^*_{B2} e^{-ik^*_b D_b} \; \frac{\langle t^*_{6,B} \rangle}{t^{*,pl}_{6,B}} \; \frac{V_{7,B}}{\langle t^*_{6,B} \rangle} \; \frac{V_{8,B}}{V_{7,B}}. \quad (3.7)$$

D_b is the buffer length. $k^*_b = k^z_b$ is the compressional wave number in the buffers and $k^*_b = k^x_b$ is the shear wave number in the buffers. $k^*_m = k^z_m$ is the compressional wave number in the specimen and $k^*_m = k^x_m$ is the shear wave number in the specimen. "pl" denotes the plane wave. $T^*_{B1} = T^z_{B1}$ and $T^*_{B2} = T^z_{B2}$ are the plane compressional wave traction transmission coefficients defined by Schmerr and Song [177]:

$$\begin{aligned} T^z_{B1} &= \frac{2R_2}{R_1 + R_2}, \qquad & T^z_{B2} &= \frac{2R_1}{R_1 + R_2}, \\ R_1 &= \rho_b c^b_P, & R_2 &= \rho_m c_P. \end{aligned} \quad (3.8)$$

$T^*_{B1} = T^x_{B1}$ and $T^*_{B2} = T^x_{B2}$ are the plane shear wave traction transmission coefficients defined by Schmerr and Song [177]:

$$\begin{aligned} T^x_{B1} &= \frac{2R_2}{R_1 + R_2}, \qquad & T^x_{B2} &= \frac{2R_1}{R_1 + R_2}, \\ R_1 &= \rho_b c^b_S, & R_2 &= \rho_m c_S. \end{aligned} \quad (3.9)$$

When two identical buffers are welded together, T^*_A is given [177]:

$$T^z_A = T^x_A = 1. \quad (3.10)$$

ρ_b and ρ_m are the densities of the buffers and the specimen, respectively. c^b_S and c^b_P are the compressional and shear wave velocity of the buffers, respectively. In this model, the medium in which the acoustic wave propagates is assumed to be a half-space. Thus, there are no unwanted sidewall reflections and the parameter "r" is left out in the expressions. $\langle t^*_{5,A} \rangle$ describes the average *- component of the traction over the receiving transducer's front surface without the transducer present in measurement A. $\langle t^*_{6,B} \rangle$ describes the average *- component of the traction over the receiving transducer's front surface without the transducer present in measurement B. The diffraction correction terms are defined

$$H^{dif}_A = \frac{\langle t^*_{5,A} \rangle}{t^{*,pl}_{5,A}}, \qquad H^{dif}_B = \frac{\langle t^*_{6,B} \rangle}{t^{*,pl}_{6,B}}. \quad (3.11)$$

Mathematical expressions for these are given in Eq. (2.8) for the solid buffer method. This way of defining the diffraction correction has previously been used in solids for compressional waves [52] and for shear waves [54]. In the system model 3.6 and 3.7,

t_3 is propagating as a plane wave to the receiver. The plane wave at the receiver in measurement A and B are defined

$$\begin{aligned} t^{*,pl}_{5,A} &= t^*_{3,A} e^{-ik^*_b D_b} T^*_A e^{-ik^*_b D_b}, \\ t^{*,pl}_{6,B} &= t^*_{3,B} e^{-ik^*_b D_b} T^*_{B1} e^{-ik^*_m d} T^*_{B2} e^{ik^*_b D_b}. \end{aligned} \tag{3.12}$$

The plane wave at node 5 in measurement A, $t^{*,pl}_{5,A}$, is the plane wave propagation of $t^*_{3,A}$ through the buffer medium. Without any sidewall reflections, the wave propagates through buffer 1 and into buffer 2. In this model (Eqs. (3.6) and (3.7)), buffer 2 is mathematically treated as a half space and the acoustic wave propagates through buffer 2 to the front of the receiving transducer without the receiving transducer present. The plane wave transmission coefficient through the buffer-buffer interface is in this work assumed to be $T_A = 1$, because the buffers are made of the same material.

Similar to measurement A, the plane wave at node 6, $t^{*,pl}_{6,B}$, on the receiving transducer's front surface in measurement B, is the plane wave propagation of $t^*_{3,B}$ through buffer 1, the specimen and the half-space buffer 2. As in measurement A, the acoustic wave propagates through buffer 2 to the front of the receiving transducer without the receiving transducer present.

3.3.4 Expressions for c_P, c_S and α_P for the solid buffer method

By dividing the modified expressions for measurement A with the modified expressions for measurement B (Eqs. (3.6) and (3.7)) the following fraction is obtained:

$$\frac{V_{8,B}}{V_{7,A}} = \frac{V_{0,B} \, \frac{V_{1,B}}{V_{0,B}} \, \frac{V_{2,B}}{V_{1,B}} \, \frac{t^*_{3,B}}{V_{2,B}} \; e^{-ik^*_b D_b} T^*_{B1} e^{-ik_m d} T^*_{B2} e^{-ik^*_b D_b} \, \frac{\langle t^*_{6,B} \rangle}{t^{*,pl}_{6,B}} \, \frac{V_{7,B}}{\langle t^*_{6,B} \rangle} \, \frac{V_{8,B}}{V_{7,B}}}{V_{0,A} \, \frac{V_{1,A}}{V_{0,A}} \, \frac{V_{2,A}}{V_{1,A}} \, \frac{t^*_{3,A}}{V_{2,A}} \; e^{-k^*_b D_b} T^*_A e^{-ik^*_b D_b} \, \frac{\langle t^*_{5,A} \rangle}{t^{*,pl}_{5,A}} \, \frac{V_{6,A}}{\langle t^*_{5,A} \rangle} \, \frac{V_{7,A}}{V_{6,A}}}. \tag{3.13}$$

From Eq. (3.13), expressions for c_P, c_S and α_P are derived. When no unwanted acoustic reflections are assumed, many of the transfer functions will cancel out, $\frac{V_{1,A}}{V_{0,A}} = \frac{V_{1,B}}{V_{0,B}}$, $\frac{V_{2,A}}{V_{1,A}} = \frac{V_{2,B}}{V_{1,B}}$, $\frac{t^*_{3,A}}{V_{2,A}} = \frac{t^*_{3,B}}{V_{2,B}}$, $\frac{V_{6,A}}{\langle t^*_{5,A} \rangle} = \frac{V_{7,B}}{\langle t^*_{6,B} \rangle}$, $\frac{V_{7,A}}{V_{6,A}} = \frac{V_{8,B}}{V_{7,B}}$. Canceling the terms above, Eq. (3.13) reduces to:

$$\frac{V_{8,B}}{V_{7,A}} = \frac{V_{0,B} e^{-ik^*_m d} T^*_{B1} T^*_{B2} H^{dif}_B}{V_{0,A} H^{dif}_A T^*_A}. \tag{3.14}$$

Compressional wave velocity

To find c_P, the compressional wavenumber, $k^*_m = k^z_m$, must be used and the phase of Eq. (3.14) must be computed:

$$\angle\Big(\frac{V_{8,B}}{V_{7,A}}\Big) = \angle\Big(\frac{V_{0,B}}{V_{0,A}}\frac{H_B^{dif}}{H_A^{dif}}\frac{T_{B1}T_{B2}}{T_A}e^{-ik_m^P d}\Big). \tag{3.15}$$

From Eqs. (3.8)-(3.10), $\angle\Big(\frac{T_{B1}T_{B2}}{T_A}\Big) = 0$. By also assuming $\angle\Big(\frac{V_{0,B}}{V_{0,A}}\Big) = 0$, the equation reduces to

$$\angle V_{8,B} - \angle V_{6,A} = \angle H_B^{dif} - \angle H_A^{dif} - K_m^P d, \tag{3.16}$$

where $K_m^z = \omega/c_P$ is the real part of the compressional wavenumber. An expression for c_P is found:

$$c_P = \frac{d}{-(\angle V_{8,B}/\omega - \angle V_{6,A}/\omega) + (\angle H_B^{dif}/\omega - \angle H_A^{dif}/\omega)}. \tag{3.17}$$

c_P can be calculated with this equation using the Fourier spectrum method, presented in Sect. 3.5.2. By defining $t_A \equiv -\angle V_{6,A}/\omega$, $t_B \equiv -\angle V_{8,B}/\omega$, $t_A^{dif} \equiv -\angle H_A^{dif}/\omega$ and $t_B^{dif} \equiv -\angle H_B^{dif}/\omega$, Eq. (3.17) may be expressed in the time domain:

$$c_P = \frac{d}{t_B - t_A + t_A^{dif} - t_B^{dif}}. \tag{3.18}$$

t_A^{dif} and t_B^{dif} are calculated for a distinct frequency using the definitions above and the diffraction correction presented in Eq. (2.8). A distinct frequency can be defined in the steady-state portion of a burst. t_A and t_B are not directly measured, however, $t_B - t_A$ can be found by measuring the time delay between the steady-state portion of a burst in measurement A and measurement B. This is described in the basic pulse method in Sect. 3.5.1.

In the literature, the typical presentation of the solid buffer method is without a rigorous system model for the frequency domain [71, 50, 124] and time domain [22, 65]. Diffraction effects are typically not included in the equation for c_P (Eqs. (3.17)-(3.18)) but addressed separately after c_P has been calculated [178, 51].

Shear wave velocity

Since the exact same procedure for calculating the wave velocity applies for both shear and compressional waves, the shear wave velocity is calculated using the shear wavenumber, $k_m^* = k_m^x$:

$$c_S = \frac{d}{-(\angle V_{8,B}/\omega - \angle V_{6,A}/\omega) + (\angle H_{6,B}^{dif}/\omega - \angle H_{5,A}^{dif}/\omega)}, \tag{3.19}$$

where the shear wave diffraction corrections from Eq. (2.8) are used. A discussion on the uncertainty of using Rogers and Buren's diffraction correction to correct for diffraction effects for shear waves are given in Ch. 6. Expressed with measured transit times, t_A and t_B:

$$c_S = \frac{d}{t_B - t_A + t_A^{dif} - t_B^{dif}}. \tag{3.20}$$

Compressional wave attenuation coefficient

When finding the compressional wave attenuation coefficient, the absolute value of Eq. (3.14) is taken with $k_m^* = k_m^z$.

$$\begin{aligned}\left|\frac{V_{8,B}}{V_{7,A}}\right| &= \left|\frac{V_{0,B}e^{-ik_m^z d}T_{B1}^z T_{B2}^z H_B^{dif}}{V_{0,A}H_A^{dif}T_A^z}\right|. \\ \ln\left|\frac{V_{8,B}}{V_{7,A}}\right| &= \ln\left|\frac{V_{0,B}}{V_{0,A}}\right| + \ln\left|\frac{H_B^{dif}}{H_A^{dif}}\right| + \ln|e^{-ik_m^z d}| + \ln\left|\frac{T_{B1}^z T_{B2}^z}{T_A^z}\right|.\end{aligned} \tag{3.21}$$

The wave numbers are complex values having real and imaginary parts: $k_m^z = K_m^z - i\alpha_P$. The equation reduces to

$$\ln\left|\frac{V_{8,B}}{V_{6,A}}\right| = \ln\left|\frac{V_{0,B}}{V_{0,A}}\right| + \ln\left|\frac{H_B^{dif}}{H_A^{dif}}\right| - \alpha_P d + \ln\left|\frac{T_{B1}^z T_{B2}^z}{T_A^z}\right|. \tag{3.22}$$

α_P may now be written

$$\alpha_P = \frac{-\ln\left|\frac{V_{8,B}}{V_{6,A}}\right| + \ln\left|\frac{H_B^{dif}}{H_A^{dif}}\right| + \ln\left|\frac{V_{0,B}}{V_{0,A}}\right| + \ln\left|\frac{T_{B1}^z T_{B2}^z}{T_A^z}\right|}{d} \tag{3.23}$$

Expression 3.23 has been used in α_p-measurements including diffraction correction terms [50] for the solid buffer method. The transmission coefficients, T_{B1}^z, T_{B2}^z and T_A^z are given in Eqs. (3.8)-(3.10).

3.3.5 Noise

Electrical noise is seen in the measurements, both as coherent noise with the same frequency and number of cycles as the input signal, and as incoherent noise, giving an unsteady acquired signal. Even if the acquired signal from the oscilloscope consists of the average of 256 individual signals, the incoherent noise did not vanish completely. In addition, some other, unidentified noise components were detected from time to time in the measurements. These may be due to other electrical equipment in the room.

In Fig. 3.12, an electrical circuit where a receiving transducer and an amplifier make out the main parts is shown. The load in the circuit, Z_L, is the oscilloscope. There are two nodes in the figure. Node 1 is located at the transducer's ground output port. Node 2 is located at the amplifier's ground input port. The transducer produces a differential signal across it's electrodes regardless of the existing electrical potential at node 1.

Both the shield and the signal wire in the coax cables inherit capacitive reactances [179]. In Fig. 3.12, the capacitive reactance in the shield of the coax-cable between the transducer and the amplifier is named C_{cx}. Z_{G1} and Z_{G2} are impedances coupling the circuit to ground $G1$ and ground $G2$, respectively.

Cables may act as antennas and pick up noise from the surroundings. However, by moving cables around, no change in the acquired signal is seen. Thus, electromagnetic cross talk between cables are assumed to be negligible.

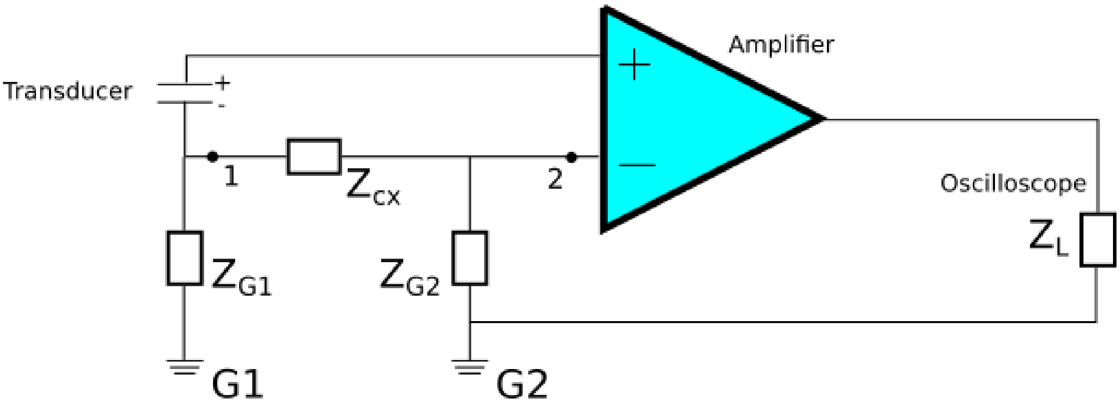

Figure 3.12: Electrical curcuit showing a receiving transducer, signal amplifier and oscilloscope (Z_L). Z_{cx} is the capacitive reactance in the coax-cable between the transducer and the amplifier. 1,2 are nodes used to explain noise mechanisms on the receiving side of the solid buffer measurement setup. Z_{G1} and Z_{G2} are impedances between node 1 and ground $G1$ and between node 2 and ground $G2$, respectively.

The ground potential, $G1$, is coupled through the metal chassis of the pressure cell and onto the ground of the transmitting transducer. Now, if $G1 \neq G2$, a small ground loop current may flow between $G1$ and $G2$ and be amplified, giving a noise signal on the oscilloscope. A small leakage from the signal on the transmitting side and into the ground, $G1$ may give rise to the coherent noise signal seen in the measurement. This signal has similar shape as the electrical signal produced by the signal generator and starts at time zero on the oscilloscope. Shortcutting node 1 and node 2 in Fig. 3.12 may reduce this noise. In this work, this has been done by attaching aluminum foil to the coax-shield as close as possible to the receiving transducer and connecting it to the ground of the Panametrics Ultrasonic Preamp. The cable-induced impedance in this very flat "aluminum cable" is close to zero and node 1 and 2 are thus short-cutted. Using the aluminum foil, Z_{cx} in Fig. 3.12 is thus greatly reduced. The differential signal on the input ports of the amplifier is now only dependent on the differential signal across the transducer. The same principles apply on the transmitting side as on the receiving side.

The shield of the coax-cable near the transducer and the shield of the signal generator is also short-cutted with aluminum foil to eliminate cable induced impedances in the shield of the coax cable.

By shortcutting node 1 and node 2 in Fig. 3.12 using aluminum foil, the signal stabilized and some of the electrical noise in the start of the signal disappeared. The variation in the amplitude of the received signal is reduced from 40-50 % to less than 5 % in very noisy measurements. The unidentified noise components mentioned above (probably due to other electrical equipment in the room) is greatly reduced with the used of aluminum foil and use of the averaging function on the oscilloscope. Using the aluminum foils and the averaging function on the oscilloscope gave a signal-to-noise ratio (SNR) of at least 40dB at maximum hydrate growth. Before hydrate growth SNR ¿ 20 dB using the aluminum foils.

The coherent noise in the start of the oscilloscope window is easily separated from the delayed acoustic signal manually. However, without using the aluminum foil, the electrical noise is large in amplitude and the logging script adjusts the settings on the signal generator and the oscilloscope to fit the largest signal in the oscilloscope window. A large (separable) noise signal and a weak acoustic signal give poor utilization of the dynamic range of the oscilloscope because the dynamic range is fitted for the noise signal. However, by using the aluminum foil, the electrical noise is usually lower in amplitude than the delayed acoustic signal and the dynamic range of the oscilloscope is adjusted to the acoustic signal. An effort is done to set the time window so that the electrical noise signal is not present at all in acquired signals. By using the aluminum foil and setting the time window on the oscilloscope to separate the electrical noise from the delayed acoustic signal, the logging script is able to automatically adjust the settings on the signal generator and the oscilloscope to acquire the acoustic signal during through the Bentheim sandstone during the days or weeks in which the hydrate experiments lasted.

3.4 Immersion method

The immersion method has been widely used to measure acoustic properties of elastic materials [72, 53, 65]. In this work, measurements on plexiglas using the immersion method has been compared with measurements on plexiglas conducted with the solid buffer method. The immersion method is thus acting as a reference method for the solid buffer method. The method has also been used to measure the acoustic properties of materials used in the transducer design, such as PVC, and tungsten-filled epoxy samples. The plexiglas and the PVC plates used in the immersion method are both 9x9 cm, with thickness 20 mm. The tungsten-epoxy samples have thicknesses 8 - 20 mm and diameter 50 mm. Tungsten-epoxy samples with tungsten grains 5 and 50-250 micron are constructed. The plexiglas plate, PVC plate and two of the tungsten-epoxy samples are shown in Fig. 3.13.

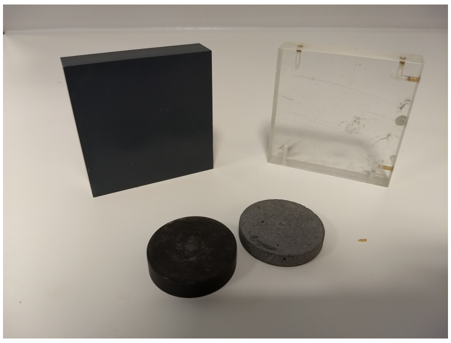

Figure 3.13: Photographs of specimen used in the immersion method. The plexiglas and PVC-plates are 9x9 cm, with thickness 20 mm. The small discs are tungsten-epoxy samples with 5 micron (dark grey) and 50-250 micron tungsten grains tungsten-epoxy (light gray). They both have 50 mm diameter. The 5 micron and 50-250 micron tungsten-epoxy samples have thicknesses 1.2 cm.

3.4.1 Experimental setup and measurements using the immersion method

As in the solid buffer method, two different measurements are used in the immersion method: Measurement A without specimen inserted, and measurement B with the specimen inserted into the wave propagation path (see Fig. 3.14). Wave velocities and attenuation coefficients for the specimen are found by comparing measurement A and measurement B. In the immersion method used in this work, the specimen is immersed in a cell containing distilled water. The transducers are at fixed positions on the wall of the water-filled cell.

In the measurements, a pair of Olympus immersion transducers (Olympus Panametrics-NDT- V302 1.0 MHz) are used in the water immersion cell shown in Fig. 3.14. In this figure, measurement A and measurement B are shown. The adapter holding the specimen can be rotated. Compressional waves are measured with the specimen aligned normal to the incident beam. Shear waves are transmitted into the specimen by rotating the adapter and the specimen. In this work, shear wave measurements are conducted by rotating the specimen to the critical angle of the compressional waves, which is the angle where the compressional waves disappear. The theoretical background of the method is presented below.

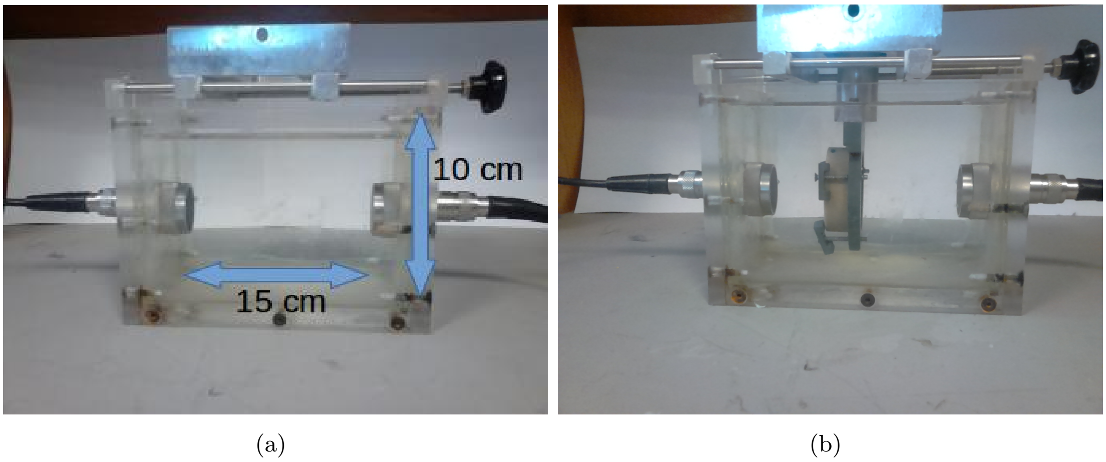

(a) (b)

Figure 3.14: **a)** Picture of water-filled cell used in measurement A. **b)** Picture of water-filled cell with specimen inserted used in measurement B.

Block diagrams of measurements A and measurement B are shown in Fig. 3.15. The transmitting transducer is driven by an Agilent 33250A signal generator. The exciting signal from the signal generator has frequency 500 kHz. One cycle pulses and bursts with 10 cycles are used with an amplitude 20 mV. The received signal is amplified with a Panametrics Ultrasonic Preamp with gain 54 dB. A HP high-pass filter with cutoff-frequency 200 kHz in series is used to remove low-frequency noise components. A Tektronix DPO 3012 oscilloscope acquires the signal by averaging 256 signals at all times. The signal acquired by the oscilloscope is triggered externally by the pulse from the signal generator. The signal generator is controlled by a PC via GPIB communication and the signal is acquired with the oscilloscope via an USB connection. The script for controlling the instruments in the immersion method is the same as for the hydrate measurements (appendix A).

The water cell is 15 cm long, 10 cm wide and 10 cm high. Water is approximately completely filling up the measurement cell and the distance between the transducers is measured to be 12.5 cm. The diameter of the active element inside the piezoelectric transducers is listed to be 25 mm [180]. By using Pythagoras' theorem, the first theoretical sidewall reflections are calculated to travel a distance 21 mm longer than the pulse traveling directly from transducer to transducer. 21 mm corresponds to approximately 7 periods in water at 500 kHz. From this it is concluded that pulses 7 periods or shorter are not affected by any sidewall reflections.

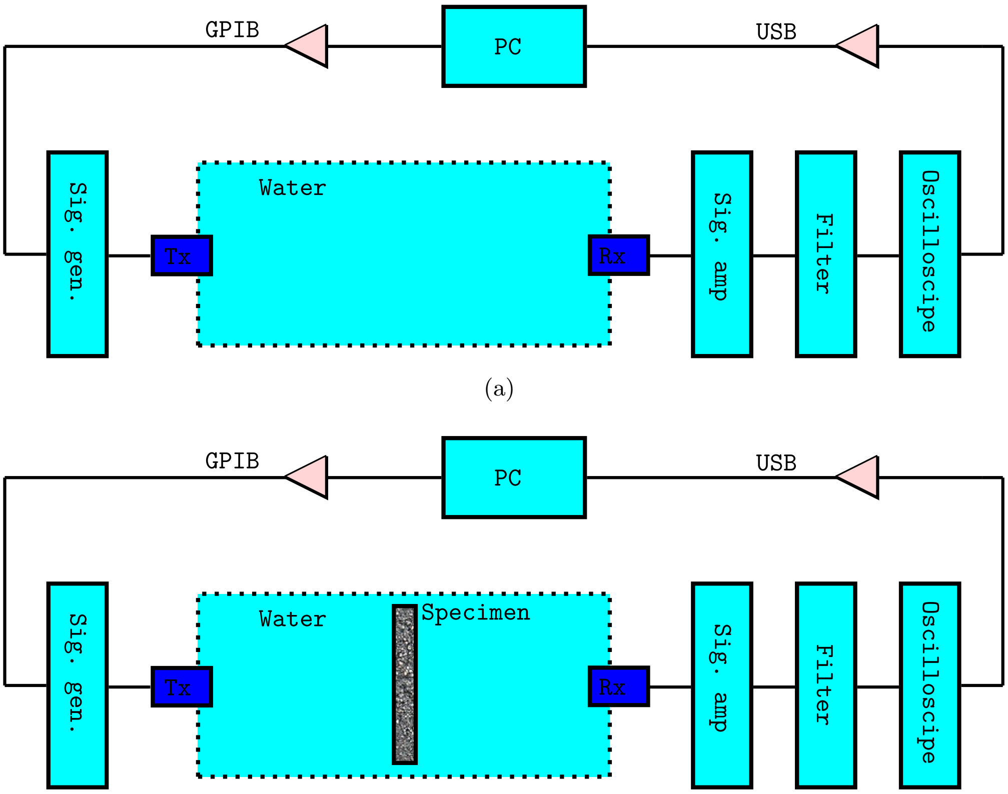

(a)

(b)

Figure 3.15: Block diagrame of the experimental setup using the immersion method. The components are described in the text above. **a)** Measurement setup for measurement A. **b)** Measurement setup for measurement B.

3.4.2 System model for the immersion method

As for the solid buffer method, the immersion method used in this work is described with block diagrams. Block diagrams of measurement A and measurement B (Fig. 3.15) are shown in Fig. 3.17 a) and b), respectively. Each block may be described with a transfer function, which enables a mathematical description of the measurement system. This block-diagram representation of a measurement setup has been used previously [181, 182, 183].

The blocks in Fig. 3.6 represent transfer functions of individual components of the measurement setup shown in Fig. 3.17. In between every block, a node is defined. Either voltage, V, the on-axis pressure, P or the on-axis particle velocity vector, v, is defined at each of these nodes. The setup principle is very similar to that presented for the solid buffer method in section 3.3.3. All variables are in the frequency domain. Each variable is labeled with the node number and A or B, denoting measurement A or measurement

B, respectively. The coordinate system is defined in Fig. 3.16.

For measurement A, the input voltage on the signal generator, transmitting electronics and the transmitting transducer are denoted as $V_{0,A}$, $V_{1,A}$ and $V_{2,A}$, respectively. The input voltage is assumed to be the same as the emf of the signal generator. In the setup, the transmitting electronics only consist of the cables between the signal generator and the transmitting transducer. $v^{z}_{3,A}$ denotes the on-axis z-component of the particle velocity at the transmitting transducer's front surface. $P_{4,A}$ is the on-axis free-field pressure at the receiving transducer's front without the transducer present. $V_{5,A}$ is the voltage at the output terminal of the receiving transducer. $V_{6,A}$ is the voltage at the output of the receiving electronics and is also the measured signal when the oscilloscope is assumed to have an infinite terminal impedance. The transmitting electronics consist of the filter and the signal amplifier seen in Fig. 3.17 a).

For measurement B, the input voltage on the signal generator, transmitting electronics and the transmitting transducer are denoted as $V_{0,B}$, $V_{1,B}$ and $V_{2,B}$, respectively. As for measurement A, the input voltage is assumed to be the same as the emf of the signal generator. In the setup, the transmitting electronics only consist of the cables between the signal generator and the transmitting transducer. $v^{z}_{3,B}$ denotes the on-axis z-component of the particle velocity at the transmitting transducer's front surface. $P_{4,A}$ is the on-axis free-field pressure at the immersed specimen's front surface without the specimen present. To avoid describing two almost identical models for shear wave measurements and compressional wave measurements using the immersion method, * decides whether compressional waves or shear waves are measured. $^{*} = z$ for compressional wave measurements and $^{*} = x'$ for shear wave measurements. $v^{z}_{5,B}$ denotes the on-axis z-component of the particle velocity at the specimen-water interface at node 5. $v^{x'}_{5,B}$ denotes the x'-component of the on-axis particle velocity along the specimen-water interface at node 5. The z, x, and x' directions are defined in Fig. 3.16. In the figure, θ_i, defines the angle of the incoming plane pressure wave. In this work, compressional waves are measured for $\theta_i = 0$. For $\theta_i > 0$, shear waves are generated inside the specimen. In this work, shear waves are measured for $\theta_i = 38^\circ$ (critical angle). θ_t is the angle relative to the normal of the specimen surface ($x' - y$-plane) of the refracted wave. L is the length inside the specimen in which the shear wave propagates (distance of the sound ray path). L_2 is the projection of L in the z-direction. θ_i, L and L_2 are variables mainly used for deriving expressions for c_S-measurements using the immersion method in Sect. 3.4.3. $P_{6,B}$ is the free-field pressure at the receiving transducer's front without the transducer present. $V_{7,B}$ is the voltage at the output terminal of the receiving transducer. $V_{8,B}$ is the voltage at the output of the receiving electronics and is also the measured signal when the oscilloscope is assumed to have an infinite terminal impedance.

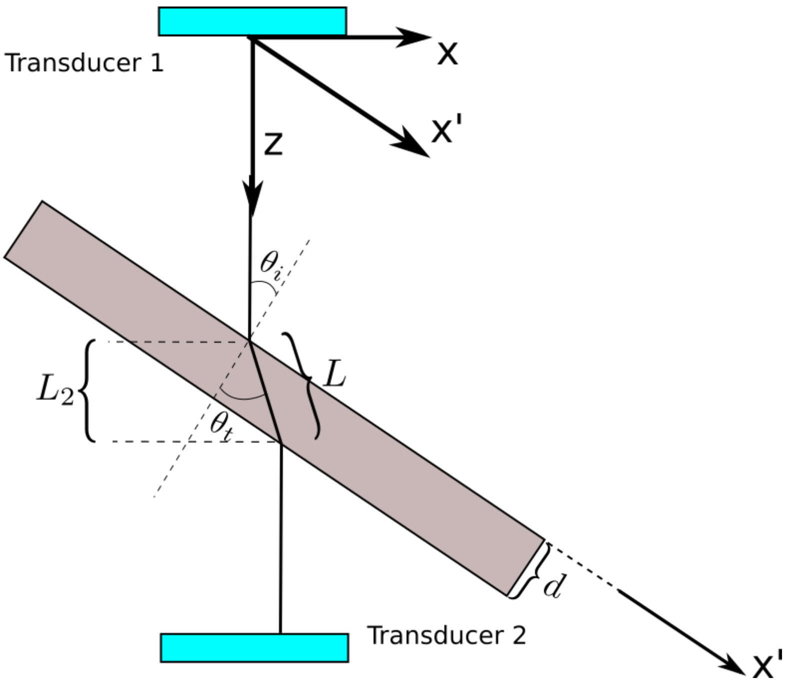

Figure 3.16: Immersion method with tilted specimen.

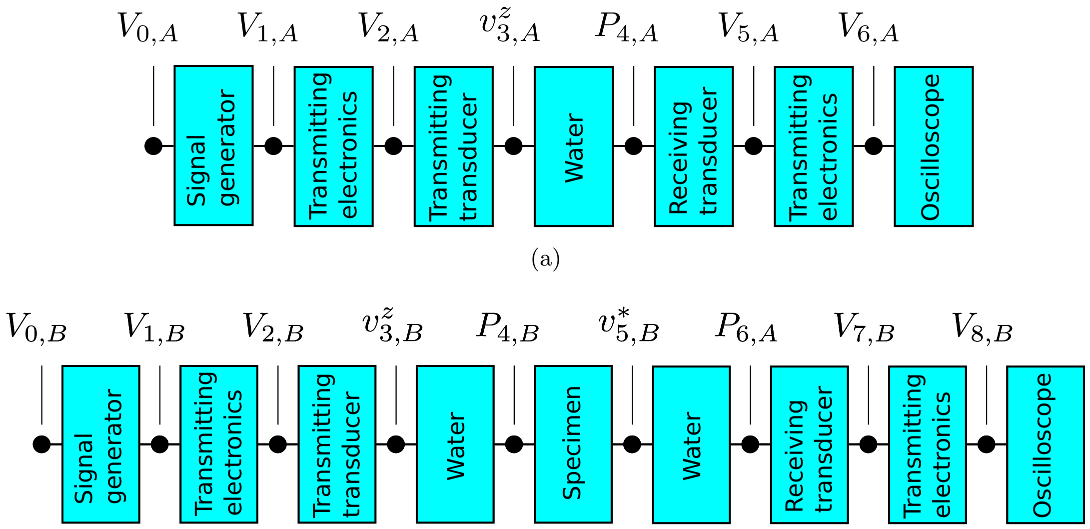

(a)

(b)

Figure 3.17: System model of the immersion method presented as a block diagram. **a)** Measurement A. **b)** Measurement B.

Mathematically, the immersion method system model for measurement A and B can be written

$$V_{6,A} = V_{0,A}\,\frac{V_{1,A}}{V_{0,A}}\,\frac{V_{2,A}}{V_{1,A}}\,\frac{v^z_{3,A}}{V_{2,A}}\,\frac{P_{4,A}}{v^z_{3,A}}\,\frac{V_{5,A}}{P_{4,A}}\,\frac{V_{6,A}}{V_{5,A}} \tag{3.24}$$

$$V_{8,B} = V_{0,B}\,\frac{V_{1,B}}{V_{0,B}}\,\frac{V_{2,B}}{V_{1,B}}\,\frac{v^z_{3,B}}{V_{2,B}}\,\frac{P_{4,B}}{v^z_{3,B}}\,\frac{v^*_{5,B}}{P_{4,A}}\,\frac{P_{6,B}}{v^*_{5,B}}\,\frac{V_{7,B}}{P_{6,B}}\,\frac{V_{8,B}}{V_{7,B}}. \tag{3.25}$$

To obtain an expression used for calculating c_P, c_S, α_P, the equation for the system model is rewritten using an uniformly vibrating, circular piston mounted in an infinite rigid baffle as the transmitting transducer. v^z_3 is then the particle velocity across the whole surface of the piston source. The wave propagation is described with a plane wave description and a diffraction correction term.

The diffraction correction term describes the deviation between the plane pressure wave and the average of the pressure across a measurement area equal to the surface of the receiving transducer. The approach of using a plane wave and a diffraction correction term to describe the wave propagation in the immersion method is used for compressional wave measurements [72] and shear wave measurements [53]. The modified system model for measurement A and B can mathematically be expressed

$$V_{6,A} = V_{0,A}\,\frac{V_{1,A}}{V_{0,A}}\,\frac{V_{2,A}}{V_{1,A}}\,\frac{v^z_{3,A}}{V_{2,A}}\,e^{-ik_w D}\,\rho_w c_w\,H^{dif}_A\,\frac{V_{5,A}}{\langle P_{4,A}\rangle}\,\frac{V_{6,A}}{V_{5,A}}, \tag{3.26}$$

$$V_{8,B} = V_{0,B}\,\frac{V_{1,B}}{V_{0,B}}\,\frac{V_{2,B}}{V_{1,B}}\,\frac{v^z_{3,B}}{V_{2,B}}\,e^{-i(k_w(D-L_2)+k^*_m L)}T^*_{w1}T^*_{w2}\,\rho_w c_w\,H^{dif}_B\,\frac{V_{7,B}}{\langle P_{6,B}\rangle}\,\frac{V_{8,B}}{V_{7,B}}. \tag{3.27}$$

$\rho_w c_w$ transfers the velocity to pressure using Euler's equation [84]. T^*_{w1} and T^*_{w2} are the plane wave transmission coefficients through the water-specimen and specimen-water interfaces, respectively. These depend on θ_i and whether shear waves or compressional waves propagate through the specimen. Wu et al. [53] obtained $\angle T^z_{w1} = \angle T^z_{w2} = \angle T^{x'}_{w1} = \angle T^{x'}_{w2} = 0$. This is also used in this work. With normal incident ($\theta_i = 0$), the plane wave transmission coefficients, T^z_{w1} and T^z_{w2} are given [53]:

$$\begin{gathered} T^z_{w1} = \frac{2R_2}{R_1 + R_2}, \qquad T^z_{w2} = \frac{2R_1}{R_1 + R_2} \\ R_1 = \rho_w c_w, \qquad R_2 = \rho_m c_P \end{gathered} \tag{3.28}$$

The plane shear wave attenuation coefficients, $T^{x'}_{w1}$ and $T^{x'}_{w1}$, are given by Wu et al. [53]. However, since α_S is not calculated in this work, these are not of interest here. k_w is the complex wavenumber in the water. $k^*_m = k^{x'}_m$ is the complex shear wave number in shear wave measurements. D is the distance between the two transducers. $D - L_2$ is the wave propagation distance in the water. Because in general the specimen is tilted, the sound ray traveling through the specimen will travel a greater distance than the thickness of the specimen, d. At normal incidence $L = L_2 = d$, where d is the thickness of the specimen. The parameters are shown in Fig. 3.16.

$\langle P_{4,A}\rangle$ is the average incoming free-field pressure over the surface of the receiving transducer in measurement A when the transducer is absent. $\langle P_{6,B}\rangle$ is the average incoming free-field pressure over the surface of the receiving transducer in measurement B when the transducer is absent. Expressions for H_A^{dif} and H_B^{dif} are given in Eq. (2.7) for the immersion method.

3.4.3 Expressions for c_P, c_S and α_P for the immersion method

By dividing the expressions for measurement A and B in Eqs. (3.26)-(3.27), expressions for c_P, c_S and α_P are obtained:

$$\frac{V_{8,B}}{V_{6,A}} = \frac{V_{0,B}\,\frac{V_{1,B}}{V_{0,B}}\,\frac{V_{2,B}}{V_{1,B}}\,\frac{v^z_{3,B}}{V_{2,B}}\,e^{-i(k_w(D-L_2)+k^*_m L)}T_{w1}T_{w2}\,\rho_w c_w\,H_B^{dif}\,\frac{V_{7,B}}{\langle P_{6,B}\rangle}\,\frac{V_{8,B}}{V_{7,B}}}{V_{0,A}\,\frac{V_{1,A}}{V_{0,A}}\,\frac{V_{2,A}}{V_{1,A}}\,\frac{v^z_{3,A}}{V_{2,A}}\,e^{-ik_w D}\,\rho_w c_w\,H_A^{dif}\,\frac{V_{5,A}}{\langle P_{4,A}\rangle}\,\frac{V_{6,A}}{V_{5,A}}} \tag{3.29}$$

The transducer and electrical transfer functions in measurement A and B, respectively, will cancel out, $\frac{V_{1,A}}{V_{0,A}} = \frac{V_{1,B}}{V_{0,B}}$, $\frac{V_{2,A}}{V_{1,A}} = \frac{V_{2,B}}{V_{1,B}}$, $\frac{v^z_{3,A}}{V_{2,A}} = \frac{v^z_{3,B}}{V_{2,B}}$, $\frac{V_{5,A}}{\langle P_{4,A}\rangle} = \frac{V_{7,B}}{\langle P_{6,B}\rangle}$, $\frac{V_{6,A}}{V_{5,A}} = \frac{V_{8,B}}{V_{7,B}}$, and Eq. (3.29) reduces to:

$$\frac{V_{8,B}}{V_{6,A}} = \frac{V_{0,B}\;H_B^{dif}}{V_{0,A}\;H_A^{dif}}T_{w1}T_{w2}e^{-i(k_w(-L_2)+k^*_m L)}. \tag{3.30}$$

For normal incidence $L = L_2 = d$ and $k^*_m = k^z_m$:

$$\frac{V_{8,B}}{V_{6,A}} = \frac{V_{0,B}\;H_B^{dif}}{V_{0,A}\;H_A^{dif}}T_{w1}T_{w2}e^{-i(k_w(-d)+k^z_m d)}. \tag{3.31}$$

Compressional wave velocity

When measuring compressional waves, the incident angle of the plane waves on the specimen is normal to the surface. The wave propagation through the specimen is equal to the specimen thickness, d. Letting $k_m = k^z_m$, c_P can be calculated by investigating the phase of Eq. (3.31):

$$\angle\Big(\frac{V_{8,B}}{V_{6,A}}\Big) = \angle\Big(\frac{V_{0,B}\;H_B^{dif}}{V_{0,A}\;H_A^{dif}}T_{w1}T_{w2}e^{-i(k_w(-d)+k^z_m d)}\Big). \tag{3.32}$$

Assuming that he phase angle pf $\frac{V_{0,B}}{V_{0,A}}$, T_{w1} and T_{w2} are zero and letting $k^z_m = K^z_m - i\alpha_P$, the equation reduces to

$$\angle V_{8,B} - \angle V_{6,A} = \angle H_B^{dif} - \angle H_A^{dif} + K_w d - K^z_m d, \tag{3.33}$$

where K_w and K_m^z are the real parts of the wave numbers in water and the specimen, respectively. Using $K_w = \omega/c_w$ and $K_m^z = \omega/c_P$, where c_w is the compressional wave velocity in water, an expression for c_P using the immersion method is found [184]:

$$c_P = \frac{d}{d/c_w - (\angle V_{8,B}/\omega - \angle V_{6,A}/\omega) + \angle H_B^{dif}/\omega - \angle H_A^{dif}/\omega)}. \tag{3.34}$$

Using the steady state portion of a burst, Eq. (3.34) may be expressed with the transit times, t_A and t_B, where $t_A \equiv -\angle V_{6,A}/\omega$ and $t_B \equiv -\angle V_{8,B}/\omega$. The diffraction correction in the time domain for distinct frequencies may also be defined, $t_A^{dif} \equiv -\angle H_A^{dif}/\omega$ and $t_B^{dif} \equiv -\angle H_B^{dif}/\omega$, giving a time-domain expression for c_P [185]:

$$c_P = \frac{d}{d/c_w + t_B - t_A + t_A^{dif} - t_B^{dif}}. \tag{3.35}$$

The wave velocity in the water, c_w, is needed in the model. The measurement depth is approximately 5 cm and the gauge pressure is thus assumed to be zero. Assuming no salinity in the water and zero gauge pressure, c_w can be approximated by [84]

$$c_w(T_s) = 1402.7 + 488T_s - 482T_s^2 + 135T_s^3 \tag{3.36}$$

where T_s is the scaled temperature $T_s = T/100$, where T is the temperature in kelvin.

Shear wave velocity

At a tilted angle θ_i, shear waves are generated inside the specimen. Fig. 3.16 shows the geometry in such a measurement. According to the shear wave model, $k_m = k_m^{x'}$ is the shear wavenumber in Eq. (3.30). The resulting equation (Eq. (3.40)) has already been presented by Wu et al. [53], however no rigorous derivation of the formula needed to calculate c_S has been found by this author. Such a derivation is presented here. By taking the phase on both sides of Eq. (3.30), gives:

$$\angle V_{8,B} - \angle V_{6,A} = \angle H_B^{dif} - \angle H_A^{dif} + K_w L_2 - K_m^{x'} L. \tag{3.37}$$

$K_m^{x'}$ is the real part of the shear wave number of the specimen. K_w is the real part of the compressional wave number of water. By inserting the trigonometric identity $\cos(\theta_t - \theta_i) = \frac{L_2}{L}$ into Eq. (3.37) and defining $\Delta\angle H^{dif} \equiv \angle H_B^{dif} - \angle H_A^{dif}$ (for shortened notation), gives

$$\begin{aligned} \angle V_{8,B} - \angle V_{6,A} - \Delta\angle H^{dif} &= K_w \cos(\theta_t - \theta_i) L - K_m^{x'} L, \\ c_S \frac{\angle V_{8,B} - \angle V_{6,A} - \Delta\angle H^{dif}}{\omega L} &= \cos(\theta_t - \theta_i)\frac{c_S}{c_w} - 1, \end{aligned} \tag{3.38}$$

where $c_S = \omega / K_m^{x'}$ is the shear wave velocity in the specimen. θ_i, θ_t L_2, L are shown in Fig. 3.16. Using the following relations

$$\begin{aligned} \cos(\theta_t - \theta_i) &= \cos(\theta_t)\cos(\theta_i) + \sin(\theta_t)\sin(\theta_i) \\ \sin(\theta_t) &= \sin(\theta_i)\frac{c_S}{c_w} \\ \cos(\theta_t) &= \sqrt{1-\sin^2(\theta_t)} = \sqrt{1-\sin^2(\theta_i)(\frac{c_S}{c_w})^2}, \end{aligned} \tag{3.39}$$

gives

$$\begin{aligned} c_S\frac{\angle V_{8,B} - \angle V_{6,A} - \Delta\angle H^{dif}}{\omega L} &= \Big(\sqrt{1-\sin^2(\theta_i)(\frac{c_S}{c_w})^2}\cos(\theta_i) + \sin^2(\theta_i)\frac{c_S}{c_w}\Big)\frac{c_S}{c_w} - 1, \\ -c_S\frac{\angle V_{8,B} - \angle V_{6,A} - \Delta\angle H^{dif}}{\omega L} &= -\frac{c_S}{c_w}\sqrt{1-\sin^2(\theta_i)(\frac{c_S}{c_w})^2}\cos(\theta_i) + \Big(1-\sin^2(\theta_i)(\frac{c_S}{c_w})^2\Big). \end{aligned} \tag{3.40}$$

Inserting $L = \frac{d}{\sqrt{1-\sin^2(\theta_t)}} = \frac{d}{\sqrt{1-\sin^2(\theta_i)(\frac{c_S}{c_w})^2}}$, gives finally

$$c_S = \frac{c_w}{\sqrt{\sin^2(\theta_i) + \Big[\frac{\angle V_{8,B} - \angle V_{6,A} - (\angle H_B^{dif} - \angle H_A^{dif})}{\omega d} + \cos(\theta_i)\Big]^2}}. \tag{3.41}$$

In the measurements conducted in this work, the incident angle, θ_i, is set to the P-wave critical angle (the angle in which no compressional waves are transmitted into the specimen) for shear wave measurements. Eq. (3.41) with $(\angle H_B^{dif} - \angle H_A^{dif}) = 0$ is consistent with the expression for c_S presented by Wu et al. [53]. Wu et al. [53] seemingly use Rogers and Buren's diffraction correction expression to discuss the diffraction effects after c_S is calculated with Eq. (3.41) (with $(\angle H_B^{dif} - \angle H_A^{dif}) = 0$). Like for c_P, c_S may also be expressed with transit time measurements.

Using the steady state portion of a burst, Eq. (3.41) may be expressed with transit times, t_A and t_B, where $t_A \equiv -\angle V_{6,A}/\omega$ and $t_B \equiv -\angle V_{8,B}/\omega$. The diffraction correction in the time domain for distinct frequencies may also be defined, $t_A^{dif} \equiv -\angle H_A^{dif}/\omega$ and $t_B^{dif} \equiv -\angle H_B^{dif}/\omega$, giving a time-domain expression for c_S

$$c_S = \frac{c_w}{\sqrt{\sin^2(\theta_i) + \Big[\frac{-t_B + t_A + (t_B - t_A)}{\omega d} + \cos(\theta_i)\Big]^2}}. \tag{3.42}$$

Compressional wave attenuation coefficient

When finding α_P, the incident acoustic wave is normal to the specimen ($\theta_i = 0$). The absolute value of Eq. (3.31) is taken:

$$
\begin{aligned}
\Big|\frac{V_{8,B}}{V_{6,A}}\Big| &= \Big|\frac{V_{0,B}\;H_B^{dif}}{V_{0,A}\;H_A^{dif}} T_{w1}T_{w2}e^{ik_w d - ik_m^z d}\Big| \\
\ln\Big|\frac{V_{8,B}}{V_{6,A}}\Big| &= \ln\Big|\frac{V_{0,B}}{V_{0,A}}\Big| + \ln\Big|\frac{H_B^{dif}}{H_A^{dif}}\Big| + \ln\big|e^{ik_w d - ik_m^z d}\big| + \ln\Big|T_{w1}T_{w2}\Big|
\end{aligned}
\tag{3.43}
$$

The wave numbers are complex values having real and imaginary parts: $k_w = K_w - i\alpha_w$, $k_m^z = K_m^z - i\alpha_P$, for water and specimen, respectively. The equation reduces to

$$
\ln\Big|\frac{V_{8,B}}{V_{6,A}}\Big| = \ln\Big|\frac{V_{0,B}}{V_{0,A}}\Big| + \ln\Big|\frac{H_B^{dif}}{H_A^{dif}}\Big| - \alpha_P d + \alpha_w d + \ln\Big|T_{w1}T_{w2}\Big|. \tag{3.44}
$$

α_P may now be written [184]

$$
\alpha_P = \alpha_w + \frac{-\ln\Big|\frac{V_{8,B}}{V_{6,A}}\Big| + \ln\Big|\frac{H_B^{dif}}{H_A^{dif}}\Big| + \ln\Big|\frac{V_{0,B}}{V_{0,A}}\Big| + \ln\Big|T_{w1}T_{w2}\Big|}{d} \tag{3.45}
$$

$|V_{0,A}|$ and $|V_{0,B}|$ are the amplitudes of the voltage signal of the emf in the signal generator in measurement A, and B, respectively. $|V_{6,A}|$ and $|V_{8,B}|$ are the amplitudes of the voltage signal acquired by the oscilloscope in measurement A, and B, respectively. The use of $|V_{0,A}|$, $|V_{0,B}|$, $|V_{6,A}|$ and $|V_{8,B}|$ are discussed in Sect. 3.5. $|H_A^{dif}|$ and $|H_B^{dif}|$ are discussed in 2.3 and are the magnitude-responses of the diffraction correction in measurement A and, B, respectively. With normal incident, the plane wave transmission coefficients, T_{w1} and T_{w2} are given in Eq. (3.28).

3.5 Signal processing methods

McSkimmin [65] outlines how the c_P and c_S in a specimen can be found using the immersion method or the solid buffer method measuring the transit times of pulses. He does not include diffraction corrections in his expressions for c_P and c_S but discuss diffraction effects in general after calculating c_P and c_S. Different features of the pulse can be used to determine the transit time. No absolute name is provided, but the method or techique is referred to as "the pulse technique", "the pulse method" or "the basic pulse method" [65]. McSkimmin also refers to transit time measurements of short pulses and longer pulses using the steady-state portion of a signal [65]. Measurements of α_P and α_S is referred to as "amplitude measurements of the pulse" [65]. Finding the acoustic parameters measuring the transit-time and the amplitude of the pulse is in this work called the basic pulse method. By using short pulses with the basic pulse method, there will be no steady-state portion of the signal and thus no defined amplitude or frequency. By using bursts with the basic pulse method and the steady-state portion of the signal, transit time measurements between two signals having a defined frequency and amplitude may be conducted.

The Fourier spectrum method is another method that can be used to find the acoustic parameters of the specimen [51, 72, 73, 74]. The pulses in measurement A and B are transformed into the frequency domain via the Fourier transform. For the hydrate experiments, this method is mainly used because of it's ability to measure dispersion and attenuation spectrum of the specimen using short pulses. Short pulses may be isolated from unwanted acoustic reflections and mode converted signals between S-waves and P-waves, interfering with the signal. Contrary to the basic pulse method, the Fourier spectrum method may be used to measure dispersion and attenuation coefficients of a specimen using short signals with no steady-state portion of the signal [51, 72, 73, 74]. The basic pulse method and the Fourier spectrum method have been compared by measuring the acoustic properties of plexiglas.

3.5.1 Basic pulse method

In the basic pulse method, the wave velocities are found by measuring $t_B - t_A$ by direct transit measurements of the pulses used in measurement A and B. t_A and t_B are defined in Sect. 3.4.2 and 3.3.4: $t_A \equiv -\angle V_{6,A}/\omega$ and $t_B \equiv -\angle V_{8,B}/\omega$. In the basic pulse method, t_A and t_B are not measured directly but $t_B - t_A$ is found by measuring the transit time of a feature in the steady-state portion of the burst used in measurement A and measurement B. This may be done by measuring the transit time to a point where the AC-signal crosses the zero-line. Such a point is here called a zerocross. Zerocrosses and the "first arrival of the signal" are defined in Fig. 3.18 a) (this signal is measurement A of the solid buffer method using the P-wave transducers at frequency 500 kHz). Many authors have used features outside the steady-state portion of the signal, such as "the first arrival" [22, 21], to measure $t_B - t_A$, however, the accuracy of this method is debated [48, 49, 50].

Mathematically, the solid buffer basic pulse method for c_P and c_S is the same as Eqs. (3.18) and (3.20):

$$c_{P,S} = \frac{d}{t_B - t_A + t_A^{dif} - t_B^{dif}}. \tag{3.46}$$

For the immersion basic pulse method, the expression for c_P is the same as Eq. (3.35):

$$c_P = \frac{d}{d/c_w + t_B - t_A + t_A^{dif} - t_B^{dif}}, \tag{3.47}$$

and c_S is found using Eq. (3.42):

$$c_S = \frac{c_w}{\sqrt{\sin^2(\theta_i) + \left[\frac{t_B - t_A - (t_B^{dif} - t_A^{dif})}{d} + \cos(\theta_i)\right]^2}}. \tag{3.48}$$

d is the thickness of the specimen, t_A^{dif} and t_B^{dif} are the time delay due to diffraction effects. c_w is the sound velocity in water. In this work, $\theta_i = 38^\circ$ is used. The feature used in the measurement to obtain $t_B - t_A$ is given in the section describing the results of the measurement.

When finding α_P using the basic pulse method, the amplitudes of the steady-state region of the signals in measurement A and B are used. For the solid buffer method, α_P is found using Eq. (3.23):

$$\alpha_P = \frac{-\ln\left|\frac{V_{8,B}}{V_{7,A}}\right| + \ln\left|\frac{H_B^{dif}}{H_A^{dif}}\right| + \ln\left|\frac{V_{0,B}}{V_{0,A}}\right| + \ln\left|\frac{T_{B1}T_{B2}}{T_A}\right|}{d} \tag{3.49}$$

and for the immersion method, α_P is found using Eq. (3.45):

$$\alpha_P = \alpha_w + \frac{-\ln\left|\frac{V_{8,B}}{V_{6,A}}\right| + \ln\left|\frac{H_B^{dif}}{H_A^{dif}}\right| + \ln\left|\frac{V_{0,B}}{V_{0,A}}\right| + \ln\left|T_{w1}T_{w2}\right|}{d}.$$

$|\frac{V_{8,B}}{V_{7,A}}|$ and $|\frac{V_{8,B}}{V_{6,A}}|$ are here denoting the ratios of the amplitudes in measurement A and B of the steady state region of a burst for the solid buffer and immersion method, respectively. $|\frac{V_{0,B}}{V_{0,A}}|$ is denoting the ratio of the amplitude-settings of the burst on the signal generator.

An example of two measured signals are shown in Fig. 3.18 b) and c). The solid buffer method is used and the in-house constructed P-wave transducers have been used. The signals have center frequency 500 kHz and are 10 cycles long. In between 2-8 periods after the first break of the signal, there is a steady-state region in the signal.

In measurement A, some noise is present, but the first peak is still detectable. There are some more ripples after the signal. This is probably due to sidewall-reflections in the buffers. The effect of the sidewall-reflections is discussed in Ch. 6. In measurement B, there is a second signal, which is a reflected signal from the end of the buffers.

In the steady-state region of the signal, the frequency and amplitude of the signal are defined. In this region, an exact feature of the signal can be identified. By using e.g. position 5 (5th zerocross) in measurement A and B to calculate $t_B - t_A$, the wave velocity can be calculated for a defined frequency. The ratio of the measured amplitudes in the steady-state region of the signals in measurement A and B, $\frac{V_B}{V_A}$ is used to calculate α_P.

In this work, the basic pulse method has been used in two ways: 1) Reference measurements on plexiglas used to compare with and increase the confidence of the Fourier spectrum method. 2) Measuring the acoustic properties of the other materials used in the transducer construction: PVC and the tungsten-epoxy specimen. 3) Measuring the wave velocities of Bentheim sandstone during hydrate growth to compare with the Fourier spectrum method.

For 1) and 2) above, signals with 10 periods and 500 kHz are used with the basic pulse method. Zerocrosses in the steady state region of the pulses are used to measure the wave velocities. For 3), short pulses must be used and there is no steady-state region in the signals. Thus zerocrosses 2 and 3 are used. When using the basic pulse method in the hydrate measurements there is no steady-state region because the pulses used are to short.

The measured α_P using the immersion method is calculated using Eq. (3.45), and the measured α_P using the solid buffer method is calculated using Eq. (3.23).

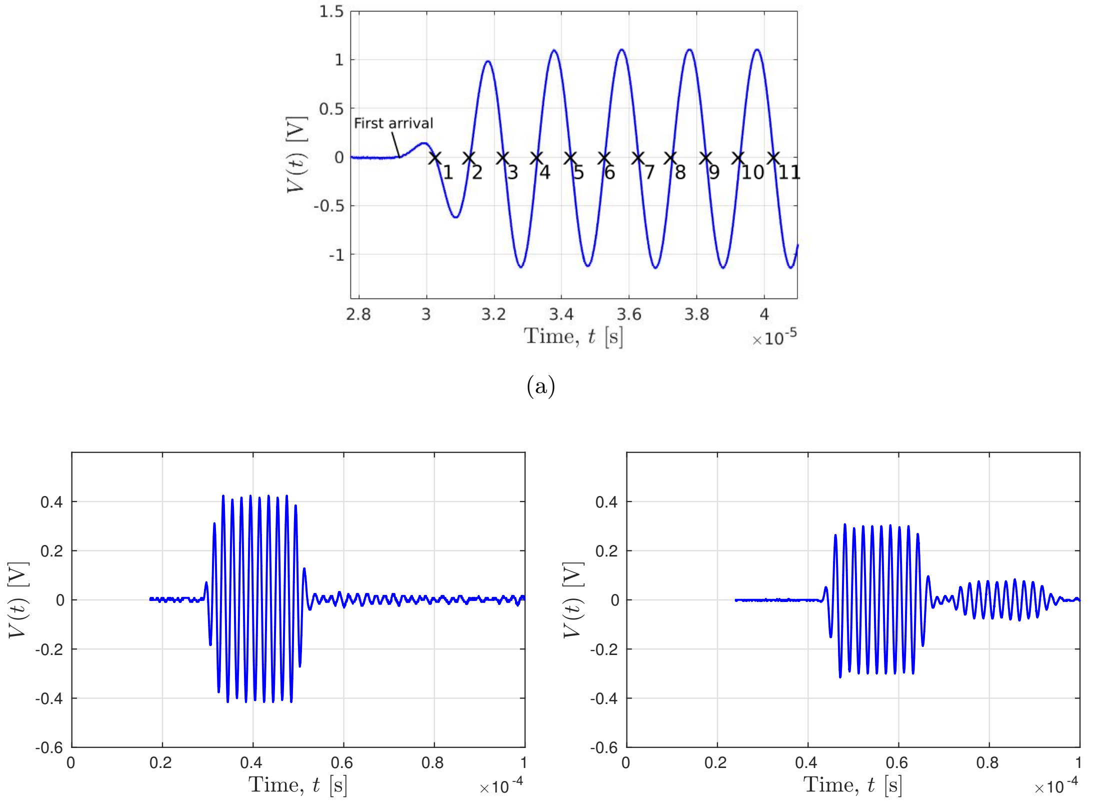

(a)

(b)

(c)

Figure 3.18: **a)** Definitions of first arrival and the zerocross numbers in a measured signal (zoomed in version of Fig. 3.18 b)). **b)** Measurement A using the solid buffer method with P-wave transducers with frequency 500 kHz. **c)** Measurement B using the solid buffer method on a plexiglas specimen (length 20 mm) with P-wave transducers with frequency 500 kHz.

3.5.2 Fourier spectrum method

In the Fourier spectrum method, the DFT (Eq. (2.5)) of the signal in measurement A and B are used to calculate the acoustic properties of the specimen [51, 72, 73, 53]. For the wave velocities, the unwrapped phase angle of the DFT is used. The unwrapping process is described below. For the compressional wave attenuation coefficient, the absolute value of the DFT is used.

The Fourier spectrum method is used with the solid buffer method inside the pressure cell and with the immersion method. The method is described here by showing an example: Measurement of the shear wave velocity of a plexiglas specimen using the solid buffer method inside the pressure cell at atmospheric conditions. Then, how to find the other acoustic parameters is described, both for the immersion and for the solid buffer method.

The Fourier spectrum method is used as the main signal processing method in this work, due to its ability to measure dispersion and attenuation spectrum of the specimen using short pulses. The use of short pulses is important to be able to separate the wanted acoustic signal from reflections or mode converted signals. The Fourier spectrum method can be used to calculate c_P, c_S, α_P in the frequency domain for the solid buffer method by slightly altering Eqs. (3.17, (3.19) and using Eq. (3.23) [51]:

$$c_{P,S} = \frac{d}{-(\frac{\angle V^{shift}_{8,B}}{\omega} - \frac{\angle V^{shift}_{7,A}}{\omega}) + t_{shift,B} - t_{shift,A} + (\frac{\angle H^{dif}_{B}}{\omega} - \frac{\angle H^{dif}_{A}}{\omega})}. \tag{3.50}$$

$$\alpha_P = \frac{-\ln\left|\frac{V_{8,B}}{V_{7,A}}\right| + \ln\left|\frac{H^{dif}_{B}}{H^{dif}_{A}}\right| + \ln\left|\frac{V_{0,B}}{V_{0,A}}\right| + \ln\left|\frac{T_{B1}T_{B2}}{T_A}\right|}{d}. \tag{3.51}$$

$V^{shift}_{8,B}$ and $V^{shift}_{7,A}$ are the DFT of $V^{shift}_{8,B}(t)$ and $V^{shift}_{7,A}(t)$, which are the measured pulses shifted with a time $t_{shift,B}$ and $t_{shift,A}$, respectively. The time shifting of the pulses is described below with Fig. 3.20, Fig. 3.21 and Eq. (3.55).

In the same way as for the solid buffer method, the immersion method can be used to calculate c_P, c_S, α_P in the frequency domain by slightly altering Eqs. (3.34) and (3.41) and using Eq. (3.45), respectively [53]:

$$c_P = \frac{d}{\frac{d}{c_w} - (\frac{\angle V^{shift}_{8,B}}{\omega} - \frac{\angle V^{shift}_{6,A}}{\omega}) + t_{shift,B} - t_{shift,A} + (\frac{\angle H^{dif}_{B}}{\omega} - \frac{\angle H^{dif}_{A}}{\omega})}. \tag{3.52}$$

$$c_S = \frac{c_w}{\sqrt{\sin^2(\theta_i) + \left[\frac{\omega t_{shift,B} - \omega t_{shift,A} - (\angle V_{8,B}^{shift} - \angle V_{6,A}^{shift}) + (\angle H_B^{dif} - \angle H_A^{dif})}{\omega d} + \cos(\theta_i)\right]^2}}. \tag{3.53}$$

$$\alpha_P = \alpha_w + \frac{-\ln\left|\frac{V_{8,B}}{V_{6,A}}\right| + \ln\left|\frac{H_B^{dif}}{H_A^{dif}}\right| + \ln\left|\frac{V_{0,B}}{V_{0,A}}\right| + \ln\left|T_{w1}T_{w2}\right|}{d}. \tag{3.54}$$

For a continuous signal in the frequency domain, acoustic reflections from e.g. the buffer sidewalls and the buffer-specimen interface are present in addition to potential mode converted signals, such as P-waves mode-converted into S-waves. From the solid buffer method system model in Eqs. (3.3)-(3.4), the acquired signals are $V_{7,Ar}$ and $V_{8,Br}$ in measurement A and B, respectively. To use Eqs. (3.17) or (3.19), $V_{7,A}$ and $V_{8,B}$ are extracted from $V_{7,Ar}$ and $V_{8,Br}$. This is done using the Fourier spectrum method with short, isolated pulses so unwanted reflections are avoided and filtered out in the time domain. In the following, an example is shown how to use the Fourier spectrum method to measure c_S of a plexiglas specimen with the S-wave transducers. It is also outlined how c_P and α_p can be found and how to obtain c_P, c_S and α_p using the immersion method. It is shown how the pulses from a S-wave transducer can be isolated and how the Fourier spectrum method is used to obtain $\angle V_{7,A}$, $|7_{6,A}|$, $\angle V_{8,B}$ and $|V_{8,B}|$, from $V_{8,Br}$ and $V_{6,Ar}$.

Identification of the pulses in the signal

Using the shear wave transducers, several pulses are present in the measurements. The in-house built shear wave transducers are able to excite short pulses, thus the arrivals of the different pulses in the measurements are separable, see Fig. 3.19. In the following example, the shear wave pulse is used. $V_{7,A}$ and $V_{8,B}$ can be found by taking the Fourier transform (Eq. (2.5)) of the isolated shear wave pulses in measurement A and measurement B.

In Fig. 3.19 a), the pulses in measurement A are shown. In this example, the different pulses are manually inspected. A_1 is the P-wave propagating directly from the transmitter to the receiver. A_3 is the S-wave propagating directly from the transmitter to the receiver. A_2 is the S-wave propagating through the first buffer, being mode converted on the buffer-buffer interface to a P-wave which propagates directly to the receiver. A_6 is the sum of two S-waves: The first shear wave is reflected one time at the receiver and the second time at the buffer-buffer interface before received by the receiver. The second shear wave is reflected one time at the buffer-buffer interface and the second time at the buffer-transmitter interface before received by the receiver. A_4 and A_5 are more complicated to interpret. However, A_4 is interpreted in this work as a sum of two waves: The first wave is the S-wave reflected into a mode converted P-wave at the buffer-receiver interface. This P-wave is again reflected at the buffer-buffer interface. The second wave is the reflected S-wave at the buffer-buffer interface. At the buffer-transmitter interface this S-wave is reflected into a mode converted P-wave which is received by the receiver. The same argument is used on A_5, however, now the original S-wave propagates through three buffer-lengths before converted into a P-wave. The mode converted P-wave travels directly to the receiver. Mode conversion between S-waves and P-waves has been documented in measurements using the solid buffer method [51]. c_S and c_P in plexiglas are measured to be approximately 1350 m/s and 2700 m/s, respectively, in Ch. 6. The identification of the different pulse arrivals in Fig. 3.19, are based on these measurements.

In Fig. 3.19 b), the pulses in measurement B are shown. B_1 is the P-wave propagating directly from the transmitter to the receiver. B_4 is the S-wave propagating directly from the transmitter to the receiver. B_2 is the S-wave propagating through the first buffer, being mode converted to a P-wave at the first buffer-specimen interface and then propagating directly to the receiver. B_3 is the S-wave propagating through the first buffer and the specimen, being mode converted to a P-wave at the second buffer-specimen interface and then propagating directly to the receiver. B_5 is believed to be the reflected S-wave at the first buffer-specimen interface. At the buffer-transmitter interface this S-wave is reflected into a mode converted P-wave which is received by the receiving transducer. B_6 is the shear wave being reflected back and forth once inside the specimen.

When shear wave measurements are performed, A_3 and B_4 are used. When compressional wave measurements are performed, A_1 and B_1 are used. In the hydrate measurements, the acquired signals (see Fig. 7.4) are similar in shape as the plexiglas measurements shown in Fig. 3.19. The signals shown in Fig. 3.19 are representative for the hydrate measurements. In the following, it is shown how the Fourier spectrum method can be used manually. However, for each of the ten hydrate experiments presented in Ch. 7, there are approximately 1000 files and a Matalb routine is made to automatically perform the procedure explained below.

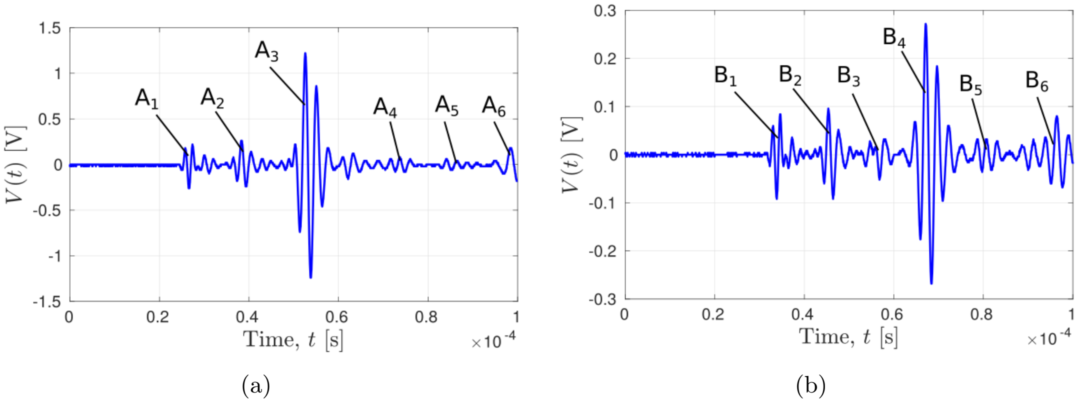

(a)

(b)

Figure 3.19: Solid buffer method using shear wave transducers. Pulse arrivals for **a**) Measurement A, **b**) Measurement B.

Isolation of the shear wave pulse

To calculate $\angle V_{7,A}$ and $\angle V_{8,B}$, the unwrapped phase of the Fourier transform of the shear wave pulses A_3 and B_4 must be calculated. To do so, these pulses are first isolated. In the start of the pulse, A_3, a hidden reflection is suspected. As the shear wave velocity is approximately half of the compressional wave velocity of plexiglas, the reflected P-wave will arrive at approximately the same time as the shear wave. This will be the case of all the measurement A's conducted with the S-wave transducers in this work. The pulse B_4 has a negative peak at the very start of the signal, while A_3 has not. The start of the isolated pulse is thus defined by the start of the first peak (Fig. 3.20).

Deciding exactly where the pulse ends, may be challenging. In this work, the signal has been cut off by smoothing the last half period in the signal. This has been doen by linearly trailing off this last half period. Potential aliasing effects due to the abrupt start and stop of the signal are assumed to be small by comparing Fig. 3.26 (signal is abruptly truncated) and 3.24 (linearly trailing off the last half period). The difference in the measured c_S at 500 kHz in Fig. 3.26 and 3.24 is small.

The isolated pulses, A_3 and B_4, with all other pulses removed are shown in Fig. 3.20. These voltage signals are now the time domain acquired signals with no unwanted reflections present, $V_{7,A}(t)$ and $V_{8,B}(t)$.

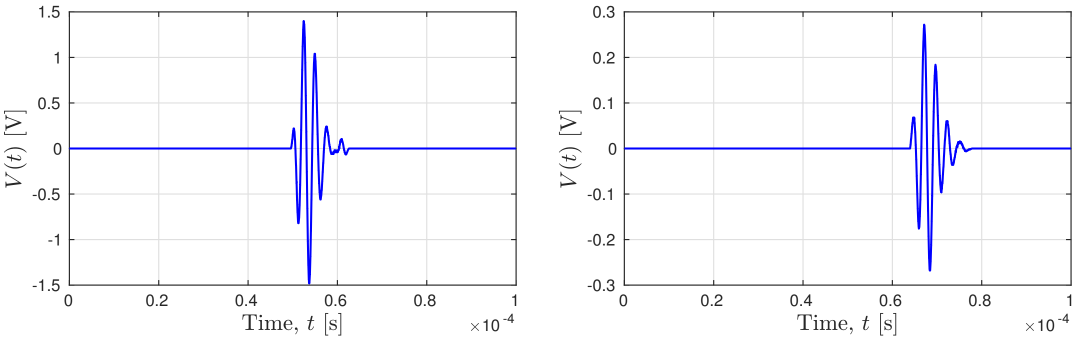

(a)

(b)

Figure 3.20: Isolated pulses based on the signal in Fig. 3.19. **a**) S-wave pulse in measurement A, A_3. **b**) S-wave pulse in measurement B, B_4.

A_3 and B_4 are located approximately in the middle of the time window. It's easier to calculate the unwrapped phase angle of the Fourier transform of a signal which is shifted to the start of the time window [72]. $\angle V_{7,A}^{shift}$ and $\angle V_{8,B}^{shift}$ are related to $\angle V_{7,A}$ and $\angle V_{8,B}$ by

$$\begin{aligned} \angle V_{7,A} &= -\omega t_A^{shift} + \angle V_{7,A}^{shift}, \\ \angle V_{8,B} &= -\omega t_A^{shift} + \angle V_{8,B}^{shift}. \end{aligned} \tag{3.55}$$

ωt_A^{shift} is the phase due to the time shift, t_A^{shift}. ωt_B^{shift} is the phase due to the time shift, t_B^{shift}. $\angle V_A^{shift}$ and $\angle V_B^{shift}$ are found by calculating the unwrapped phase of the DFT of the shifted pulses.

The frequency resolution of the discrete Fourier transform is dependent on the length of the time signal (Sect. 2.2). The time-signal is zero-padded so that the total length of the signal is 100 000 samples long or 100 µs, see Fig. 3.21. This is found to give sufficient frequency resolution for investigating details in the phase spectrum.

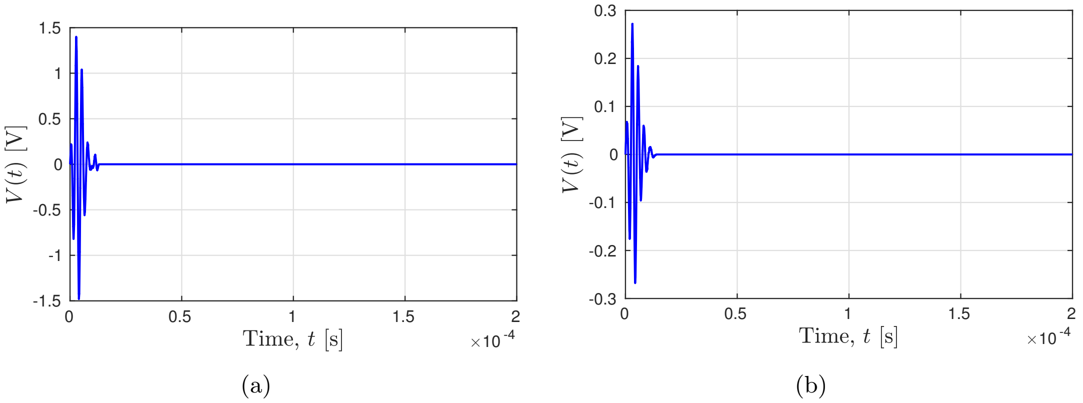

(a) (b)

Figure 3.21: Time-shifted and zero-padded signals based on the signals in Fig. 3.20. **a**) Shear wave signal in measurement A, A_3. **b**) Shear wave signal in measurement B, B_4.

The Fourier transform of the isolated pulse

The DFT of the pulses A_3 and B_4 are presented as the magnitude of the DFT in Fig. 3.22 and the wrapped phase angle of the DFT in Fig. 3.23 a) and b). In this work, the bandwidth of a signal is defined as the frequency band where the magnitude spectrum is more than half it's maximum value.

Using Matlab to calculate the DFT (Eq. (2.5)), the phase angle is presented as the wrapped phase angle. It is wrapped within $-\pi$ and π radians. Sudden jumps in the wrapped phase is seen in the Fig. 3.23 a) and b). These "phase-jumps" would be exactly 2π for an infinitely long signal trace. Because of the frequency resolution of a finite length sampled signal, the jumps are less than 2π. Here, the definition of a jump is set to 6 radians.

The unwrapped phase angle is obtained by subtracting 2π to the wrapped phases whenever there is a phase-jump in the signal. The unwrapped phase is shown in Fig. 3.23 c) and d). Even if the frequency resolution is good enough, noise and unwanted reflections interfering with the signal may distort the frequency spectrum. Outside the bandwidth of the signal, when the SNR is low, distortion of the phase spectrum may be observable. Here, the phase spectrum below 200 kHz and above 600 kHz is seen to be distorted.

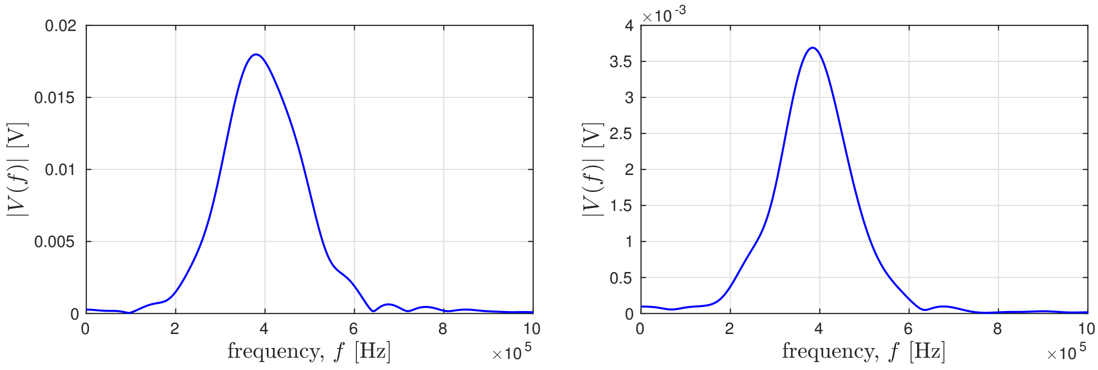

(a)

(b)

Figure 3.22: Magnitude spectrum of the signals in Fig. 3.21. **a**) Shear wave signal in measurement A, A_3. **b**) Shear wave signal in measurement B, B_4.

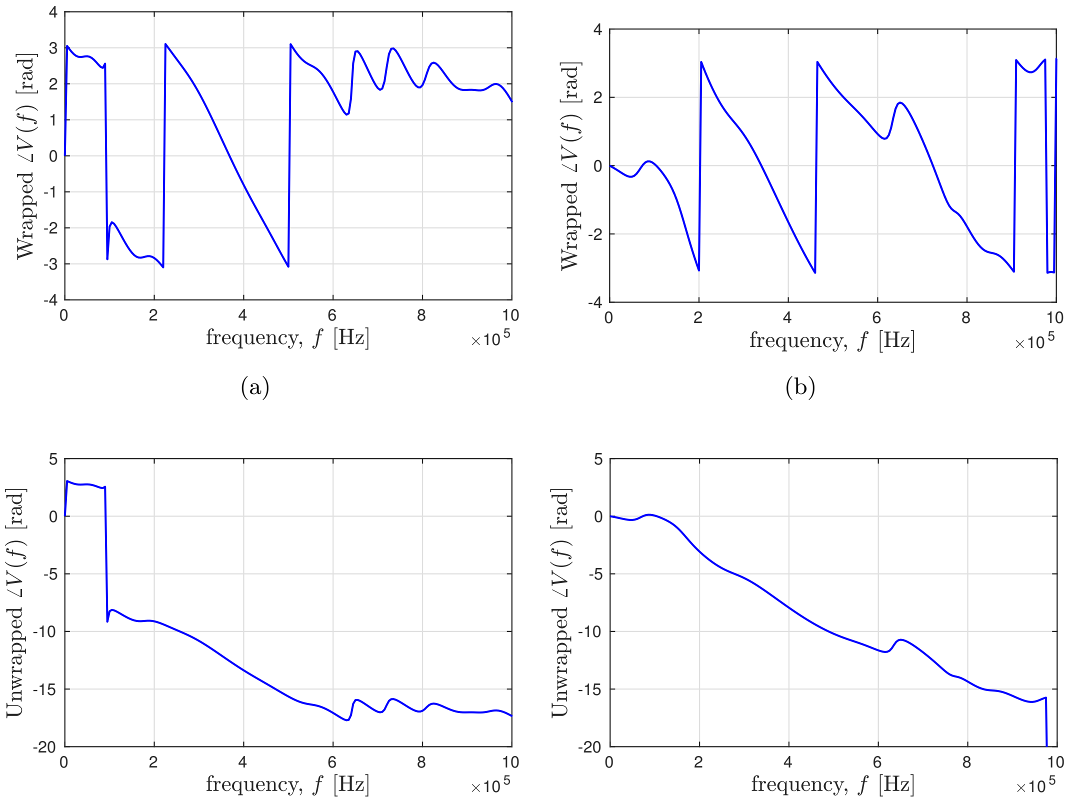

(c)

(d)

Figure 3.23: Phase spectra of the shifted pulses A_3 and B_4 from Fig. 3.21. **a**) Wrapped phase, measurement A, A_3. **b**) Wrapped phase, measurement B, B_4. **c**) Unwrapped phase, measurement A, A_3. **d**) Unwrapped phase, measurement B, B_4.

The unwrapped phase from Fig. 3.23 c) and d) can be used with Eq. (3.55) and inserted into Eq. (3.19) to find the shear wave velocity in Eq. (3.50).

The shear wave velocity is presented in Fig. 3.24. For the red curve, labeled "Diffraction correction," the diffraction corrections in Eq. (2.6) are used to calculate H_A^{dif} and H_B^{dif}. For the blue curve, labeled "No diffraction correction," $\angle H_A^{dif} = \angle H_B^{dif}$.

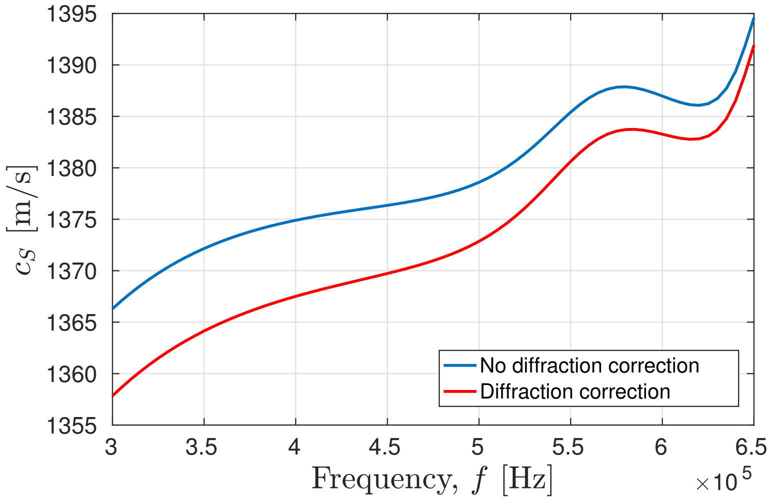

Figure 3.24: c_S for the 60 mm plexiglas specimen using the solid buffer method with the Fourier spectrum method on the signals presented in Fig. 3.23.

A shear wave velocity around 1370 m/s for 500 kHz is found to be reasonable in Ch. 6. The unwrapped phase spectrum shown in Fig. 3.23 c) and) are thus assumed to be reasonable. If one of the jumps in the wrapped phase was not registered in the unwrapping process, there would be an error in the unwrapped phase of $\pm 2\pi$. The corresponding error in the shear wave velocity is approximately ±200 m/s.

The basic pulse method can be used in comparison with the Fourier spectrum method. The use of the short pulses in the Fourier spectrum method gives signals without a steady-state region. However, the use of the first arrival of the signal has been widely used in acoustic velocity measurements [66, 67, 68, 69, 70]. Transit time measurements of different zerocrosses outside the steady state region has also been used to measure the wave velocities [186]. The measured transit times using features of the signal outside the steady-state region of the signal are assumed to be correct within a margin of error less than a period for a given frequency. In this example (measurement A and B shown in Fig. 3.19), c_S calculated with the basic pulse method and the first arrival of the signal, $c_S = 1409$ m/s. For zerocross 1-5, c_S is calculated to be 1377 m/s, 1376 m/s, 1374 m/s, 1371 m/s and 1369 m/s, respectively. These values correspond to c_S calculated with the

Fourier spectrum method within "2π phase error margin" of ±200 m/s.

In the hydrate measurements, the transit time through the specimen has been found with both the basic pulse method and the Fourier spectrum method. If these differ with more than one period, 2π has been added or subtracted to the unwrapped phase.

Interference from a weak non-separable signal component

As mentioned above, In the start of the pulse, A_3, a hidden non-separable P-wave signal component is suspected to be present. As the shear wave velocity is approximately half of the compressional wave velocity of plexiglas, the reflected P-wave will arrive at approximately the same time as the shear wave. No thorough investigation of this effect has been conducted, but an illustrative example is shown here. In Fig. 3.25 a), the same isolated signal as in Fig. 3.20 is shown (the signal is truncated 1 period earlier and indexes are shown on th x-axis). A noise signal shown in figure b) is added to the signal and the superposition of these give the signal in figure c). The noise signal in b) is half a period "500 kHz pulse" with the same amplitude as the first peak in the signal in figure a). By using signal c) instead of the signal shown in Fig. 3.20, a new graph of c_S is obtained, figure d). Comparing the new value of c_S in d) with the original in Fig. 3.24 it is concluded that this half period noise signal is not critically affecting the measured c_S. No thorough investigation of how different noise signals might affect the measurements. By looking at the half period noise component, it is indicated here that noise is not critically affecting the measurements. No absolute explanation is given in this work of the shape of the c_S curves in Fig. 3.25. However, some considerations on the accuracy of the measurements are given in Ch. 6.

By abruptly truncating the signal and using no smoothing function on the last period of the original signal, slightly different values of c_S are obtained. In Fig. 3.26 the signals in measurement A and B are abruptly truncated after 4 periods. When abruptly truncating a signal, aliasing effects may occur. The effect of this abrupt truncation is also not critically affecting the measured c_S.

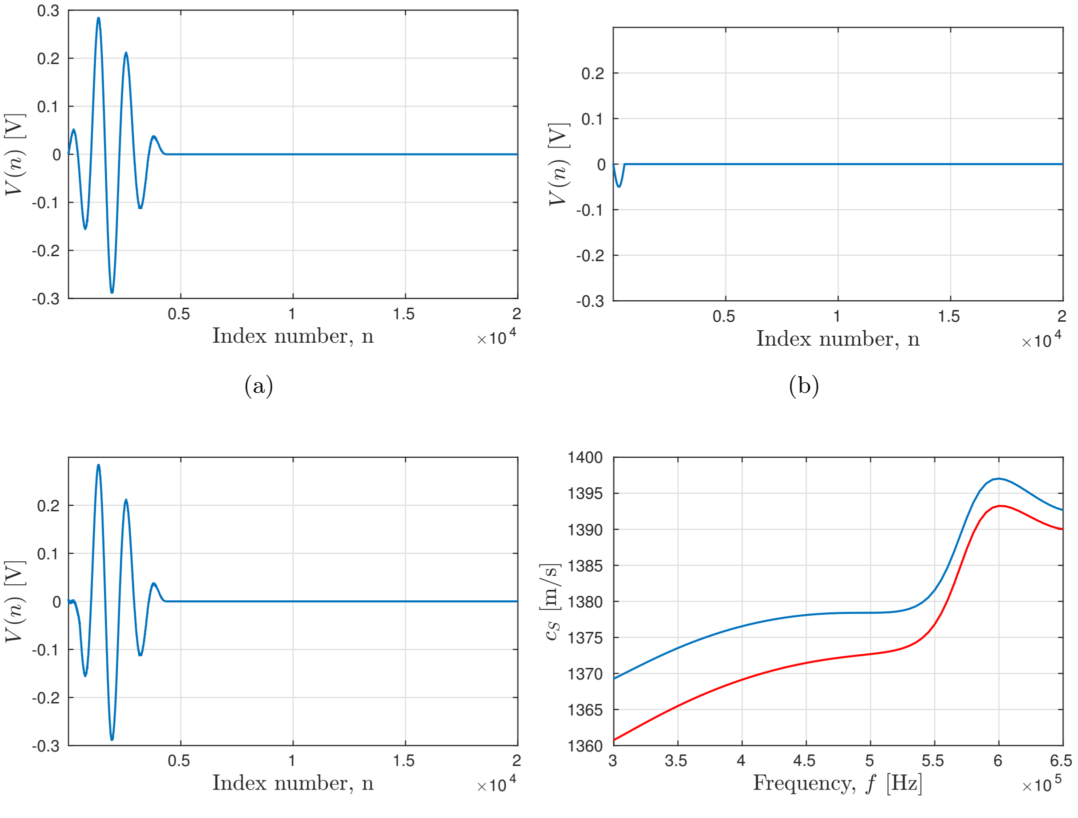

(a) (b)

(c) (d)

Figure 3.25: Figure showing the effect of small non-separable noise component on the measured c_S of plexiglas using the solid buffer method and the Fourier spectrum method. **a**) Measurement A for the solid buffer method (same as Fig. 3.21 a)). **b**) Synthetic signal, half a period "500 kHz pulse" noise-component. **c**) Superposition of the measured signal in figure a) and the synthetic signal in figure b). **d**) c_S of plexiglas using the solid buffer method and the Fourier spectrum method. Measurement A for the example shown above is substituted with measurement A shown in figure c). For the red curve, the diffraction corrections in Eq. (2.6) are used to calculate H_A^{dif} and H_B^{dif}. For the blue curve, $\angle H_A^{dif} = \angle H_B^{dif}$.

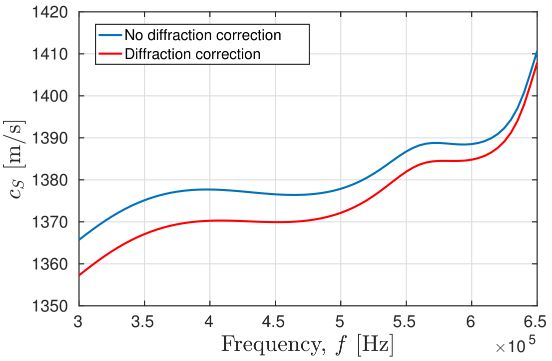

Figure 3.26: Measured c_S using the signals in Fig. 3.21 and abruptly truncating them after 4 periods.

Using the Fourier spectrum method with the solid buffer method and the immersion method

The Fourier spectrum method can be used with the immersion method and the solid buffer method. Above, an example with shear wave transducers has been described for the solid buffer method. The shear wave velocity can be found by isolating A_3 and B_4 and using Eq. (3.19).

For the same signals, c_P and α_P are found with the solid buffer method by isolating the compressional wave pulses A_1 and B_1 and calculating the DFT ($V_{6,A}$ and $V_{8,B}$). The approach is analogue as described for the shear waves above. c_P can be found using the phase of $V_{6,A}$ and $V_{8,B}$ and inserting the them in Eq. (3.17). The compressional wave attenuation coefficient can be found using the magnitude of $V_{6,A}$ and $V_{8,B}$ and inserting the them in Eq. (3.23). $V_{0,A}$ and $V_{0,B}$ are the DFT of the electrical input signal on the signal generator (emf), ($V_{0,A}(t)$ and $V_{0,B}(t)$), respectively.

In Ch. 6, plexiglas measurements with both the P-wave and the S-wave transducers are presented. When using the P-wave transducers, the shear wave signals in Fig. 3.19 are not present and the isolation of the pulses is simpler. Solid buffer method measurements conducted with the S-wave transducers and P-wave transducers are compared. Plexiglas measurements with the immersion method is used as reference measurements.

The Fourier spectrum method can also be used with the immersion method. The isolation of the pulses is analogue to the description above. The shear wave pulses must be isolated for shear wave measurements and the compressional wave pulses must be isolated for compressional wave measurements. The compressional wave velocity and attenuation coefficient is calculated by the equations 3.34 and 3.45, respectively. The shear wave velocity is found by rotating the specimen to the critical angle. The shear wave propagating through the specimen can then be detected and isolated. The shear wave velocity is calculated with Eq. (3.41).

3.6 Impedance Analyzer Setup

The electrical admittance of the P-wave transducers and S-wave transducers is measured in all the important stages of the transducer building process presented Ch. 4. The P-wave transducers electrical admittance measurements are compared with FEM simulations of the electrical admittance. The measurements are conducted with a HP4192A impedance analyzer from Agilent connected to a PC with a USB-GPIB adapter. The piezoelectric element is attached to the impedance analyzer with small copper wires. To reduce the effects of inner electrical circuits of the impedance analyzer and the small copper wires, the instrument with the copper-wires is zero-adjusted before the measurements [187]. The use of the impedance analyzer is detailed further by Aanes [188]. The impedance analyzer with a polystyrene holder for piezoelectric element measurements is shown in Fig. 3.27.

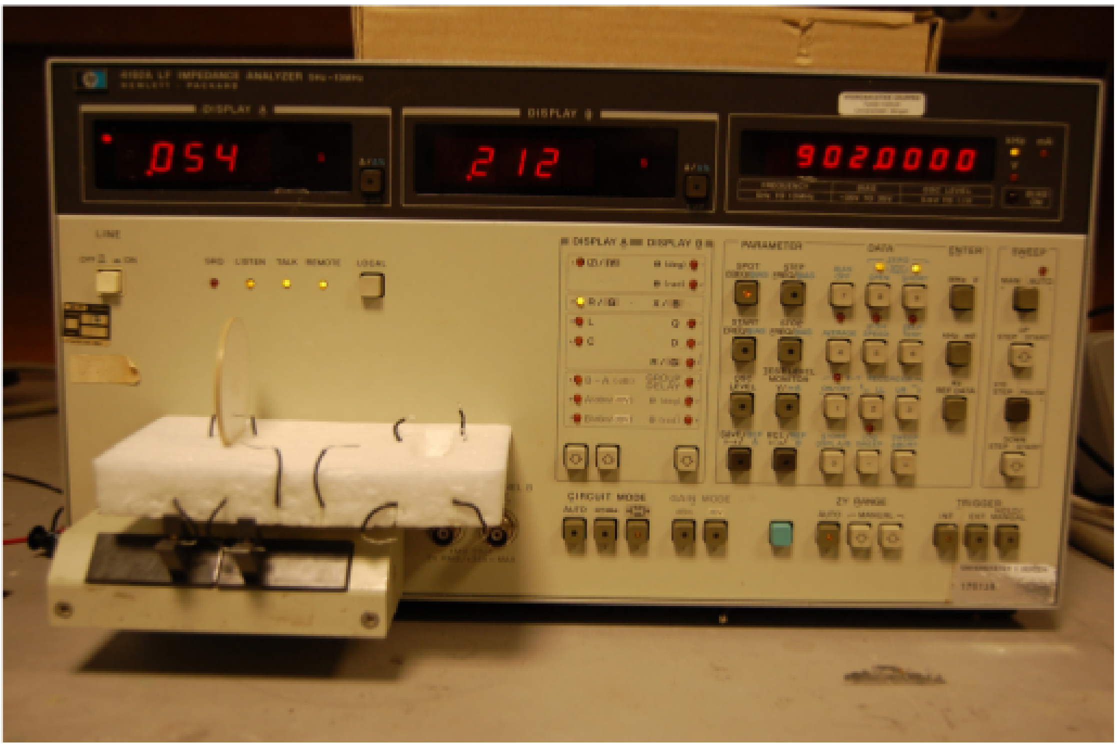

Figure 3.27: Picture of the HP4192A impedance analyzer used measure the admittance of the transducers.

Chapter 4

Transducer design

In this chapter, the design and construction of the P-wave and S-wave transducers used with the solid buffer method inside the pressure cell is presented. The limited space and the pressure and temperature conditions inside the pressure cell impose some restrictions on the transducer design and some general considerations on the transducer design are given in Sect. 4.1. The construction and design of the P-wave and S-wave transducers are presented in Sect. 4.2 and Sect. 4.3, respectively. In Sect. 4.4, electrical conductance measurements and simulations of the P-wave transducers during the important steps of the transducer construction process are presented. In Sect. 4.5, the measured electrical conductance of the S-wave transducers during the important steps of the transducer construction process are presented.

4.1 Considerations

Some general considerations must be taken into account when designing the transducers for use in this work. The transducers are to be used with the solid buffer method inside the pressure cell (Sect. 3.3). The limited space within the pressure cell poses some restrictions on the dimensions of the transducers. The pressure inside the pressure cell is cycled from atmospheric conditions to 83 bar and back to atmospheric conditions again during the test period. The hydrate measurements lasts for weeks and the transducers must withstand the pressure of 83 bar during the measurement period.

The available space inside the pressure cell is a tube-formed chamber with inner diameter 50 mm and length approximately 35 cm (see Fig. 3.8). The Bentheim sandstone specimen have a diameter of 50 mm. The porous rock needs to have a certain surface exposed to the gas for the gas to efficiently seep into the porous rock. The diameters of the constructed transducers and the buffers are thus 35 mm.

The Bentheim sandstone or plexiglas specimen, transducers, buffers and transducer holders must all fit inside the inner chamber of length 35 cm. A total length of 20 cm is given the transducers and the buffers, that is 10 cm available space for one buffer and one transducer combined. The transducers consists of a piezoelectric element, a frontlayer, a backing layer, a pressure tight seal behind the backinglayer and a lid at the back. The S-wave transducers have length 69 mm and the P-wave transducers have length 66 mm.

As discussed in Sect. 3.5.2, the buffers must be long enough so that the different reflected acoustic pulses are separable in each measurement. To have maximum acoustic energy transmitted through the system, buffers with characteristic acoustic impedance in between the transducer's and the specimen's characteristic impedance should be chosen. The compressional wave characteristic acoustic impedance, Z_P, in a medium having density ρ and compressional wave velocity c_P, is $Z_P = \rho c_P$. The shear wave characteristic acoustic impedance is defined $Z_S = \rho c_S$. Aluminum has such an acoustic impedance (approximately $Z_P = 17$ MRayl [189]), however, aluminum has a compressional wavelength of approximately 13 mm for a 500 kHz compressional wave ($c_P \approx 6420$ m/s [189]). This will only give room for a few periods before reflections from the end of the buffer interfere with the signal. Aluminum is also electrically conductive and the ground electrodes using aluminum buffers would be electrically coupled. This may give ground current loops as discussed in Sect. 3. Plexiglas buffers with length 31 mm and $Z_P = 3.2$ Mrayl and c_P 2709 m/s (Tab. 4.1) where chosen for the shear wave transducers. In these plexiglas buffers there are room for 11 compressional wavelengths at frequency 500 kHz before reflections from the end of the buffer interfere with the direct signal. Plexiglas buffers have been used in the solid buffer method previously [51].

Acoustic waves in a medium with high wave velocity will in theory be diffracted more than acoustic waves in a medium with lower wave velocity. A lower wave velocity in the buffers may thus give less reflections from the sidewalls. PVC has a compressional wave velocity 2380 m/s and Z_P approximately the same as plexiglas [189]. 34 mm PVC-buffers where chosen for the P-wave transducers. In these PVC buffers there are room for 13 compressional wavelengths at frequency 500 kHz before reflections from the end of the buffer interfere with the direct signal.

As discussed in Sect. 3.5.2, short pulses are needed to use the Fourier spectrum method. Broadband transducers with tungsten-filled epoxy quarter-wavelength front layers are designed and constructed in this work. The characteristic acoustic impedance of the backing layer is designed to be as close as possible to the characteristic acoustic impedance of the piezoelectric element used in the design (Pz37 for P-wave transducers and Pz27 for S-wave transducers). This way, acoustic energy on the backside of the piezoelectric element will radiate into the backinglayer. For maximum transmitted energy into the buffer, the acoustic characteristic impedance of the front layer is designed to be the geometrical mean of the impedance of the transducer and the buffer. The content and construction procedure of the tungsten-epoxy backing and front layers are presented in Sect. 4.2. In Tab. 4.1, there is a list of the elastic materials with material parameters used in the transducer construction. In the table there is either a literature reference or a label, (m), denoting that the parameter is measured in this work.

Table 4.1: Materials used in the transducer construction. Tungsten-epoxy frontlayer F1 and F2 are used in the P-wave and S-wave transducers, respectively. c_S for the tungsten-epoxy-mixtures are typically approximately half the value of c_P [190]. Thus $c_S = 800$ m/s is assumed for all the tungsten-epoxy coupling layers. (m): parameter is measured by this author.

Material	c_P [m/s]	c_S [m/s]	Q_P	ρ [kg/m^3]	ρc_P [Mrayl]
Tungsten-epoxy backing layer	1600 (m)	800	13.5 (m)	7470 (m)	11.9
Tungsten-epoxy front layer F1	1600 (m)	800	28.5 (m)	4590 (m)	7.3
Tungsten-epoxy front layer F2	1600 (m)	800 [191]	28.5 (m)	5470 (m)	8.7
Aluminum	6420 [189]	3040 [189]	500 [189]	2700 [189]	17.3
Plexiglas	2709 (m)	1347 (m)	63 (m)	1184 (m)	3.2
PVC	2380 (m)	1190	51 (m)	1380 (m)	3.3
Polyurothane	1760 [189]	345 [189]	14 [189]	1100 [189]	1.9

The material properties of polyurethane and aluminum are found in the literature [189]. The acoustic parameters of plexiglas have been measured with the immersion method. c_P and α_P for PVC, the tungsten-epoxy backing layer and front layers have been measured with the immersion basic pulse method at 500 kHz. Q_P is calculated with $Q_P = \frac{K_m^z}{2\alpha_P}$, where $K_m^z = \omega / c_P$. c_S is typically approximately half the value of c_P in tungsten-epoxy mixtures [191] and in PVC [189], and has thus been used in this work.

A full set of anisotropic material parameters for Meggitt Pz27 is provided by the manufacturer [192]. However, the material parameters of Pz27 has been studied extensively [193, 188] and another full set of anisotropic material parameters for Pz27 are given in Tab. 4.3 [193]. These material constants have been found to better fit electrical measurements than that of the manufacturer.

To the best of this author's knowledge, a full set of anisotropic material constants for Meggit Pz37 has not been published. The manufacturer of Pz37 (Meggitt) does only provide a limited set of the piezoelectric material parameters [192], shown in Tab. 4.2. The parameters are defined in the IEEE piezoelectric standard [194] and are consistent with the definitions found on the manufacturers web page [192]. K_{33}^T is the relative dielectric permittivity. $\tan\delta$ is the dielectric dissipation factor. k_p and k_t are the planar and thickness coupling factors, respectively. $N_p = f_p l$ and $N_t = f_s l$ are the planar and thickness frequency constants, respectively. f_p and f_s are the parallel and series resonance frequencies, respectively. l is the thickness of the piezoelectric element.

Table 4.2: Material parameters of Pz37 [192].

K_{33}^T	$\tan\delta$	k_p	k_t	N_p	N_t	Q_p	ρ
1200	0.017	0.35	0.52	1550 Hz m	1400 Hz m	50	6000 kg/m^3

From k_t, N_p and ρ, the compressional wave velocity and characteristic impedance can be calculated, which are useful in the transducer design. $c_P = 2800$ m/s and $Z_P = \rho c_P \approx$ 17 Mrayl for Pz37 are obtained by inserting k_t, N_p and ρ into Eq. 4.1 [194]:

$$\begin{aligned} c_{33}^E &= 4\rho N_p^2(1-k_t^2), \\ c_{33}^D &= \frac{c_{33}^E}{1-k_t^2}, \\ c_P &= \sqrt{\frac{c_{33}^D}{\rho}}. \end{aligned} \tag{4.1}$$

$c_P = 4347$ m/s and $Z_P = \rho c_P = 33.5$ Mrayl for Pz27 are obtained by using the listed parameters in Tab. 4.3 and inserting them into Eq. 4.2 [194].

$$\begin{aligned} c_{33}^D &= c_{33}^E + \frac{e_{33}^2}{\epsilon_{33}^S}, \\ c_P &= \sqrt{\frac{c_{33}^D}{\rho}}. \end{aligned} \tag{4.2}$$

$c_S = 1655$ m/s and $Z_S = \rho c_S = 12.7$ Mrayl for Pz27 are obtained by using the listed parameters in Tab. 4.3 and inserting them into Eq. 4.3 [194]. In the shear wave transducers, shear-wave polarized piezoelectric elements Pz27 have been used. The piezoelectric crystals in these have been polarized so that a voltage signal across the electrodes give a displacement along the surface of the shear-wave polarized piezoelectric elements.

$$c_S = \sqrt{\frac{c_{44}^E}{\rho}}. \tag{4.3}$$

In this work, a backinglayer with Z_P approximately 12 Mrayl is constructed and used in both the S-wave and the P-wave transducers (see Tab. 4.1). Pz37 have $Z_P \approx 17$ Mrayl which is significantly closer to Z_P of the backing layer than Pz27 (33.5 Mrayl). Thus, Pz37 piezoelectric elements are chosen as the active element for the P-wave transducers. The S-wave transducers have $Z_S \approx 12.7$ Mrayl. The backinglayer have $Z_S = \rho c_S \approx 6$ Mrayl.

Table 4.3: Material parameters for Pz27 [193].

Variable	Pz27
$c_{11}^E[10^{10}\ \mathrm{N/m^2}]$	$12.025(1+i/96)$
$c_{12}^E[10^{10}\ \mathrm{N/m^2}]$	$7.62(1+i/70)$
$c_{13}^E[10^{10}\ \mathrm{N/m^2}]$	$7.42(1+i/120)$
$c_{33}^E[10^{10}\ \mathrm{N/m^2}]$	$11.005(1+i/190)$
$c_{44}^E[10^{10}\ \mathrm{N/m^2}]$	$2.11000(1+i/75)$
$e_{31}[\ \mathrm{C/m^2}]$	$-5.4(1-i/166)$
$e_{33}[\ \mathrm{C/m^2}]$	$17(1-i/324)$
$e_{15}[\ \mathrm{C/m^2}]$	$11.20(1-i/200)$
$\epsilon_{11}^S[10^{-9}\ \mathrm{F/m}]$	$8.11044(1-i/50)$
$\epsilon_{33}^S[10^{-9}\ \mathrm{F/m}]$	$8.14585(1-i/130)$
$\rho\ [\mathrm{kg/m^3}]$	7700

The full set of anisotropic material constants for the Pz27 elements in Tab. 4.3 may be used to do 3D finite element simulations. In Ch. 5, a rough estimate of a full set of anisotropic material constants for the Pz37 elements are given so 3D FE-simulations may be performed for the Pz37 P-wave transducers.

4.2 Construction and design of P-wave transducers

Pz37 [192] piezoelectric elements with 23 mm diameter and thickness 2.9 mm are used as the active elements in the P-wave transducers. From conductance measurements presented in Sect. 4.4, the series resonance frequency (maximum conductance)[194] is measured to be $f_s \approx 570$ kHz. The P-wave transducers design is presented in Fig. 4.1. Dimensions and measurement uncertainties are shown. Many of the components are manufactured with the turning machine at the University of Bergen, having accuracy 0.2 mm. The piezoelectric elements from Meggitt are measured with a Mitutoyo MDH-25M digital micrometer gauge [195] having a listed uncertainty of 0.5 µm. However this author was only able to obtain an accuracy of ±0.02 mm using this tool. Because the backing layer and the polyurothane pressure seal is poured into the transducer construction, there is a big uncertainty in the thicknesses of these layers. Better accuracy of the backinglayer might have been achieved if this was manufactured separately and attached as a solid coupling layer instead of pouring it into the transducer construction. The construction of the transducer and the different components are described in detail below.

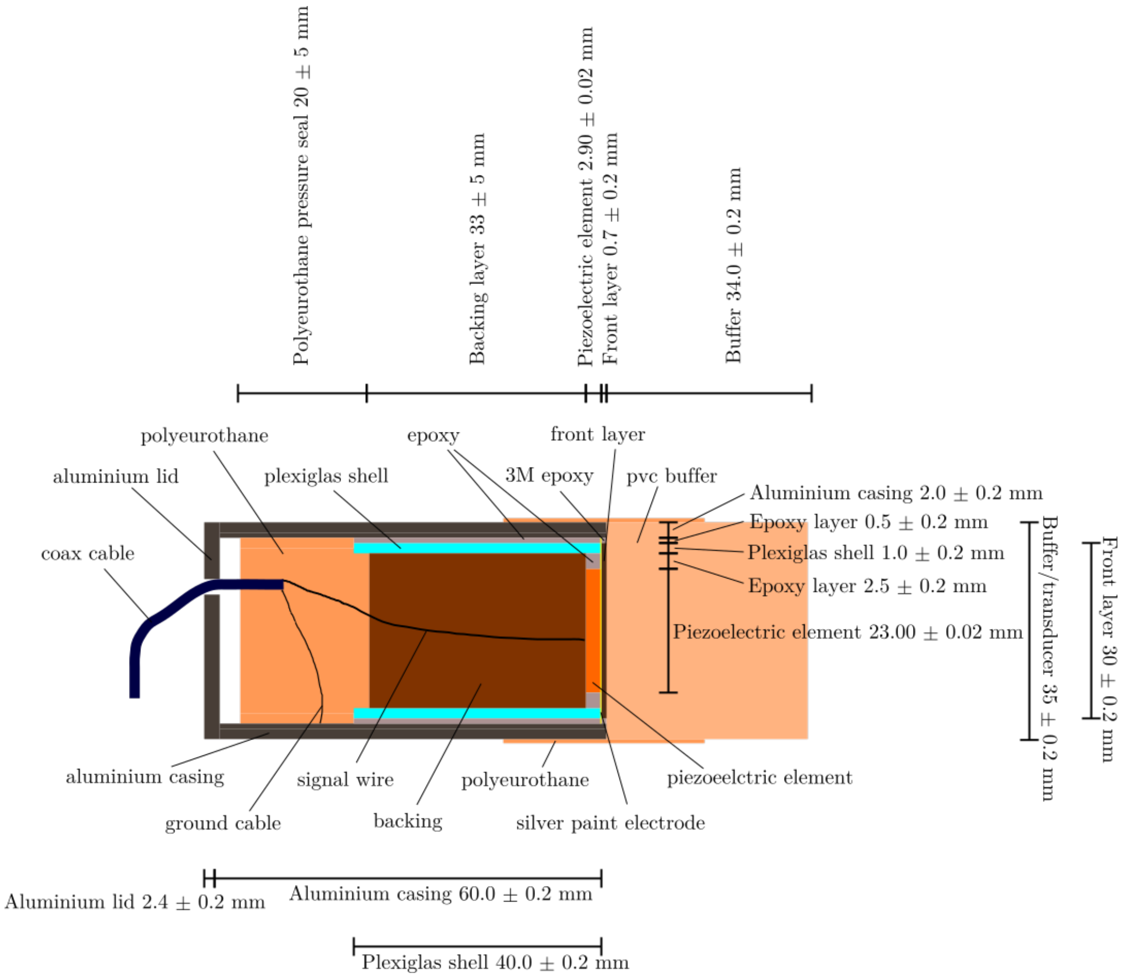

Figure 4.1: Schematics of the P-wave transducer design.

First, 7 cm of the outer insulation layer on a coax cable is cut off and the inner wire of the coax cable is separated from the shielding. The coax cable is bent and put down on the piezoelectric element in a way so that the mechanical stress of the cable presses itself down onto the back electrode of the piezoelectric element. The inner wire is glued on to the piezoelectric element with several drops of Ted Pella silver paint [196] to ensure good electrical conductivity. The silver paint is a poor adhesive and a drop of rapid drying Loctite epoxy is used after the silver paint dries to ensure good adhesion, see Fig. 4.2 a).

For high voltages, the tungsten-filled epoxy backing layer may theoretically be weakly electrically conductive. A plexiglas cylinder, open in both ends, with inner and outer diameter 28 mm and 29 mm, respectively, 1 mm thick and 4 cm high, is used as an insulator between the aluminum casing and the tungsten-filled epoxy. The Pz37 element with the wire attached, is glued with Epofix epoxy [197] into this cylindrical plexiglas shell, see Fig. 4.2 b).

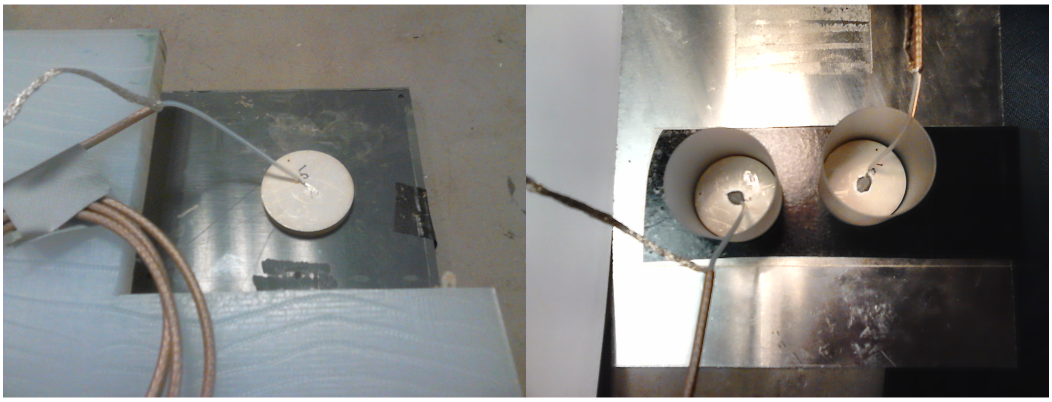
(a) (b)

Figure 4.2: Pictures of a) inner coax cable wire, glued onto the Pz37 element, b) piezoelectric element glued into the plexiglas shell.

In the following, sketches of the transducer design is shown to illustrate the construction process. In Fig. 4.3 a) the piezoelectric element with the plexiglas shell glued on, is shown. The next step is to attach the aluminum casing. The casing is a cylinder open in both ends, 2 mm thick, has an outer diameter of 35 mm and is 63 mm long. It is glued on to the plexiglas shell so that there is space available for the frontlayer (more than 0.7 mm), see Fig. 4.3 c). This has been achieved by first flipping the plexiglas shell with the piezoelectric element and placing it on a custom made fitting tool with grooves for the plexiglas shell, see Fig. 4.3 b). Now, a small amount of rapid drying Loctite epoxy is put on between the aluminum casing and the plexiglas shell, sealing the opening. After a few minutes the whole structure is flipped again, and Epofix epoxy is poured in between the aluminum casing and the plexiglas shell from the other side, filling the space and solidifying the transducer construction.

The coax - cable inner wire is threaded. In a high pressure environment, gas may creep along the threaded wire, down to the piezoelectric element. When the system is depressurized again, gas inside the transducer might expand, possible damaging the structure. To avoid this, some of the inner wire is removed and a single wire is soldered onto the threaded wire. The ground cable is glued onto the aluminum casing with Ted Pella silver paint and Loctite epoxy. The signal wire and the ground wire is gathered in a coax cable (Fig. 4.3 d).

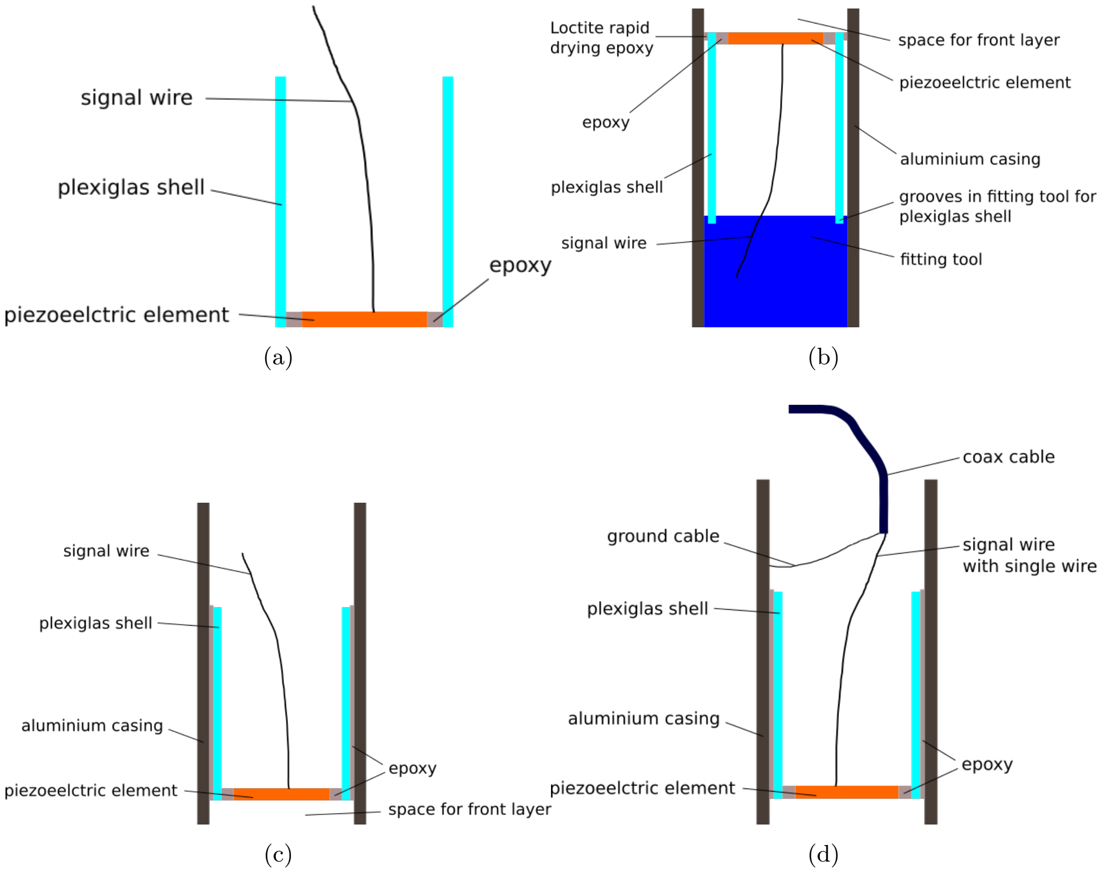

Figure 4.3: Schematics of a) Piezoelectric element with the plexiglas shell. b) Use of Loctite rapid drying epoxy to seal the space in between the plexiglas shell and the aluminum casing. c) Epofix epoxy poured down in between the plexiglas shell and the aluminum casing. d) Ground cable, single wire signal cable and coax cable attached to the threaded inner wire.

Ted Pella silver paint is then applied to electrically connect the ground electrode of the piezoelectric element to the aluminum casing. A thin layer of silver paint is used on the whole front of the transducer. The thickness of this is assumed to be negligible. In Fig. 4.4, the transducer is shown with the applied silver paint on the front, connecting the electrode of the piezoelectric element and the aluminum casing. In Fig. 4.4 b) the transducer is flipped upside down and placed in a plastic holder compared with the schematics in a). The white silver electrode is seen on the front of the transducer.

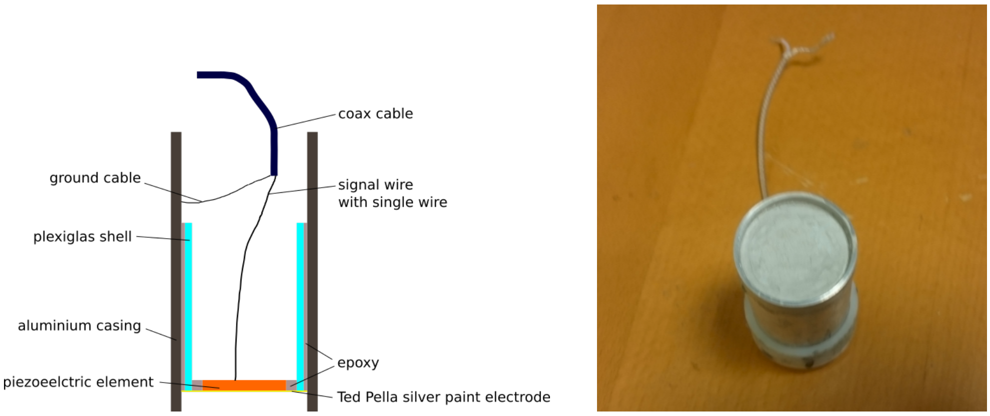

(a) (b)

Figure 4.4: Ted Pella silver paint is applied to electrically connect the ground electrode of the piezoelectric element and the aluminum casing. b) Schematics, a) Picture.

The next steps are adding backing layer, front layer and a pressure tight seal behind the transducer. Tungsten-filled epoxy mixtures are suitable as backing layers in transducer applications [191, 190]. Mixtures containing large tungsten grains are reported to have higher attenuation and acoustic impedance than mixtures with smaller tungsten grains [191, 190].

For the backing layer, tungsten-epoxy mass ratio of 10 is used. The tungsten grains have diameters 50-250 µm. In the transducer design, the backing layer tungsten-epoxy mixture is poured into the open space behind the piezoelectric element, almost filling the plexiglas cylinder (see Fig. 4.5 a)). The thickness of the backing layer is set to 33 mm. The backing layer of a maximum damped transducer has characteristic acoustic impedance equal to the piezoelectric element. A backing layer with acoustic impedance 12 Mrayl is successfully constructed in this work. First, the two component Epofix epoxy is mixed. The tungsten grains are then added to the mixture. Approximately 1 hour passed from the epoxy was mixed and to the tungsten-epoxy mixture was poured into the space behind the piezoelectric element. The backing layer was poured into the transducer construction. By vacuuming the tungsten-epoxy mix, a higher Z_P might been achieved, however this was not done. The acoustic parameters for the backing layer presented in Tab. 4.1 are obtained by constructing another sample with tungsten-epoxy ratio 10 using 50-250 µm tungsten grains. The tungsten-epoxy mixture is stirred for the last time 1 hour after the two-component epoxy is mixed (same as used for the backinglayer). The diameter of this test sample is 44 mm and has thickness 1.8 cm.

To radiate maximum of the acoustic energy from the piezoelectric element and into the buffer, a quarter wavelength front layer with characteristic impedance $Z_m =$

$\sqrt{Z_P^{Pz37} Z_P^{PVC}}$ should be used. With $Z_P^{Pz37} = 17$ Mrayl (characteristic compressional wave acoustic impedance of Pz37) and $Z_P^{PVC} = 3.3$ Mrayl (characteristic compressional wave acoustic impedance of the PVC-buffer), Z_m should be 7.5 Mrayl. The front layer is constructed as a quarter wave front layer with respect to the series resonance frequency, $f_s \approx 570$ kHz. The front layer has thus thickness 0.7 mm. To find a way to manufacture the front layer, three tungsten-epoxy test samples were constructed.

Tungsten grains with diameter 5 µm are used to make the three tungsten-epoxy test samples with diameter 44 mm and lengths approximately 1 cm. Tungsten-epoxy mass ratios 4, 4.5 and 5 are used. As for the backing layer, the two-component Epofix epoxy is mixed. The 5 µm tungsten grains are added and the mixture is stirred. The tungsten-epoxy mixture is then vacuumed for 10 minutes, removing air bubbles. The compressional wave velocity for the samples are measured with the immersion method and the density is found by measuring the mass of the sample and calculating the volume using the dimensions of the sample. The three test samples are presented in Tab. 4.4. The first arrival of the pulse is used with the immersion method to calculate the compressional wave velocity. The surface of the test-samples are rough and there is an uncertainty in the thickness of approximately 0.4 mm (the uncertainity in specimen thickness dominates the uncertainty in c_P). The uncertainty in the acoustic impedance in Tab. 4.4 is thus approximately 1 Mrayl.

Table 4.4: Material parameters for tungsten-epoxy samples with tungsten grain diameter 5 µm.

Specimen	F1	F2	F3
Tungsten-epoxy mass ratio	4.0	4.5	5.0
Density [kg/m^3]	4.59	5.47	5.34
Compressional wave velocity c_p [m/s]	1604	1595	1557
ρc_P [MRayl]	7.3	8.7	8.3

In Tab. 4.4 the specimen closest to the geometrical mean, $Z_m = 7.5$ Mrayl, is the front layer with tungsten-epoxy mass ratio of 4. The diameter of the specimen is shaped in a turning machine to fit in the space in front of the piezoelectric element. The front layer is then glued onto the piezoelectric element with 3M Epoxy [198]. The silver paint electrode underneath the frontlayer ensures electrical contact from the piezoelectric element and to the aluminum chassis. The 3M epoxy squeezes out on the sides of the piezoelectric element, filling the small space in between the aluminum chasses and the front layer, Fig. 4.5) b). After the 3M epoxy cures, the front of the transducer is turned down so that the front layer has thickness equal to quarter of a wavelength at $f_s = 570$ kHz, 0.7 mm (see Fig. 4.5 c)). The accuracy of the turning machine is 0.1-0.2 mm.

After adding the front and backing layer to the transducer, Sol-Res 01 polyurothane [199] is poured into the back of the backing layer, immersing the single signal wire and sealing the transducer from behind (see Fig. 4.5 d)).

6

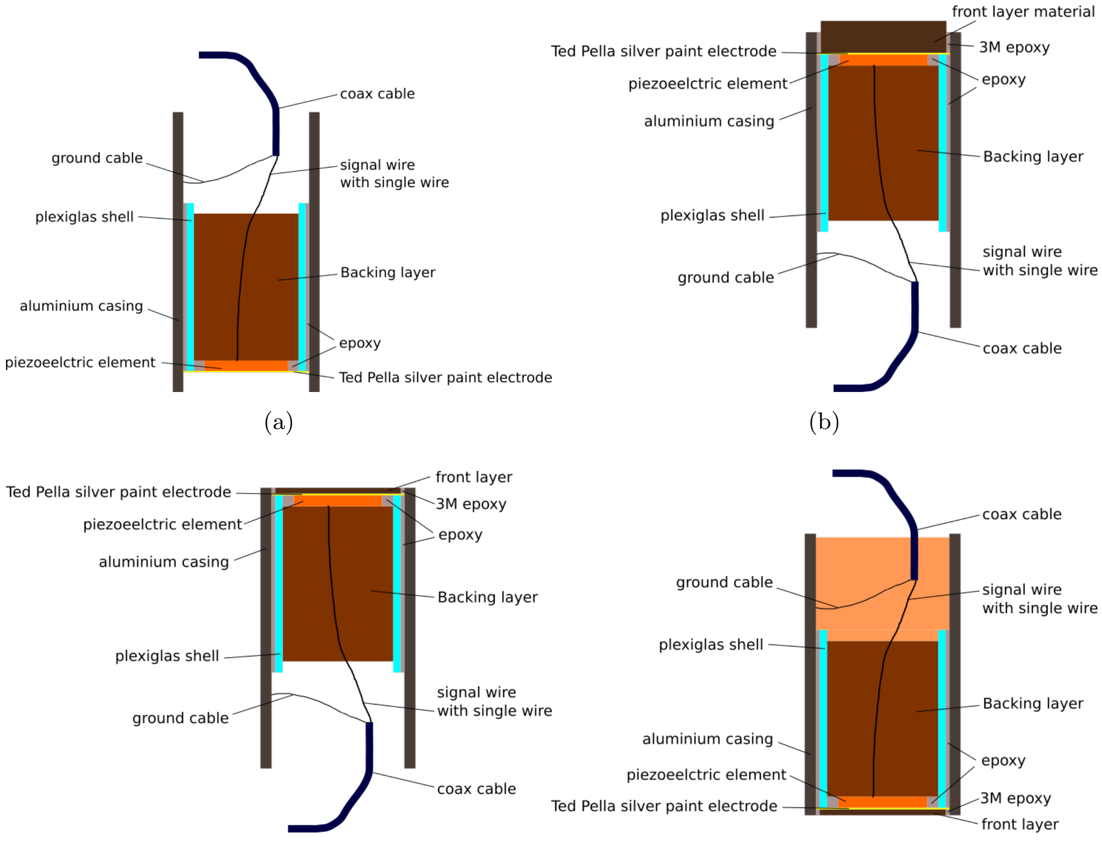

(a)

(b)

(c)

(d)

Figure 4.5: Schematics of a) Tungsten-epoxy backing layer poured in behind the piezoelectric element. b) Front layer material glued onto the piezoelectric element with 3M epoxy. c) Front of the transducer turned down so that the front layer is 0.7 mm (quarter wave length). d) Polyeurothane poured in behind the backing layer.

The last steps of the transducer construction is to attach the lid behind the transducer and the buffer. The final transducer construction is shown in Fig. 4.1. To have a minimum of loose parts inside the pressure cell, the buffers are glued onto the transducers with 3M epoxy. 3M epoxy is seen in to provide better adhesive strength than Epofix epoxy or rapid-drying Loctite epoxy inside the pressure cell at hydrate conditions. Thus, 3M epoxy is chosen as the adhesive on between the piezoelectric element and the frontlayer, and between the the front layer and the buffer.

To protect against potentially creeping gas in between the buffer and the aluminum casing, a thin layer of polyurethane is applied around the transducer and the buffer to seal the structure.

Electrical conductance measurements and simulations are conducted for important steps in the transducer design. These are presented in Sect. 4.4.

4.3 Construction and design of S-wave transducers

The design and construction process of the S-wave transducers and P-wave transducers are almost identical. The piezoelectric element of the shear wave transducer is a 15×15 mm square-shaped shear wave polarized Pz27 element with thickness 2.0 mm. The piezoelectric crystals in these have been polarized so that a voltage signal across the electrodes give a displacement along the surface of the shear-wave polarized piezoelectric elements. From conductance measurements presented in Sect. 4.5, the series resonance frequency of the piezoelectric element is measured at maximum conductance, $f_s \approx 430$ kHz.

Plexiglas buffers have previously been used in the solid buffer method [51] and are chosen as the buffers for the shear wave transducers. The length of the aluminum casing used in the shear wave transducer is 66 mm. The buffers have length 31 mm so that aluminum casing + aluminum lid + buffer = 10 cm. This is also true for the P-wave transducers.

The shear wave characteristic acoustic impedances (Z_S) for plexiglas and Pz27 are 1.6 Mrayl and 12.7 Mrayl, respectively. The geometrical mean of these are 4.5 Mrayl. As no c_S-measurements where conducted on the tungsten-epoxy specimen, Z_S for the frontlayers presented in Tab. 4.4 are assumed to be half the values as Z_P. F2 is the sample with the closest value for ρc_S. The tungsten-epoxy mass ratio of the chosen front layer is thus 4.5. The front layer is constructed to as a quarter wave front layer with respect to the series resonance frequency, $f_s \approx 430$ kHz. The front layer has thus thickness 0.4 mm.

Another small difference between the P-wave transducers and the S-wave transducers, is the inner epoxy-layer covering the area between the piezoelectric element and the plexiglas shell. Since the S-wave piezoelectric element is square-shaped, the amount of epoxy on the side of the piezoelectric element in the two transducer constructions are slightly different (see Fig. 4.6). For the construction of the S-wave transducers, refer to the procedure described above. The shear wave transducer with dimensions is shown in Fig. 4.7.

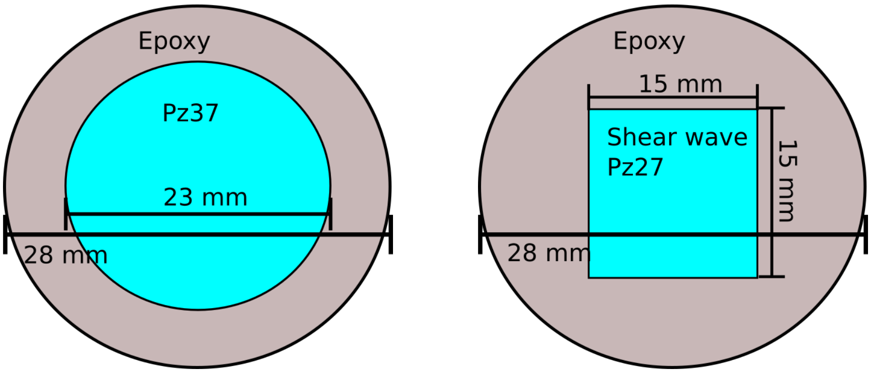

(a) (b)

Figure 4.6: Illustration of the difference between the a) P-wave tansducer and b) the S-wave transducer.

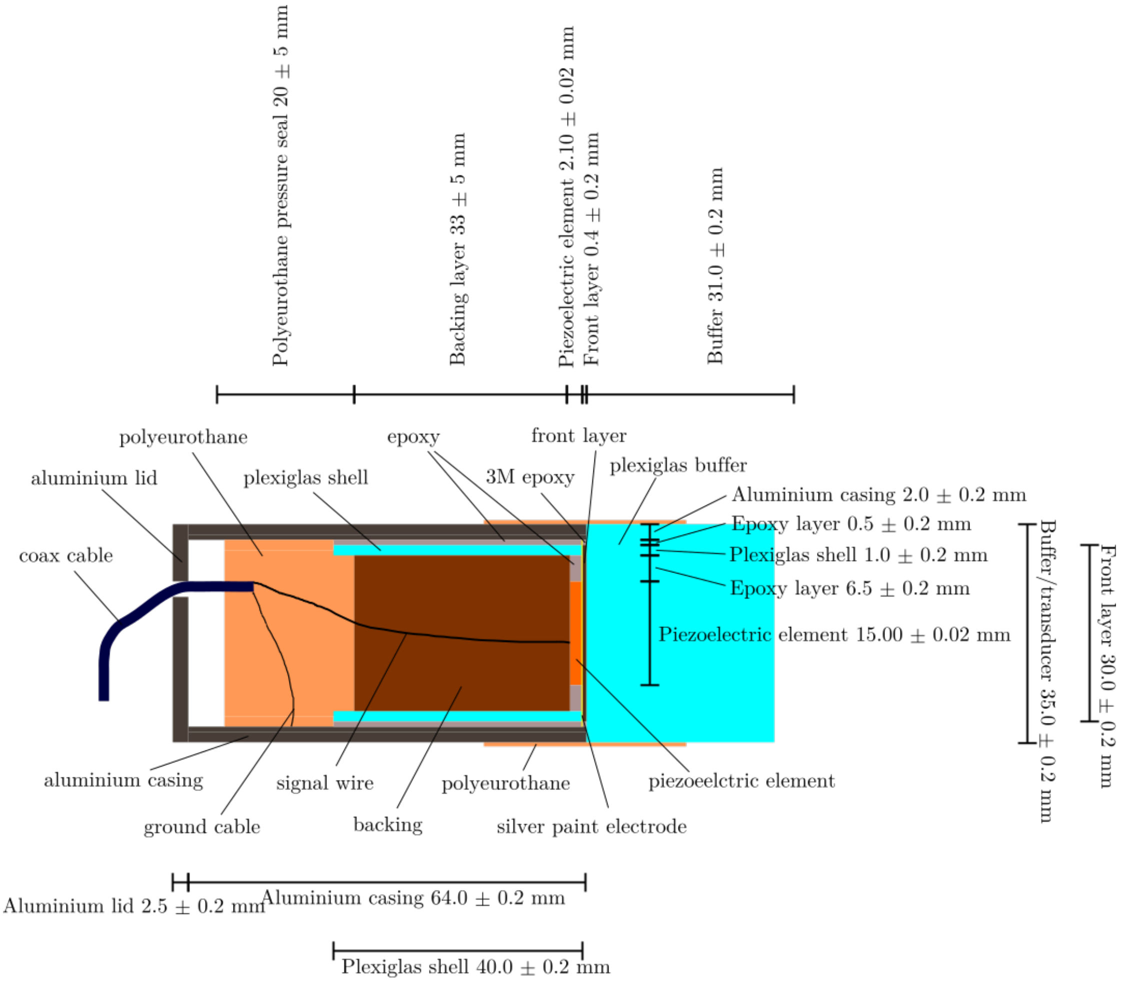

Figure 4.7: Schematics of the S-wave transducer design.

It is also worth to mention that several transducers were made and tested in the pressure cell before the design presented here was found. A general problem was seen to be that the frontlayer detached from the transducers under depressurization in the pressure cell. In the early designs, other types of epoxy were used between the frontlayer and the piezoelectric element (e.g. Epofix epoxy) that seemed to more easily break compared with the 3M epoxy used in the final design. One attempt was also made to pour a tungsten-epoxy mixture into the open space in the front of the transducers, which did not work either. Even if the transducers presented in this work was used for almost a year for the hydrate experiments, they eventually broke down as well. However, the transducers showed no signs of wear during the experiments presented in this work.

4.4 Simulated and measured conductance of P-wave transducers with buffers

The electrical conductance of the transducer has been measured and simulated during the important steps of the transducer construction process, starting from the single Pz37 element (Fig. 4.8). All measurements are conducted at room temperature, atmospheric conditions. Comsol multiphysics has been used to perform finite element simulations of transducer's conductance for the same steps. By comparing the measured and simulated conductance for the different stages of the transducer design, potential flaws in the transducer construction may be discovered. Consistency between the simulated and measured conductance gives confidence in the finite element simulations of solid buffer method presented in chapter 5. The simulation setup with all material parameters used in the simulations are detailed in chapter 5. The same structure as shown in Fig. 4.7 is simulated except from the aluminum lid, the wires and the silver electrode. The dimensions used in the simulations are the nominal dimensions shown in Fig. 4.7.

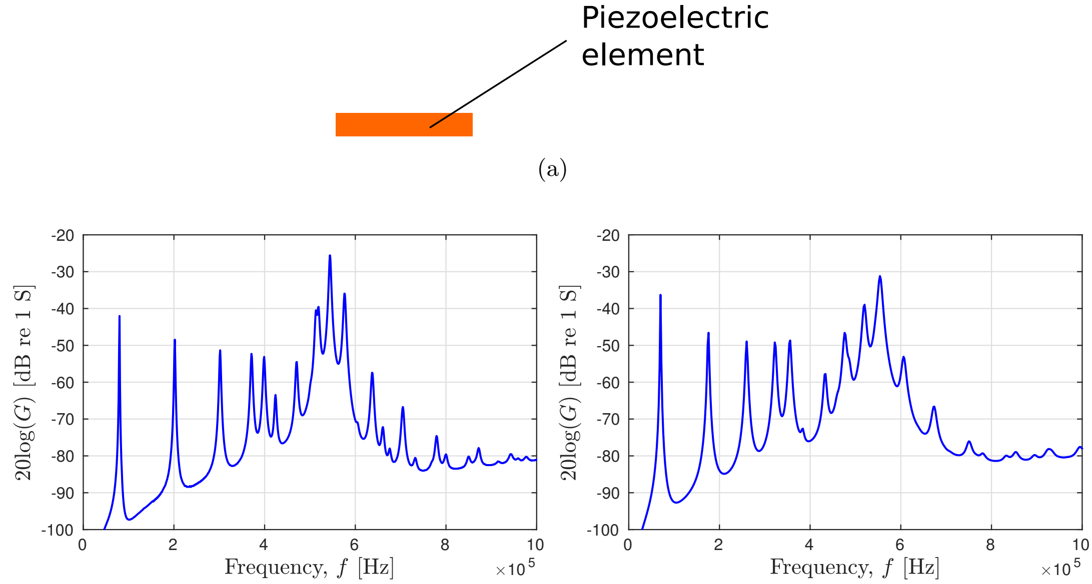

(a)

(b)

(c)

Figure 4.8: First step of the P-wave transducer construction. **a)** Piezoelectric element Pz37 with diameter 23.0 mm and thickness 2.90 mm. **b)** Measured conductance. **c)** Simulated conductance.

The peaks in the measured and simulated conductance are not perfectly aligned in Fig. 4.8. The uncertainties in the measured dimensions are not big enough to explain the deviations between measurements and simulations. The deviations are believed to be because the assumptions regarding the piezoelectric parameters presented in chapter 5 are too rough. However, in this work, the thickness-extensional mode (TE) of the Pz37 element inside the P-wave transducers is used. The thickness mode is split for the Pz37 element but is located around 550 kHz in both the simulation and the measurement. The backing layer and front layer are heavily influencing the thickness mode, and the simulated and measured conductance is seen to be more comparable after adding the front and the backing layer (Fig. 4.10).

Both the measured and the simulated electrical conductance are affected when attaching the plexiglas shell and the outer aluminum casing to the piezoelectric element (Fig. 4.9). An extensively study of all the modes of the piezoelectric element is not conducted here. However, a mass added at the the outer edge of the element, is assumed to affect radial modes. The main features of the thickness mode around 550 kHz in Fig. 4.8 are still present in Fig. 4.9.

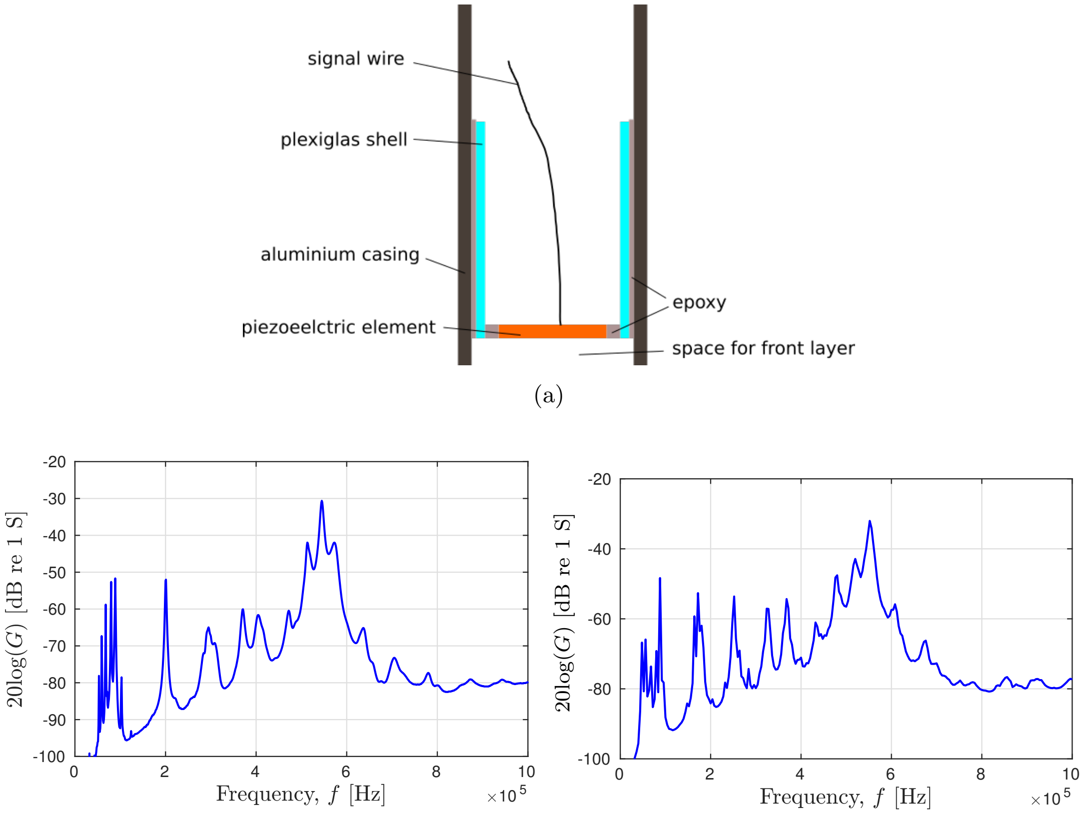

(a)

(b)

(c)

Figure 4.9: Second step of the P-wave transducer construction. **a)** Transducer configuration with the plexiglas shell and the aluminum casing glued on to the piezoelectric element **b)** Measured conductance. **c)** Simulated conductance.

Adding the tungsten-epoxy backinglayer to the back of the piezoelectric element, heavily dampens and widens the thickness mode peak of the transducer (Fig. 4.10). The simulated and measured conductance at this stage is in well agreement. A mode at around 200 kHz has survived the effect of the backinglayer and is visible in both the simulation and the measurement. There are some more ripples in the measured conductance than in the simulated conductance below 400 kHz. This is indicating that the constant Q-value from Tab. 4.1 used for the backing layer is not entirely representing the attenuation at frequencies below 400 kHz. The conductance is measured at the end of the 50 cm long coax cable of the transducer.

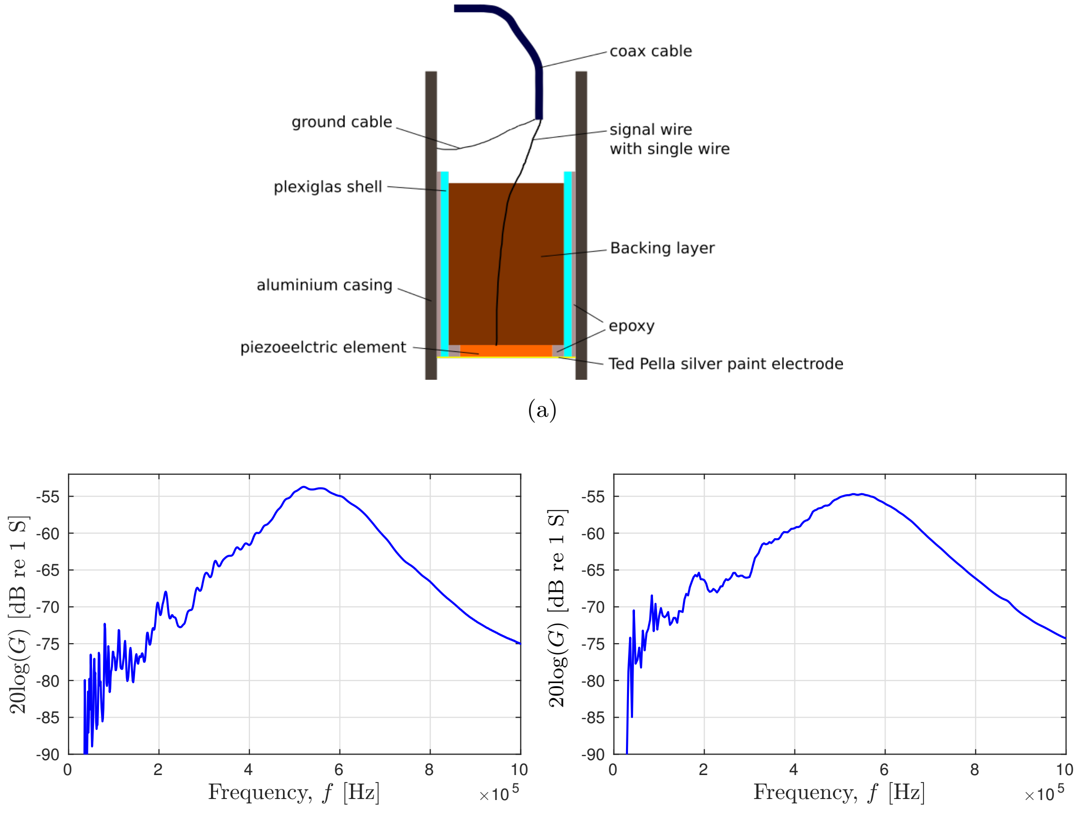

(a)

(b)

(c)

Figure 4.10: Third step of the P-wave transducer construction. **a)** Transducer configuration with the tungsten-epoxy backing layer. **b)** Measured conductance. **c)** Simulated conductance.

When the quarter wavelength frontlayer is added onto the transducer configuration, there is a dip in the measured and simulated electrical conductance (Fig. 4.11). The measured and simulated conductance give the same main features. However, the simulated peak above 600 kHz and the dip between the peaks are shifted towards higher frequencies relative to the measured conductance.

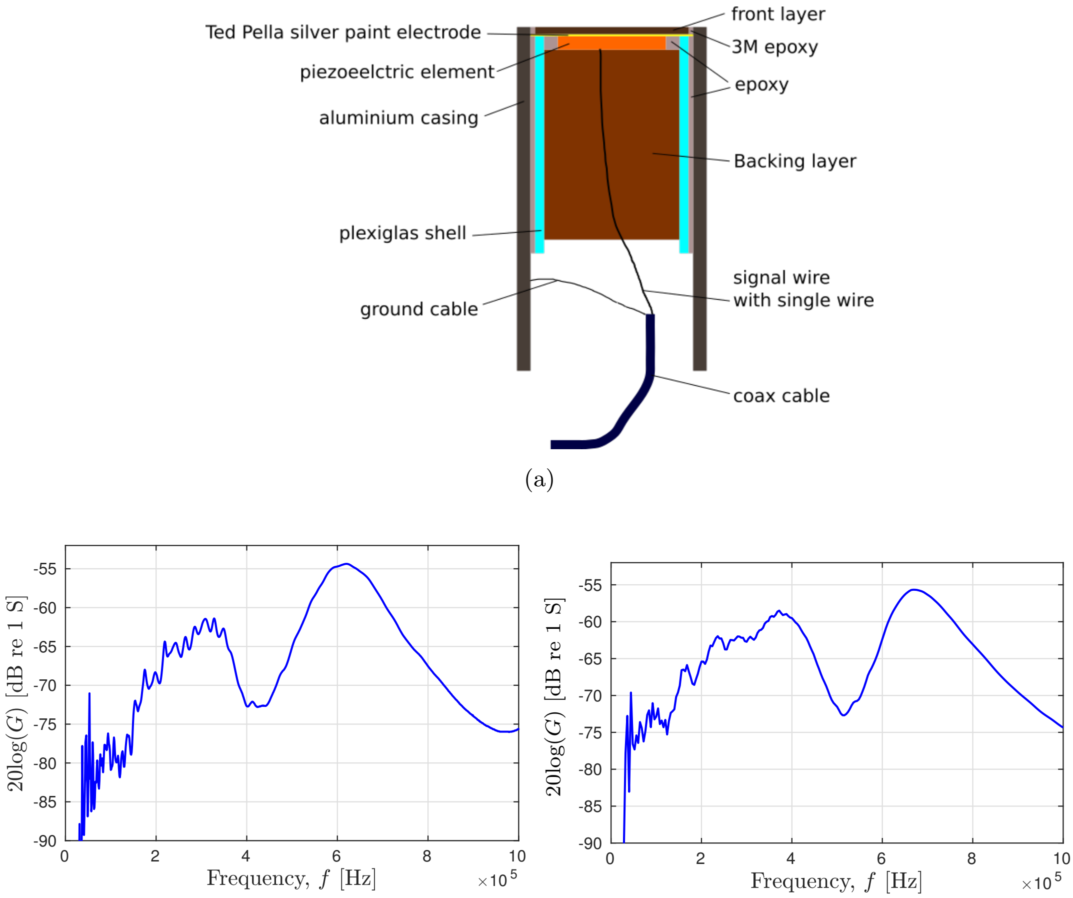

(a)

(b)

(c)

Figure 4.11: Fourth step of the P-wave transducer construction. **a)** Transducer configuration with the tungsten-epoxy backing and front layer. **b)** Measured conductance. **c)** Simulated conductance.

In Fig. 4.12 the measured and simulated electrical conductance of the final P-wave transducer construction with buffer is shown. The buffer acts as the medium in which the transducer radiates acoustic energy into. Because the medium is a finite medium, the sound will reflect back and forth giving rise to ripples in the conductance spectrum. The ripples are bigger in the simulation compared with the measurement. This is believed to be because the attenuation is set too low in the simulation compared to the measurements.

The deviations between the simulations and the measurements indicate that the material parameters are not describing the materials used in the transducer construction perfectly. The thin silver electrode between the front layer and the piezoelectric element is left out in the simulations. The simulation setup is detailed in chapter 5. As the main features of the simulated and the measured conductance plots are consistent, there are assumed to be no major flaws in the transducer. The finite element simulations are assumed to be representative for the transducers and will be used to analyze the effects of unwanted acoustic sidewall reflections the buffers in chapter 6.

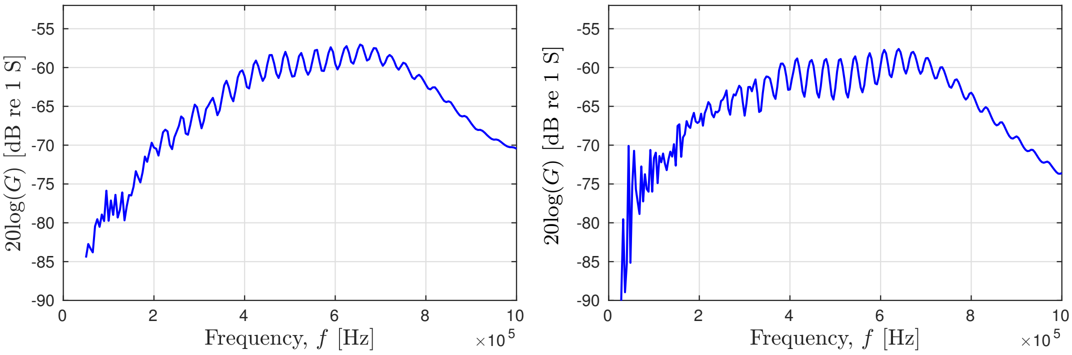

(a)

(b)

Figure 4.12: **a)** Measured conductance of the final P-wave transducer construction with the buffer attached. **b)** Simulated conductance of the final transducer construction with the buffer attached.

4.5 Measured conductance of S-wave transducers with buffers

The measured electrical conductance of the shear wave transducer is shown in Fig. 4.13. In Fig. 4.13 a) the electrical conductance of the shear wave Pz27 piezoelectric element is shown. The thickness-shear (TS) mode is located around 430 kHz. In Fig. 4.13 b) the electrical conductance of the shear wave transducer configuration with the backing layer is shown (analogue to the P-wave transducer configuration in Fig. 4.10).

As for the conductance of the P-wave transducer, the TS-mode for the Pz27 element inside the S-wave transducer is heavily dampened by the backing layer. In 4.13 c) the electrical conductance of the shear wave transducer configuration with the front layer is shown (analogue to the P-wave transducer configuration in Fig. 4.11). The thickness mode is split in two in the same way as for the P-wave transducers. In 4.13 d) the electrical conductance of the final shear wave transducer with the buffer attached is shown. The conductance measurements of the shear wave transducer are similar to the conductance measurements of the P-wave transducer. Thus there are assumed to be no major flaws in the shear wave transducers.

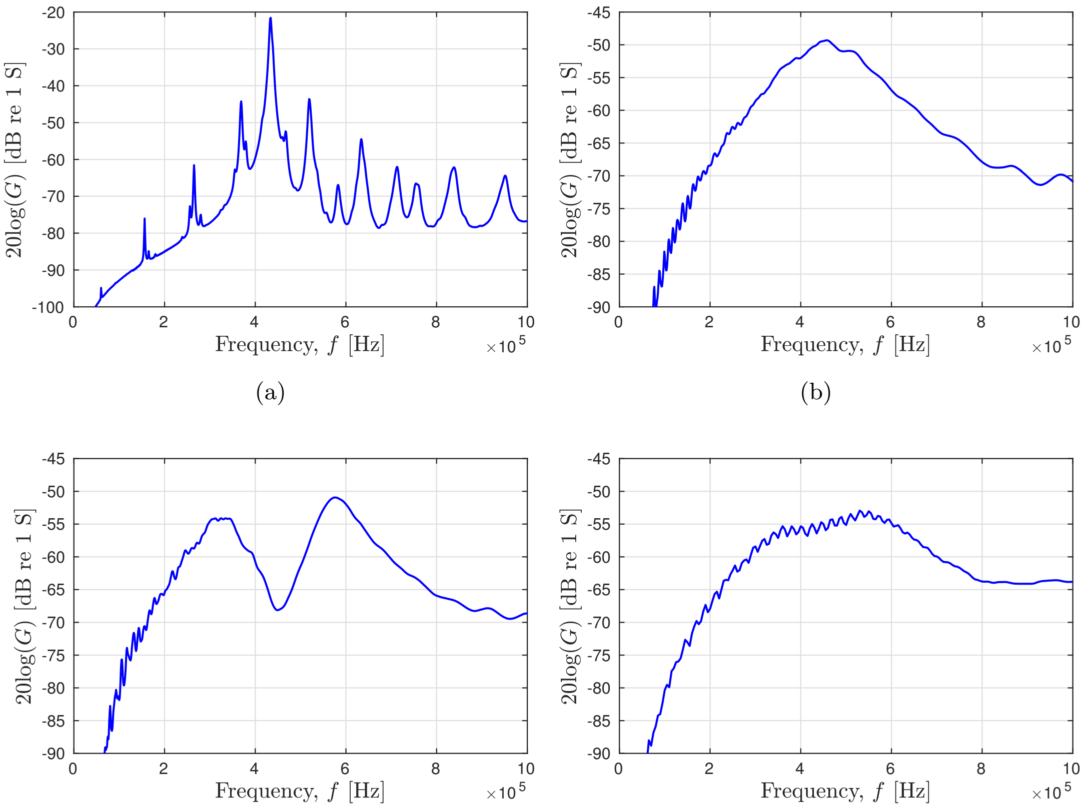

(a)

(b)

(c)

(d)

Figure 4.13: Measured electrical conductance of **a)** a 15 × 15 mm shear wave Pz27 piezoelectric element with 2.0 mm thickness, **b)** the transducer configuration with the backing layer added (analogue to the P-wave transducer configuration in Fig. 4.10), **c)** the transducer configuration with the backing layer and the front layer (analogue to the P-wave transducer configuration in Fig. 4.11), **d)** the final transducer with the buffer attached.

Chapter 5

Simulation setup for conductance simulations and simulation of the solid buffer method

Two different types of simulations are presented in this chapter. 1) Finite element modeling (FEM) is conducted to investigate the electrical conductance of the transducer using Comsol Multiphysics 4.2a [?]. By comparing the simulated electrical conductance with the measured electrical conductance presented in Sec. 4, potential flaws in the transducer construction may be discovered. The simulation setup for the electrical conductance of the P-wave transducer is presented in Sec. 5.1. The S-wave transducer has not been simulated due to lack of computing power. 2) Simulation of the solid buffer method with use of Comsol and Fourier synthesis is performed to investigate the effects of unwanted reflections in the solid buffer measurement setup. The results of the simulations are shown in Ch. 6. The simulation setup for the solid buffer method is presented in Sec. 5.2. A simulation example for the solid buffer method is given. A third set of simulations are the numerical models used to investigate attenuation mechanisms inside the Bentheim sandstones in Ch. 7. These numerical models are already presented in Ch. 2 and left out of this chapter.

5.1 Finite element simulations of the P-wave transducers using Comsol Multiphysics

The setup for the finite element simulations of the P-wave transducers using Comsol Multiphysics 4.2a [?] is presented here. The available material parameters and how to obtain a rough estimate for a full set of anisotropic material parameters for Pz37 is discussed.

5.1.1 Material parameters used in the finite element simulations

The mechanical properties of the materials used in the Comsol model are presented in Tab. 5.1. Many of these are already presented in Tab. 4.1. However, the shear wave Q-value (Q_S) is given here and is assumed to be equal to the compressional wave Q-value (Q_P) in the simulations. The values of c_P and c_S for plexiglas used in the Comsol simulations where measured at an early stage using the solid buffer method. The values measured using the immersion method in Tab. 4.1 where measured later and are assumed to be more accurate.

The Q-values of the elastic materials are implemented in the FE simulations by using complex wave velocities, $\hat{c}_S = c_S + i\frac{c_S}{2Q_S}$ and $\hat{c}_P = c_P + i\frac{c_P}{2Q_P}$ [200].

Table 5.1: Materials used in the FE-simulations.

Material	c_P [m/s]	c_S [m/s]	Q_P	Q_S	ρ [kg/m^3]
Backing layer	1600	800	13.5	13.5	7470
Front layer (F1)	1600	800	28.5	28.5	4590
Aluminum	6420	3040	500	500	2700
Plexiglas	2715	1358	63	63	1184
PVC	2380	1190	51	51	1380
Polyurothane	1760	345	14	14	1100

To do 3D finite element simulations a full set of the anisotropic piezoelectric material constants is needed. As mentioned in Ch. 4, the manufacturer of Pz37 does only provide a limited set of the piezoelectric material parameters [192], shown in Tab. 4.2. The parameters in Tab. 4.2 are used to calculate some of the Pz37 material parameters needed for the 3D finite element simulations [194]:

$$\begin{aligned}\epsilon_{33}^S &= (1-k_p^2)(1-k_t^2)\epsilon_0 K_{33}^T \\ c_{33}^E &= 4\rho N_p^2(1-k_t^2) \\ e_{33} &= k_t\sqrt{\epsilon_{33}^S 4\rho N_p^2}.\end{aligned} \tag{5.1}$$

c_{33}^E is the Pz37 stiffness constant at a constant electrical field in the thickness-direction (the directions are defined in the IEEE piezoelectric standard [194]). ϵ_{33}^S is the relative permittivity at constant strain in the thickness-direction. e_{33} is the piezoelectric constant in the 33-direction. To the best of this authors knowledge, a full set of anisotropic Pz37 material constants are not published. A full set of anisotropic Pz27 material parameters are presented in Tab. 4.3 and repeated in the first column in Tab. 5.2 [188, 193] and used as a basis to obtain a rough estimate of a full anisotropic set of Pz37 material parameters.

First the ratios of the Pz27 stiffness constants $\left(\frac{c_{11}^E}{c_{33}^E}\right)_{Pz27}$, $\left(\frac{c_{12}^E}{c_{33}^E}\right)_{Pz27}$, $\left(\frac{c_{13}^E}{c_{33}^E}\right)_{Pz27}$ and $\left(\frac{c_{44}^E}{c_{33}^E}\right)_{Pz27}$ are calculated. These ratios are assumed to be the same as the ratios for the Pz37 stiffness constants: $\left(\frac{c_{11}^E}{c_{33}^E}\right)_{Pz37}$, $\left(\frac{c_{12}^E}{c_{33}^E}\right)_{Pz37}$, $\left(\frac{c_{13}^E}{c_{33}^E}\right)_{Pz37}$ and $\left(\frac{c_{44}^E}{c_{33}^E}\right)_{Pz37}$. From this assumption the Pz37 material constants c_{11}^E, c_{12}^E, c_{13}^E and c_{44}^E are obtained. The listed Q_P-value of 50 is used for all the Pz37 stiffness constants.

The same technique is used on the other Pz37 material parameters as well. First the Pz27 ratios of the piezoelectric constants $\left(\frac{e_{31}}{e_{33}}\right)_{Pz27}$ and $\left(\frac{e_{15}}{e_{33}}\right)_{Pz27}$ are obtained. These ratios are assumed to be the same for the Pz37 piezoelectric constants $\left(\frac{e_{31}}{e_{33}}\right)_{Pz37}$ and $\left(\frac{e_{15}}{e_{33}}\right)_{Pz37}$. From this assumption the Pz37 piezoelectric constants e_{15} and e_{31} are obtained. ϵ_{11}^S for Pz37 is found in the same way as the stiffness and piezoelectric constants (assuming $\left(\frac{\epsilon_{11}^S}{\epsilon_{33}^S}\right)_{Pz27}=\left(\frac{\epsilon_{11}^S}{\epsilon_{33}^S}\right)_{Pz37}$). The Q-value for ϵ_{11}^S and ϵ_{33}^S are obtained by $Q_E = \frac{1}{\tan\delta}$. This value is used for all the Pz37 permittivity constants.

Table 5.2: Material constants for Pz27 [188, 193] and Pz37 (rough estimate).

Variable	Pz27	Pz37
$c_{11}^E[10^{10}\ \mathrm{N/m^2}]$	$12.025(1+i/96)$	$6(1+i/50)$
$c_{12}^E[10^{10}\ \mathrm{N/m^2}]$	$7.62(1+i/70)$	$3.8(1+i/50)$
$c_{13}^E[10^{10}\ \mathrm{N/m^2}]$	$7.42(1+i/120)$	$3.7(1+i/50)$
$c_{33}^E[10^{10}\ \mathrm{N/m^2}]$	$11.005(1+i/190)$	$5.3(1+i/50)$
$c_{44}^E[10^{10}\ \mathrm{N/m^2}]$	$2.11000(1+i/75)$	$1.03(1+i/50)$
$e_{31}[\ \mathrm{C/m^2}]$	$-5.4(1-i/166)$	-4
$e_{33}[\ \mathrm{C/m^2}]$	$17(1-i/324)$	11.3
$e_{15}[\ \mathrm{C/m^2}]$	$11.20(1-i/200)$	7
$\epsilon_{11}^S[10^{-9}\ \mathrm{F/m}]$	$8.11044(1-i/50)$	$5.75(1-i/59)$
$\epsilon_{33}^S[10^{-9}\ \mathrm{F/m}]$	$8.14585(1-i/130)$	$5.77(1-i/59)$
ρ [kg/m^3]	7700	6000
Q_p	-	50
$\tan\delta$	-	0.017

Using the ratio of Pz27 piezoelectric constants to calculate the anisotropic piezoelectric constants for Pz37 gives only a rough estimate. Deviations are seen between conductance measurements and simulations. However, by comparing the conductance measurements and simulations in Sec. 4.4 there is a fair agreement for the thickness mode of the transducer.

5.1.2 Conductance simulations of the P-wave transducers

An axisymmetric geometry is defined for the important stages of the transducer construction process (Figs. 5.1, 5.2 and 5.3). Comsol Multiphysics is used to simulate the electrical conductance of the important stages of the transducer construction. The simulation setup for the electrical conductance of the different stages of the transducers design is presented here.

The electrical conductance is obtained between the electrodes of the transducer. The Piezoelectric-Acoustics Module package is used without fluid-domains. Outside the the defined structure, there is vacuum. A frequency domain study is performed with the frequency range 50 kHz - 1.2 MHz and frequency resolution 2 kHz.

Second order, triangular elements are used to mesh the transducer structure. For all domains (piezoelectric and elastic), the mesh has minimum 10 elements/λ_P, where λ_P is defined as the compressional wavelength calculated using frequency 500 kHz and c_P =2715 m/s (compressional wave velocity of plexiglas). The piezoelectric disc is defined as a piezoelectric domain, and the rest are defined as elastic domains. A convergence test of the phase and magnitude of a received voltage signal indicates that 10 elements/wavelength is sufficient resolution (see Sec. 5.2.3). The simulated and measured electrical conductance of the P-wave transducer is presented in Ch. 4. A full 3D simulation is performed using the axisymmetric geometry.

The first simulation stage of the transducer design is the piezoelectric disc. The piezoelectric disc is shown in Fig. 5.1 b) with the symmetry-axis at r=0. The mesh of the axisymmetric FEM of the piezoelectric element is shown in Fig. 5.1 a). The piezoelectric disc is meshed in 2D from the symmetry axis to the outer edge of the disc. The axisymmetric solution in Comsol ensures that a full 3D solution of the problem shown in 5.1 a) is obtained. The meshed part is used in the axisymmetric FEM.

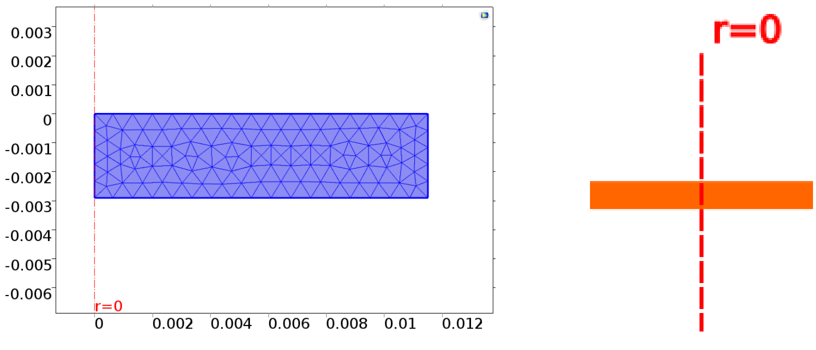

(a)

(b)

Figure 5.1: **a)**) Meshing of the axisymmetric finite element model of the Pz37 element. **b)** A schematic of the simulated Pz37 element.

The simulated transducer structures during the construction process are shown in Fig. 5.2. In Fig. 5.2 a), the piezoelectric element with the isolation and the housing is shown. In Fig. 5.2 b), the backing layer is added to the simulation model. In Fig. 5.2 c), the frontlayer is added to the simulation model and the. In Fig. 5.2 d), polyurethane potting material is added behind the backing layer. The final simulated P-wave transducer with the buffer attached is shown in Fig. 5.3. The symmetry axis is shown in the same way as for the piezoelectric disc in Fig. 5.1 b).

The mesh is obtained in all the transducer configurations in Figs. 5.2 and 5.3 in the same way as in Fig. 5.1 b): meshing the structure from the symmetry axis to the outer edge of the structure. Like above; for all domains (piezoelectric and elastic), the mesh has minimum 10 elements/λ_P. The mesh is not shown here. The dimensions of the transducer construction is presented in Fig. 4.1. These are used in the simulations as well. The silver paint electrode is left out in the simulations. The Pz37 material data used in the simulations are given in Tab. 5.2, the rest of the material parameters are given in Tab. 5.1. A 3D simulation of the S-wave transducers can not be performed with the 2D axisymmetric simulation setup and require more computing power than available. Simulations of the S-wave transducers have therefore not been performed.

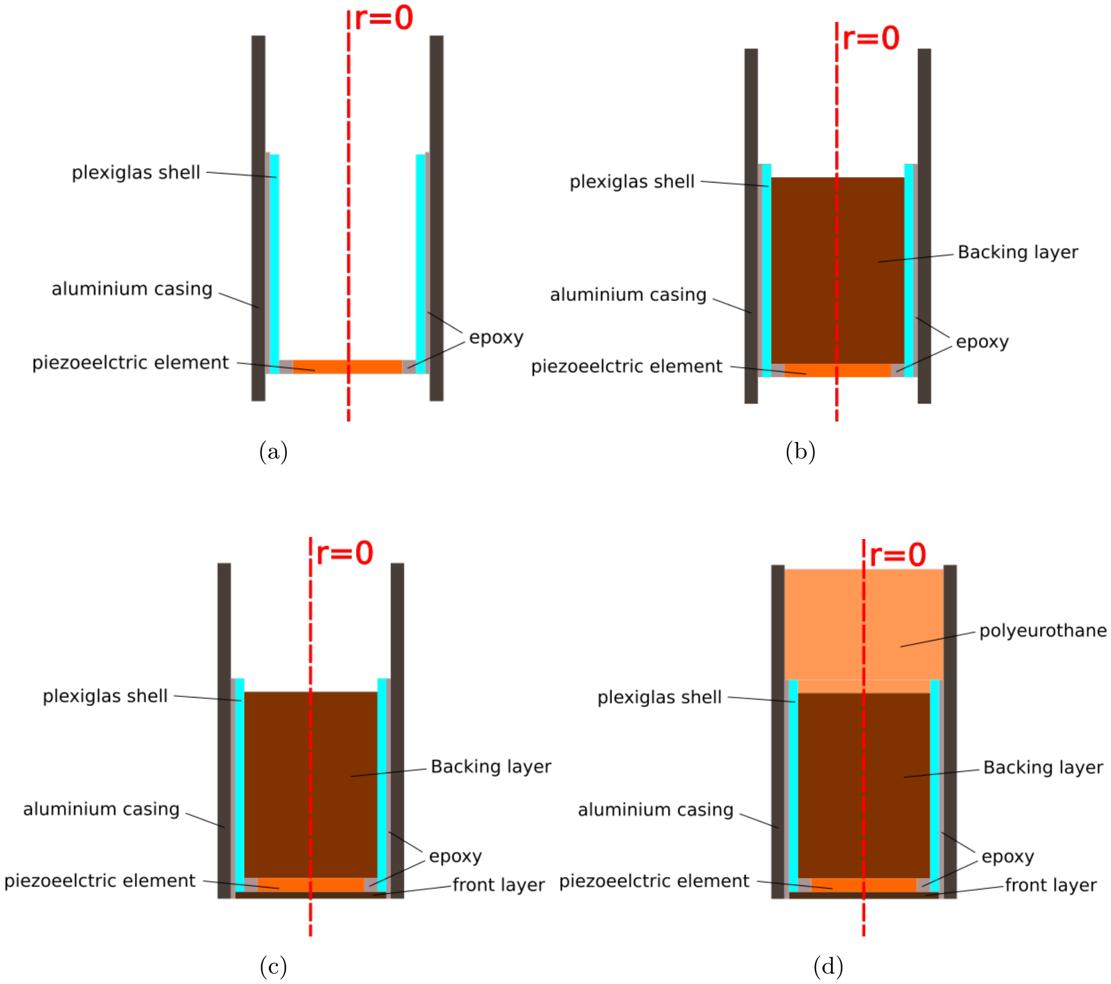

Figure 5.2: Schematics of simulated P-wave transducer configurations. **a)** Piezoelectric element with plexiglas insulation and aluminum casing glued on with epoxy. **b)** Transducer configuration a) with backinglayer attached. **c)** Transducer configuration b) with frontlayer. **d)** Transducer configuration c) with polyurethane as sealing material.

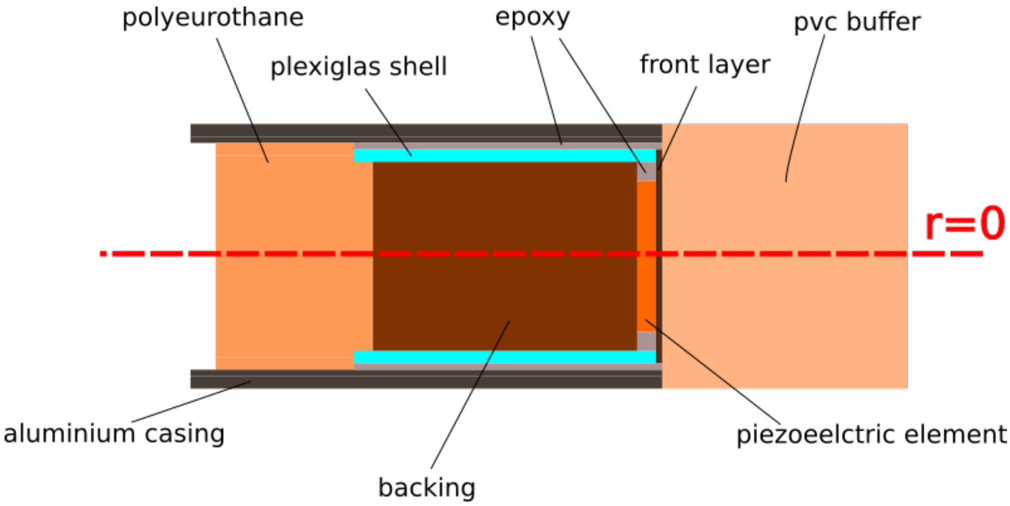

Figure 5.3: A schematic of the final simulated P-wave transducer.

5.2 Simulation of the solid buffer method

The solid buffer method is simulated by the use of finite element modeling and Fourier synthesis. These simulations are used to investigate the effects of unwanted reflections in the solid buffer measurement setup.

5.2.1 Equations for the simulated solid buffer method

The equation used for calculating c_P and α_P with the solid buffer method (Eq. (3.14)), depends on the input quantities $V_{7,A}$ and $V_{8,B}$, $V_{0,A}$ and $V_{0,B}$. Since no models for electrical equipment such as cables, signal generator, amplifiers etc. are used in this work, the equation for the solid buffer method is rewritten so that $V_{6,A}^{open}$ and $V_{7,B}^{open}$, $V_{2,A}$ and $V_{2,B}$ can be used instead. $V_{6,A}^{open}$ and $V_{7,B}^{open}$ are defined in Sec. 3.3.3. In this work, whenever measurement A is simulated, this is called "simulation A," and whenever measurement B is simulated, this is called "simulation B."

From the system model describing measurement A and B (Eqs. 3.6 and 3.7, respectively), $V_{7,A}$ and $V_{8,B}$ are defined as signals in the frequency domain propagating through the measurement system with no reflections from buffers or speimen. Thus it is assumed $\frac{V_{0,B}}{V_{0,A}} = \frac{V_{2,B}}{V_{2,A}}$ and $\frac{V_{8,B}}{V_{7,A}} = \frac{V_{7,B}^{open}}{V_{6,A}^{open}}$. With these assumptions, Eq. (3.14) is rewritten

$$\frac{V_{7,B}^{open}}{V_{6,A}^{open}} = \frac{V_{2,B} e^{-ik_m d} T_{B1} T_{B2} H_B^{dif}}{V_{2,A} H_A^{dif} T_A}. \tag{5.2}$$

$V_{6,A}^{open}$ and $V_{7,B}^{open}$ are the signals at the open circuit output terminals of the receiving transducer in simulation A and B, respectively, with no reflections from buffers or specimen present. In such a system, $V_{2,A}$ and $V_{2,B}$ are the electrical signals across the electrodes of the piezoelectric element of the transmitting transducer in simulation A and B, respectively, with no reflections from buffers or specimen. For each frequency step in the Comsol simulations, $V_{2,Ar}$ and $V_{2,Br}$ are predefined by the user and $\frac{V_{6,Ar}^{open}}{V_{2,Ar}}$ and $\frac{V_{7,Br}^{open}}{V_{2,Br}}$ are obtained directly from the simulations. By doing the isolation process described in Sec. 3.5.2, simulations of $\frac{V_{6,A}^{open}}{V_{2,A}}$ and $\frac{V_{7,B}^{open}}{V_{2,B}}$ may be obtained.

Simulation of the solid buffer method using voltage to voltage transfer functions

$\frac{V_{6,A}^{open}}{V_{2,A}}$ and $\frac{V_{7,B}^{open}}{V_{2,B}}$ may be obtained through five steps:

1. Obtaining the transfer functions from Comsol: $H_{26,Ar}^{VV,open} = \frac{V_{6,Ar}^{open}}{V_{2,Ar}}$ and $H_{27,Br}^{VV,open} = \frac{V_{7,Br}^{open}}{V_{2,Br}}$ in simulation A and simulation B, respectively (Eq. (3.5)).
2. Defining $V_{2,Ar}$ and $V_{2,Br}$ as the frequency spectrum of a short pulse. Thus $V_{2,Ar} = V_{2,A}$ and $V_{2,Br} = V_{2,B}$. Obtaining $V_{6,Ar}^{open}$ and $V_{7,Br}^{open}$ by multiplying the transfer functions in (1) with $V_{2,A}$ and $V_{2,B}$, respectively.
3. Obtaining time domain signal trace, $V(t)_{6,Ar}^{open}$ and $V(t)_{7,Br}^{open}$ with Fourier synthesis. These are the full traces of the simulated time signals in simulation A and B, respectively.
4. Isolating the pulse traveling directly from the transmitter to the receiver, $V(t)_{6,A}^{open}$ and $V(t)_{7,B}^{open}$ from $V(t)_{6,Ar}^{open}$ and $V(t)_{7,Br}^{open}$, respectively.
5. Taking the discrete Fourier transform of $V(t)_{6,A}^{open}$ and $V(t)_{7,B}^{open}$ to obtain $V_{6,A}^{open}$ and $V_{7,B}^{open}$.

Now, $V_{6,A}^{open}$ and $V_{7,B}^{open}$ are the simulated voltage signals, resulting from the input signals, $V_{2,A}$ and $V_{2,B}$ in simulation A and B, respectively. $V_{6,A}^{open}$, $V_{7,B}^{open}$ $V_{2,A}$ and $V_{2,B}$ are used in Eqs. (3.50) and (3.51) instead of $V_{7,A}$, $V_{8,B}$, $V_{0,A}$ and $V_{0,B}$, respectively.

Simulation of the solid buffer method using a baffled piston as transmitter and the buffers approximated with synthetic "fluid-buffers"

The diffraction corrections (Eq. (2.8)) used in this work are originally developed for fluids [79]. To investigate how well the proposed diffraction corrections correct for diffraction effects in a solid, the solid buffer method is simulated using synthetic fluids as buffers and specimen. The buffers and the specimen are modeled as inviscid fluids and have c_P and

Q_P equal to that of PVC and plexiglas, respectively. The fluid-buffers are wide enough so that no reflections are interfereing with the direct pulse. The transmitting transducer is modeled as a circular, uniformly vibrating, piston mounted in an infinite, rigid baffle. The receiver is modeled as the average free-field pressure over a measurement area equal to the receiving transducer (see Fig. 5.4).

The transfer functions obtained with Comsol are now $\frac{\langle P_A \rangle}{v_A^z}$ and $\frac{\langle P_B \rangle}{v_B^z}$ for simulation A and B, respectively. $\langle P_A \rangle$ and $\langle P_B \rangle$ are the average free-field "pressure" in the synthetic fluid buffer over the measurement area in Fig. 5.4. v_A^z and v_B^z are the piston velocities in the z-direction in simulation A and B, respectively. By assuming $\frac{V_{7,B}^{open}}{V_{6,A}^{open}} = \frac{\langle P_B \rangle}{\langle P_A \rangle}$ and $\frac{v_B}{v_A} = \frac{V_{2,B}}{V_{2,A}}$ the "solid buffer method" may be expressed:

$$\frac{\langle P_B \rangle}{\langle P_A \rangle} = \frac{v_B^z e^{-ik_m d} T_{B1} T_{B2} H_B^{dif}}{v_A^z H_A^{dif} T_A}. \tag{5.3}$$

The five steps listed above can now also be used for the "solid buffer method" defined here with synthetic fluids. However, $\langle P_A \rangle$ and $\langle P_B \rangle$ are used instead of $V_{6,A}^{open}$ and $V_{7,B}^{open}$, respectively. v_A^z and v_B^z are used instead of $V_{2,A}$ and $V_{2,B}$, respectively.

In the following, the simulation setup for four different solid buffer methods are presented. In three of them, the transfer functions $\frac{V_{6,A}^{open}}{V_{2,A}}$ and $\frac{V_{7,B}^{open}}{V_{2,B}}$ for simulation A and simulation B are obtained and Eq. (5.2) is used. In the fourth, a baffled piston has been used to model the transmitting transducer. The transfer functions $\frac{\langle P_A \rangle}{v_A^z}$ and $\frac{\langle P_B \rangle}{v_B^z}$ are obtained and Eq. (5.3) is used to calculate c_P and α_P.

5.2.2 Simulation setup for the solid buffer method

By simulating the solid buffer method with solid buffers and synthetic fluid buffers of different widths, the effect of the buffer sidewall reflections and diffraction effects are analyzed. In the same way as for the conductance simulations above, axisymmetric geometries are defined to describe the simulated solid buffer method. Four different simulations of the solid buffer method are conducted: Simulation 1: solid buffer method with wide synthetic fluid PVC buffers and a baffled piston as source. The receiver is sensitive to the average free-field "pressure" in the buffers over the measurement area (Fig. 5.4). Simulation 2: solid buffer method with wide synthetic fluid buffers (Fig. 5.5) with piezoelectric transducers as source and receiver. Simulation 3: solid buffer method with with wide elastic buffers (Fig. 5.6) with piezoelectric transducers as source and receiver. Simulation 4: solid buffer method with with narrow elastic buffers (Fig. 5.7) with piezoelectric transducers as source and receiver. The synthetic PVC fluid buffers have a complex c_P with the imaginary part corresponding to Q_P. The elastic PVC buffers have a complex c_P and c_S with the imaginary part corresponding to Q_P and Q_S, respectively (see Tab. 5.1 for material data). The synthetic fluid plexiglas specimen have a complex c_P with the imaginary part corresponding to Q_P. The elastic plexiglas specimen have a complex c_P and c_S with the imaginary part corresponding to Q_P and Q_S, respectively (see Tab. 5.1 for material data).

Comsol Multiphysics version 4.2a is used to solve the wave equations 2.12, 2.9 and 2.14 for the elastic, piezoelectric and fluid domains for the axisymmetric problems shown in Figs. 5.4-5.7. In the figures, a symmetry-line at r=0 is defined in the same way as for the electrical conductance simulation in Fig. 5.1. The Piezoelectric-Acoustics Module package is used. A frequency domain study is performed with the frequency range 50 kHz - 1.2 MHz with a frequency resolution 2 kHz. The mesh is defined in the same way as for the conductance simulations presented in Sec. 5.1.2.

In simulation 1, a baffled piston with diameter 23 mm is modeled by a prescribed velocity in the z-direction at a line segment 23 mm long (see Fig. 5.4). The buffers are wide enough so that potential sidewall reflections do not interfere with the direct signal. As the diffraction correction in this work is described in a fluid with a baffled piston as the source, this simulation is supposed to simulate the exact compressional wave velocity and compressional wave Q-factor. The velocity to pressure transfer functions $\frac{\langle P_A \rangle}{v_A^z}$ and $\frac{\langle P_B \rangle}{v_B^z}$ are simulated in simulation A and B, respectively. In this simulation the buffers and the specimen are defined as synthetic fluids, and modeled as fluid domains. The buffers have length 34 mm and diameter 18 cm. The specimen has length 60 mm and diameter 18 cm. Simulation 1-4 are presented and discussed in Sec. 6.1.

Simulation model 2 (Fig. 5.5) has the same simulation setup as simulation 1, except that the source is now the piezoelectric transducer shown in Fig. 5.2 c). The voltage to voltage transfer functions $\frac{V_{6,Ar}^{open}}{V_{2,Ar}}$ and $\frac{V_{7,Br}^{open}}{V_{2,Br}}$ (Eq. (3.5)) are simulated. The user is free to define $V_{2,Ar}$ or $V_{2,Br}$ on the input terminal of the transducer, thus the transmitting transducer is exited with a prescribed voltage at the input terminals. The received signal is retrieved on the output terminal of the receiving transducer. The use of the baffled piston diffraction correction model to describe the diffraction of the transducer can be analyzed by comparing simulation 1 and 2.

Simulation 3 (Fig. 5.6) is the same as simulation 2, except from that the buffers and specimen are now modeled as elastic domains. The voltage to voltage transfer functions $\frac{V_{6,Ar}^{open}}{V_{2,Ar}}$ and $\frac{V_{7,Br}^{open}}{V_{2,Br}}$ are simulated. Simulation 2 where the buffers are modeled with elastic domains should give approximately the same results as simulation 3, where the buffers are modeled as fluid domains for the proposed diffraction correction to be valid in elastic materials.

In simulation 4 (Fig. 5.7) the solid buffer method presented in Ch. 3 is simulated. This is the same simulation setup as simulation 3, but the specimen and buffers have the same dimensions as in the real measurement setup. Again the voltage to voltage transfer functions $\frac{V_{6,Ar}^{open}}{V_{2,Ar}}$ and $\frac{V_{7,Br}^{open}}{V_{2,Br}}$ are simulated. The transducer with buffers is presented in Fig. 5.3. The specimen have diameter 50 mm and length 60 mm. By comparing simulation 4 with simulation 1-3, the effect of unwanted sidewall reflections in the buffers and diffraction effects can be investigated.

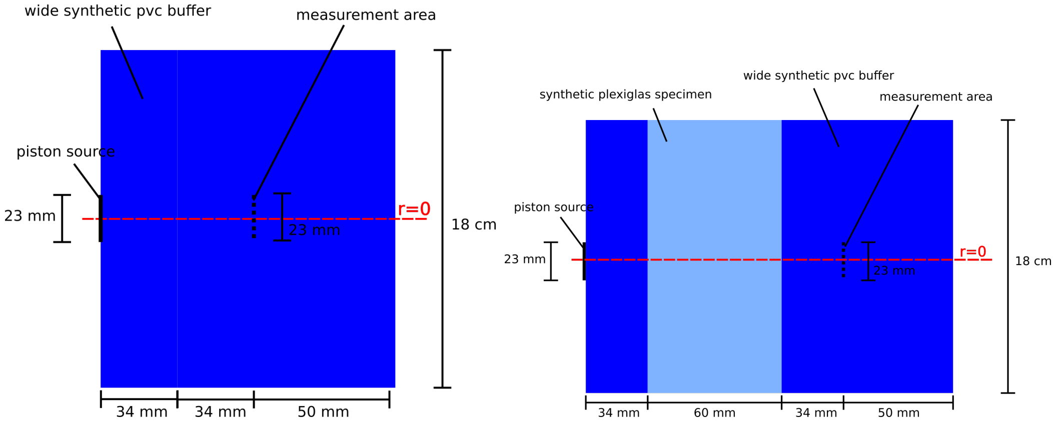

(a) (b)

Figure 5.4: Simulation 1. **a)**) Simulation 1 A. **b)** Simulation 1 B (with the specimen present).

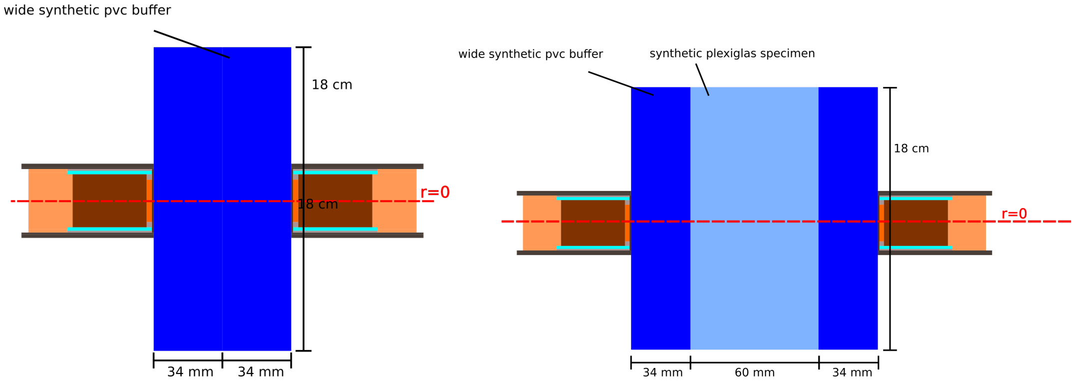

(a) (b)

Figure 5.5: Simulation 2. **a)**) Simulation 2 A. **b)** Simulation 2 B (with the specimen present).

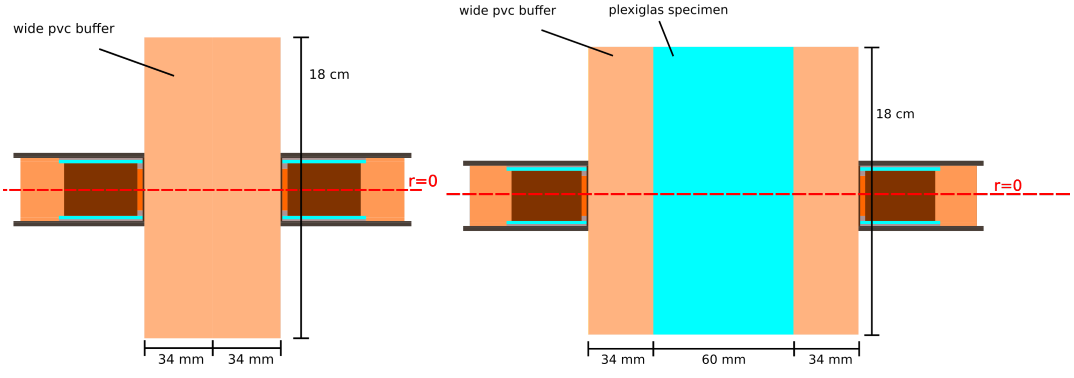

(a) (b)

Figure 5.6: Simulation 3. **a)**) Simulation 3 A. **b)** Simulation 3 B (with the specimen present).

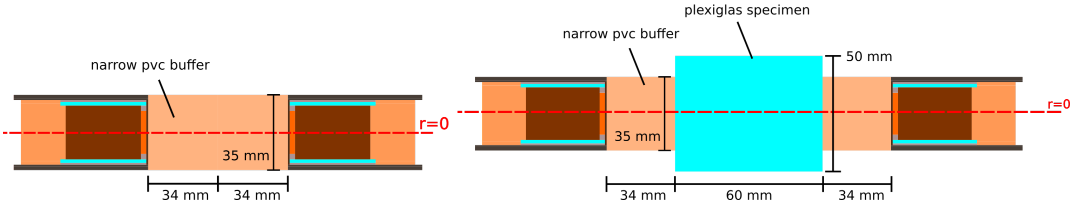

(a) (b)

Figure 5.7: Simulation 4. **a)**) Simulation 4 A. **b)** Simulation 4 B (with the specimen present).

5.2.3 Convergence

A brief study of the convergence in the Comsol simulations with respect to the grid mesh is conducted. In Fig. 5.8, the results of simulation 4B (Fig. 5.7 b)) is presented at 500 kHz for different elements/λ_P (calculated for 500 kHz and c_P=2715 m/s). In a), the magnitude of the voltage across the electrodes of the receiving transducer is plotted and in b) the phase of the voltage across the electrodes of the receiving transducer is plotted. Assuming that elements/λ_P = 30 is correct, the deviation in magnitude from the "correct" value at 10 elements/λ_P is less than 1.3 %. The deviation in the phase from 30 to 10 elements/λ_P is maximum 0.02 rad. This corresponds to a transit time of approximately 6 ns which gives a difference in c_P less than 1 m/s using the solid buffer method with the basic pulse method (Eq. (3.18)).

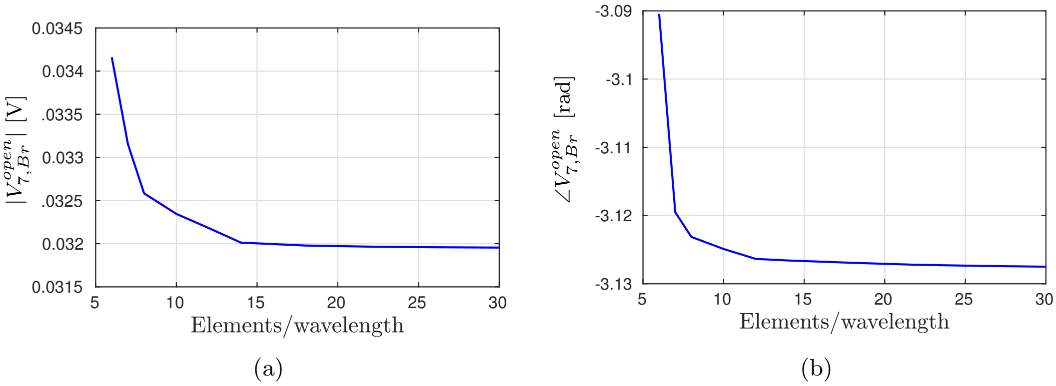

Figure 5.8: Convergence test for the mesh in the Comsol simulations for different elements/wavelength (or elements/λ_P). Simulation 4B is used (Fig. 5.7 b)). **a)** Shows the magnitude of the voltage across the electrodes of the receiving transducer. **b)** Shows the phase angle of the voltage across the electrodes of the receiving transducer.

The electrical conductance simulation results presented in Fig. 4.8 for the Pz37 element have been found to agree with simulations conducted with another finite element simulation program FEMP [201]. The electrical conductance simulation result from the two finite element simulation programs, FEMP and Comsol, was indistinguishable ($<$ 0.1%). The FEMP simulation setup apart from the Pz37 material constants is described by Aanes [193].

5.2.4 Fourier synthesis example

The five step (Sec. 5.2.1) procedure of simulating the solid buffer method (simulation 4) is shown here. In step 1, the transfer functions $H(f)_{26,Ar}^{VV,open}$ and $H(f)_{27,Br}^{VV,open}$ are obtained (Fig. 5.9). They have a frequency resolution, Δf =2 kHz, and a frequency range 2 kHz - 1.2 MHz. The sampling frequency, F_s, is set to 50 MHz (100 samples/period at 500 kHz) and the transfer functions from 0 Hz to F_s = 50 MHz are obtained by zeropadding. The transfer functions from Comsol are first zeropadded from 1.2 MHz to $F_s/2$. The transfer function spectrum from frequencies $F_s/2$ to $F_s - \Delta f$ is the complex conjugate of the transfer function spectra from $F_s/2$ to 0 (Fig. 5.9) [155].

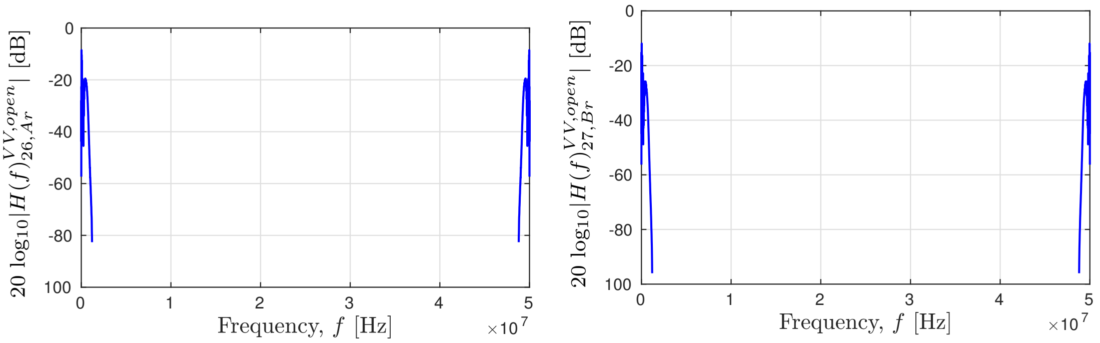

(a) (b)

Figure 5.9: Padded transfer functions from Comsol. **a)** Simulation A, $H^{VV,open}_{26,Ar}(f)$. **b)** Simulation B, $H^{VV,open}_{27,Br}(f)$.

In step 2, $V^{open}_{6,Ar}$ and $V^{open}_{7,Br}$ (Fig. 5.11) are obtained by multiplying the transfer functions, $H^{VV,open}_{26,Ar}$ and $H^{VV,open}_{27,Br}$ (Fig. 5.9), with V_2 (magnitude of V_2 shown in Fig. 5.10 b)). In the simulations, the same input signal is used in simulation A and B. $V_2(t)$ is a short, zeropadded pulse with $F_s = 50$ MHz and length 500 µs (25 000 samples, Fig. 5.10 a)). The frequency components of this short pulse (with $\Delta f = 2$ kHz) do not contain any reflections, thus $V_{2,Ar} = V_{2,Br} = V_2$.

Because the user is free to define V_2 and only the transfer functions $\frac{V^{open}_{6,A}}{V_{2,A}}$ and $\frac{V^{open}_{7,B}}{V_{2,B}}$ are needed in Eq. (5.2) to find c_P and α_P, no Thevenin circuit is needed to describe the signal from the signal generator in this work.

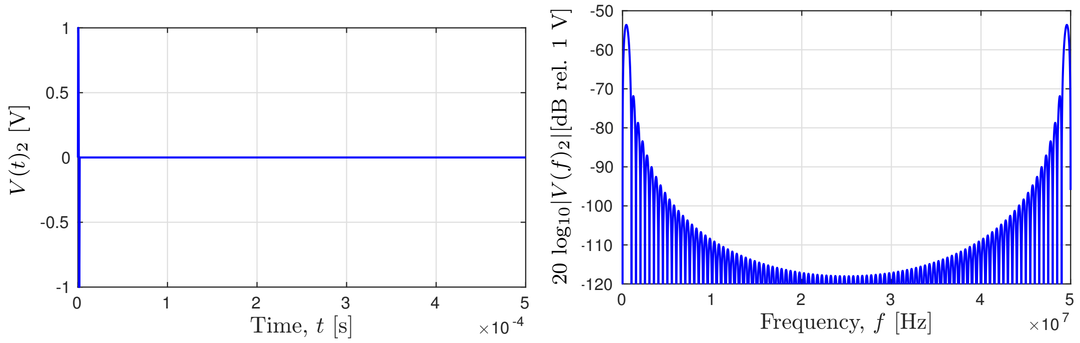

(a) (b)

Figure 5.10: Input signal on the transmitting transducer. **a)** Zeropadded input signal $V(t)_2$. **b)** Magnitude of input signal, $V(f)_2$.

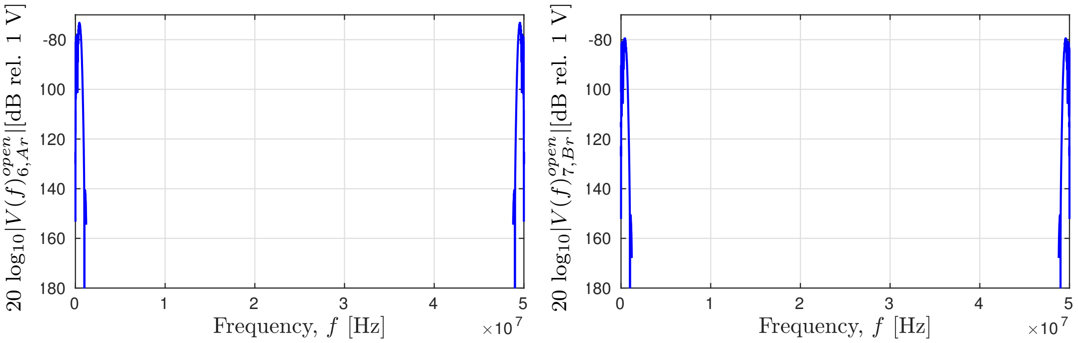

(a) (b)

Figure 5.11: Magnitude of the received signals. **a)** $V(f)_{6,Ar}^{open}$, **b)** $V(f)_{7,Br}^{open}$.

In step 3, $V(t)_{6,Ar}^{open}$ and $V(t)_{7,Br}^{open}$ (Fig. 5.12) are obtained by taking the inverse DFT of $V(f)_{6,Ar}^{open}$ and $V(f)_{7,Br}^{open}$ (Fig. 5.11), respectively.

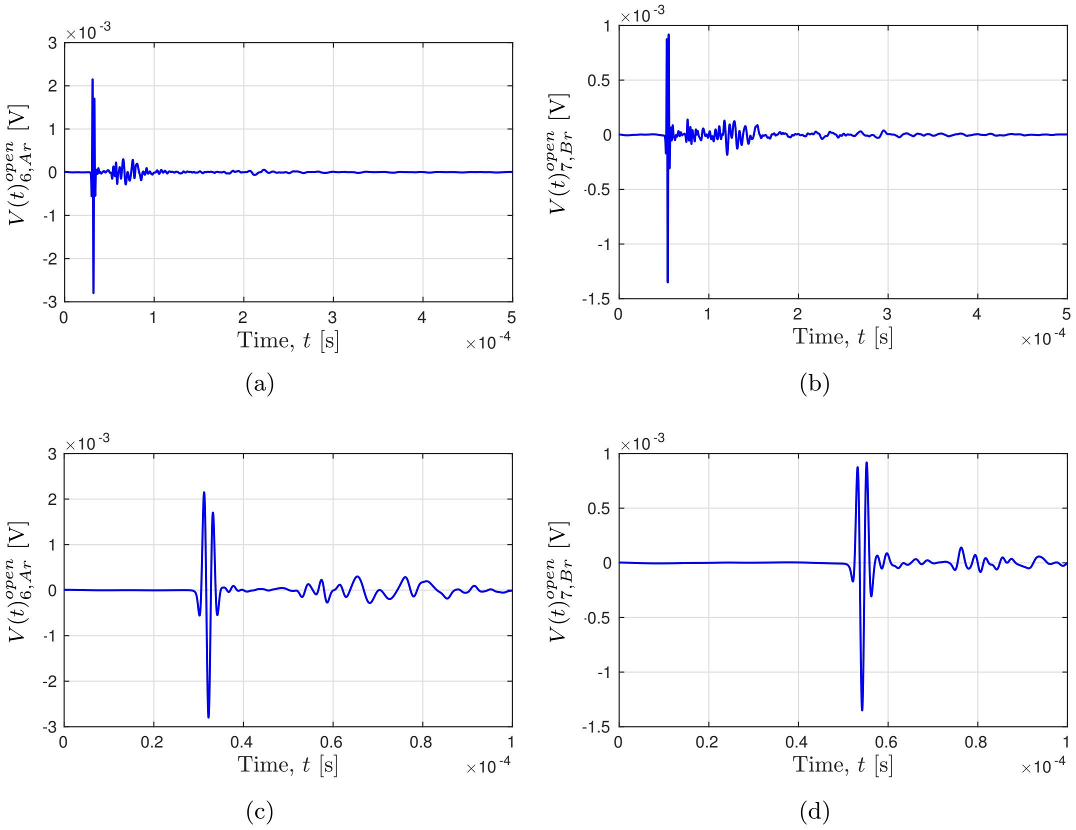

Figure 5.12: Received time domain signal on receiving transducer. **a)** $V(t)_{6,Ar}^{open}$, **b)** $V(t)_{7,Br}^{open}$, **c)** zoomed $V(t)_{6,Ar}^{open}$, **d)** zoomed $V(t)_{7,Br}^{open}$.

In step 4, the main signal seen Fig. 5.12 c) and d) are isolated and zeropadded as described in the isolation process in Sec. 3.5.2. From this process the signals containing no reflections, $V(t)_{6,A}^{open}$ and $V(t)_{7,B}^{open}$ are obtained.

In step 5, the DFT of the isolated signals $V(t)_{6,A}^{open}$ and $V(t)_{7,B}^{open}$ are taken so that the solid buffer Fourier spectrum method can be used to calculate c_P and α_P, using Eqs. (3.50) and (3.51). Due to folding, echoes or other reflections arriving later than the time trace shown in Fig. 5.12 a) and b), will be folded into the time window. By examining the time trace in Fig. 5.12 a) and b), there is no signal towards 500 µs. It is thus assumed that errors due to folding are minimal. The simulation results for plexiglas specimen are presented in Ch. 6 and compared with measurements to consider the accuracy of the solid buffer method used inside the pressure cell.

Chapter 6

On the accuracy of the solid buffer method for use inside the pressure cell

The accuracy of the measurements conducted with the solid buffer method inside the pressure cell is considered. To do this, compressional and shear wave measurements with the solid buffer method are compared with compressional and shear wave measurements using the immersion method. Measurements conducted with the P-wave and S-wave transducers are treated separately. Simulations of the solid buffer method (presented in Sec. 5.2) using the P-wave transducers are used to investigate the effects of diffraction of sound waves and sidewall reflections in the buffers and specimen. The simulations are compared with plexiglas measurements. In the hydrate experiments in Ch. 7, both the P-wave and the S-wave transducers are used.

In Sec. 6.1, c_P and α_P for plexiglas specimen are measured with both the immersion method and the solid buffer method using P-wave transducers. The solid buffer method is simulated to investigate the effects of diffraction of sound waves and unwanted reflections from the sidewalls (described in Ch. 5). The accuracy of c_P and α_P- measurements using the P-wave transducers is considered based on the simulations and comparing the solid buffer method with the immersion method. c_P obtained with the Fourier spectrum method is also compared with c_P obtained with the basic pulse method for confidence in the Fourier spectrum method. The effect on c_P and α_P- measurements for Bentheim sandstones due to the torque exerted on the transducers and the pressure exerted on the sandstones due to the confining sleeve is commented. The presented sensitivity analysis on the measured c_P using the solid buffer method gives an estimate of the combined sensitivity due to the listed uncertainty contributions, $\Delta c_P^{sens} \approx 12$ m/s.

In Sec. 6.2, c_P and α_P for plexiglas measured with the solid buffer method using S-wave transducers are presented. c_P and α_P measured with the S-wave transducers are compared with measurements using the immersion method and measurements using the solid buffer method with the P-wave transducers. The difference in the measured c_P using the S-wave transducers and the immersion method is estimated to be $\Delta c_P^{compare} \approx$ 60 m/s.

In Sec. 6.3, c_S for plexiglas specimen is measured and compared with c_S measured with the immersion method. The difference in the measured c_S from the methods is estimated to be $\Delta c_S^{compare} \approx 60$ m/s.

6.1 On the accuracy of the solid buffer method using the P-wave transducers

The accuracy of the measurements conducted with the solid buffer method using P-wave transducers inside the pressure cell is considered. To do this, c_P and α_P for plexiglas specimen are measured with the solid buffer method (Sec. 3.3.4) and compared with measurements conducted with the immersion method (Sec. 3.4.3). To investigate the effect of unwanted sidewall reflections and diffraction effects, the results are compared with simulations of c_P and α_P using the solid buffer method (the simulation setup is described in Sec. 5.2.2).

In the derivation of the solid buffer Fourier spectrum method (Eq. (3.50) and Eq. 3.51), it is assumed that $V_{7,A}$ and $V_{8,B}$ contain no unwanted sidewall reflections and that the electrical and transducer transfer functions cancel out in Eq. (3.13). It is assumed that the transducers, buffers and specimen surfaces in contact with each other are plane and aligned so that the specimen can precisely be defined with a length d and the buffers with a length x. The diffraction correction is assumed to be described with Eq. (2.8). The phase of the plane wave transmission coefficients are assumed to be zero. Any uncertainties in the components in Eqs. (3.50) and (3.51), or any deviation from the assumption listed above will contribute to the uncertainty in c_P and α_P-measurements.

In the following, measurements and simulations are conducted to investigate and consider the accuracy of the solid buffer method used inside the pressure cell.

6.1.1 Simulations of c_P and α_P in plexiglas using the solid buffer method

To investigate how diffraction effects and unwanted acoustic reflections affect the measurements, the solid buffer method is simulated as described in Sec. 5.2. The acquired time signals in measurement A and B in the solid buffer method are simulated. c_P and

α_P in plexiglas are input values in the simulations, and are thus known. The acoustic reflections from the buffer-sidewalls are investigated by using buffers of different widths. Diffraction effects are investigated by comparing simulations where a piezoelectric transducers are used with simulations where a baffled piston is used as the transmitter. The main goal in this subsection is to indicate an uncertainty in the simulated c_P and α_P due to diffraction effects and sidewall reflections. These uncertainties are labeled Δc_P^{refl}, $\Delta \alpha_P^{refl}$, Δc_P^{dif} and $\Delta \alpha_P^{dif}$ and are also assumed to be valid for the plexiglas measurements presented in Sec. 6.1.2.

As detailed in Sec. 5.2, transfer functions representing measurement A and B are obtained by FE-simulations and the time-domain signals are obtained by using Fourier synthesis. These time-domain pulses are used with the Fourier spectrum method and the basic pulse method to calculate c_P and α_P. Four different simulations are performed. Simulation 1 (Fig. 5.4) is an idealized model where no unwanted acoustic reflections from sidewalls are present due to wide buffers. The buffers are modeled as fluids and the transmitting transducer is modeled as a baffled piston with radius equal to the piezoelectric element. The receiver is modeled as the average free-field pressure over a measurement area equal to the receiving transducer and the diffraction Rogers and Buren's diffraction correction model [79] is assumed to be accurate. Simulation 2 use the same buffers and specimen as simulation 1, however, the transmitter and receiver are modeled with the P-wave piezoelectric transducers (see Fig. 5.5). Simulation 3 use the same transducers and dimensions as simulation 2, however, the fluid buffers are replaced with elastic buffers (see Fig. 5.6). In simulation 4, the solid buffer method, with realistic dimensions is simulated (see Fig. 5.7).

By stepwise simulating c_P and α_P for the four simulation models listed above, the effect of acoustic reflections from buffer sidewalls and the validity of Rogers and Buren's diffraction correction model are investigated.

Simulation 1

In simulation 1, the transmitting transducer is simulated as a baffled piston (piston mounted in an infinite, rigid baffle) with radius 11.5 mm (radius of the piezoelectric element) and the receiver is sensitive to the average pressure over a measurement area the same size of the transducer. The buffers and specimen are modeled as "synthetic fluids", that is inviscid fluids having c_P and α_P equal to the buffers and the specimen. The simulation setup is presented in Fig. 5.4 in Sec. 5.2.2. The schematic of simulation 1 is repeated in Fig. 6.1. The transfer functions $\frac{\langle P_A \rangle}{v_A^z}$ and $\frac{\langle P_B \rangle}{v_B^z}$ defined in Sec. 5.2.2 are simulated for measurement A and B, respectively. The piston oscillates with a particle velocity amplitude $-i\omega U_0$ where $U_0 = 1$ nm is the displacement amplitude.

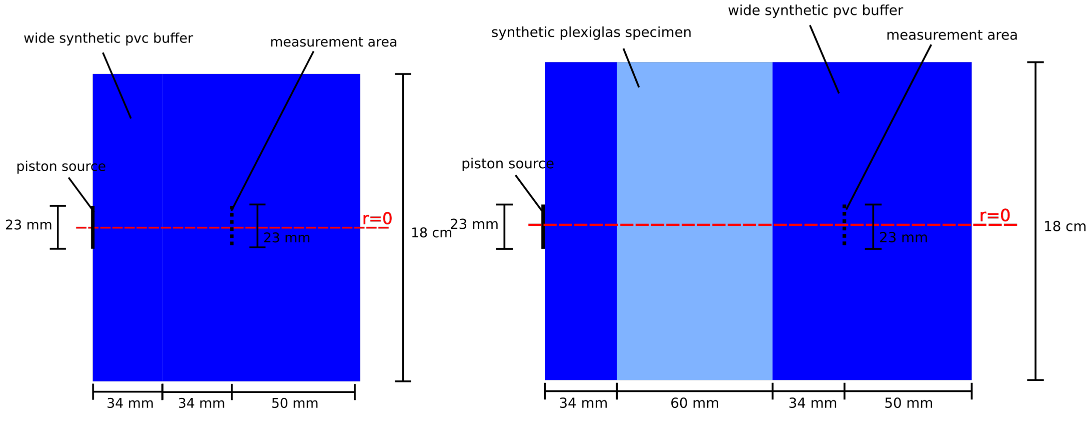

(a)

(b)

Figure 6.1: Simulation 1: Wide synthetic fluid buffers and a baffled piston as the transmitting transducer (same as Fig. 5.4). **a)**) Simulation of measurement A. **b)** Simulation of measurement B.

The synthetic fluid-buffers have diameter 18 cm and length 34 mm. The specimen have diameter 18 cm and length 60 mm. c_P and α_P are expressed with a complex $\hat{c}_P = c_P + i\frac{c_P}{2Q_P}$, where $Q_P = \frac{\omega}{2\alpha_P c_P}$. From Tab. 5.1, $c_P = 2380$ m/s and $Q_P = 51$ for PVC and $c_P = 2715$ m/s and $Q_P = 63$ for plexiglas. α_P due to $Q_P = 63$ is 0.4 dB/cm at 250 kHz and 0.8 dB/cm at 500 kHz.

By geometrical considerations, the first potential reflections from the specimen sidewalls arrive 15-20 periods after the first arrival of the direct pulse in simulation B. Thus, no sidewall reflections are assumed to interfere with the signals when simulating c_P and α_P.

In the simulations, c_P and α_P are known from the input parameters. The diffraction correction model of Rogers and Buren is based on the same setup as the simulation 1: A baffled piston radiating into a fluid of infinite extent (no unwanted reflections interfering with the signal). Thus, the use of the baffled piston diffraction correction model should therefore accurately correct for the diffraction effects in simulation 1.

In Figs. 6.2 a) and b), the simulated α_P and c_P are obtained using simulation 1 (Fig. 5.4) using the Fourier spectrum method. A 1 cycle 500 kHz pulse with displacement amplitude 1 nm is used. The simulation procedure is detailed in Sec. 5.2.2. In c) the simulated c_P is obtained using the basic pulse method. After the sine signals have been simulated, the basic pulse method is used in the same way as described in Sec. 3.5.1. For the basic pulse method a 10 cycles, 500 kHz tone burst is used.

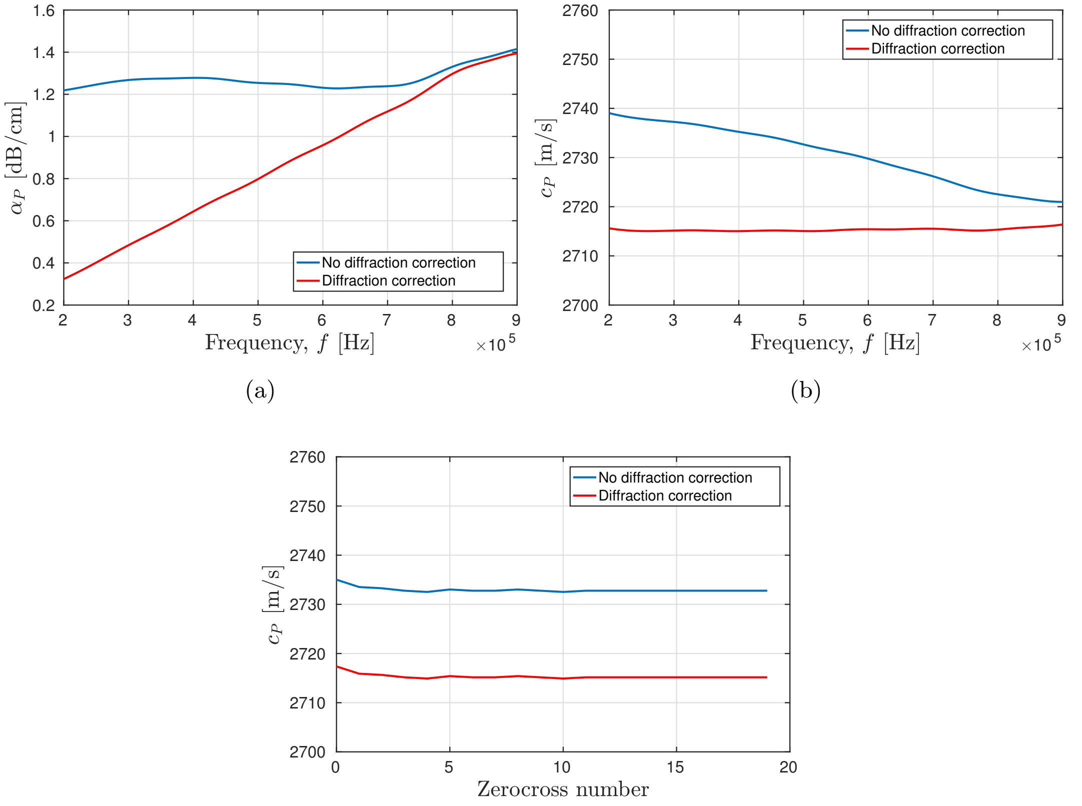

(a) (b)

(c)

Figure 6.2: Simulation of c_P and α_P using the solid buffer method with the transmitter modeled as a baffled piston and the the buffers modeled as wide fluid-buffers (simulation 1). **a)**) α_P using the Fourier spectrum method. **b)** c_P using the Fourier spectrum method. **c)** c_P using the basic pulse method with a 10 cycles, 500 kHz toneburst.

Using the proposed diffraction correction model [79], a close to exact agreement is found between the input parameters of the FE-simulation and c_P and α_P obtained using simulation 1 (red curve). Only a small deviation is seen at high frequencies for the Fourier spectrum method. These might be due to aliasing effects (described in Sec. 3.5.2, Fig. 3.26). For the basic pulse method, there is a small deviation for early zero-crosses. As higher frequencies components are more protruding in the early features of the received signal [49] the same potential aliasing effects seen in Fig. 6.2 b) may be present in the basic pulse method shown in Fig. 6.2 b). However, in this work, acoustic properties within the bandwidth 300 - 620 kHz are of main interest. For the ble curve labeled ”no diffraction correction” in Fig. 6.2, $H_A^{dif} = H_B^{dif}$. The blue curve clearly overestimates α_P and c_P, giving strong indications that $H_A^{dif} \neg H_B^{dif}$. The close agreement between the simulated c_P and α_P with the input parameters (red curve) gives confidence in the FE-simulations and the signal processing methods used to obtain c_P and α_P. It also indicates that the diffraction correction model detailed in Sec. 2.3 is describing diffraction effects properly for simulation 1.

Simulation 2

Simulation 2 uses the same buffers and specimen as simulation 1, however, in simulation 2, the transmitter and receiver are modeled with piezoelectric transducers (presented in Sec. 5.1). The dimensions of the transducer is presented in Fig. 4.12. Due to the wide buffers with diameter 18 cm used in simulation 2 (see Sec. 5.2), there are assumed to be no unwanted reflections in the simulations. However, the diffraction can no longer be expected to accurately be described with Rogers and Buren's diffraction correction model, which is based on the use of a baffled piston as the transmitting transducer. The simulation setup is presented in Sec. 5.2.2, Fig. 6.3. The schematic of simulation 2 is repeated in Fig. 6.3. The open circuit voltage to voltage transfer functions $H^{VV,open}_{36,Ar}$ and $H^{VV,open}_{37,Br}$ for measurement A and B, respectively, are simulated. The transmitting transducer is exited with a 1 cycle pulse with 1 V amplitude, across the input terminals.

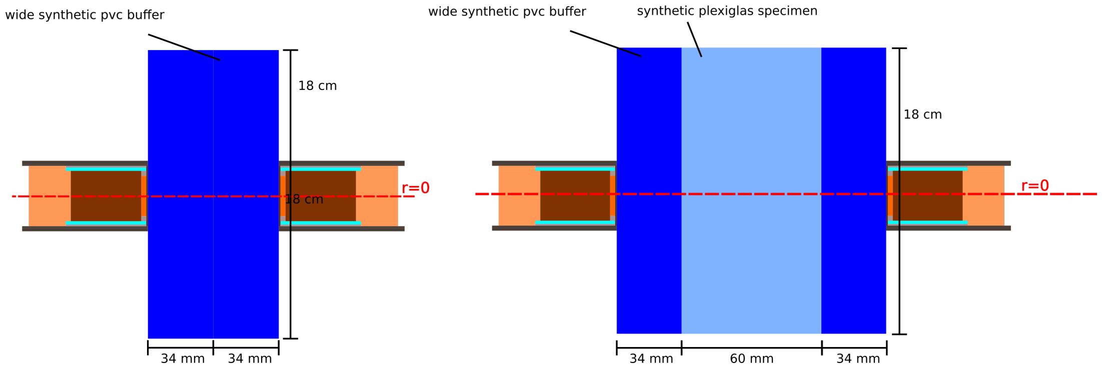

(a)

(b)

Figure 6.3: Simulation 2: Wide synthetic fluid buffers and piezoelectric transducers as transmitter and receiver (same as Fig. 5.5). **a)** Simulation of measurement A. **b)** Simulation of measurement B.

c_P and α_P simulated with simulation 2 is shown in Fig. 6.4. The simulated values can largely be compared with the piston model in simulation 1. By using Rogers and Buren's diffraction correction model, a c_P in the range 2709-2717 m/s is obtained within the 6 dB bandwidth 300-620 kHz defined in Sec. 6.1. The simulated α_P coefficient is approximately 0.85 dB/cm at 500 kHz, which is close to the true value of the input parameter, 0.80 dB/cm at 500 kHz. This indicates that the diffraction correction model is representing the diffraction from the transducer fairly well around 500 kHz. Compared to simulation 1 (Fig. 6.2), α_P is in general slightly overestimated for higher frequencies and underestimated for lower frequencies within the bandwidth 300 - 620 kHz. The only difference between simulation 1 and 2 is that piezoelectric transducers are introduced in simulation 2. It is concluded here that the deviations seen between c_P and α_P in Figs. 6.2 and 6.4 are due to a non-perfect description of the diffraction effects. However, using the proposed diffraction correction gives a value for c_P and α_P closer to the true value than not using the diffraction correction ($H_A^{dif} \neq H_B^{dif}$).

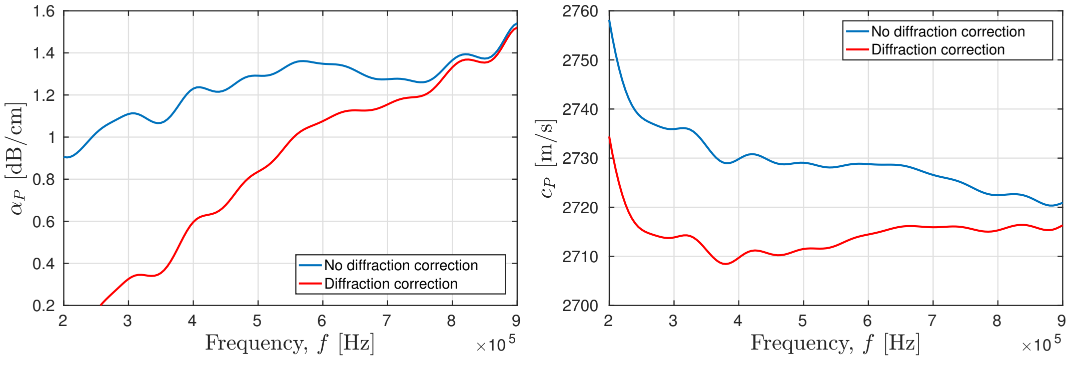

(a) (b)

Figure 6.4: Simulation of c_P and α_P using the solid buffer method with the transmitter and receiver modeled as a piezoelectric transducers and the buffers modeled as wide buffer-fluids (simulation 2). **a)**) Compressional attenuation coefficient using the Fourier spectrum method. **b)** c_P using the Fourier spectrum method.

Simulation 3

In simulation 3, the fluid buffers and specimen in simulation 2 are replaced with elastic PVC buffers with $c_P = 2380$ m/s, $c_S = 1190$ m/s, $Q_P = Q_S = 51$ and a plexiglas specimen with with $c_P = 2715$ m/s, $c_S = 1358$ m/s and $Q_P = Q_S = 63$ (Tab. 5.1).

The simulation setup is presented in Sec. 5.2.2. The schematic of simulation 3 is repeated in Fig. 6.5. This simulation with elastic buffers and specimen is completely analogue with simulation 2 with fluid buffers and specimen. Simulation 2 (Fig. 6.4) and simulation 3 (Fig. 6.5) are very similar. At 500 kHz the difference in α_P and c_P are less than 0.02 dB/cm and 1 m/s, respectively. Due to the close match, the description of simulation 2 is also valid for simulation 3. The small differences seen between the simulated c_P and α_P in Figs. 6.4 and 6.6 are probably because shear wave components in the elastic buffers affect the simulations. However, these are small and using the proposed diffraction correction model (red curve) and (as for simulation 2) the simulated values of c_P and α_P in simulation 3 are close to the input values.

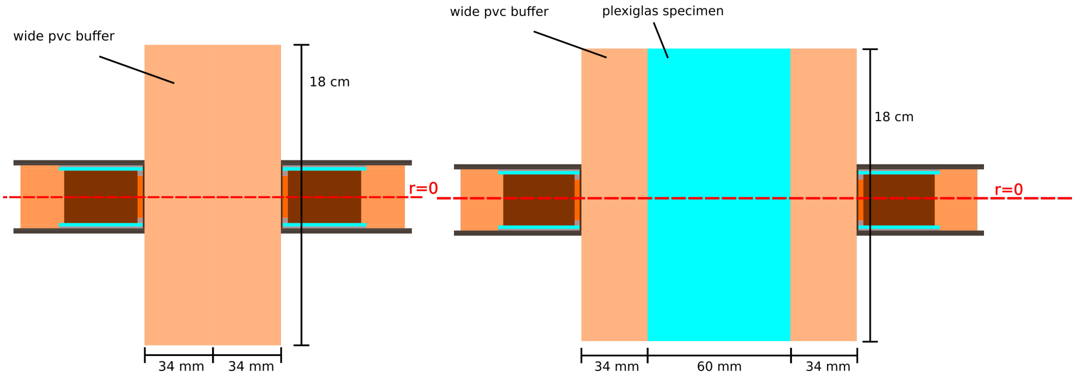

(a) (b)

Figure 6.5: Simulation 3: Wide elastic PVC-buffers and piezoelectric transducers as transmitter and receiver (same as Fig. 5.6). **a)**) Simulation of measurement A. **b)** Simulation of measurement B.

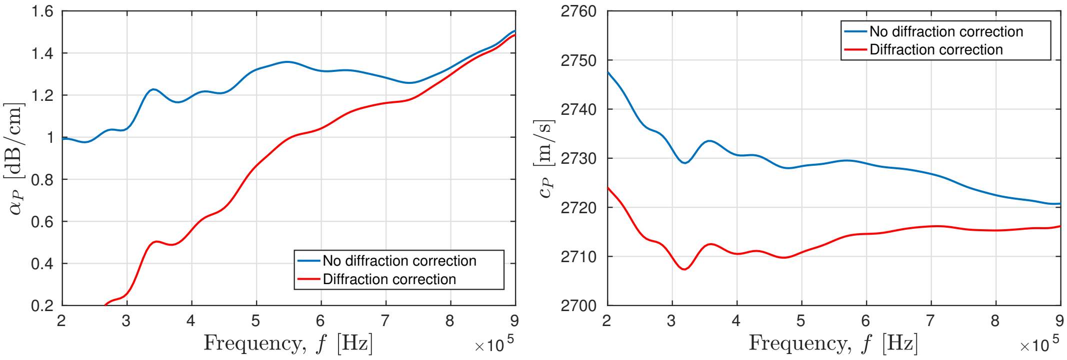

(a) (b)

Figure 6.6: Simulation of c_P and α_P using the solid buffer method with the transmitter and receiver modeled as a piezoelectric transducers and wide elastic buffers (simulation 3). **a)**) Compressional attenuation coefficient using the Fourier spectrum method. **b)** c_P using the Fourier spectrum method.

Simulation 4

In simulation 4 (Fig. 5.7) the solid buffer method presented in Ch. 3 is simulated. This is the same simulation setup as simulation 3, but the specimen and buffers have the same dimensions as in the real measurement setup. The specimen has diameter 50 mm and length 60 mm. The buffers are 34 mm long and have diameter 35 mm. The simulation setup is presented in Sec. 5.2.2, Fig. 5.7. The simulation setup is repeated in Fig. 6.7. The open circuit voltage to voltage transfer functions $H_{36,Ar}^{VV,open}$ and $H_{37,Br}^{VV,open}$ for measurement A and B, respectively, are simulated. The transmitting transducer is exited with 1 cycle, 1 V amplitude pulse across the input terminals.

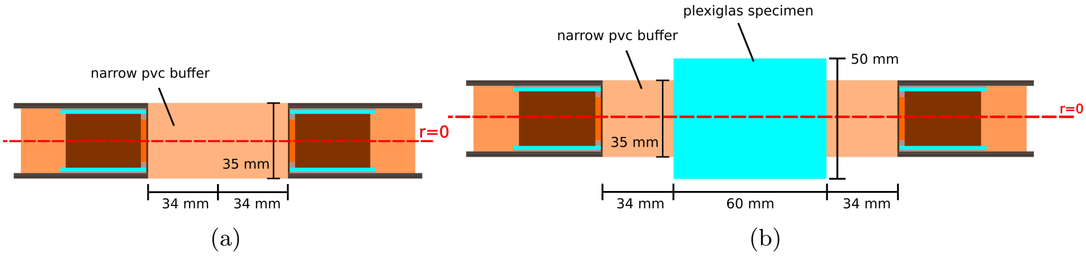

(a) (b)

Figure 6.7: Simulation 4: Narrow, elastic PVC-buffers and piezoelectric transducers as transmitter and receiver (same as Fig. 5.7). **a)** Simulation of measurement A. **b)** Simulation of measurement B.

The simulated c_P and α_P for simulation 4 using the Fourier spectrum method are shown in Figs. 6.8 a) and b), respectively. In 6.8 c), c_P is shown using the basic pulse method with a 500 kHz, 10 cycles long tone burst. For both the basic pulse method and the Fourier spectrum method, c_P is found to be approximately 2711 m/s at 500 kHz. This is very similar to value obtained in simulation 3 for 500 kHz and is 4 m/s less than the input value of 2715 m/s. α_P is seen to be approximately 0.6 dB/cm at 500 kHz which is 0.20 dB/cm less than the input value of 0.80 dB/cm at 500 kHz.

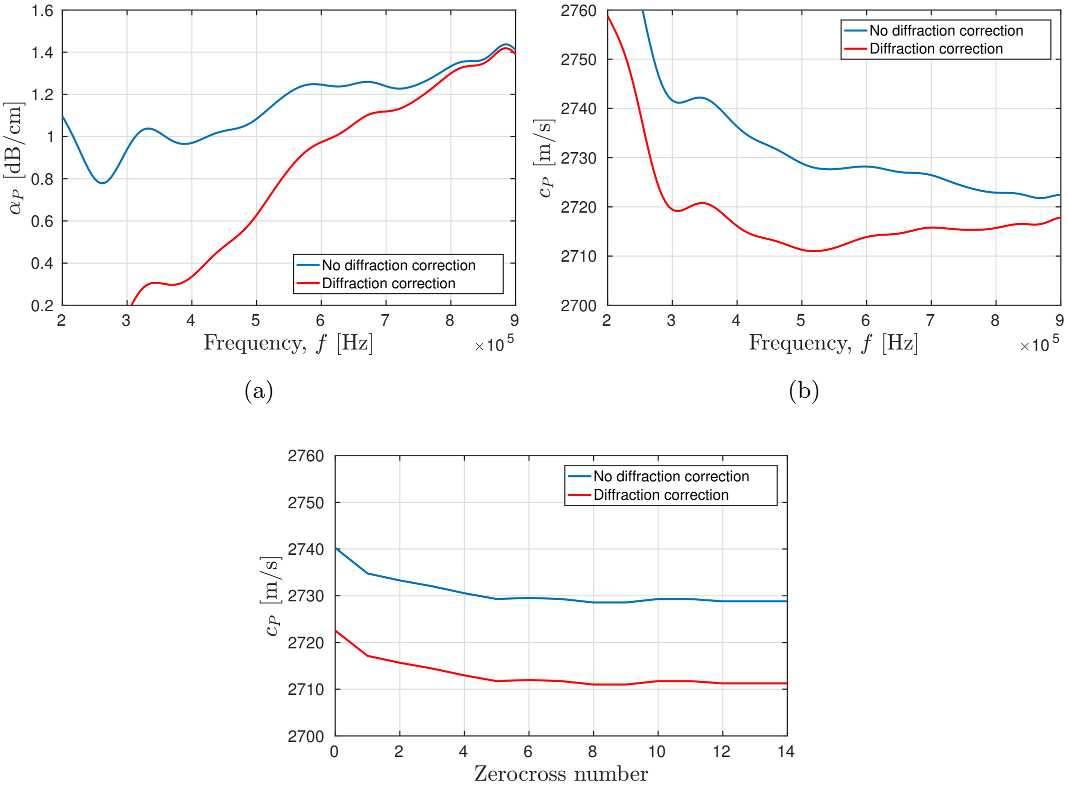

(a)

(b)

(c)

Figure 6.8: Simulation of c_P and α_P using the solid buffer method with the transmitter and receiver modeled as a piezoelectric transducers and narrow elastic buffers (simulation 4). **a)**) Compressional attenuation coefficient using the Fourier spectrum method. **b)** c_P using the Fourier spectrum method. **c)** c_P using the basic pulse method with a 10 cycles, 500 kHz tone burst.

Summary of simulation 1-4

Simulation 1 is an idealized model and gives the same c_P and attenuation coefficient as used for the input parameter for the specimen. The close agreement between the simulated c_P and α_P with the input parameters gives confidence in the FE-simulations, the signal processing methods and the measurement methods used to obtain c_P and α_P. Using the proposed diffraction correction model, gives more accurate results than not using the proposed diffraction correction. It is thus concluded that $H_A^{dif} \neq H_B^{dif}$.

In simulation 2 and 3 the buffers are wide and there are assumed to be no reflections from the buffer sidewalls interfering with the direct measurement signal. The deviations between simulation 2-3 and 1 are assumed to be mainly because the Rogers and Buren's diffraction correction model is not accurately describing the diffraction effects from the transmitting piezoelectric transducer. However, comparing the results presented Figs. 6.4-6.6 with Fig. 6.1 it is assumed that Rogers and Buren's diffraction correction model is representing the diffraction from the transducer fairly well around 500 kHz. α_P is seen to be slightly overestimated for higher frequencies and underestimated for lower frequencies within the bandwidth 300 - 620 kHz. This gives a sensitivity in the simulated α_P and c_P due to the uncertainty in Rogers and Buren's diffraction correction model of $\Delta\alpha_P^{dif} =$ 0.1 dB/cm and $\Delta c_P^{dif} = 4$ m/s at 500 kHz.

The deviation between the simulated c_P and α_P in Fig. 6.8 (simulation 4) and Figs. 6.4-6.6 (simulation 2-3) are assumed to be due to reflections from the sidewalls of the buffers and the plexiglas specimen in simulation 4. α_P in simulation 4 is approximately 0.2-0.3 dB/cm less than α_P in simulation 2 and 3 at 500 kHz. This gives a sensitivity in the simulated α_P due to sidewall reflections of $\Delta\alpha_P^{refl} \approx 0.3$ dB/cm for simulation 4 at 500 kHz. c_P in simulation 4 and simulation 2-3 is approximately the same at 500 kHz (less than 1 m/s difference). However, at frequencies 300-400 kHz, the difference is larger. This gives a sensitivity in c_P due to sidewall reflections of $\Delta c_P^{refl} = 1$ m/s for simulation 4 for at 500 kHz.

$\Delta\alpha_P^{dif}$, Δc_P^{dif}, $\Delta\alpha_P^{refl}$ and Δc_P^{refl} are also assumed to be valid for the plexiglas measurements presented in Sec. 6.1.2.

6.1.2 Comparison of the measured c_P and α_P in plexiglas using the solid buffer method and the immersion method

In this subsection, measurements of c_P and α_P in plexiglas using the immersion method and the solid buffer method, are presented. The immersion method is widely used and regarded as a reliable measurement method for measuring c_P and α_P for plates made of plastics such as plexiglas plates [72, 53, 73].

The immersion method is assumed to be more reliable than the solid buffer method as the ”water-buffers” are much wider than the PVC solid buffers. The geometries of the immersion cell and the plexiglas specimen plate (Fig. 3.14) are such that the pulse traveling directly from transducer to transducer arrives at least 7 periods before any theoretical sidewall reflections (or other interfering reflections) from the immersion cell or the specimen at 500 kHz. For short pulses used with the Fourier spectrum method, no sidewall reflections should be present.

Kline et al. summarize studies in the literature on the measured c_P and α_P for plexiglas [73] and found some deviations in the reported c_P and α_P. However, the trends for the measured c_P and α_P in plexiglas that Kline et al. present, agree well with α_P and c_P measured with the immersion method in Fig. 6.9 a) between 300 kHz and

600 kHz. Kline et al. report the α_P to be between 0.5 dB/cm and 1 dB/cm at 500 kHz [73] and measures c_P to be between 2700 m/s and 2800 m/s at 5 MHz. These values for c_P and α_P are consistent with the measurements conducted in this work (Figs. 6.9 b) and c)).

He et al. [72] conduct measurements on different plastic specimen using the immersion method with the Fourier spectrum method. He et al. use Rogers and Buren's diffraction correction model [79] and neglects all other uncertainty effects than the uncertainty in the plane wave transmission coefficients and the thickness of the specimen, d. In this work, Rogers and Van Buren's diffraction correction is used in all α_P, c_P and c_S-measurements not labeled with "no diffraction correction." For measurements labeled with "no diffraction correction" $H_A^{dif} = H_B^{dif}$. In all other measurements Eq. (2.8) is used for the solid buffer method and Eq. (2.7) is used for the immersion method. The radius of the piezoelectric element inside the transducer (a) is used as the radius of the baffled piston used in the diffraction correction model. $ka \approx 26$ for 500 kHz in water and $ka \approx 16$ for 500 kHz in PVC.

In Fig. 6.9 a), the Fourier spectrum method is used to measure α_P for three different plexiglas specimen. The in-house built P-wave transducers are used in the solid buffer method (see Sec. 3.3) and the Olympus transducers are used in the immersion method (see Sec. 3.4). The input signal settings on the signal generator is a 20 mV, 1 cycle, 500 kHz pulse (measured time signals using the P-wave transducers are shown in Ch. 7, Fig. 7.1 a). All the tree specimen are manufactured from the same batch order at the workshop at the University of Bergen. The blue curve shows the measured α_P for the 20 mm plexiglas plate using the immersion method. The red curve shows the measured α_P for the 20 mm plexiglas disc using the solid buffer method and the black curve shows the measured α_P for the 60 mm plexiglas cylinder using the solid buffer method. For measurement frequencies close to 300 kHz, the measured α_P attain negative, unphysical values for the solid buffer methods. In Fig. 6.9 c), the magnitude spectrum of measurement B ($|V_{7,B}(f)|$) for the 60 mm specimen using the solid buffer method is shown. The 6 dB - bandwidth (where the signal amplitude is within 6 dB of it's maximum value) is approximately 300 kHz - 620 kHz. Only attenuation spectra and dispersion curves within this bandwidth are investigated. The measured α_P for the 20 mm disc and the 60 mm cylinder shown in Fig. 6.9 a) deviates from α_P measured with the immersion method. The same kind of deviation is clearly seen between the simulated α_P using the solid buffer method (Fig. 6.8) and the "idealized" piston solid buffer method (Fig. 6.2). For the 60 mm specimen, the solid buffer method gives measured values for α_P systematically lower than α_P-measurements of the 20 mm plexiglas plate using the immersion method. This is also the case when comparing α_P simulated with simulation 4 (Fig. 6.8) and the input values or using the "idealized" piston solid buffer method (Fig. 6.2).

In Fig. 6.9 b), the Fourier spectrum method is used to measure c_P for the three different plexiglas specimen. The measured c_P for the 20 mm disc and the 60 mm cylinder deviates from c_P measured with the immersion method. There is a dip in the dispersion curves around 500 kHz in the simulations (Fig. 6.8 b)) and in the measurements (Fig. 6.10 b)). Because of the relatively close similarities between the α_P and c_P curves obtained by the simulations and the measurements, it seems likely that the deviations seen in the measurements in Figs. 6.9 a and b) at least partly can be explained with sidewall reflections and diffraction effects not explained with the proposed diffraction correction model.

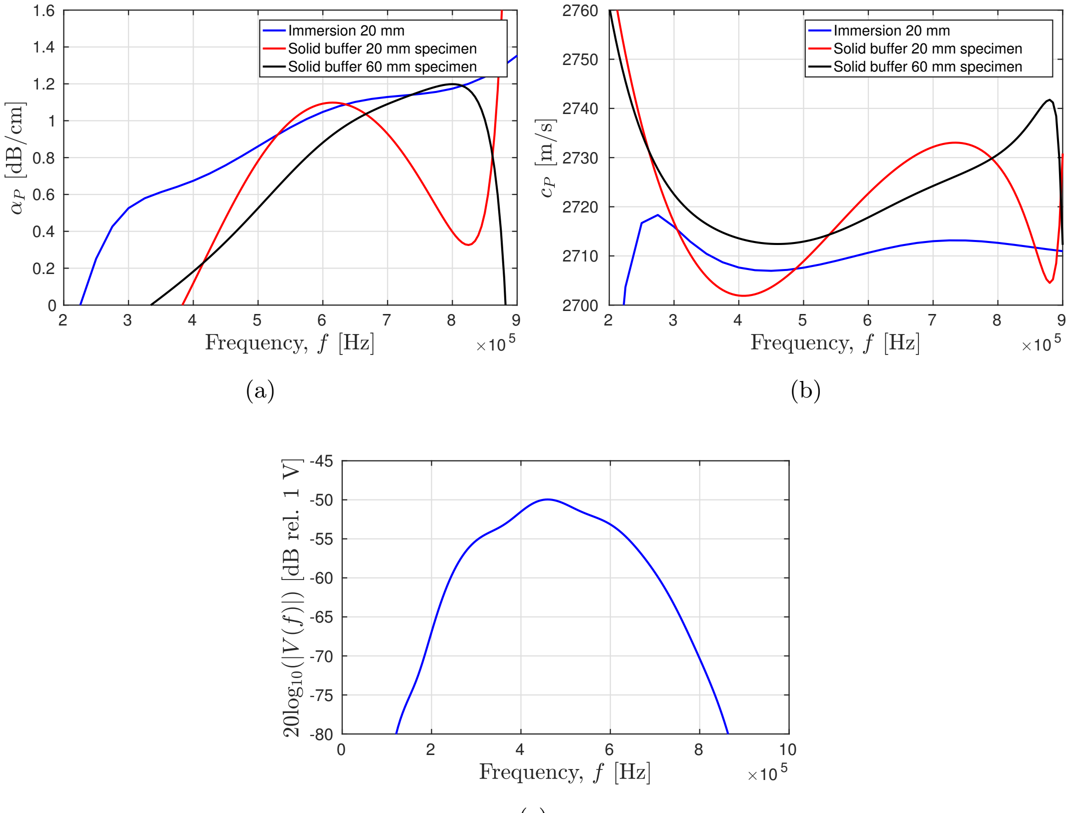

(a)

(b)

(c)

Figure 6.9: Measurements of three plexiglas specimen using the Fourier spectrum method. **a)** Measured α_P for the three different plexiglas specimen using the immersion method and the solid buffer method. **b)** Measured c_P for three different plexiglas specimen using the immersion method and the solid buffer method. **c)** Magnitude spectrum of received pulse in measurement B for the 60 mm specimen.

The Fourier spectrum method is also compared with the basic pulse method to give further confidence in the measurements (Figs. 6.10 b) and c)). In the basic pulse method (Sec. 3.5.1), the input signal settings on the signal generator is a 20 mV, 10 cycles, 500 kHz burst.

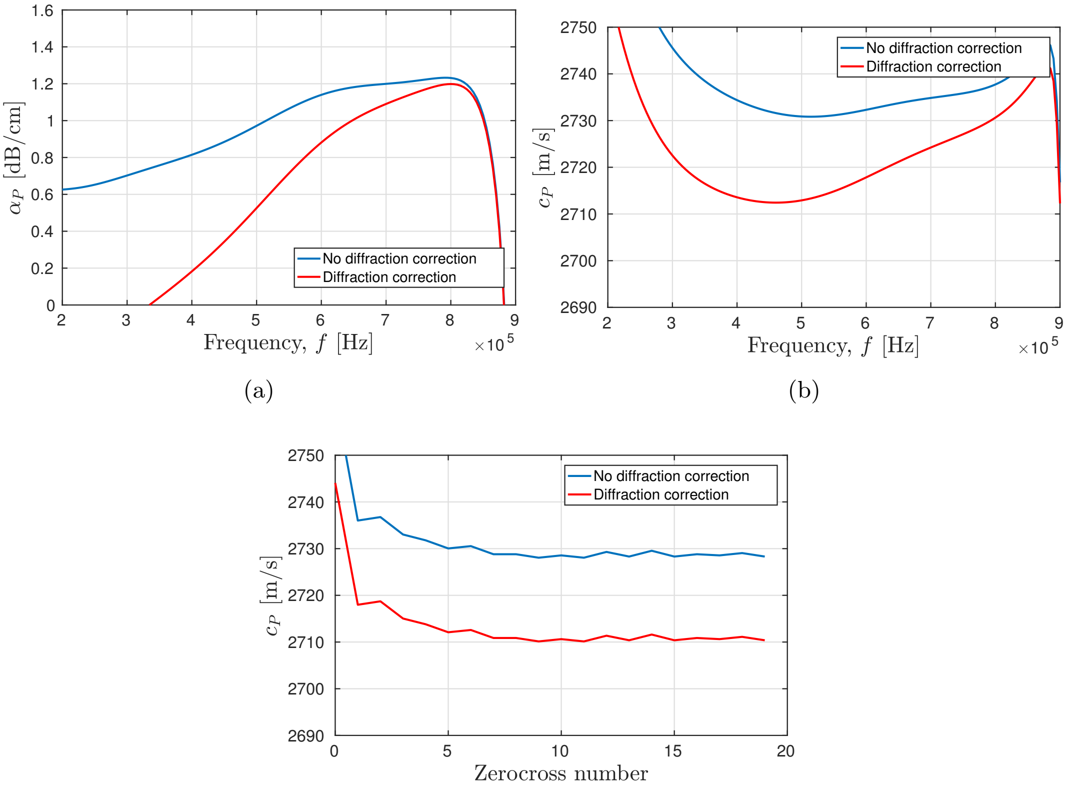

(a)

(b)

(c)

Figure 6.10: Measurements conducted on the 60 mm pleciglas specimen with the solid buffer method. **a)** Measured α_P using Fourier spectrum method. **b)** Measured c_P using Fourier spectrum method. **c)** Measured c_P using the basic pulse method.

In Figs. 6.10 a) and b) the measured α_P and c_P for the 60 mm plexiglas cylinder are shown. The Fourier spectrum method is used. The blue curve shows the measured c_P and α_P assuming $H_A^{dif} = H_B^{dif}$ ("no diffraction correction") in the figures. The red curve is shows the measured c_P and α_P when using the diffraction corrections Eq. (2.8). c_P and α_P are approximately 2712 m/s and 0.55 dB/cm, respectively, using the Fourier spectrum method. The basic pulse method is also used to find c_P of the 60 mm plexiglas cylinder for frequency 500 kHz. c_P is measured to be approximately 2710 m/s using zerocrosses higher than 6 (Fig. 6.10 c)). Zerocross 6 corresponds to the zerocross three periods into the signal and is within the steady-state region. A close agreement between the basic pulse method and the Fourier spectrum method is seen. In the basic pulse method (Fig. 6.10 c)) the diffraction correction for the basic pulse method is calculated at 500 kHz.

There are uncertainty contributions in the acquired signals (V_6^A and V_8^B) and all the transfer functions and the diffraction correction expressions describing the system model for the immersion method, Eq. (3.27). However, He et al. [72] argue that uncertainty contributions cancel out in the calculation of the immersion Fourier spectrum method (Eqs. (3.52)-(3.54)) and they neglect all other uncertainty effects than the uncertainty in the plane wave transmission coefficients and the thickness of the specimen, d. No thorough uncertainty analysis for the immersion method is presented in this work, however, some uncertainty contributions are considered.

The reproducibility of the α_P and c_P-measurements are $\Delta\alpha_P^{reproduce} = 0.05$ dB/cm and $\Delta c_P^{reproduce} = 9$ m/s, respectively, for the immersion method (decoupling and recoupling the measurement setup). The uncertainty in the measured length of the plexiglas plate is 0.02 mm. By using Eqs. (3.51) and (3.50), the sensitivity in α_P and c_P due to this change in the specimen length are $\Delta\alpha_P^{length} = 0.09$ dB/cm and $\Delta c_P^{length} = 3$ m/s, respectively, for the 20 mm plexiglas plate. The sensitivity in α_P and c_P due to the uncertainty in the plane wave transmission coefficient is assumed to be smaller in the immersion method compared with that in the solid buffer method. From the analysis shown in Eq. (6.3), this contribution is neglected.

The combinded sensitivity in the measured α_P due to $\Delta\alpha_P^{reproduce}$ and $\Delta\alpha_P^{length}$ is:

$$\begin{aligned}\Delta\alpha_P^{sens} &= \sqrt{(\Delta\alpha_P^{length})^2 + (\Delta\alpha_P^{reproduce})^2} \\ &= \sqrt{(0.09 \text{ dB/cm})^2 + (0.05 \text{ dB/cm})^2} \approx 0.1 \text{ dB/cm}.\end{aligned} \tag{6.1}$$

Very little dispersion is reported for plexiglas [73] and plastics having similar acoustic properties such as polyethylene [72]. In the frequency range 300 - 620 kHz, c_P varies from 2708-2716 m/s for the immersion method (blue curve in Fig. 6.9 a)). This is an indication that there are other uncertainty contributions than $\Delta c_P^{reproduce}$ and Δc_P^{length}. However, the combined sensitivity in c_P due to $\Delta c_P^{reproduce}$ and Δc_P^{length} is

$$\begin{aligned}\Delta c_P^{sens} &= \sqrt{(\Delta c_P^{length})^2 + (\Delta c_P^{reproduce})^2} \\ &= \sqrt{(3 \text{ m/s})^2 + (9 \text{ m/s})^2} \approx 10 \text{ m/s}.\end{aligned} \tag{6.2}$$

As for the immersion method, the solid buffer method is sensitive to all the component in the system model, Eq. (3.4). No thorough uncertainty analysis is provided here for the solid buffer method either. However, in addition to the uncertainty components given in Eqs. (6.1)-(6.2), uncertainty contributions due to the diffraction correction and reflections from buffer sidewalls are considered for the solid buffer method.

The reproducibility of the α_P and c_P-measurements are $\Delta\alpha_P^{reproduce} = 0.2$ dB/cm and $\Delta c_P^{reproduce} = 11$ m/s, respectively, for the solid buffer method.

$V_{7,A}$ and $V_{8,B}$ in Eqs. (3.50)-(3.51) do not contain any reflections and are obtained by assuming that buffers, specimen and transducers are perfectly aligned. The acquired signals in measurement A and B ($V_{7,Ar}$ and $V_{8,Br}$) contain some unwanted reflections and are not exactly representing $V_{7,A}$ and $V_{8,B}$. The analysis presented in Sec. 6.1.1 indicates that the sensitivity in α_P due to the uncertainty in $(V_{8,B}/V_{7,A})$ due to sidewall reflections ($\Delta\alpha_P^{refl}$) are approximately 0.3 dB/cm at 500 kHz.

The same analysis in Sec. 6.1.1 does not show any drastic change in the simulated c_P when the narrow buffers are introduced (Figs. 6.6-6.8). The change in c_P from Fig. 6.6 to Fig. 6.8 is set to be 1 m/s at 500 kHz. Thus, the sensitivity in c_P due to the uncertainty in $(\angle V_{8,B} - \angle V_{7,A})$ due to sidewall reflections is set to Δc_P^{refl}=1 m/s for the 60 mm plexiglas specimen at 500 kHz. The uncertainty in the measured length of the plexiglas cylinder is 0.02 mm. By using Eqs. (3.50)-(3.51), the sensitivity in α_P and c_P due to this change in the specimen length are $\Delta\alpha_P^{length} = 0.03$ dB/cm and $\Delta c_P^{length} = 1$ m/s, respectively, for the 60 mm plexiglas specimen.

There is an uncertainty in the combination of the plane wave transmission coefficient, $T = T_{B1}T_{B2}/T_A$. T_A is assumed to be 1 and $\angle T$ is assumed to be zero (see Sec. 3.3.3), thus

$$T = \Big(\frac{2\rho_{buff}c_{buff}}{\rho_{buff}c_{buff} + \rho_m c_P}\Big)\Big(\frac{2\rho_m c_P}{\rho_{buff}c_{buff} + \rho_m c_P}\Big) = \frac{4\rho_m c_P \rho_{buff}c_{buff}}{(\rho_{buff}c_{buff} + \rho_m c_P)^2}. \tag{6.3}$$

From Eq. (3.51), α_P is sensitive to T and thus to the compressional wave velocities of buffers (PVC) and the specimen (plexiglas), c_{buff} and c_P, respectively. ρ_{buff} is the density of the buffer and ρ_m is the density of the specimen (here plexiglas). All specimen are machined with a tolerance of 0.2 mm. By using the high-accuracy weight A&D GF-3000 [202] with listed accuracy 0.01 g, dimensions are assumed to be the main uncertainty factor in any density calculations $\rho = \frac{m}{V}$ where V is the volume and m is the mass of a test specimen. A sensitivity study on the density due to an uncertainty in the volume for a plexiglas and a PVC cylinder gives $\Delta\rho_{buff} \approx 10$ kg/m^3, $\Delta\rho_m \approx 10$ kg/m^3.

In a sensitivity analysis for T in Eq. (6.3), Δc_{buff}, Δc_P, $\Delta\rho_{buff}$ and $\Delta\rho_m$ contribute. $\Delta T^{c_P} = 0.001$ and $\Delta T^{c_{buff}} = 0.001$ are the sensitivities in T due to $\Delta c_P^{sens} = 10$ m/s and $\Delta c_{buff}^{sens} = 10$ m/s, respectively (calculated using Eq. (6.2)). $\Delta T^{\rho_m} = 0.001$ and $\Delta T^{\rho_{buff}} = 0.001$ are the sensitivities in T due to $\Delta\rho_m = 10$ kg/m^3 and $\Delta\rho_{buff} = 10$ kg/m^3, respectively. The sensitivity in T is thus given:

$$\begin{aligned}\Delta T &= \sqrt{(\Delta T^{c_P})^2 + (\Delta T^{c_buff})^2 + (\Delta T^{\rho_{buff}})^2 + (\Delta T^{\rho_m})^2} \\ &= \sqrt{(0.001)^2 + (0.001)^2 + (0.001)^2 + (0.001)^2} = 0.002.\end{aligned} \tag{6.4}$$

From Eq. (6.4), the sensitivity is ΔT =0.002. By using Eq. (3.51), the sensitivity in α_P due to this change in T is $\Delta\alpha_P^{Trans} = 0.004$ dB/cm. This is based upon the assumption that the buffers and specimen are perfectly welded together.

From the analysis in Sec. 6.1.1, the diffraction correction in the simulated solid buffer method is seen to be fairly well described with Rogers and Buren's diffraction correction model within the bandwidth 300-620 kHz. The sensitivity in the simlated c_P and α_P due to diffraction effects are thus approximately $\Delta\alpha_P^{dif} = 0.1$ dB/cm and $\Delta c_P^{dif} = 4$ m/s for 500 kHz. These sensitivities are assumed to be valid for the measurements as well.

As mentioned above, it is assumed that the transducers, buffers and specimen are in contact with each other. It is assumed that the contact surfaces are plane and aligned so that the specimen can precisely be defined with a length d and the buffers with a length L_{buff}. It is assumed that the electrical transfer functions can be canceled and that the transducers are symmetric so that rotation of the transducers does not affect the transmitted sound field.

The fact that the measurements are reproducible within 0.05 dB/cm and 5 m/s indicates that not all the assumptions listed above are entirely correct. For example, if the transducers are asymmetric, this might affect the sound diffraction and the proposed diffraction correction may be less accurate than estimated in Sec. 6.1.1. If there are irregularities across the buffer-specimen interface, the plane wave transmission coefficient can not be precisely defined on this surface with the buffer and specimen compressional wave velocities and densities. Also the frequency dependence seen in the plexiglas measurements using the solid buffer method indicates that other sources of uncertainties are present. However, a combined sensitivity study of the measured c_P and α_P on the 60 mm plexiglas specimen due to the listed uncertainty contributions give:

$$\begin{aligned}
\Delta c_P^{sens} &= \sqrt{(\Delta c_P^{reproduce})^2 + (\Delta c_P^{length})^2 + (\Delta c_P^{dif})^2 + (\Delta c_P^{refl})^2} \\
&= \sqrt{(11m/s)^2 + (1m/s)^2 + (4m/s)^2 + (1m/s)^2} \approx 11m/s, \\
\Delta\alpha_P^{sens} &= \sqrt{(\Delta\alpha_P^{reproduce})^2 + (\Delta\alpha_P^{length})^2 + (\Delta\alpha_P^{dif})^2 + (\Delta\alpha_P^{refl})^2 + (\Delta\alpha_P^{Trans})^2} \\
&= \sqrt{(0.2dB/cm)^2 + (0.03dB/cm)^2 + (0.1dB/cm)^2 + (0.3dB/cm)^2 + (0.004dB/cm)^2} \\
&\approx 0.4dB/cm.
\end{aligned} \tag{6.5}$$

Δc_P^{sens} and $\Delta\alpha_P^{sens}$ in Eq. (6.5) are found by partly considering the simulations in Sec. 6.1.1 at 500 kHz.

Considering that $\alpha_P \approx 0.85$ dB/cm at 500 kHz in plexiglas (immersion method, Fig. 6.9 a)), the sensitivity of $\Delta\alpha_P^{sens} = 0.4$ dB/cm from Eq. (6.5) is large for the 60 mm plexiglas specimen. However, this uncertainty is not so large when considering partially water-saturated Bentheim sandstones where α_P may be in the range 5-10 dB/cm. By assuming that the uncertainty contributions do not change during hydrate growth, the sensitivity in $\Delta\alpha_P$ (hydrate experiments) should be less than $\Delta\alpha_P^{sens}$ =0.4 dB/cm. The uncertainty due to sidewall reflections are systematic, however, in this work no attempt has been made to correct for these reflections in c_P and α_P. The reflections are treated as a component of uncertainty.

α_P and c_P obtained with the solid buffer method and the immersion method (Fig. 6.9 a)) give consistent results by using the sensitivities of $\Delta\alpha_P^{sens} \approx 0.4$ dB/cm and $\Delta c_P^{sens} \approx 12$ m/s at 500 kHz as indicated measurement uncertainties. At lower frequencies the deviations between α_P measured with the immersion method and the solid buffer method is higher ($\Delta\alpha_P^{sens} \approx 0.6$ dB/cm). In the hydrate experiments, one of the main goals is to monitor the change in c_P and α_P during hydrate growth.

6.1.3 Reproducibility of the measured c_P and α_P for Bentheim sandstones during hydrate growth using P-wave transducers

In addition to the uncertainty contributions discussed for the solid buffer method in Sec. 6.1.2, there are at least three more important factors that affect c_P and α_P - measurements for Bentheim sandstones during hydrate growth: The applied torque on the transducer holders, the confining pressure around the sandstone and when pressurizing the inne chamber with methane gas.

In the plexiglas measurements, torques in the range 2-8 Nm are not seen to affect the measurements. For the Bentheim sandstones however, the torque has a clear impact on the measured c_P and α_P. In Tabs. 6.1-6.2, c_P and α_P are measured for a Bentheim sandstone with unknown water content using the basic pulse method. The signal generator is set to produce a 10 cycles, 500 kHz burst with 100 mV amplitude. The experimental setup is detailed in Sec. 3.3.1. In Tab. 6.1 the torque is varying from 1-10 Nm. α_P is varying from 7.7 dB/cm to 6.6 dB/cm by changing the applied torque from 1 Nm to 10 Nm. c_P is varying from 2730 m/s to 2850 m/s by changing the applied torque from 1 Nm to 10 Nm.

In the hydrate measurements presented in Ch. 7 a torque of 10 Nm is used in all measurements. Due to friction in the threads, the absolute force exerted on the transducer holder can not be directly calculated from the applied torque. By user experience, the accuracy of the torque exerted on the transducer holders are believed to be within 1-2 Nm.

Table 6.1: Measured α_P and c_P using the solid buffer method inside the pressure cell, applying different torques.

Applied torque	α_P [dB/cm]	c_P [m/s]
1 Nm	7.7	2730
3 Nm	7.5	2750
4 Nm	7.4	2760
10 Nm	6.6	2850

In Tab. 6.2, the torque is held constant at 10 Nm. α_P is varying from 6.6 dB/cm to 4.6 dB/cm and c_P is varying from 2850 m/s to 2965 m/s by varying the confining oil pressure from 0 to 30 bar.

Table 6.2: Measured α_P and c_P using the solid buffer method inside the pressure cell, applying 10 Nm torque and different confining pressures.

Applied torque and confining pressure	α_P [dB/cm]	c_P [m/s]
10 Nm, 0	6.6	2850
10 Nm, 10 bar	5.5	2895
10 Nm, 20 bar	4.9	2940
10 Nm, 30 bar	4.6	2965

The moment when the inner chamber in the pressure cell is pressurized with methane gas, the measured c_P is seen to systematically increase 20-80 m/s from before to after pressurizing the inner chamber. The amplitude is also seen to systematically drop so that the measured α_P decrease by 1-3 dB/cm (no tables presenting such measurements are shown here). These effects on the measured c_P and α_P are not investigated further in this work and are not fully understood. An explanation may be that the pressurized gas inside the pressure cell is pushing on the transducer holders so that the contact force between the buffer and the specimen is reduced. Another explanation may be that the 83 bar methane gas creeps in between the sleeve and the sandstone so that the sandstone itself experiences a lower pressure from the confining sleeve.

The uncertainties due to the applied torque, confining pressure and the effect of pressurizing the inner chamber of the pressure cell are not treated as uncertainties in the sense discussed in Sec. 6.1.2. The acoustic measurements are assumed to be accurate to the level described in Sec. 6.1.2 for a given pressurized sandstone at a given torque and confining pressure. However, the acoustic properties of the Bentheim sandstones are assumed to change due to these effects, making measurements hard to reproduce. Even if absolute measurements of c_P and c_S are fairly accurate, comparing measurements of different sandstones are proven challenging. Also, the sandstones are not homogeneous media as plexiglas and the acoustic properties may change from specimen to specimen.

Due to this, many of the measurements in Ch. 7 are presented as relative measurements, that is, the change in c_P, c_S and α_P are reported during hydrate growth. No absolute measurements of α_P is resented for the hydrate experiments. In such relative measurements, uncertainties due to sidewall reflections should also decrease because sidewall reflections are present in all measurements during hydrate growth (assuming that the effect of the sidewall reflections are constant during hydrate growth). This argument may also be used for other uncertainty contributions such as uncertainties in the specimen length, diffraction correction and transmission coefficient (Eq. (6.5)).

To conduct more reproducible measurements, better control of the effects presented here is needed. As discussed in Sec. 3.3.1, potential non-linear effects are assumed to not effect c_P and c_S- measurements (not more than other uncertainty contributions). No thorough analysis is provided, but some indications are seen that non-linear effects are affecting the measured α_P for $S_H < 0.2$. Due to this, α_P-measurements for hydrate-bearing sandstones are only presented for $S_H > 0.2$ in Ch 7.

In previous studies on c_P in hydrate bearing sediments, the measurement uncertainty is typically not addressed [22, 21, 30, 31, 33, 35]. Priest et al. [32] report a measurement uncertainty in c_P of 100-400 m/s during hydrate growth in sandy sediments. Zhang et al. [34] offer no uncertainty analysis but claim an uncertainty in the measured c_P of 1 %.

6.2 On the accuracy of P-wave measurements with the solid buffer method using the S-wave transducers

The S-wave transducers transmit both compressional and shear waves. In this section the accuracy of the P-wave measurements using the S-wave transducers is considered.

3D finite element simulations for the shear wave transducers are not conducted due to lack of computing power. Thus, no sensitivity study on c_P and α_P due to sidewall reflections and uncertainty in the diffraction correction is provided. However, the P-wave measurements with the solid buffer method using in-house built S-wave transducers are compared with measurements conducted with the immersion method.

In Sec. 6.1, c_P and α_P in plexiglas is measured to be 2709 m/s and 0.85 dB/cm at 500 kHz, respectively using the immersion method. In Eqs. (6.1) and (6.2) the combined sensitivity in c_P and α_P due to the listed uncertainty contributions for the plexiglas measurements using the immersion method is indicated to be $\Delta c_P^{sens} \approx 10$ m/s and $\Delta \alpha_P^{sens} \approx 0.1$ dB/cm.

c_P (Eq. (3.19)) and α_P (Eq. (3.23)) for the 60 mm plexiglas specimen are measured with the S-wave transducers using the solid buffer method. The measurement setup is detailed in Sec. 3.3, Fig. 3.11. The input signal settings on the signal generator is a 20 mV, 1 cycle, 500 kHz pulse. The acquired voltage signals in measurement A and B are shown in Fig. 6.11. The compressional wave is the first pulse arriving at approximately 40 µs and 60 µs in measurement A and B, respectively. A time window is used to isolate the P-wave signal as illustrated with Fig. 3.19. The Fourier spectrum method is used to obtain c_P and α_P (Fig. 6.12). Refer to Fig. 3.19 to identify the different pulses seen in the measurements. Rogers and Buren's diffraction correction model is used (Eq. (2.8)). The piezoelectric element used in the S-wave transducers are square-shaped with width 15 mm giving an surface area of $15mm \times 15mm = 225$ mm^2. The radius of the piston used in the diffraction correction model is 8.5 mm, which is the radius which gives a piston surface area 225 mm^2. This gives a ka-number in PVC and plexiglas of approximately 11 and 10, respectively, at 500 kHz.

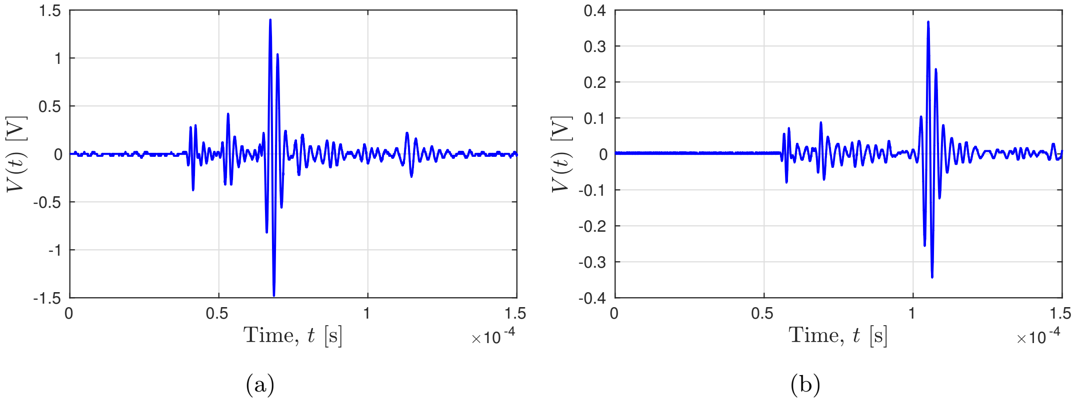

Figure 6.11: Measured time signals with S-wave transducers using the solid buffer method. **a**) Acquired voltage signal in measurement A. **b**) Acquired voltage signal in measurement B for the 60 mm plexiglas cylinder.

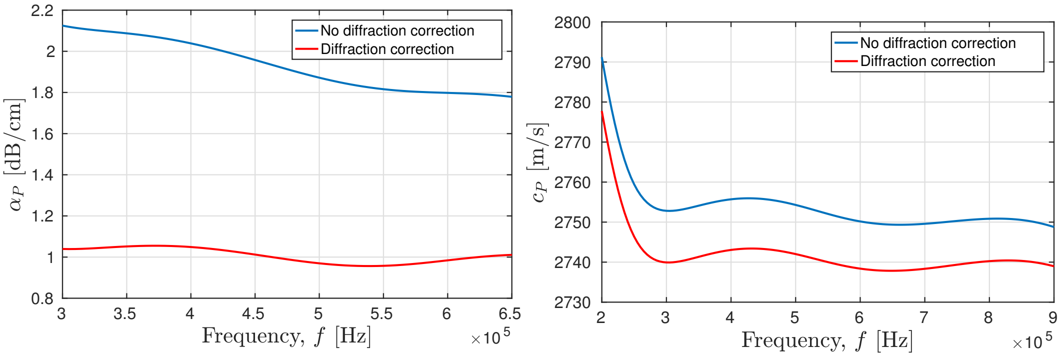

(a) (b)

Figure 6.12: Compressional wave measurements for the 60 mm plexiglas cylinder conducted with the S-wave transducers using the solid buffer method. **a**) Measurement of α_P. **b**) Measurement of c_P.

In Fig. 6.12, typical measured c_P and α_P for the 60 mm plexiglas specimen are shown. However, the measured α_P and c_P for the 60 mm plexiglas specimen using the S-wave transducers are differing from measurement to measurement. The reproducibility in the measurements are poor. α_P is measured in other measurements in the range 0.5 dB/cm to 1.6 dB/cm. c_P is measured in other measurements in the range 2720 m/s to 2765 m/s.

The poor reproducibility may be due to several reasons. Small irregularities on the end face of the solid buffers may affect the plane wave transmission coefficient. The polyurethane film used on the surface of the buffers in the S-wave transducers (see transducer design, Ch. 4.3) may alter the transmission coefficient. An important feature of the S-wave transducers is the fact that they are asymmetric. The piezoelectric elements in the S-wave transducers are square shaped, thus the receiving and transmitting properties are affected by the rotation of the transducers. Because the transducers are hidden inside the pressure cell, visual inspection is challenging.

c_P seem to systematically be measured to high compared with the immersion method (Fig. 6.9 a), $c_P \approx 2710$ m/s). Rogers and Buren's diffraction correction model (Eq. (2.8)) is based on describing the transducer as a baffled circular piston. The assumption that the transmitting S-wave transducer can be described as a baffled circular piston with an effective radius, is not necessarily correct. However from Fig. 6.12 b), using the diffraction correction seem to give a value closer to $c_P \approx 2710$ m/s measured with the immersion method.

No simulations are conducted to aid in an uncertainty analysis of the measurements conducted with the S-wave transducers. However, c_P and α_P - measurements conducted with the S-wave transducers are compared with the measurements from the immersion method presented in Fig. 6.9 a). The maximum measured value of α_P (1.6 dB/cm) is compared with the measured α_P from the immersion method giving $\Delta\alpha_P^{compare} \approx 0.8$ dB/cm. The same is done for c_P, giving $\Delta c_P^{compare} \approx 60$ m/s.

The uncertainties are larger using the S-wave transducers than using the P-wave transducers. However, as mentioned in Sec. 6.1.3, many of the measurements in Ch. 7 are presented as relative measurements. Thus, the uncertainties listed in Eq. (6.5) should also reduce for the solid buffer method using the S-wave transducers. For the hydrate experiments in Ch. 7, c_P measurements using the S-wave transducers is only presented for 500 kHz.

6.3 On the accuracy of S-wave measurements with the solid buffer method using S-wave transducers

To investigate the accuracy of the measured shear wave velocity in plexiglas, measurements conducted with the solid buffer Fourier spectrum method (Eq. (3.50)) are compared with measurements conducted with the immersion Fourier spectrum method (Eq. (3.53)).

In the immersion method Olympus transducers are used as the sound transmitter and receiver. The measurement setup is detailed in Sec. 3.4.1. The input signal settings on the signal generator is a 20 mV, 1 cycle, 500 kHz pulse. The 20 mm plexiglas specimen is rotated to the critical P-wave angle 38°. At this angle and above the compressional waves are not seen in the acquired signal from the oscilloscope. The acquired signal for measurement B using the immersion method is shown in Figs. 6.13 a) and b) for the time domain and the frequency domain, respectively.

The Fourier spectrum method is used to calculate c_S and is presented in Fig. 6.14 for the immersion method. Wu et al. [53] propose to use Rogers and Buren's diffraction correction model [79] to correct for diffraction effects for shear waves in the immersion method. This approach is used in this work as well, however, the diffraction correction has little effect on the measurements. Around 400 kHz there is a ripple in the dispersion curve. This ripple is probably because the signal is weak around 400 kHz (see Fig. 6.13 b)) and noise will be more protruding around 400 kHz. In Fig. 6.14, $c_S = 1347$ m/s at 500 kHz using the immersion method. For the hydrate experiments in Ch. 7, c_S is only presented for 500 kHz.

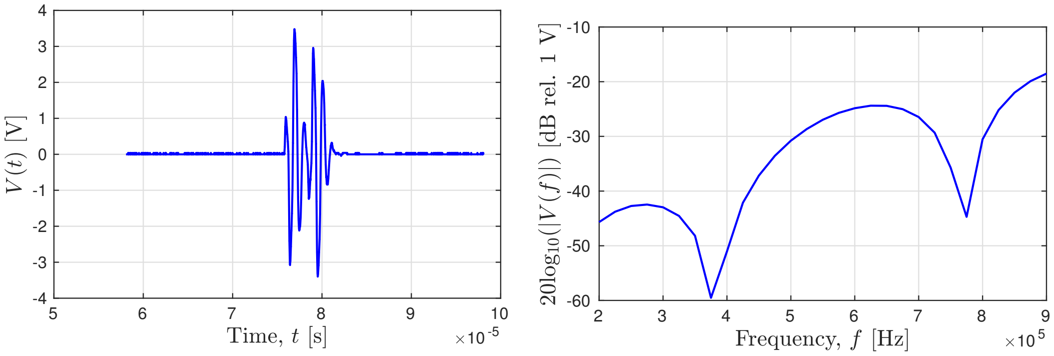

(a) (b)

Figure 6.13: Acquired signal for measurement B in the immersion method. Plexiglas plate rotated to $\theta_i = 38°$. **a**) Acquired signal in the time domain. **b**) Magnitude of the acquired signal in the frequency domain.

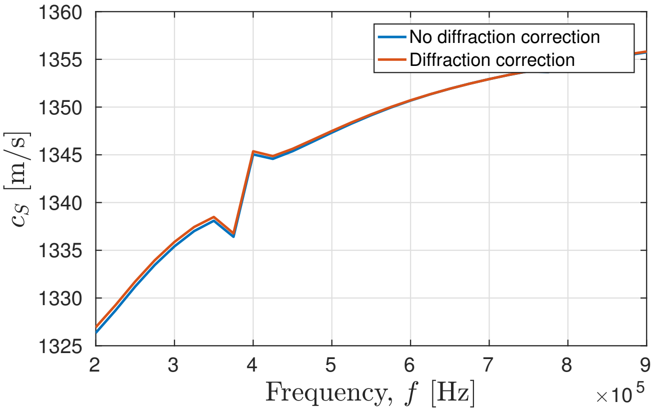

Figure 6.14: c_S for the 20 mm plexiglas plate measured with the immersion method using the Fourier spectrum method.

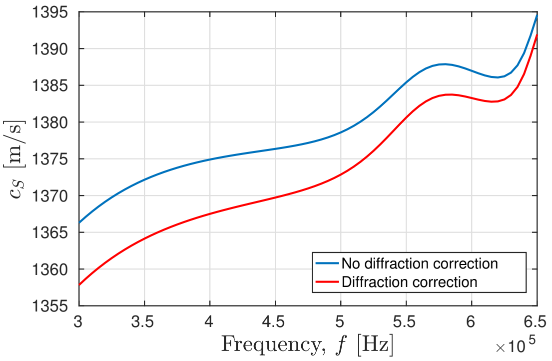

Figure 6.15: Measured c_S for the 60 mm plexiglas specimen using the solid buffer method with the Fourier spectrum method.

As discussed for the P-wave measurements, small irregularities on the end-face of the solid buffers may affect the plane wave transmission coefficient. The polyurethane film used on the surface of the buffers in the S-wave transducers (see transducer design, Ch. 4.3) may alter the transmission coefficient. Rogers and Buren's diffraction correction model is defined for P-waves. Using this diffraction correction is not necessarily correct. The shear wave piezoelectric elements are only sensitive to shear waves parallel to the polarization direction. From observations, a relative rotation between the transmitting and receiving transducer affects the phase of the acquired signal.

In Fig. 6.15, Fig. 3.24 is repeated. It shows a typical measurement for c_S for the 60 mm plexiglas cylinder using the solid buffer method. Other measurements show that the reproducibility is within 20 m/s at 500 kHz. Time signals and magnitude responses for this particular measurement is shown in Sec. 3.5.2. No simulations are conducted to aid in an uncertainty analysis of the measurements conducted with the S-wave transducers. However, the measurements (giving maximum c_S) conducted with the S-wave transducers are compared with measurements from the immersion method presented in Fig. 6.14. This give $\Delta c_S^{compare} \approx 60$ m/s at 500 kHz.

Chapter 7

Results Hydrate

c_P, c_S and the change in α_P are measured for ten Bentheim sandstone specimen (cut from the same batch) during hydrate growth. The final hydrate saturation (S_H) is limited by S_{w0} and different values of S_{w0} are thus used in the experiments. One experiment is performed for each of the sandstones. Each experiment may last to up to two weeks. A list of the ten experiments is shown in Tab. 7.1. The measurement setup is detailed in Sec. 3.3. In experiments 1-4, P-wave transducers are used and in experiment 5-10, S-wave transducers are used.

In Sec. 7.1 the development in c_P and c_S during hydrate growth is presented. c_P and c_S measured in the different experiments are compared at $S_H = 0.5$. The numerical models presented in Secs. 2.5.1-2.5.3 are used to analyze the hydrate growth pattern inside the Bentheim sandstones.

Similar to the Bentheim sandstone sound velocity measurements, the development in α_P during hydrate growth is presented in Sec. 7.2. Due to the uncertainties discussed in Sec. 6.1.3, the compressional wave attenuation is presented as α_P relative to α_P at hydrate saturation $S_H = 0.2$: $\Delta\alpha_P = \alpha_P - \alpha_P(S_H = 0.2)$. The numerical models presented in Sec. 2.5.4-2.5.7 are used to discuss which attenuation mechanisms that may be present in the hydrate bearing sandstones.

In Sec. 7.3, the frequency dependent value ($c_P(f) - c_P(f_0)$) at $S_H = 0.5$ are presented. The attenuation spectrum ($\alpha_P(f) - \alpha_P(f_0)$) is presented at $S_H = 0.2$ and $S_H = 0.5$. $f_0 = 350$ kHz. Due to missing data points and large measurement uncertainty for the S-wave transducers, dispersion and attenuation spectrum plots are not provided for all ten experiments.

A summary of the measurement results and a discussion is given in Sec. 7.4.

Table 7.1: List of S_{w0}, final S_H and transducers used in experiment 1-10.

Experiment nr.	S_{w0}	Transducers used	Final S_H
1	0.48	P-transducers	0.58
2	0.55	P-transducers	0.54
3	0.65	P-transducers	0.67
4	0.69	P-transducers	0.73
5	0.73	S-transducers	0.62
6	0.76	S-transducers	0.73
7	0.78	S-transducers	0.85
8	0.92	S-transducers	0.85
9	0.94	S-transducers	0.78
10	0.95	S-transducers	0.85

7.1 Development in c_P and c_S during hydrate growth for Bentheim sandstones in experiment 1-10

c_P and c_S are measured and modeled using the lossless HFl, HFr and HC-models described in Secs. 2.5.1, 2.5.2 and 2.5.3, respectively, during hydrate growth for experiment 1-10 (listed in Tab. 7.1). To monitor S_H in the Bentheim sandstone core, the consumed methane gas is continuously logged. From the consumed methane gas and volume of the pores inside the Bentheim sandstone core, S_H is calculated using the iteration scheme presented in Eq. (2.3). The measurements are presented as a function of S_H for experiment 1-10 and as a function of S_{w0} at fixed hydrate saturations for experiment 1-10.

7.1.1 Measurements of c_P and c_S for Bentheim sandstones hydrate growth in experiment 1-10

The solid buffer method is used to measure c_P and c_S during hydrate growth for the ten experiments presented in Tab. 7.1. In experiment 1-4, the initial water saturation, S_{w0}, of the sandstones range from 0.48 to 0.69 and the in-house built P-wave transducers are used. In experiment 5-10, S_{w0} range from 0.73 to 0.95 and the in-house built S-wave transducers are used.

The solid buffer method is used in all the experiments (Sec. 3.3). As detailed in Sec. 3.3.1, the amplitude of the EMF inside the signal generator is dynamically reduced from 100 mV before hydrate growth to a minimum of 1 mV after hydrate growth. A one cycle 500 kHz input signal is used. The oscilloscope is programmed to log the acoustic signal every 15th min and to automatically adjust the window so that the logged signal is not clipped. For the P-wave transducers (experiment 1-4), the Fourier spectrum method (Eq. (3.50)) is used to find c_P at frequencies 350 kHz, 500 kHz and 600 kHz. Also the basic pulse method using the first arrival of the signal is used with the P-wave transducers (Eq. (3.46)). For the S-wave transducers (experiment 5-10), the Fourier spectrum method is used to find c_S at frequency 500 kHz (Eq. (3.50)).

Experiment 1-2: Measured c_P for hydrate-bearing Bentheim sandstones with S_{w0} 0.48 and 0.55

Acquired time signals using the in-house built P-wave transducers are shown for experiment 1 in Fig. 7.1. The measured voltage signals presented in Fig. 7.1 are representative for experiment 1-4. In a), measurement A is shown, where the buffers are face to face. In b), a time signal for measurement B is presented before hydrates start to form and in c), a time signal for measurement B at the end of the hydrate growth process is presented.

The input settings of the EMF in the signal generator is a 1 cycle, 500 kHz pulse in all measurements presented in Fig. 7.1. In a), b) and c), the input voltage amplitudes are 1 mV, 100 mV and 5 mV, respectively. From figure b) to figure c) the main pulse is shifted in time due to the change in c_P. The pulses arriving later than the main pulse, are reflections. In b) there is a small signal arriving before the main pulse. It arrives at (approximately) the same time as the pulse in figure a). If this is a P-wave traveling through the specimen, this would correspond to a $c_P \to \infty$ in the specimen. It is not clear what this signal is. It is here suggested that there may exist an electrical noise signal at time 0 (not seen in the figure). This electrical noise signal excites the receiving transducer and an acoustic signal is generated. The small pulse at around 35 µs in the figure may then be the acoustic signal traveling to the buffer-specimen interface at the receiving side and being reflected back to the receiving transducer. This way the receiving transducer is acting as the transducer in a "pulse'-echo" measurement. In figure c), this unintended pulse-echo measurement is not seen because the input voltage on the transmitting side is much smaller and the electrical noise on the receiving side is much smaller too.

In b) there is also seen to be more noise in general. However, the repeatability of measurements conducted before hydrates start to grow is seen to be approximately the same as for the plexiglas measurements (Eq. (6.5)). Thus the noise seen in figure b) is assumed to not affect the measurements critically. The sensitivity study for the plexiglas measurements given in Sec. 6.1 is also assumed to be valid for the hydrate experiments, that is $\Delta c_P^{sens} \approx 12$ m/s.

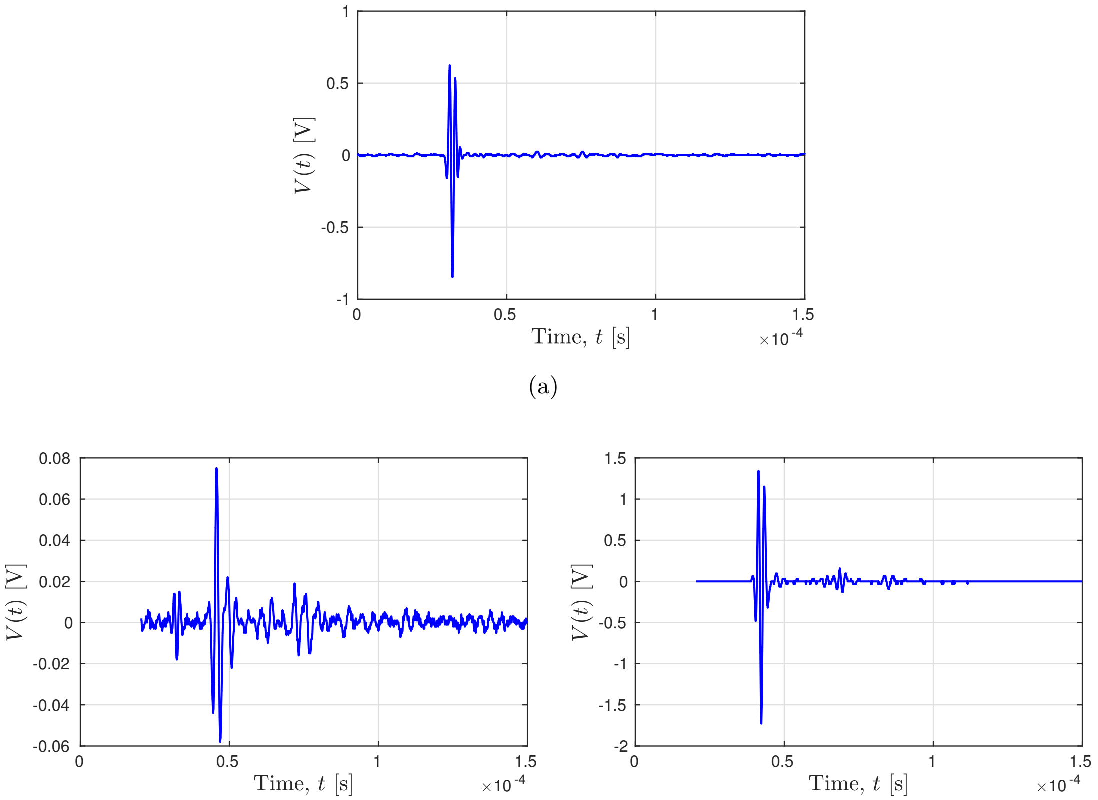

(a)

(b)

(c)

Figure 7.1: Typical measured time signals during experiment 1 for **a)** the reference measurement (measurement A), **b)** the sandstone before hydrate growth (measurement B), $S_H = 0$ and **c)** the sandstone at maximum hydrate saturation (measurement B), $S_H \approx 0.55$.

For experiments 1-2 shown in Fig. 7.2, the P-wave transducers are used. In experiment 1 presented in Fig. 7.2 a), c_P increases with approximately 1000 m/s during hydrate growth for the measurement frequencies 350 kHz, 500 kHz and 600 kHz. In experiment 2 presented in Fig. 7.2 b), c_P increases with approximately 1100 m/s during hydrate growth using frequency 350 kHz. c_P increases with approximately 900 m/s during hydrate growth using the 500 kHz and 600 kHz. In general, higher frequencies give a higher c_P. Dispersion mechanisms are discussed further in Sec. 7.3. The maximum S_H is approximately the same in experiment 1 and 2, i.e ranging from $S_H = 0.5$ to 0.6. Experiments 1-2 have the lowest S_{w0}, 0.48 and 0.55, respectively of all 10 experiments. At zero hydrate growth, c_P at 500 kHz is approximately 3000 m/s for experiment 2 and 2900 m/s for experiment 1. This difference may be due to several factors:

c_P may differ from specimen to specimen depending on porosity, cracks or mineral distribution [124]. From the literature, the pore fluid distribution is also known to affect

c_P of the porous rock [42, 26, 24]. If some regions are fully water-saturated and other regions contain gas ("patchy saturation"), c_P is higher than if the water is uniformly distributed in the pores. Even though 10 Nm torque is used in experiment 1 and 2, the effective force exerted on the transducers may be different due to friction in the threads. This may give different confining pressures on the sandstones and different c_P. The confining pressure may close partially water-saturated compliant pores or cracks, giving fully water saturated pores [111, 112]. The difference seen in c_P before hydrate growth between Fig. 7.2 a) and b) may be due to the gas and water distribution. The higher measured c_P in Fig. 7.2 b) compared with a) indicates that the sandstone in experiment 2 have a more "patchy" saturation than the sandstone in experiment 1.

In experiment 1 and 2, the logging script malfunctioned in the early stage during hydrate growth. In these experiments there are only three data points from S_H =0-0.3. For S_H larger than 0.3, the data points are much denser.

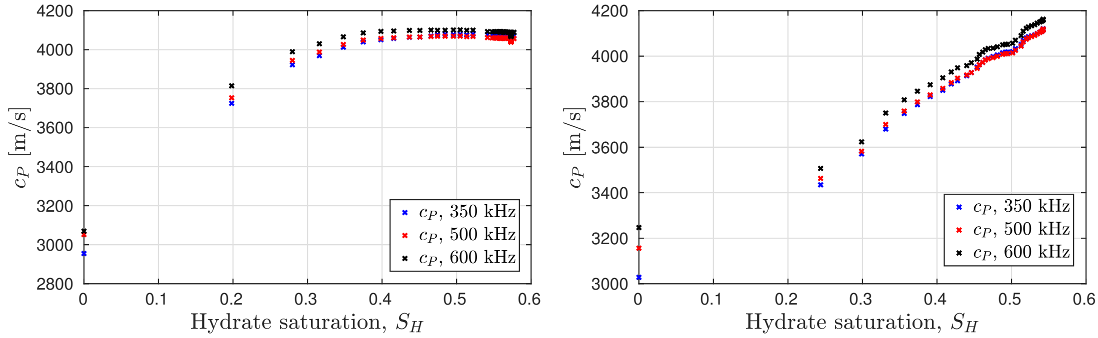

(a)

(b)

Figure 7.2: Measured c_P with increasing S_H for experiment 1 and 2. **a)** Experiment 1, S_{w0} 0.48. **b)** Experiment 2, S_{w0} 0.55.

Experiment 3-4: Measured c_P for hydrate-bearing Bentheim sandstones with S_{w0} 0.65 and 0.69

As for experiment 1 and 2, c_P for experiment 3 and 4 are measured. In Fig. 7.3, the measured c_P for two Bentheim sandstones during hydrate growth are presented. S_{w0} for experiment 1 and 2 are 0.65 and 0.69, respectively giving a maximum S_H of 0.67 and 0.72, respectively (Tab. 7.1). The vertical lines at maximum S_H in a) and c) are due to further development in wave velocity after hydrates stop to form. This development is plotted in b) and d) with time after hydrates start to form on the x-axis (hours).

The c_P-profile in Fig. 7.3 a) and b) are more similar to the profile in Fig. 7.2 b), than the profile in Fig. 7.2 a). For experiment 2 (Fig. 7.2 b)), the S_{w0} is 0.55, which is closer to the S_{w0}s of experiment 3 and 4 than the S_{w0} in experiment 1 (Fig. 7.2 a)).

For experiment 3 in Fig. 7.3 a), the measured c_P is seen to increase with approximately 1100 m/s from zero to maximum hydrate growth. For experiment 4 in Fig. 7.3 c), the measured c_P is seen to increase with approximately 900 m/s from zero to maximum hydrate growth. The measured c_P in experiment 3 and 4 are similar to the measured c_P in experiment 2. However, there are some development in c_P after maximum hydrate growth is reached. The development after maximum S_H seen in Fig. 7.3 b) and d) may be due to redistribution of the hydrates. That is, hydrates earlier forming in the pore fluid, reforming for example into the frame, becoming a load bearing grain. Redistribution of hydrates have been observed earlier in sandstones [203]. Hydrates are not in thermal equilibrium and it is seen from micro-model experiments that redistribution may occur [204].

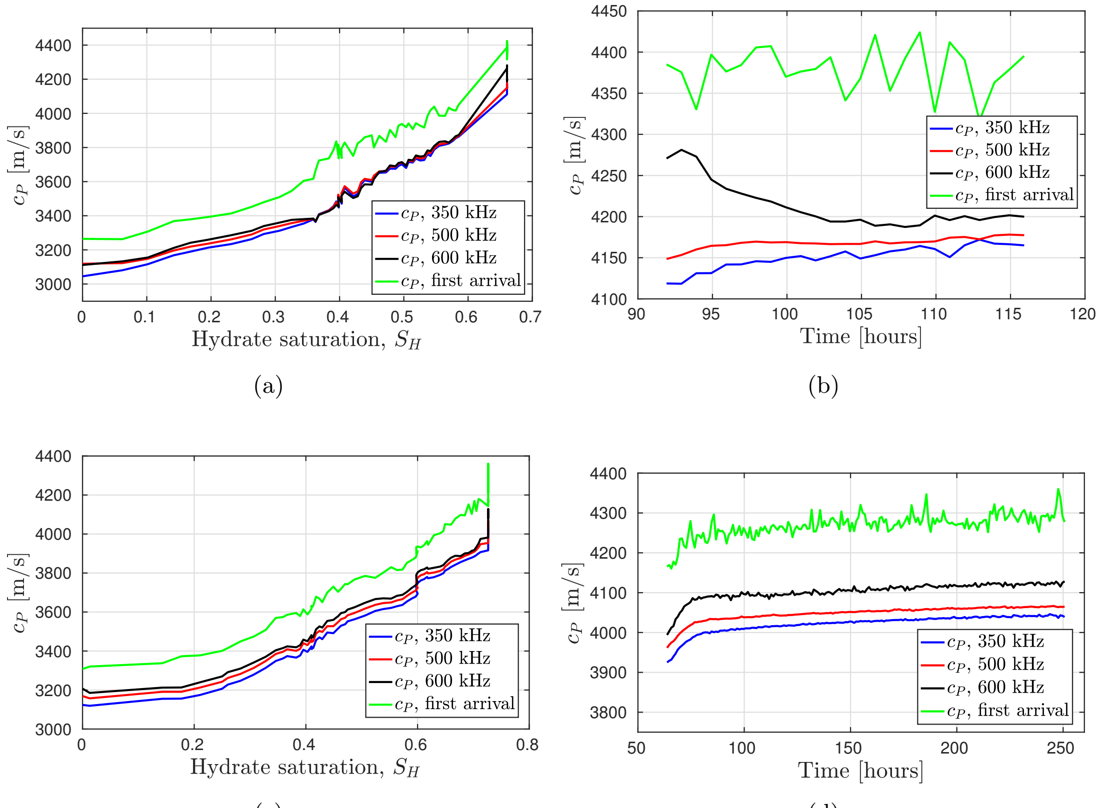

(a) (b)

(c) (d)

Figure 7.3: Measured c_P for experiment 3 and 4 during hydrate growth and by time after maximum S_H. The data points are so dense that a continuous line is representative. **a)** Experiment 3, hydrate growth. S_{w0} 0.65. **b)** Experiment 3, wave velocity development at maximum S_H. **c)** Experiment 4, hydrate growth. $S_{w0} = 0.69$. **b)** Experiment 4, wave velocity development at maximum S_H.

In the same way as for experiment 1 and 2, c_P is obtained using the Fourier spectrum method for frequencies 350 kHz, 500 kHz and 600 kHz. In addition to these three measurement frequencies, the first arrival of the signal is used to find c_P. The increase in c_P for low S_H is seen to be more moderate in experiment 3-4 compared with experiments 1-2.

The accuracy of using the fist arrival in wave velocity measurements is debated [50, 49], however this method is widely used to find the compressional and shear wave velocities in porous rocks [22, 21]. As seen in Fig. 7.3, the measured c_P is higher using the first arrival of the signal compared with the Fourier spectrum method. As discussed by Molyneux et al. [50, 49], the first arrival of the signal may be challenging to find. Also, higher frequency-components are known to be well represented in the first period of a signal propagating through porous rocks [50, 49]. Thus, dispersion effects may give a high c_P using the first arrival of the signal.

Experiment 5-7: Measured c_P and c_S for hydrate-bearing Bentheim sandstones with S_{w0} 0.73-0.78

By measuring both c_P and c_S during hydrate growth, more insight may be gained compared with measurements where only the compressional wave velocity is measured. In experiment 5, 6 and 7, c_P and c_S are measured for sandstone specimen having S_{w0} 0.73, 0.76 and 0.78, respectively, giving maximum S_H of 0.62, 0.72 and 0.85 respectively (see Tab. 7.1).

As described in Sec. 3.3.1, the solid buffer Fourier spectrum method is used with the in-house built S-wave transducers to measure c_P and c_S during hydrate growth. 10 Nm torque is applied on the transducer holders. Care is taken so that the transducers do not twist when using the torque key. The receiving and transmitting properties of the shear-polarized piezoelectric elements are depending on the orientation of the piezoelectric element. The S-wave transducers are aligned so that the square shaped piezoelectric elements inside the transducers are positioned along the same direction.

In Fig. 7.4 a) the acquired voltage signal in measurement A for the solid buffer method is shown. The compressional wave pulse arrives at approximately 25 µs. The shear wave pulse arrives approximately after 45 µs. Identification of the other pulses are discussed in 3.5.2, Fig. 3.19.

In Fig. 7.4 b) and c), the acquired voltage signals in measurement B before and at full hydrate growth are shown, respectively for experiment 5. The input settings of the EMF in the signal generator is a 1 cycle 500 kHz pulse with amplitude 100 mV and 10 mV, respectively. The compressional wave pulse arrives at approximately 40 µs and 35 µs in figure b) ($S_H = 0$) and c) ($S_H \approx 0.62$), respectively. The shear wave pulse arrives at approximately 75 µs and 70 µs in figure b) and c), respectively.

No exact number for the uncertainty in the c_S and c_P measurements using the S-wave transducers are given. However the "comparison" studies for the plexiglas measurements given in Secs. 6.2, and 6.3 are also assumed to be valid for the hydrate experiments, that is $\Delta c_P^{compare} \approx 60$ m/s and $\Delta c_S^{compare} \approx 60$ m/s.

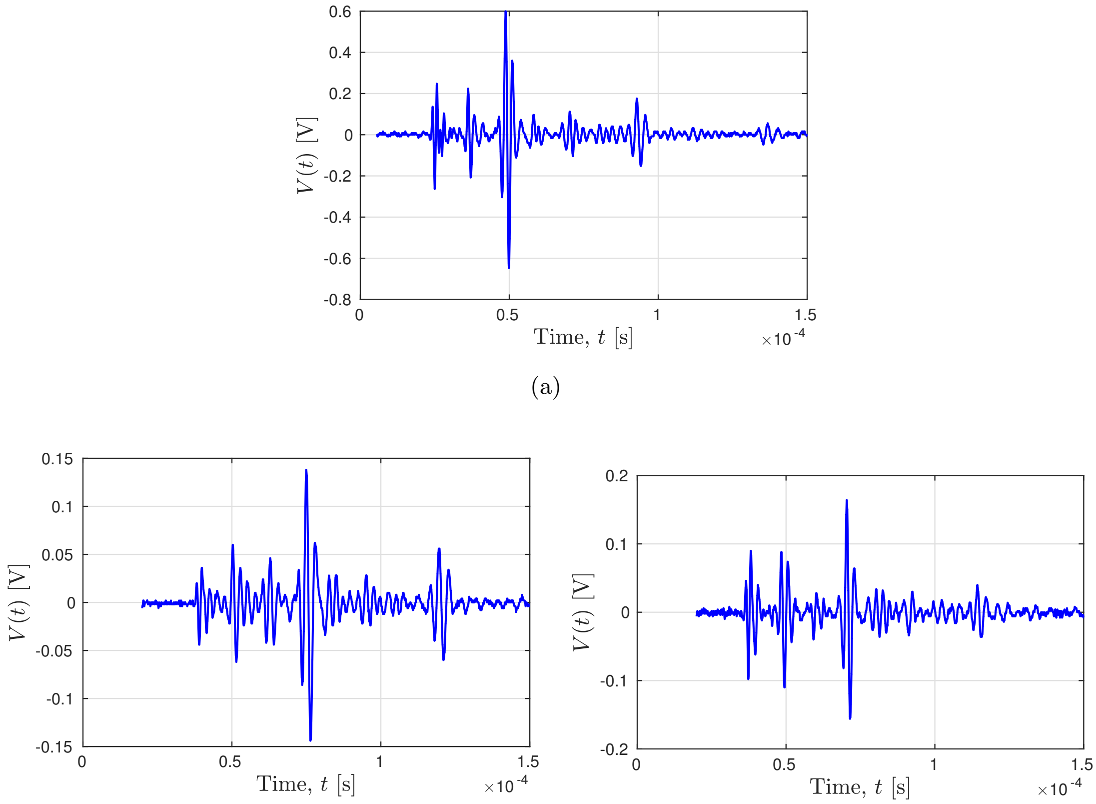

(a)

(b)

(c)

Figure 7.4: Typical measured time signals during experiment 5 for **a)** the reference measurement (measurement A), **b)** the sandstone before hydrate growth (measurement B), $S_H = 0$ and **c)** the sandstone at maximum hydrate saturation (measurement B), $S_H \approx 0.6$.

The measured c_P (blue curve) in experiment 5-7, shown in Fig. 7.5 a), c) and e), exhibits some of the same features as c_P measured in experiment 3 and 4 (Fig. 7.2). At low S_H, there is almost no increase in c_P. Before hydrates start to grow, c_P is approximately 3400 m/s for experiment 5, and 3250 m/s for experiment 6-7. A power outage at University of Bergen during experiment 6, left a gap in the data, which is marked by the red circles.

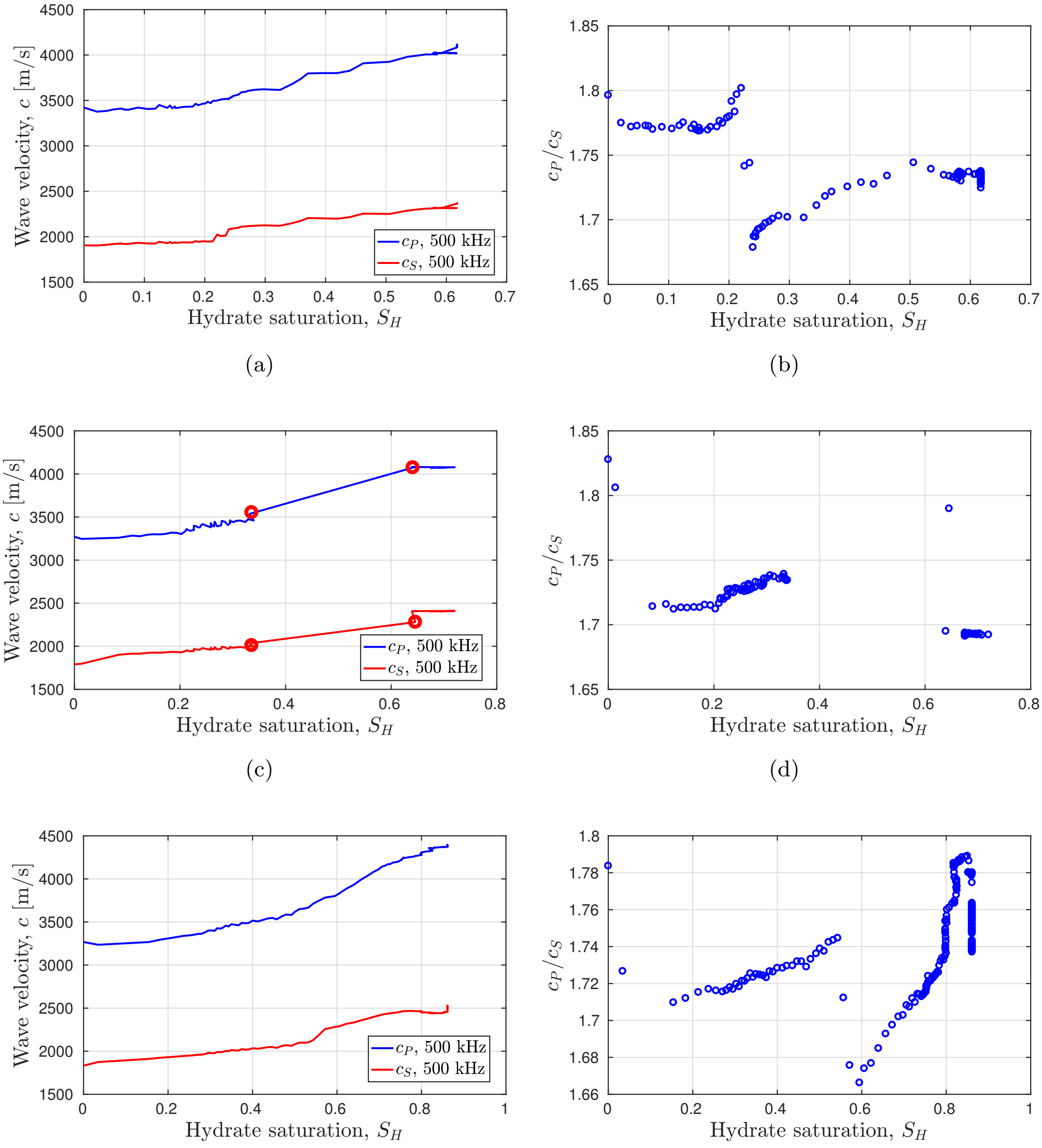

(a) (b)

(c) (d)

(e) (f)

Figure 7.5: Measured c_P and c_S for experiment 5-7 at 500 kHz. There are no data-points in between the red markers in experiment 6 due to a power outage. **a)** Experiment 5: $S_{w0} = 0.73$. **b)** Experiment 5: c_P/c_S- ratio. **c)** Experiment 6: $S_{w0} = 0.76$. **d)** Experiment 6: c_P/c_S- ratio. **e)** Experiment 7: $S_{w0} = 0.78$. **f)** Experiment 7: c_P/c_S- ratio.

Of the three experiments the highest c_P is measured for experiment 7 where S_H is highest. The measured c_P changes from zero to maximum S_H in experiment 5-7 as 3400-4150 m/s, 3250-4100 m/s and 3250-4400 m/s respectively. Contrary to experiment

3-4, there seems to be little development in the measured c_P in experiment 5-7 after full hydrate growth.

The measured c_S shown in Fig. 7.5, changes from zero to maximum S_H in experiment 5-7 as 1900-2400 m/s, 1800-2400 m/s and 1800-2500 m/s, respectively (red curve). The measured c_S (red curve) shows similar behavior as c_P (blue curve). A small increase in c_S and c_P is seen at low S_H and a higher increase is seen towards higher S_H.

In Fig. 7.5 b), d) and f) the ratio between the compressional and shear wave velocity (c_P/c_S) is plotted. In 7.5 d) and f) there seem to be an increase in the c_P/c_S-ratio until a drop of approximately 0.1 in the c_P/c_S-ratio is seen at around S_H =0.6. In figure d), this drop is seen immediately after the measurements continued after the power outage. In b), there seems to be a drop in the c_P/c_S- ratio at around S_H =0.2. There might be a drop starting right after $S_H = 0.6$. However hydrates ceased growing at this S_H and no conclusion can be made. In f) there seems also to be a drop at around $S_H = 0.85$. There is a general trend of a growing c_P/c_S-ratio with one or two sudden drops.

Experiment 8-10: Measured c_P and c_S for hydrate-bearing Bentheim sandstones with S_{w0} 0.92 and 0.95

As for experiment 5-7, c_P and c_S are measured in experiment 8-10 and presented in Fig. 7.6. In experiment 8-10, the S_{w0} are 0.92, 0.94 and 0.95 respectively, giving maximum S_H of 0.85, 0.78 and 0.85 respectively (Tab. 7.1). The same experimental setup as is used for experiment 5-7, is used in experiment 8-10.

Neither the measured c_P or c_S in Fig. 7.6 a), c) and e) are showing any sign of increase for low S_H. A possible decrease in c_P for low S_H is observed. S_H reaches the highest value in experiment 8 (figure a)) where the highest wave velocities are observed as well. c_P increase from 3500 m/s-4400 m/s, 3500 m/s - 4200 m/s and 3300 m/s - 4200 m/s for experiment 8, 9 and 10, respectively. c_S increase from 1990 m/s-2550 m/s, 1900 m/s - 2450 m/s and 1900 m/s - 2400 m/s for experiment 8, 9 and 10, respectively.

In 7.6 b), d) and f) the c_P/c_S-ratio is plotted for experiment 8-10. In b), d) and f) there is a drop in the c_P/c_S-ratio at around S_H =0.4. There seem to be a slight increase in the c_P/c_S-ratio after the drop. There also seems to be a drop at around $S_H = 0.8$

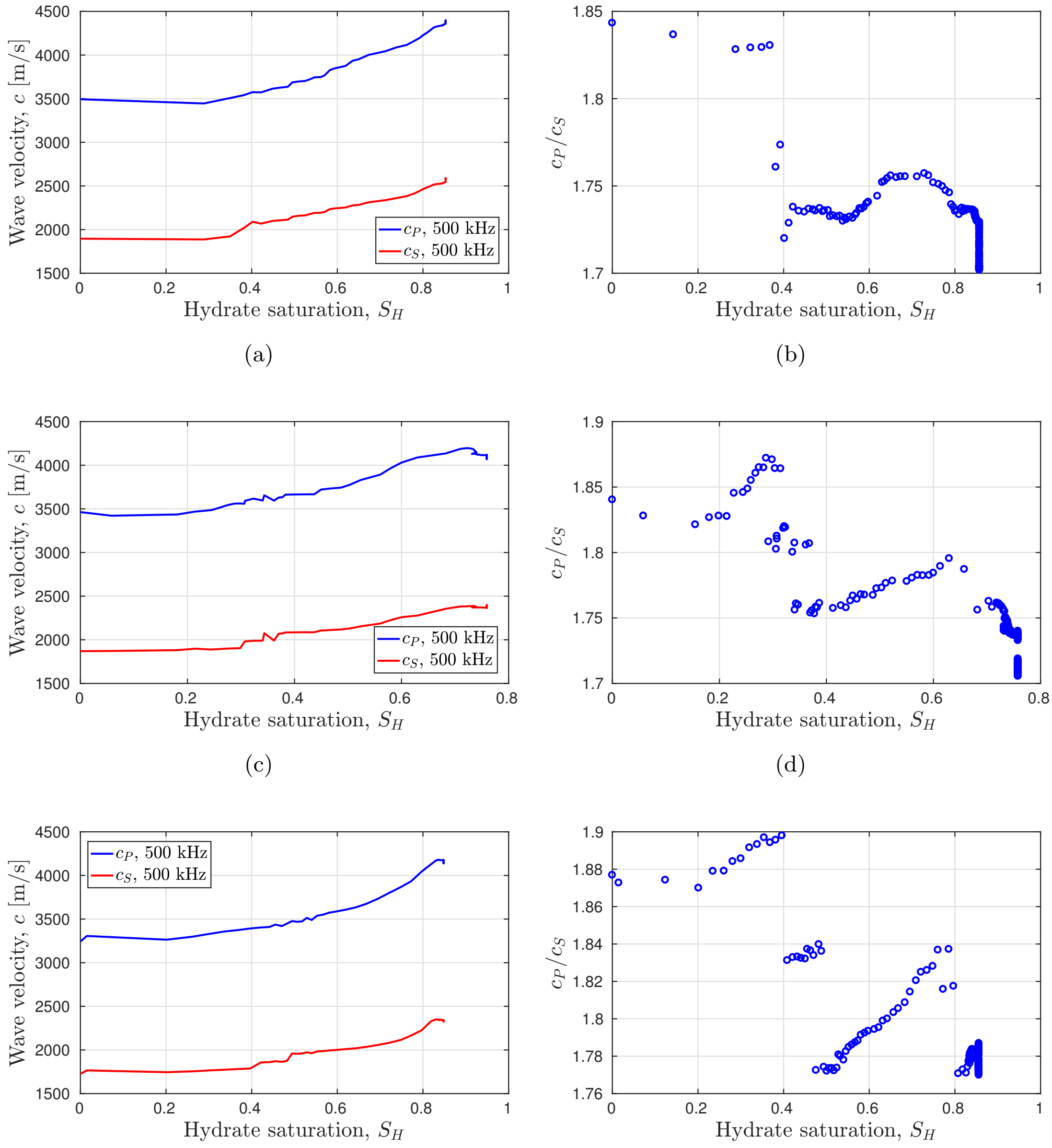

(a) (b)

(c) (d)

(e) (f)

Figure 7.6: Measured c_P and c_S for experiment 8-10 at 500 kHz. **a)** Experiment 8: $S_{w0} = 0.92$. **b)** Experiment 8: c_P/c_S- ratio. **c)** Experiment 9: $S_{w0} = 0.94$. **d)** Experiment 9: c_P/c_S- ratio. **e)** Experiment 10: $S_{w0} = 0.95$. **f)** Experiment 10: c_P/c_S- ratio.

7.1.2 Measured c_P and c_S at fixed S_H for experiment 1-10 as function of S_{w0}

From the measurements shown in the previous section, it is clear that higher S_H gives higher compressional and shear wave velocities. To compare results for the 10 experiments, the wave velocities have been plotted at S_H =0.5. In Fig. 7.7 a), c_P at $S_H = 0.5$ is plotted as a function of S_{w0} for the ten measurements.

In Fig. 7.7 a), c_P at $S_H = 0.5$ is plotted as a function of S_{w0} for the ten measurements. No clear relation between c_P and S_{w0} is seen. As discussed in Sec. 6.1.3, even if measurements are fairly accurate, the acoustic properties of two different Bentheim sandstones may be different due to for example different confining pressures in the pressure cell and non-uniformity of water and gas distribution.

In Fig. 7.7 b) the increase in c_P from $S_H = 0$ to $S_H = 0.5$ is plotted. This increase is labeled Δc_P. Δc_P as a function of S_{w0} shows a clear trend: Bentheim sandstones having low S_{w0} exhibit a larger Δc_P than Bentheim sandstones having higher S_{w0}. To the best of this authors knowledge this finding has not been reported.

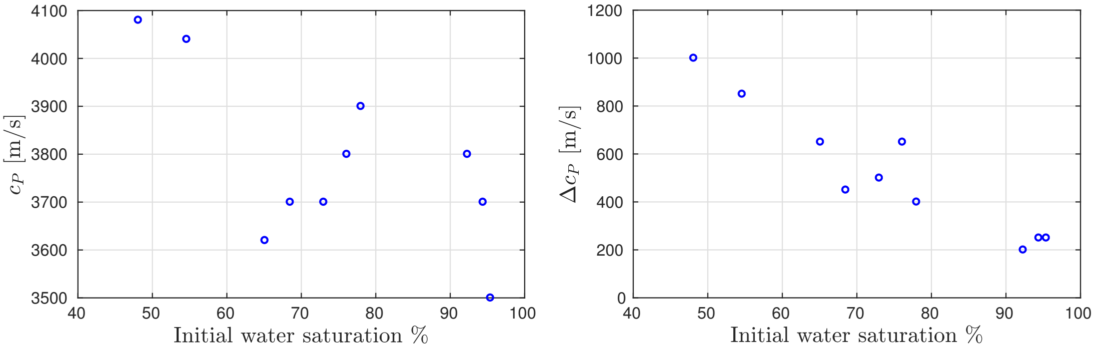

(a) (b)

Figure 7.7: Measured absolute and relative compressional wave velocity at $S_H = 0.5$ for experiment 1-10. **a)** Absolute compressional wave velocity (c_P) at $S_H = 0.5$. **b)** Increase in c_P from $S_H = 0$ to $S_H = 0.5$ (Δc_P).

In the same way as for the P-waves, c_S and the relative shear wave velocity (Δc_S) are plotted as a function of S_{w0} for the six shear wave experiments (Fig. 7.8). In Fig. 7.8 a) c_S is plotted and in figure b), Δc_S is plotted.

The measurements shown in Fig. 7.8 indicates the same trend as for the compressional wave measurements presented in Fig. 7.7. Sandstones having low S_{w0} have a larger Δc_S than sandstones having higher S_{w0}. The trend is, however, much weaker than the compressional wave measurements shown in Fig. 7.7.

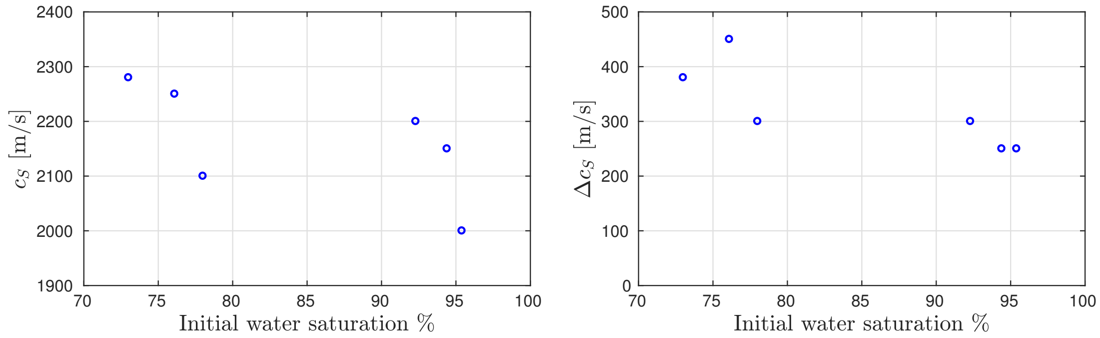

(a)

(b)

Figure 7.8: Measured absolute and relative shear wave velocity at $S_H = 0.5$ for experiment 5-10. **a)** Absolute shear wave velocity (c_S) at $S_H = 0.5$. **b)** Increase in c_S from $S_H = 0$ to $S_H = 0.5$ (Δc_S).

7.1.3 Numerical models and discussion of the development in c_P and c_S during hydrate growth in Bentheim sandstones

By comparison with measurements, numerical models (presented in Sec. 2.5) may give insight in how methane hydrates grow inside a porous rock or sandy sediment [119, 25, 28, 22, 21, 24]. Waite et al. [22] and Winters et al. [21] outlines three main categories in which hydrates may form inside a porous rock or sandy sediment.

The first main category is hydrate forming primarily in the pore fluid. In this work, this model is called HFl-model and is detailed in Sec. 2.5.1. There are two versions of this model. One version where the fluid and hydrates are uniformly distributed in the sandstone (”HFlU”) and one version where the fluid and the hydrates are distributed in patches (”HFlP”).

HFlU and HFlP are plotted for $S_{w0} = 0.5$ and 0.8 in Fig. 7.9 and 7.10, respectively. The other input parameters are given in Tab. 2.1. As water expands into methane hydrates with a volume expansion factor 1.26 (see Sec. 2.1.3), the maximum theoretical S_H with $S_{w0} = 0.5$ is $S_H = 0.5 \cdot 1.26 = 0.63$ if all water is converted to hydrates. For $S_{w0} = 0.5$ and 0.8, S_H is calculated up to 0.6 and 0.9, respectively, using Eqs. 2.18, 2.19 and 2.20. When hydrates uniformly distribute in the fluid, the hydrates in fluid model (HFlU) predicts no increase in c_P except for high S_H (blue curve in Fig. 7.9 a) and 7.10 a)). This is because the fluid bulk modulus is calculated with the Reuss average for this model (Eq. (2.23)). At high S_H, there is almost no free methane gas left in the sandstone and the gas bulk modulus stops to dominate the effective fluid bluk modulus calculated with te Reuss average. When water and gas are distributed in patches, the

HFlP-model predicts an increase in c_P of approximately 200 m/s from zero to $S_H = 0.5$. Neither the HFlU-model or the HFlP-model predict any change in c_S. This is because the shear modulus is not affected by the pore fluid [24]. c_S and c_P are slightly higher for $S_{w0} = 0.5$ (Fig. 7.9 a)) compared with $S_{w0} = 0.8$ (Fig. 7.10 a)). Even if increased water content stiffens the effective fluid bulk modulus, the effective fluid density is also larger which results in lower c_P and c_S. As fluids do not support shear waves [24], there is no shear modulus to be affected by the hydrate growth in the HFlU-model or the HFlP-model.

The c_P/c_S-ratio is similar in Fig. 7.9 b) ($S_{w0} = 0.5$) and 7.10 b) ($S_{w0} = 0.8$) for the HFlU-model and HFlP-model.

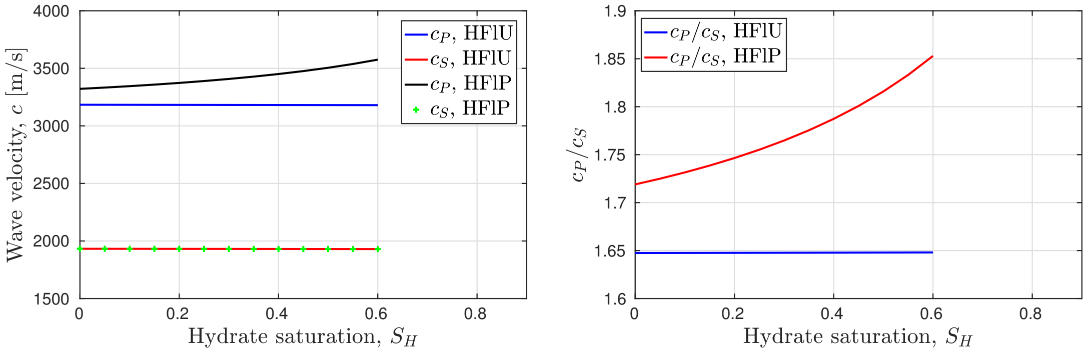

(a) (b)

Figure 7.9: Modeling of c_P and c_S using the "hydrates growing in fluid model" with $S_{w0} = 0.5$ for both uniform (HFlU-model) and patchy fluid distribution (HFlP-model). The models are presented in Sec. 2.5.1 with input parameters given in Tab. 2.1. **a)**) c_P and c_S using the HFlU-model and the HFlP-model. **b)** c_P/c_S-ratio using the HFlU-model and the HFlP-model.

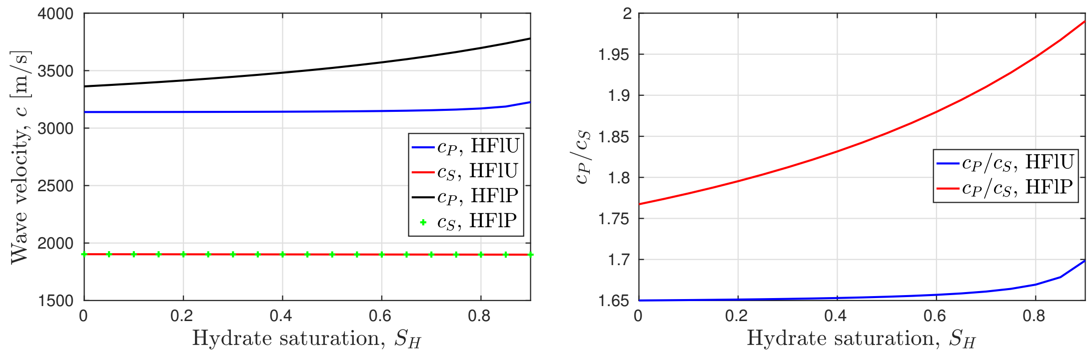

(a) (b)

Figure 7.10: Modeling of c_P and c_S using the "hydrates growing in fluid model" with $S_{w0} = 0.8$ for both uniform (HFlU-model) and patchy fluid distribution (HFlP-model). The models are presented in Sec. 2.5.1 with input parameters given in Tab. 2.1. **a)**) c_P and c_S using the HFlU-model and the HFlP-model. **b)** c_P/c_S-ratio using the HFlU-model and the HFlP-model.

Before the HFl-model is used to discuss the experimental results, the theoretical results from the other hydrate growth models, "hydrates grow in the frame-model" (HFr) (Sec. 2.5.2) and the cementation model (HC) (Sec. 2.5.3) are presented.

The second way hydrates can grow in a sandstone is becoming a load-bearing member of the dry frame, acting as second type of sediment grain. As for the HFl-model, there is one version where the fluid-components are uniformly distributed (HFrU-model) in the sandstone and one version where the fluid-components are distributed in patches (HFrP-model) throughout the sandstone. In Fig. 7.11 and 7.12 these models are presented for $S_{w0} = 0.5$ and $S_{w0} = 0.8$, respectively. When water and gas are uniformly distributed (blue curve in Fig. 7.11 a) and 7.12 a)) there is an increase in c_P of approximately 700 m/s from S_H 0 to 0.5. When water and gas are distributed in patches (black curve in Fig. 7.11 a) and 7.12 a)) there is an increase in c_P of approximately 600 m/s from S_H 0 to 0.5. The HFrU-model and HFrP-model give the same c_P at maximum hydrate growth in which all water is included in methane hydrates.

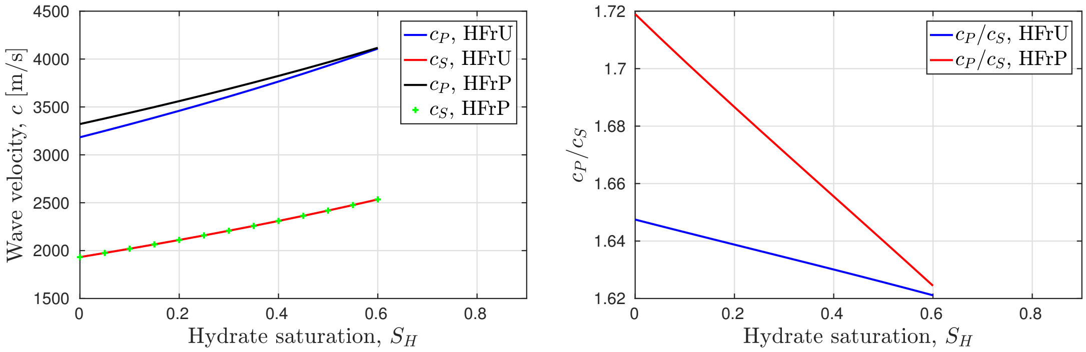

(a) (b)

Figure 7.11: Modeling of c_P and c_S using the HFr-model with $S_{w0} = 0.5$ for both uniform (HFrU-model) and patchy fluid distribution (HFrP-model). The models are presented in Sec. 2.5.2 with input parameters given in Tab. 2.1. **a)**) c_P and c_S using the HFrU-model and the HFrP-model. **b)** c_P/c_S-ratio using the HFrU-model and the HFrP-model.

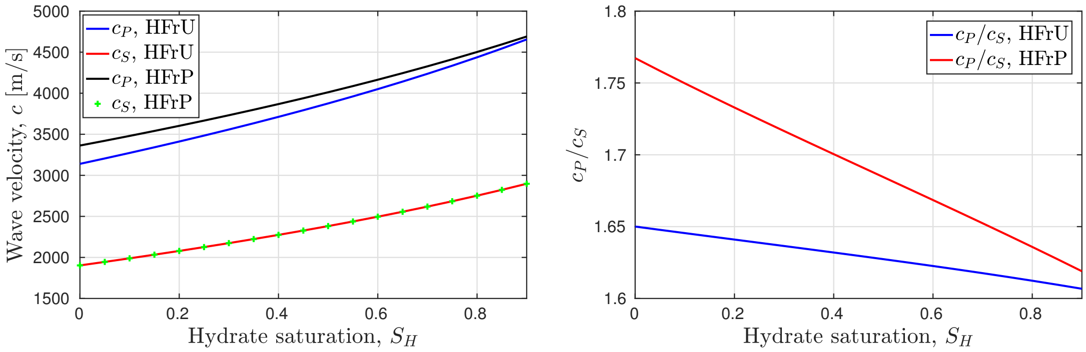

(a) (b)

Figure 7.12: Modeling of c_P and c_S using the HFr-model with $S_{w0} = 0.8$ for both uniform (HFrU-model) and patchy fluid distribution (HFrP-model). The models are presented in Sec. 2.5.2 with input parameters given in Tab. 2.1. **a)**) c_P and c_S using the HFrU-model and the HFrP-model. **b)** c_P/c_S-ratio using the HFrU-model and the HFrP-model.

For the HFr-model, both the effective bulk and shear moduli are affected. c_S is increasing approximately 500 m/s from $S_H = 0$ to $S_H = 0.5$ in Fig. 7.11 a) and 7.12 a). The c_P/c_S-ratio is dropping more for the HFrP-model compared with the HFrU-model.

The third way hydrates can grow in a sandstone is if hydrate act as cement around grain contacts, stiffening the dry frame. This model is based on Dvorkin et al. [25] and developed by Avseth et al. [27]. As described in Sec. 2.5.3 this model is developed for packs of sand at atmospheric pressure. This model is only used qualitatively to understand the hydrate growth pattern and not to model the absolute values of c_P and c_S in Bentheim sandstones.

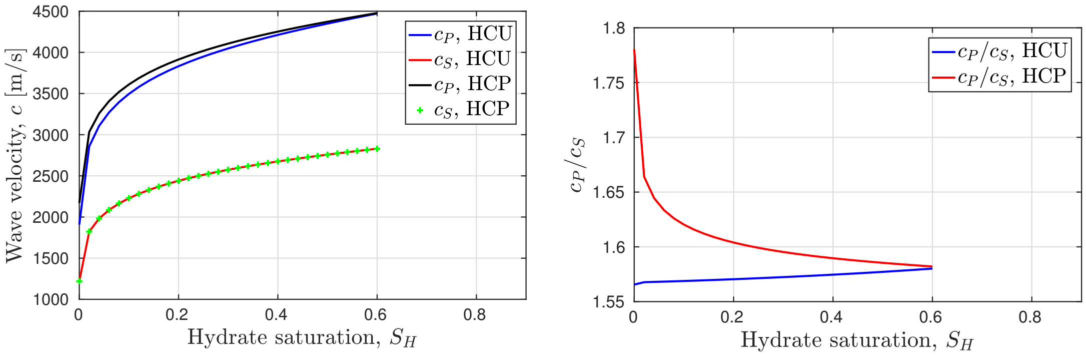

(a) (b)

Figure 7.13: Modeling of c_P and c_S using the "cementation model" with $s_{w0} = 0.5$ for both uniform (HCU-model) and patchy water and gas distribution (HCP-model). The models are presented in Sec. 2.5.3 with input parameters given in Tab. 2.1. **a)**) c_P and c_S using the HCU-model and the HCP-model. **b)** c_P/c_S-ratio using the HCU-model and the HCP-model.

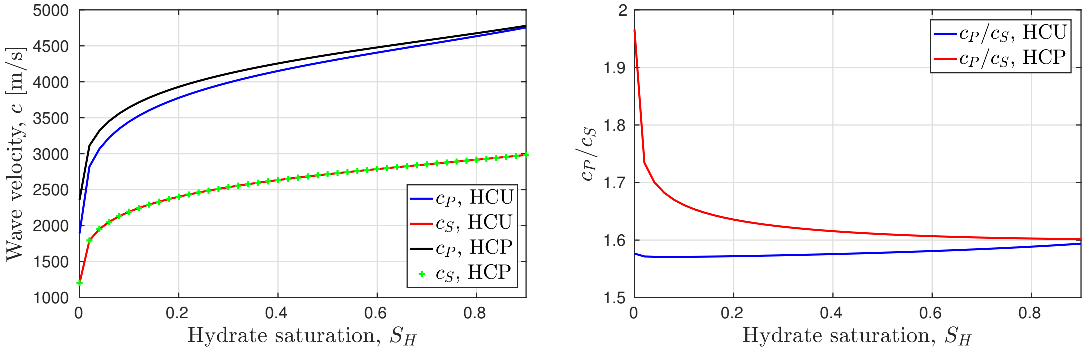

(a) (b)

Figure 7.14: Modeling of c_P and c_S using the "cementation model" with $s_{w0} = 0.8$ for both uniform (HCU-model) and patchy water and gas distribution (HCP-model). The models are presented in Sec. 2.5.3 with input parameters given in Tab. 2.1. **a)**) c_P and c_S using the HCU-model and the HCP-model. **b)** c_P/c_S-ratio using the HCU-model and the HCP-model.

The cementation model with uniform (HCU) and patchy (HCP) gas and water distribution give a dramatic increase in c_P and c_S at small levels of S_H for $S_{w0} = 0.5$ and $S_{w0} = 0.8$ (Figs. 7.13 a) and 7.14 a), respectively). For patchy water and gas distribution there is also a significant drop in the c_P/c_S-ratio shown in Figs. 7.13 b) and 7.14 b). For the HCU-model the c_P/c_S-ratio is almost constant for increasing hydrate content.

These three models describing the three categories of hydrate growth (fluid, frame and cementation) inside the sandstone are used to interpret the measurement results in experiment 1-10.

Experiment 1-2

By comparing the measured c_P for experiment 1 shown in Fig. 7.2 a) with the modeled c_P using the HFlU and HFlP shown in Fig. 7.9 a), a strong indication is seen that the increase in c_P is likely not due to hydrate growing inside the pore fluid. The modeled increase in c_P is approximately 200 m/s using the HFlP-model and the measured c_P shows an incrase of 900 - 1000 m/s for experiment 1 from S_H 0 - 0.5.

The total increase in the measured c_P of approximately 1000 m/s (in Fig. 7.2 a)) may partly be described by the HFrU-model or HFrP-model which predicts an increase in c_P of 900 - 1000 m/s depending on the fluid distribution (Fig. 7.11 a)). However, by examining the shape of the measured $c_P - S_H$ - curve for low S_H (Fig. 7.2 a)), the hydrate in frame models do not predict the increase in c_P from $S_H = 0$ to $S_H = 0.3$. The hydrate cementing model, which is developed for packs of sand at atmospheric pressure, is used to qualitatively describe the hydrate growth pattern.

In Fig. 7.13, the two versions of the cementing model with $S_{w0} = 0.5$ is plotted. Here, methane hydrates coat and cement the grains in the sandstone. Hydrate acting as cement around grain contacts may explain the dramatic increase seen for low S_H in Fig. 7.2 a). For $S_H > 0.4$, there is no development in the measured c_P. The only model able to explain this among the three models presented above is the HFlU-model (blue curve in Fig. 7.9 a)).

The measured c_P for experiment 2 in Fig. 7.2 b) shows a development that can fairly well be described with hydrate in frame model. There is an increase in c_P around $S_H = 0.3$ that is not well explained with the hydrate in frame models. The 500 kHz measurement (red curve in Fig. 7.2 b)) is plotted in the same figure as the HFrU and HFrP-models in Fig. 7.15. No absolute conclusion can be made whether the hydrate growth pattern can be solely described by the hydrate in frame model or if it is a combination between the hydrates in fluid model, hydrates in frame model and hydrate cementing model.

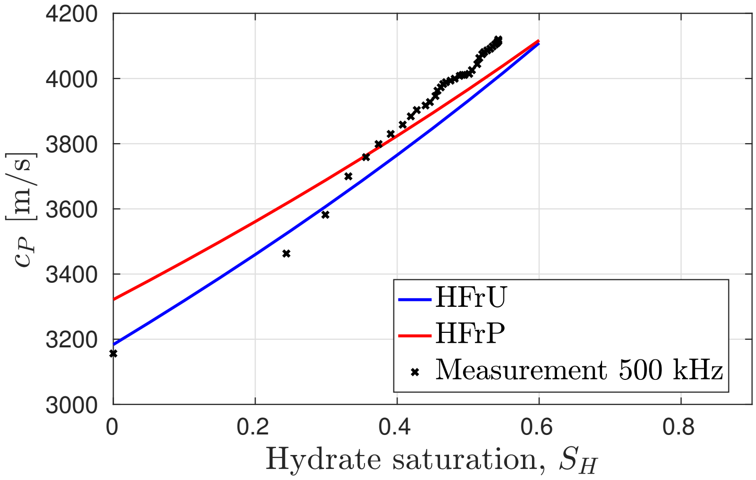

Figure 7.15: Measured c_P for experiment 2 with the solid buffer Fourier spectrum method at frequency 500 kHz plotted together with the HFrU and HFrP-models with $S_{w0} = 0.5$.

Experiment 3-4

The measured increase in c_P during hydrate growth in experiment 3-4 (Fig. 7.3) is similar to the measurements in experiment 2 (Fig. 7.2 b)). Whether $S_{w0} = 0.5$ or $S_{w0} = 0.8$ is not seen to affect the simulated c_P with the HFrU or HFrP-models (Fig. 7.11 a) and Fig. 7.12 a)). $S_{w0} = 0.8$ is used to compare with the 500 kHz measurement in experiment 4, shown in Fig. 7.16.

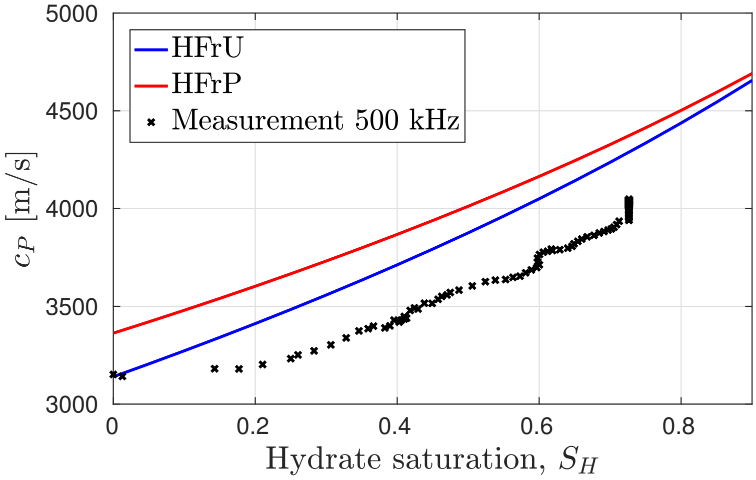

Figure 7.16: Measured c_P for experiment 4 with the solid buffer Fourier spectrum method at frequency 500 kHz plotted together with the HFrU and HFrP-models with $S_{w0} = 0.8$.

Similar, however, the increase in c_P is smaller for S_H below 0.2 in experiment 4 (red curve in Fig. 7.3 b)) compared with experiment 2 (red curve in Fig. 7.2 b)). The hydrate in frame model shown in Fig. 7.16 is not describing the measured c_P in experiment 4 well for S_H less than 0.2. It seems likely that hydrates are at least partially forming in the pore fluid below $S_H = 0.2$. For higher S_H, there is a better fit between the HFr-model and the measured c_P in experiment 4. Like for experiment 1-2, no absolute conclusion can be made, however, it seems likely that there is a combination between hydrates forming in the pore fluid and on the frame. To gain further insight in the hydrate growth pattern, shear wave transducers are used to measure both the compressional and shear wave velocity during hydrate growth in experiment 5-10.

Experiment 5-10

c_P in experiment 5-7 increases with less than 100 m/s from $S_H = 0$ to $S_H = 0.2$. (Fig. 7.5 a), c) and e)). c_S in experiment 5 and 7 also increase with less than 100 m/s. c_S in experiment 6 increase with less than 200 m/s from $S_H = 0$ to $S_H = 0.2$. As water does not support shear waves, any change in c_S must be due to changes in the solid frame. The c_P/c_S-ratios for experiment 5-7 are plotted in Fig. 7.5 b), d) and f). As detailed in Ch. 6, the uncertainty in the sound velocity measurements are at least 60 m/s, using the S-wave transducers with the solid buffer method. This means that there is at least an uncertainty of 0.1 in the c_P/c_S-measurements. Therefore extra care is taken when analyzing the c_P/c_S-ratio.

The drop in the measured c_P/c_S-ratio for low S_H in Fig. 7.5 b), d) and f) can theoretically be described with the cementation model if the gas is distributed in patches (HCP-model, Fig. 7.14). However, a combination of hydrates forming in the frame and hydrates forming in the fluid may also explain the c_P and c_S measurements for experiment 5-7.

For experiment 8-10 shown in Fig. 7.6, no increase is seen in neither c_P nor c_S for $S_H < 0.2$. This is a feature of the HFl-model (Fig. 7.10) which indicates that all hydrates are formed in the pore fluid for $S_H < 0.2$ in experiments 8-10. In Fig. 7.17, c_P and c_S are plotted for experiment 9 together with the HFrU and HFrP-models. In this figure it seems like the patchy distribution of the gas and water gives the best fit with the measurements before hydrates start to grow. However, there is no measured increase in c_P or c_S, and the HFlU (uniform gas and fluid distribution) is the best suited model when there is no increase in c_P. One explanation may be that gas and water are mostly distributed in patches, however, methane hydrates are only forming in pores where both water and gas exist. This way the Reuss average must be used with the pores where hydrates form, and thus c_P is not affected.

As for c_P in experiment 4 shown in Fig. 7.16, the increase in c_P for S_H larger than 0.2 is fairly well described with hydrates in frame model. This is also true for c_S. In experiment 8-10 (Fig. 7.6) there is a clear measured drop in c_P/c_S at around $S_H = 0.4$. As the measurement uncertainty is at least 0.1 (see Ch. 6), this drop is not necessarily physical. However, it is measured in three different sandstone specimen in three independent experiments, which indicates at least that c_S increase relative to c_P. The HCP-model is able to explain such a drop in the c_P/c_S-ratio directly. However, hydrates floating around in the pore fluid may start to grow into the frame at higher S_H [204]. This way, hydrates previously floating in the fluid may suddenly act as frame building hydrates in the HFr-model. This specific hydrate growth pattern has been reported [205, 204]. This may be seen as a sudden drop in the measured c_P/c_S-ratio.

In experiment 8-10 (Fig. 7.6), where $S_{w0} \approx 0.9$, the measured c_P/c_S-ratio seems to be slightly higher than in experiment 5-7 (Fig. 7.5), where $S_{w0} \approx 0.75$. This agrees with reported Poisson's ratios (ν) for consolidated sandstones [206] and unconsolidated sediments [26] ($\nu = \frac{(c_P/c_S)^2-2}{2(c_P/c_S)^2-2}$ [206]).

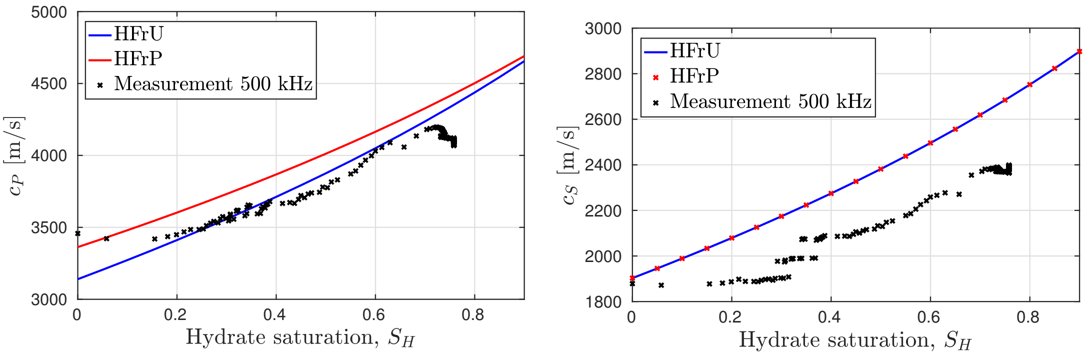

(a)

(b)

Figure 7.17: Measured c_P and c_S for experiment 9 with the solid buffer Fourier spectrum method at frequency 500 kHz plotted together with the HFrU and HFrP-models with $S_{w0} = 0.8$. **a)**) c_P. **a)**) c_S.

As discussed here, a combination of different hydrate growth patterns are possible. For sandstones having high S_{w0} (especially experiment 5-10, Fig. 7.5 and 7.6) it seems likely that hydrates are forming in the pore fluid for low S_H. This finding has been reported earlier [46]. When S_H further increases, hydrate are at least partially growing into the frame acting as additional grains in the sandstone. In the unconsolidated sand-packs that Waite et al. [22] studied, the hydrates where found to act as cement around grain contacts.

Seismic data obtained from the Blake Ridge where analyzed by Ecker et al. [207] and Helgerud et al. [24]. They concluded that the hydrate acted as a mineral grain supporting the sediment frame. However, Chand et al. [57] suggested that hydrates acted as a cement from the same data. These contradictory conclusions regarding the interaction between hydrate and sediment highlight the importance of validating seismic models with laboratory data. Hu et al. [35] measured c_P in consolidated sediments and found no increase in c_P for S_H below 0.1. This is consistent with the findings in this work as well. Hu et al. presented no thorough analysis on hydrate growth patterns but report an increase in c_P for S_H between 0.1 and 0.3. For unconsolidated sediments, Hu et al. indicated hydrates acted both as cement and as load bearing grains.

7.2 Development in α_P during hydrate growth for Bentheim sandstones in experiment 1-10

The relative attenuation $\Delta\alpha_P = \alpha_P - \alpha_P(S_H = 0.2)$ is measured to see if there are any development in the α_P during hydrate growth. The BiotHFrU (Biot model with hydrates growing in the frame), BiSqHFrU (Biot-squirt flow model with hydrates growing in the frame), WaTrHFrU (Waterman and Truell multiple scattering model with hydrates growing into the frame) and WaTrBiSqHFrU-models (combination of the BiSqHFrU-model and the WaTrHFrU-model) detailed in Secs. 2.5.4, 2.5.5, 2.5.6 and 2.5.7, respectively, are used to simulate α_P and discuss which attenuation mechanisms may be present in the hydrate bearing Bentheim sandstone during hydrate growth.

7.2.1 Measurements of $\Delta\alpha_P$ for the Bentheim sandstones during hydrate growth in experiment 1-10

The solid buffer method (detailed in Sec. 3.3) is used to measure $\Delta\alpha_P$ during hydrate growth for the ten experiments presented in Tab. 7.1. Because of the considerations regarding possible non-linear effects detailed in Sec. 3.3.1, the attenuation measurements are presented with $\Delta\alpha_P = \alpha_P - \alpha_P(S_H = 0.2)$. The Fourier spectrum method (Eq. (3.51)) is used to measure $\Delta\alpha_P$ in all the experiments. $\Delta\alpha_P$ is measured using the same signals as for c_P.

Typical signals for S_H at maximum hydrate growth for experiment 1-4 and 5-10 are already shown in Figs. 7.1 b), and 7.4 b), respectively. A signal for $S_H = 0.2$ in experiment 2 is shown in Fig. 7.18 a). This signal is representative for experiment 1-4. A signal for $S_H = 0.2$ in experiment 7 is shown in Fig. 7.18 b). This signal is representative for experiment 5-10. The P-wave signal is the signal arriving after approximately 30 µs.

A one cycle, 500 kHz is used as the input settings on the signal generator.

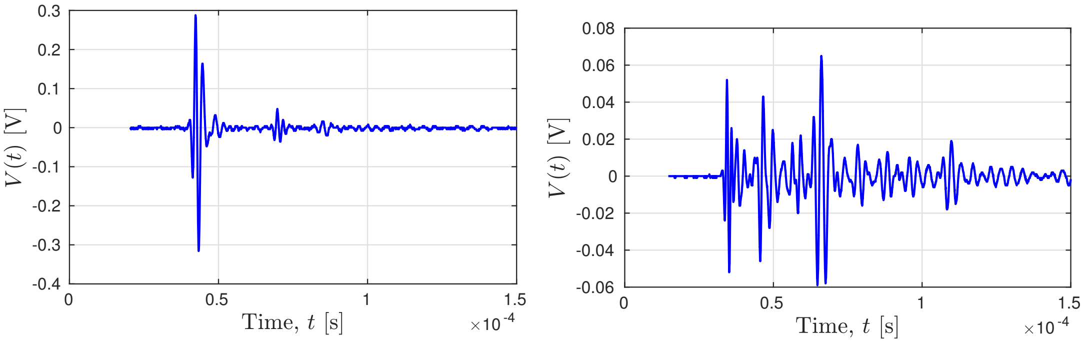

(a)

(b)

Figure 7.18: Measured time signals at $S_H = 0.2$ for **a)** experiment 2 using P-wave transducers and **b)** experiment 7 using S-wave transducers.

Experiment 1-2: Measured $\Delta\alpha_P$ for hydrate-bearing Bentheim sandstones with $S_{w0} = 0.48 - 0.55$

In Fig. 7.19, $\Delta\alpha_P$ is presented for experiment 1 ($S_{w0} = 0.48$) and experiment 2 ($S_{w0} = 0.55$). In general α_P decrease during hydrate growth.

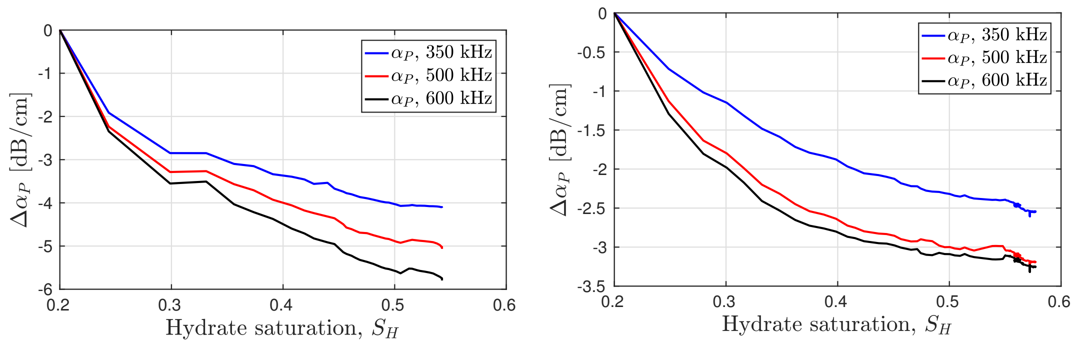

(a)

(b)

Figure 7.19: Measured $\Delta\alpha_P$ with increasing S_H for experiment 1 and 2. a) Experiment 1, S_{w0} =0.48. b) Experiment 2, S_{w0} =0.55.

There is a drop in the measured $\Delta\alpha_P$ at 500 kHz in experiment 1 and 2 from $S_H = 0.2$ to $S_H = 0.5$ of approximately 5 dB/cm and 3 dB/cm, respectively. For 350 kHz this drop is approximately 4 and 2.3 dB/cm, respectively and for 600 kHz 5.5 and 3.1, respectively. The decrease in $\Delta\alpha_P$ is largest from $S_H = 0.2$ to $S_H = 0.3$. The total drop in $\Delta\alpha_P$ from $S_H = 0.2$ to $S_H = 0.5$ is largest in measurements using measurement frequency 600 kHz and lowest using measurement frequency 350 kHz. As will be seen in this section, $\Delta\alpha_P$ seem to generally decrease for higher frequencies for $S_H < 0.5$.

Experiment 3-4: Measured $\Delta\alpha_P$ for hydrate-bearing Bentheim sandstones with $S_{w0} = 0.65 - 0.69$

In Fig. 7.20, $\Delta\alpha_P$ is presented for experiment 3 ($S_{w0} = 0.65$) and experiment 4 ($S_{w0} = 0.69$) during hydrate growth.

There is a drop in the measured $\Delta\alpha_P$ for 350 kHz and 600 kHz of approximately 2 dB/cm from $S_H = 0.2$ to $S_H = 0.5$ in experiment 3 (figure a)). For 500 kHz this drop is approximately 2.1 dB/cm. In experiment 4 (figure b)), the 350 kHz, 500 kHz and 600 kHz measurement curves are decreasing 2.8, 3.2 and 3.5 dB/cm, respectively from $S_H = 0.2$ to $S_H = 0.5$.

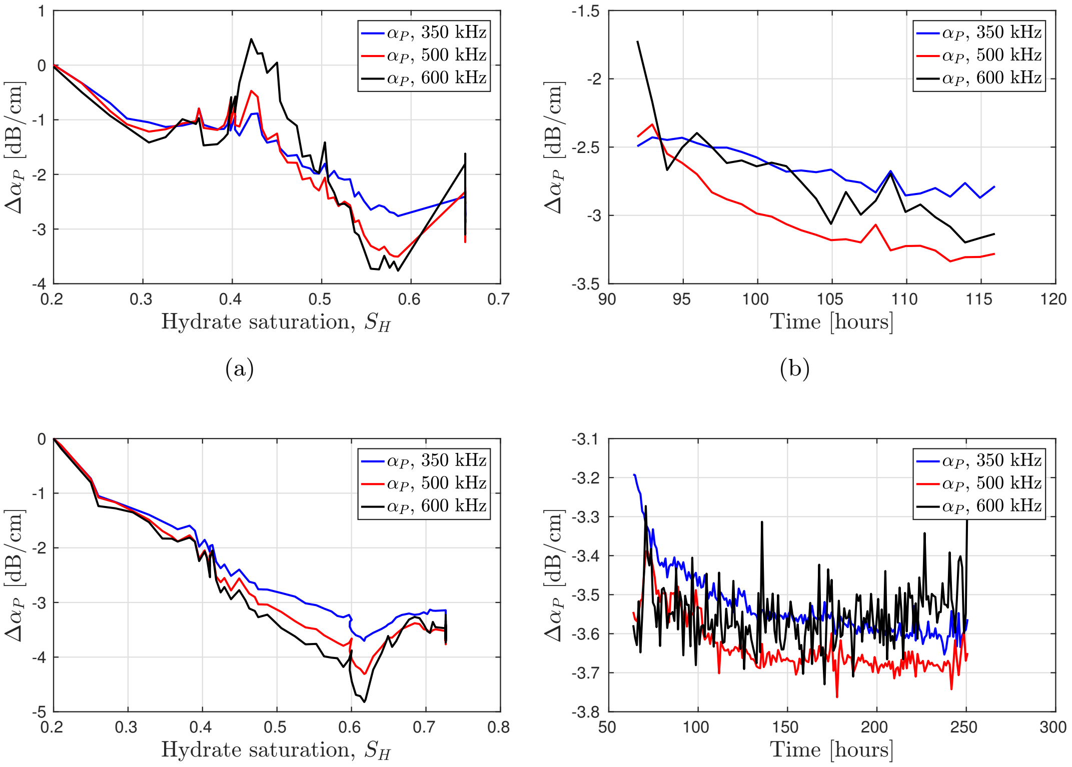

(a)

(b)

(c)

(d)

Figure 7.20: Measured $\Delta\alpha_P$ during hydrate growth for experiment 3 and 4. a) development in $\Delta\alpha_P$ during hydrate growth in experiment 3 (S_{w0} =0.65). b) development in $\Delta\alpha_P$ after maximum S_H in experiment 3. c) development in $\Delta\alpha_P$ during hydrate growth in experiment 4 (S_{w0} =0.69). d) development in $\Delta\alpha_P$ after maximum S_H in experiment 4.

In Fig. 7.20 a) and c) there is a general decrease in $\Delta\alpha_P$, however, the curves have more ripples, dips and peaks compared with Fig. 7.19. There is a peak in $\Delta\alpha_P$ for 600 kHz (black curve) in Fig. 7.20 a) for $S_H \approx 0.4 - 0.5$. At $S_H \approx 0.6$, there are dips in the measured curve for $\Delta\alpha_P$ in a) and c).

Like for the c_P- measurements presented in Fig. 7.3, there is a development in the measured $\Delta\alpha_P$ after full hydrate growth. In experiment 3, for 350 kHz, 500 kHz and 600 kHz, there is a drop in the measured $\Delta\alpha_P$ of 0.5, 1 and 1.5 dB/cm, respectively, after maximum S_H is reached. In experiment 4 (figure d)) there is a drop for 350 kHz, but the development in $\Delta\alpha_P$ after full hydrate saturation is not as clear for 500 kHz and 600 kHz.

Experiment 5-7: Measured $\Delta\alpha_P$ for hydrate-bearing Bentheim sandstones with $S_{w0} = 0.73 - 0.78$

In Fig. 7.21, $\Delta\alpha_P$ is presented for experiment 5 ($S_{w0} = 0.73$), experiment 6 ($S_{w0} = 0.76$) and experiment 7 ($S_{w0} = 0.78$) during hydrate growth. The total drop in $\Delta\alpha_P$ is in general measured to be larger for higher frequencies in experiment 5-7.

There is a drop in the measured $\Delta\alpha_P$ for 350 kHz in experiment 5 and 7 from $S_H = 0.2$ to $S_H = 0.5$ of approximately 2 dB/cm. For 500 kHz this drop is approximately 2 and 2.5 dB/cm, respectively. For 600 kHz this drop is approximately 3 dB/cm. Due to the power outage there is no information of α_P at $S_H = 0.5$ for experiment 6. In experiment 6, Red circles are showing the last data point before and after the power outage. A line is drawn to show interpolated values.

In experiment 5 (figure b)), there is a clear development in $\Delta\alpha_P$ after maximum S_H is reached. α_P increases 0.5-1 dB/cm over time at maximum S_H for all the measurement frequencies. There is a small peak in $\Delta\alpha_P$ at approximately $S_H = 0.33$ in figure a) (experiment 5).

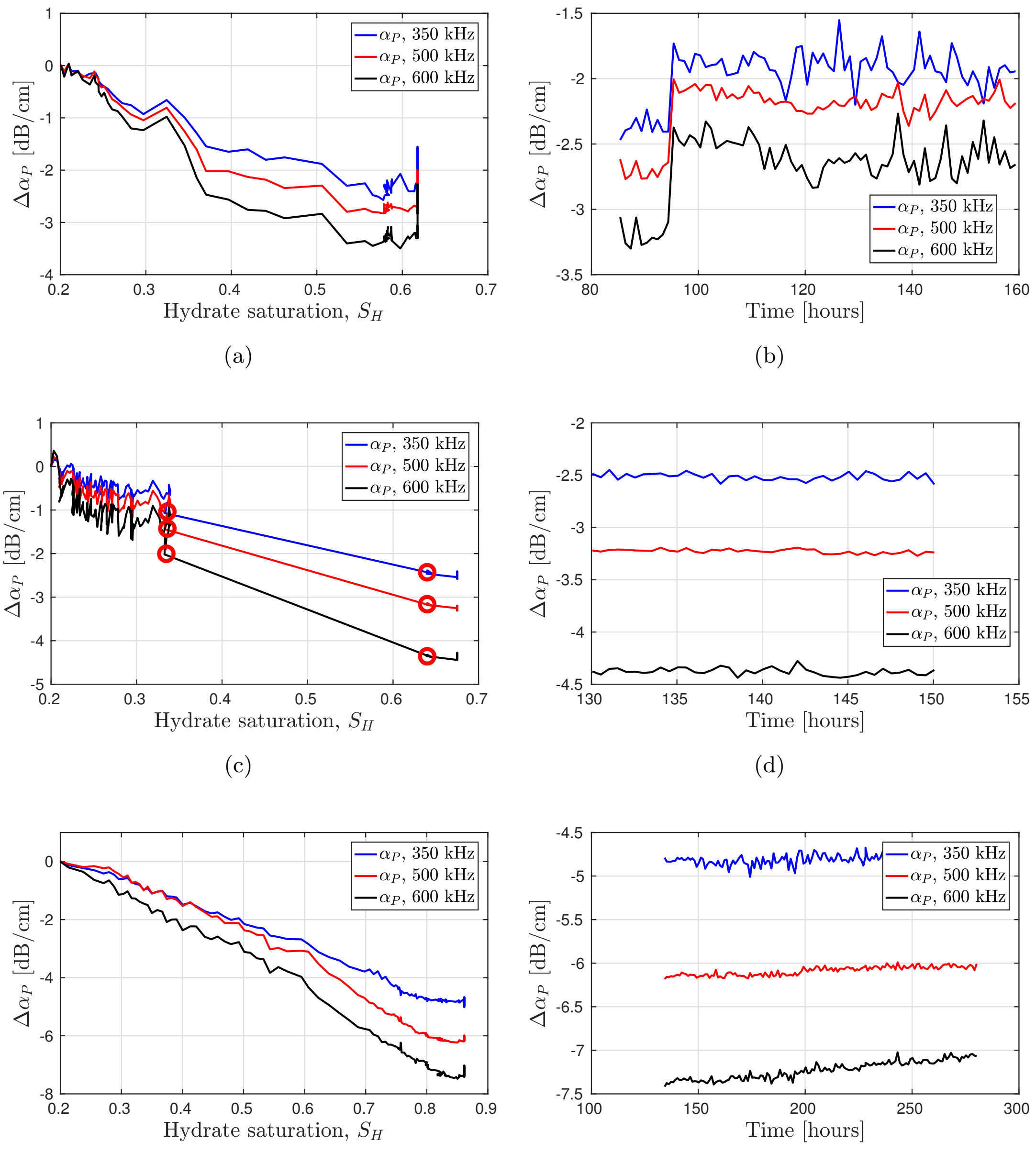

Figure 7.21: Measured $\Delta\alpha_P$ during hydrate growth for experiment 5, 6 and 7. a) development in $\Delta\alpha_P$ during hydrate growth in experiment 5 (S_{w0} =0.73). b) development in $\Delta\alpha_P$ after maximum S_H in experiment 5. c) development in $\Delta\alpha_P$ during hydrate growth in experiment 6 (S_{w0} =0.76). d) development in $\Delta\alpha_P$ after maximum S_H in experiment 6. e) development in $\Delta\alpha_P$ during hydrate growth in experiment 7 (S_{w0} =0.78). f) development in $\Delta\alpha_P$ after maximum S_H in experiment 7.

Experiment 8-10: Measured $\Delta\alpha_P$ for hydrate-bearing Bentheim sandstones with $S_{w0} = 0.92 - 0.95$

In Fig. 7.22, $\Delta\alpha_P$ is presented for experiment 8 (S_{w0}=0.92), experiment 9 (S_{w0}=0.94) and experiment 10 (S_{w0}=0.95) during hydrate growth.

There is a drop in the measured $\Delta\alpha_P$ at 350 kHz in experiment 8, 9 and 10 from $S_H = 0.2$ to $S_H = 0.5$ of approximately 1 dB/cm, respectively. For 500 kHz this drop is approximately 2, 1.4 and 1.3 respectively. For 600 kHz this drop is approximately 3.9, 1.9 and 1.9 respectively. Within each experiment 8-10, from $S_H = 0.2 - 0.5$, the drop in $\Delta\alpha_P$ is measured to be larger for higer frequencies. In experiment 8 (figure a)), the blue and red curves are crossing, meaning that $\Delta\alpha_P$ is measured to drop more for 350 kHz than for 500 kHz from $S_H = 0.2$ to maximum S_H. There is a clear peak in $\Delta\alpha_P$ for 350 kHz at $S_H = 0.45$ for experiment 8. In experiment 9 and 10 (figure c) and e)), no clear peaks in $\Delta\alpha_P$ are detected at $S_H \approx 0.45$. For 350 kHz there is no clear decrease in α_P for $S_H < 0.45$.

In experiment 8 and 9 there is a development in $\Delta\alpha_P$ after maximum S_H is reached (figure b) and d)). In experiment 8, $\Delta\alpha_P$ is slightly decreasing (figure b)), In experiment 9 (figure d)), $\Delta\alpha_P$ is decreasing for 350 kHz but increase for 600 kHz and 500 kHz.

In experiment 9, measurement frequency 350 kHz gives a larger drop in $\Delta\alpha_P$ compared with 500 kHz and 600 kHz. This is a contradiction to the general trend seen in experiment 1-10, where 350 kHz typically gives the smallest drop in $\Delta\alpha_P$. Numerical models presented in Sec. 7.2.3 may give some insight in these attenuation mechanisms. The effect of frequency on $\Delta\alpha_P$ is discussed in Sec. 7.4.

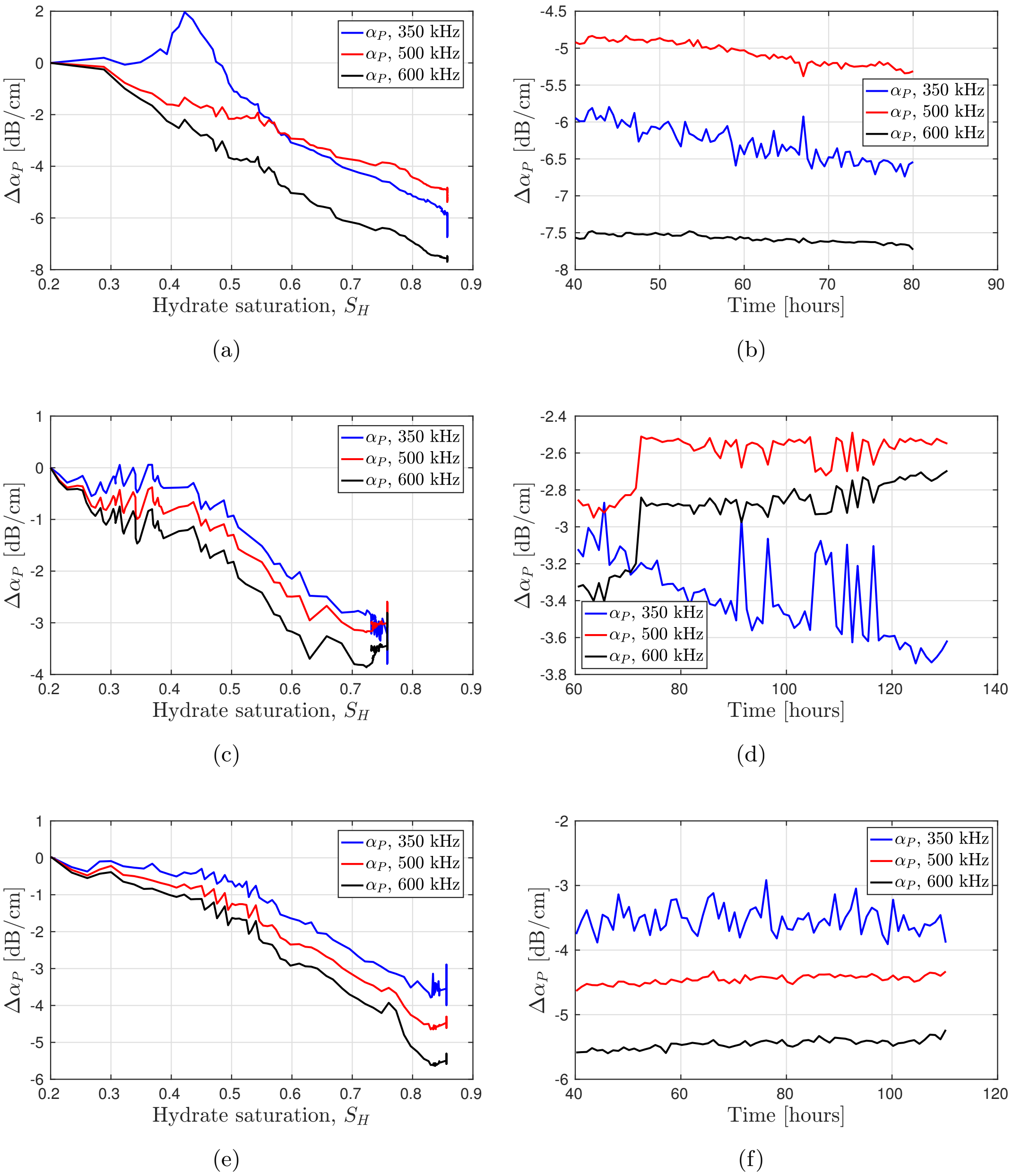

Figure 7.22: Measured $\Delta\alpha_P$ during hydrate growth for experiment 8, 9 and 10. a) development in $\Delta\alpha_P$ during hydrate growth in experiment 8 (S_{w0} =0.92). b) development in $\Delta\alpha_P$ after maximum S_H in experiment 8. c) development in $\Delta\alpha_P$ during hydrate growth in experiment 9 (S_{w0} =0.94). d) development in $\Delta\alpha_P$ after maximum S_H in experiment 9. e) development in $\Delta\alpha_P$ during hydrate growth in experiment 10 (S_{w0} =0.95). f) development in $\Delta\alpha_P$ after maximum S_H in experiment 10.

7.2.2 Measured α_P at fixed S_H for experiment 1-10 as function of S_{w0}

From the measurements shown in the previous section, it is clear that higher S_H give a decrease in α_P .

In Fig. 7.23 a), the drop in $\Delta\alpha_P$ from S_H 0.2 to 0.5 ($\Delta\alpha_P|_{S_H=0.5}$) is plotted for the ten experiments as a function of S_{w0} for frequency 350 kHz. $\Delta\alpha_P|_{S_H=0.5}$ is measured to be larger for sandstones with low S_{w0} compared with sandstones having high S_{w0}.

The measured $\Delta\alpha_P|_{S_H=0.5}$ as a function of S_{w0} in figure a) (350 kHz) are shifted towards lower values compared with the measurements shown in figure b) (500 kHz). For a given S_{w0}, α_P seem to generally decrease more for lower frequencies.

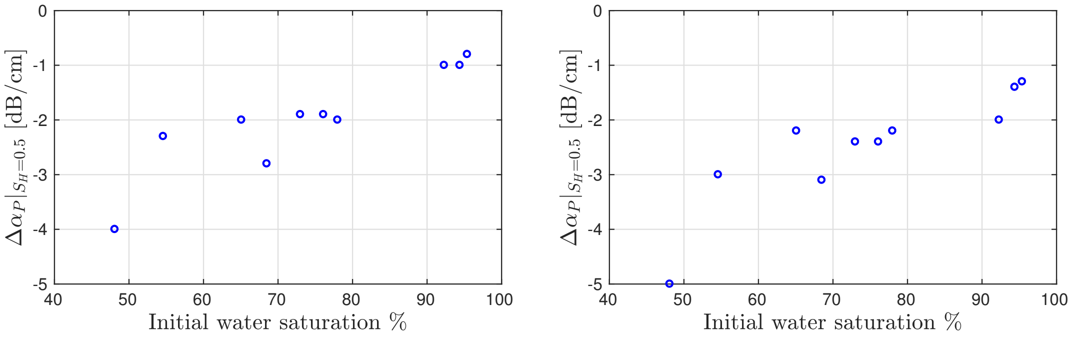

(a)

(b)

Figure 7.23: Measured $\Delta\alpha_P$ at $S_H = 0.5$ for experiment 1-10. **a)** Measurement frequency 350 kHz. **b)** Measurement frequency 500 kHz.

7.2.3 Numerical models and discussion of the development in α_P during hydrate growth in Bentheim sandstones

Numerical models are used to model α_P to gain further insight in which attenuation mechanisms are present in the sandstone. The models used in Sec. 7.1.3 to model c_P do not contain information about attenuation. To model attenuation, the Biot model is used [23] together with models accounting for attenuation due to squirt flow [55] and scattering [56] inside the porous rock. In the following, four models containing information about attenuation are presented and compared with the results in Sec. 7.2.1. In the four models it is assumed that hydrates are growing in the frame and that the gas and water are uniformly distributed. The models are detailed in Ch. 2: The BiotHfrU-model (Sec. 2.5.4), the BiSqHfrU-model (Sec. 2.5.5), the WaTrHfrU-model (Sec. 2.5.6) and the WaTrBiSqHfrU-model (Sec. 2.5.7).

Simulation of α_P using Biot's model during hydrate growth (BiotHfrU-model)

In the original Biot model [23], α_P is found by modeling the pressure-induced flow inside the sandstone. The fluid flow is governed by the viscosity of the fluid and the permeability of the sandstone, (Eq. (2.36)). How to use the Biot-model during hydrate growth (labeled BiotHfrU-model) is detailed in Sec.2.5.4.

The permeability of the hydrate-bearing sandstone depends on the hydrate growth pattern, i.e whether hydrates grow on pore walls, or if the hydrates float around in the pore fluid or if hydrates grow in pore throats, plugging the passage of the fluid flow. A precise description of this permeability is complex and empirical models are typically used for different growth patterns [166, 167, 168]. In Eq. (2.36), a simple model for the permeability in a hydrate-bearing porous rock is presented [166]. In Fig. 7.24, the BiotHFrU-model is used with different S_{w0} and N_{perm}. As detailed in Sec.2.5.4, $N_{perm} = 2$ describes the situation in which hydrates coat the cylindrical walls with a uniform layer. For $N_{perm} > 2$, the hydrates are plugging the pores in a more efficient way than when hydrates coat the cylindrical walls with a uniform layer. Almenningen et. al [208] found $N_{perm} = 14$ for hydrates growing in Bentheim sandstones.

In Fig. 7.24 a), $N_{perm} = 2$ is used to calculate the permeability in Eq.(2.36). With $N_{perm} = 2$, the BiotHfrU-model predicts very little attenuation. Using $N_{perm} = 10$ and $N_{perm} = 14$, a peak is seen around $S_H = 0.2$ and $S_H = 0.3$, respectively, in α_P during hydrate growth. The frequency is 500 kHz.

α_P does not exceed 0.7 dB/cm using the BiotHFrU -model for the simulations in Fig. 7.24. The model predicts an attenuation peak due to the global flow which decreases for growing S_H. However, the simulated attenuation due to Biot flow can not by itself explain the measured attenuation presented in Figs. 7.19, 7.20, 7.21 and 7.22. It is well-known that the Biot-theory underestimates α_P in sandstones [128, 55] and this is also strongly indicated in the attenuation measurements in this work (Figs.7.19, 7.20, 7.21 and 7.22).

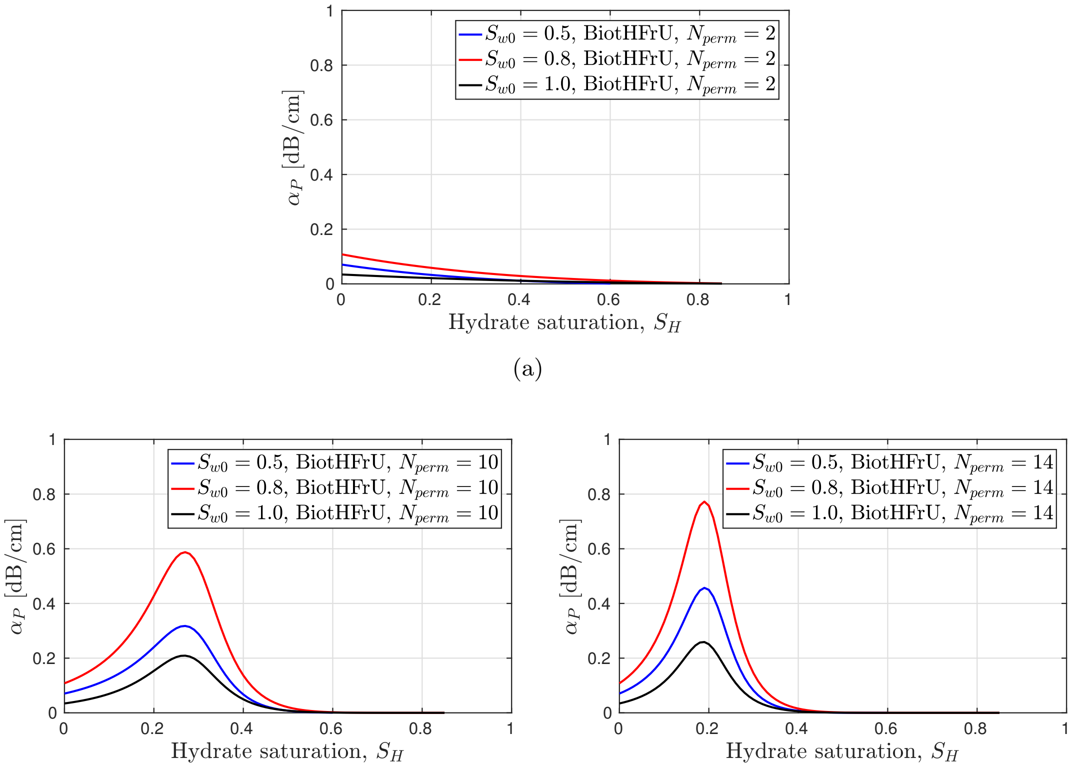

(a)

(b)

(c)

Figure 7.24: Simulated α_P using the BiotHFrU -model detailed in Sec.2.5.4. **a)** BiotHFrU -model using $N_{perm} = 2$, **b)** BiotHFrU -model using $N_{perm} = 10$ and **c)** BiotHFrU -model using $N_{perm} = 14$.

Simulation of α_P using Biot flow and squirting flow during hydrate growth (BiSqHfrU-model)

When a pressure wave passes a compliant pore, the fluid is pressed in and out of the compliant pore. This type of flow is called squirt flow and attenuates the acoustic waves. Dvorkin et al. developed an unified theory taking into account both the Biot flow and the squirting flow [55]. This model is called BISQ (Biot squirt). In this work, the BISQ-model is used together with the HFrU-model and is labeled the BiSqHfrU-model (detailed in Sec.2.5.5). The frequency is 500 kHz.

In Fig. 7.25, α_P calculated with the BiSqHfrU model is presented with $R_{sq} = 170$ µm. In a) where $N_{perm} = 2$, little attenuation is predicted. For $S_{w0} = 1.0$, in b), $N_{perm} = 10$ and a region with increased α_P (approximately 1 dB/cm) is predicted for values of $S_H = 0.3 - 0.5$. In b) $N_{perm} = 14$ and this region gives approximately $\alpha_P = 1.2$ dB/cm for $S_H = 0.2 - 0.3$.

In Fig. 7.25 b) and c), S_{w0} is clearly affecting the simulated α_P. In general the attenuation increase with increasing S_{w0}.

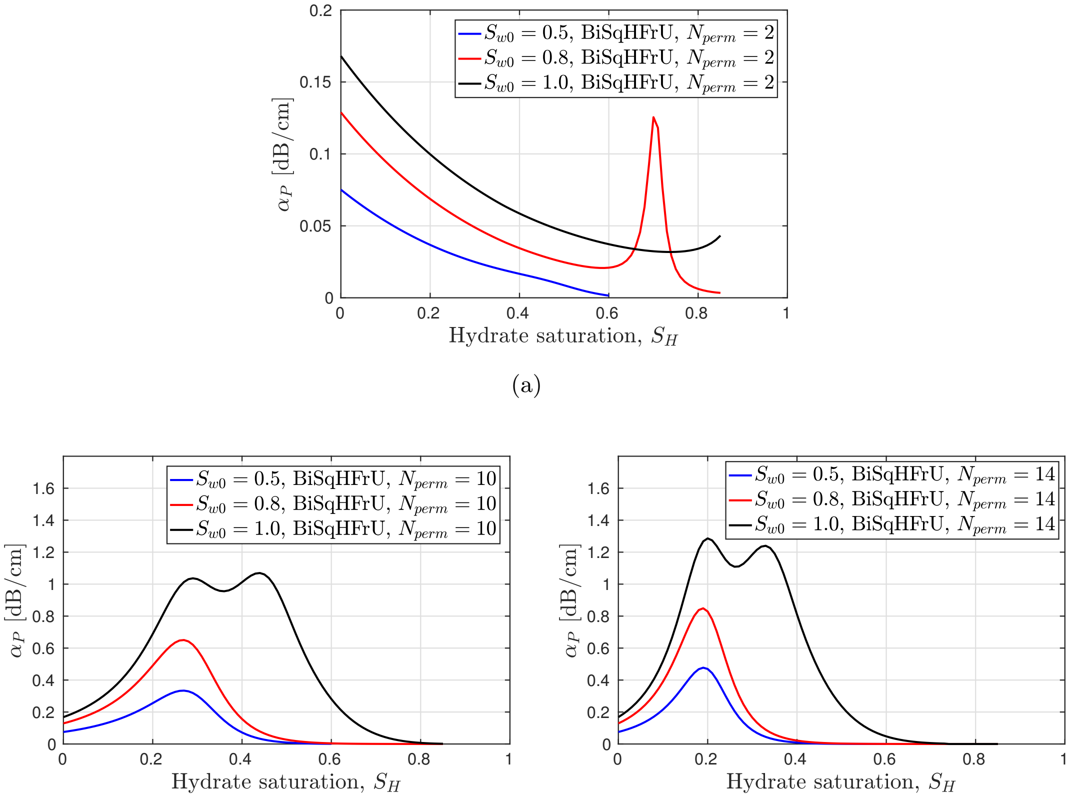

(a)

(b)

(c)

Figure 7.25: Simulated α_P using the BiSqHFrU -model detailed in Sec.2.5.5 with $R_{sq} =$ 170 µ**a)** BiSqHFrU-model using $N_{perm} = 2$, **b)** BiSqHFrU-model using $N_{perm} = 10$ and **c)** BiSqHFrU-model using $N_{perm} = 14$.

The BiSqHFrU-model (Fig. 7.25) predicts more attenuation than the BiotHFrU-model (Fig. 7.24), however it is not enough to explain the levels of attenuation seen in the experiments (Figs. 7.19, 7.20, 7.21 and 7.22). The simulations (Fig. 7.25) provide for example a poor fit with the attenuation measurements in experiments having low S_{w0} (Fig. 7.19). However, some features in the experiments having high S_{w0} may be seen in the simulations. The peak in the simulations (Fig. 7.25) around S_H 0.2-0.5 for $S_{w0} = 1$, may partly explain the flat region in $\Delta\alpha_P$ around S_H 0.2-0.5 in Fig. 7.22) c) and d).

In the simulations shown in Fig. 7.25, $R_{sq} = 170$ µm, which is a typical size of the quartz-grains in Bentheim sandstone [37] and has also been used for sandstones by Dvorkin et al. [55]. R_{sq} is illustrated in Fig. 2.4 b). In a real Bentheim sandstone, there sure exist different sized pores and cracks [37, 136]. No thorough investigation of squirting flow in cracks or sandstones with pores of different sizes is performed in this work (a more detailed study is conducted by Jakobsen et al. [170]). However, by describing the pores and cracks with other values for R_{sq}, the BiSqHFrU-model potentially predicts higher attenuation. In Fig. 7.26 this is illustrated, where the attenuation is clearly affected by R_{sq}. A combination of the curves seen in Fig. 7.26 might describe some of the attenuation seen in the experiment shown in Figs. 7.19, 7.20, 7.21 and 7.22. In this work, R_{sq} is fixed in each simulation and does not change for increasing S_H. This is probably a simplification because the hydrates are changing the pore structure, possible altering R_{sq} as hydrate grows and S_H increases.

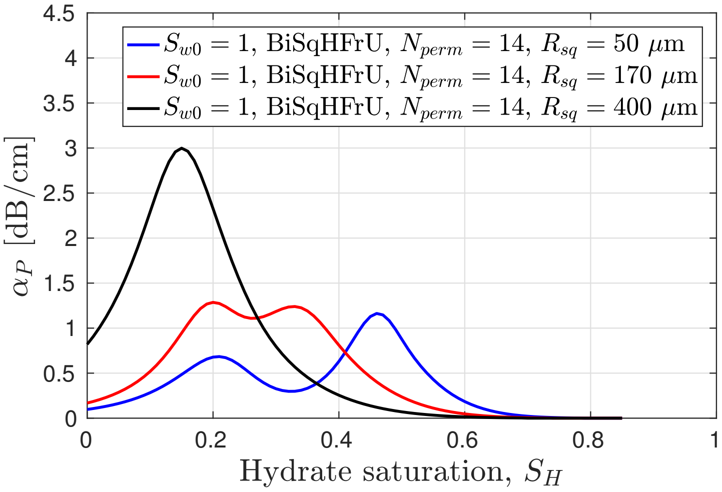

Figure 7.26: Simulated α_P using the BiSqHFrU -model detailed in Sec.2.5.5 for $N_{perm} = 14$ with $R_{sq} = 50$ µ, $R_{sq} = 170$ µand $R_{sq} = 400$ µ.

Simulation of α_P using Waterman and Truell's multiple scattering theory during hydrate growth (WaTrHFrU)

Heterogeneities in the sandstone may give rise to scattering effects [43, 124]. Hydrates are assumed to grow into the frame in the scattering model used in this work, thus contributing to the effective background medium needed in the multiple scattering model (wavenumber k_0 in Eq. (2.50)). S_{w0} contributes only to the background medium and not to the inclusions. The inclusions used in the scattering model are treated as either 100 % water inclusions (and Eq. (2.58) is used to calculate the scattering coefficients A_n) or cavities ("vacuum spheres", and Eq. (2.60) is used to calculate A_n). As hydrates grow, the volume and thus the number of scatterers decrease. The model is further detailed in Sec. 2.5.6.

In Fig. 7.27 a), α_P calculated with the WaTrHFrU-model is plotted using inclusions with radius 100 µm radius which is the size of a typical pore inside the Bentheim sandstone [83]. For the blue curve, the inclusions are cavities and for the red curve the inclusions are water. Little attenuation is predicted for both water-inclusions and the cavities for the 100 µm - inclusions.

In Fig. 7.27 b), α_P calculated with the WaTrHFrU-model using cavity inclusions with different radii are shown. Larger cavity-inclusions give higher attenuation. As hydrate grows, the porosity decreases and the number of cavitiy-inclusions decrease, giving a lower simulated α_P. In this figure, the background medium is calculated with $S_{w0} = 0.5$, giving a maximum $S_H \approx 0.6$.

In Fig. 7.27 c), water-inclusions are used with the WaTrHFrU-model. In the simulations the frequency is 500 kHz and $c_w = 1500$ m/s. A big difference is seen between figure b) and c) for the 1000 µm inclusions (black curve). This is probably because 1000 µm is close to the half-wavelength in water (1500 µm at 500 kHz) which defines the resonance frequency of a water-droplet.

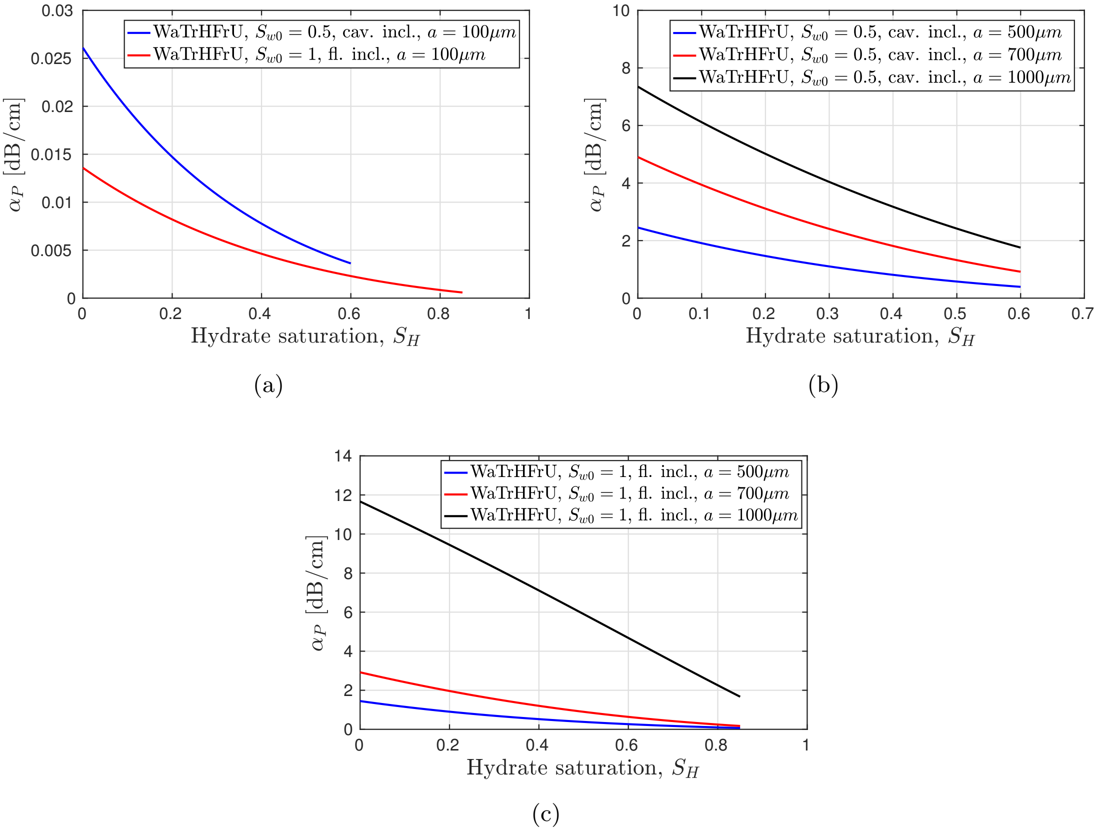

(a)

(b)

(c)

Figure 7.27: Simulated α_P using the WaTrHFrU-model detailed in Sec. 2.5.6. **a)** Cavity and water-inclusions using a = 100 µm. **b)** Cavity inclusions using different inclusion radii. **c)** Water inclusions using different inclusion radii.

From the simulations shown in Fig. 7.27, it's concluded that pore-sized heterogeneities are too small to cause significant attenuation due to scattering at 500 kHz. If however, the heterogeneities are larger, the model predicts significant scattering. It may be argued that few pores with radius 1000 µm are present in the Bentheim sandstone specimen used in this work. However, cracks with complex geometries may be present in Bentheim sandstones, especially at low confining pressures [162]. A scattering model for such cracks is not provided here but can be found in a previous paper by Hudson [44].

In this work it is assumed that the WaTrHFrU-model using spherical scatterers with radius a, gives an indication of α_P caused by circular cracks with radius a. Thus, the WaTrHFrU-model indicates that cracks in the Bentheim sandstones must be larger than the cross-section of the average-sized pore (approximately 100 µm for Bentheim sandstone) to give significant attenuation.

The attenuation predicted by the WaTrHFrU-model are in the same order of the attenuation seen in the experiments 1-10 (Figs. 7.19, 7.20, 7.21 and 7.22).

The attenuation measurements results plotted in Figs. 7.19, 7.20, 7.21 and 7.22 are presented as $\Delta\alpha_P$. The simulated attenuation values are presented as α_P and can not be directly compared. However, certain features found in the measurements may be discussed with the simulations. For experiment 1-2, where the water-content is lowest (Fig. 7.19), there are no peaks in the measured $\Delta\alpha_P$ during hydrate growth. As less attenuation is predicted by the BiSqHFrU-model when S_{w0} is low, this gives an indication that pressure-induced fluid flow is not the dominating attenuation-mechanism. For 1000 µm cavities, the WaTrHFrU-model (Fig. 7.27 b)) predicts a drop in α_P of approximately 2.5 dB/cm from $S_H = 0.2$ to 0.5. For 1000 µm water inclusions, the WaTrHFrU-model in c) predicts a drop in α_P of approximate 3.5 dB/cm from $S_H = 0.2$ to 0.5. In experiment 1 and 2 in Fig. 7.19, this drop is approximately 5 and 3 dB/cm, respectively. Some of this attenuation might be from scattering effects.

Using the the WaTrHFrU-model, it is not possible to conclude whether scattering is the main attenuating mechanism in the sandstone. This model use spherical scatterers and can not directly predict attenuation from other inclusion-geometries, such as cracks.

Simulation of α_P using combined multiple scattering and fluid flow (WaTrBiSqHFrU) during hydrate growth

Both the Watermann and Truell based scattering model (WaTrHFrU) and the fluid-flow attenuation model (BiSqHFrU) might explain some of the attenuation seen in experiment 1-10 (Figs. 7.19, 7.20, 7.21 and 7.22). The WaTrBiSqHFrU-model (detailed in Sec. 2.5.7) is a combination of the WaTrHFrU (Sec. 2.5.6) and the BiSqHFrU (Sec.2.5.5)-models and considers attenuation to both multiple scattering and pressure-induced fluid flow.

In Fig. 7.28 a), the WaTrBiSqHFrU-model is plotted for different pore radii using $R_{sq} = 50$ µm. In b) the WaTrBiSqHFrU-model is plotted for different pore radii using $R_{sq} = 170$ µm. $N_{perm} = 14$ in this model. Neither the WaTrHFrU nor the BiSqHFrU-model give a precise description of the attenuation mechanisms seen in the experiments (Figs. 7.19, 7.20, 7.21 and 7.22).

However, by comparing for example the 700 µm inclusions in Fig. 7.28 b) with the measurements in Figs. 7.22 c) and e), some resemblance is seen from $S_H = 0.2 - 0.6$. In general there are some dips and peaks in the measured $\Delta\alpha_P$ in experiment 1-10. In Fig. 7.28 a), the WaTrBiSqHFrU-model predicts a peak in α_P around $S_H = 0.45$.

In Fig. 7.29, the WaTrBiSqHFrU-model is plotted for different frequencies using $R_{sq} = 170$ µm and $a = 500$ µm. Fig. 7.29 is analogue to Figs. 7.19, 7.20, 7.21 and 7.22, describing the measured decrease in α_P during hydrate growth. The red curve is equal to the blue curve in Fig. 7.28 b). In Fig. 7.29 higher frequencies are seen to decrease more than low frequencies during hydrate growth. This is also a general trend seen in the measurements. However, in Fig. 7.29, the 600 kHz-curve decreases more compared with the 350 kHz-curve than for the measurements, Figs. 7.19, 7.20, 7.21 and 7.22.

The numerical models used in this work do not give a precise description of the α_P-measurements. However, due to the resemblance between measurements and the simulations, the simulations indicate that attenuation mechanisms due to both scattering and due to pressure-induced fluid are present in the measurements.

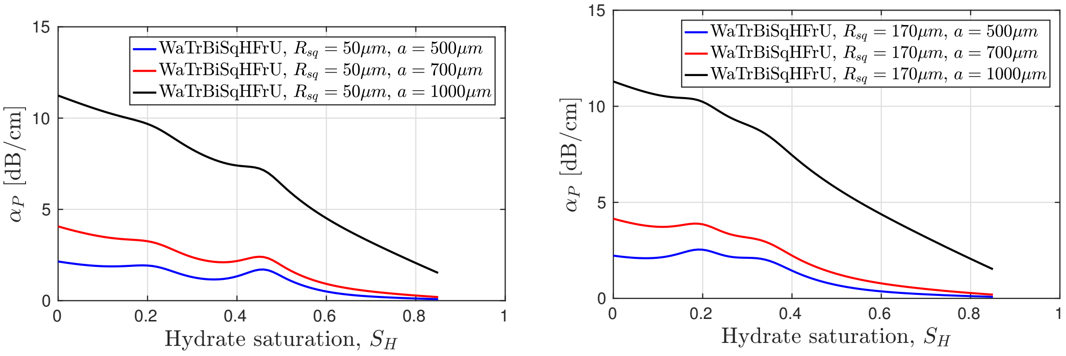

(a)

(b)

Figure 7.28: Simulated α_P using the WaTrBiSqHFrU-model with water inclusions and $N_{perm} = 14$, detailed in Sec. 2.5.7. The frequency is 500 kHz. **a)** WaTrBiSqHFrU-model using $R_{sq} = 50$ µm. **b)** WaTrBiSqHFrU-model using $R_{sq} = 170$ µm.

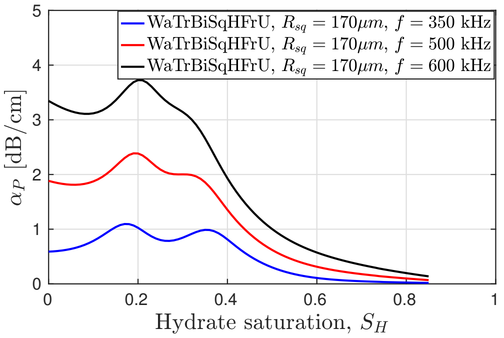

Figure 7.29: Simulated α_P using the WaTrBiSqHFrU-model for different frequencies detailed in Sec. 2.5.7. $R_{sq} = 170$ µm, water-inclusions with radii 500 µm and $N_{perm} = 14$ are used.

7.3 Dispersion and attenuation spectrum measurements at $S_H = 0.2$ and $S_H = 0.5$

The results presented in the two previous sections describe how the α_P, c_P and c_S change with S_H. In this section the attenuation spectra and the frequency-dependent c_P (dispersion curves) of the measurements are investigated for frequencies 350 kHz-600 kHz. The attenuation spectrum and dispersion curves are presented at S_H 0.2 and 0.5. Very few data-points are logged for low S_H in experiments 1 and 2 due to a program failure. Also, due to a power outage at the University of Bergen during experiment 6, no data is available for $S_H = 0.5$. Thus, results from these experiment are omitted. In Ch. 6, the uncertainty of the c_P and c_S - measurements using the S-wave transducers are seen to be at least 60 m/s. While the range in the $c_P - S_H$ and $c_S - S_H$-curves presented in Sec. 7.1 are several hundred m/s, the range of the dispersion curves are typically below 60 m/s. Thus, only dispersion curves for experiment 3-4, where the P-wave transducers are used, are presented.

Using the Fourier spectrum method, the acquired time signals at $S_H = 0.2$ and $S_H = 0.5$ are used in the experiments to obtain the attenuation spectra (Eq. (3.51)) and the dispersion curves (Eq. (3.50)).

Experiment 3-4

In Fig. 7.30 a) and b), the difference in α_P and α_P at frequency $f_0 = 350$ kHz for experiment 3 and 4 are shown, respectively. For experiment 3, the increase in the measured α_P from $f_0 = 350$ kHz to $f_1 = 600$ kHz is 4.3 dB/ cm and 3.8 dB/cm at $S_H = 0.2$ and $S_H = 0.5$, respectively. For experiment 4, the increase in α_P from

$f_0 = 350$ kHz to $f_1 = 600$ kHz is 4 dB/ cm and 3.5 dB/cm at $S_H = 0.2$ and $S_H = 0.5$, respectively.

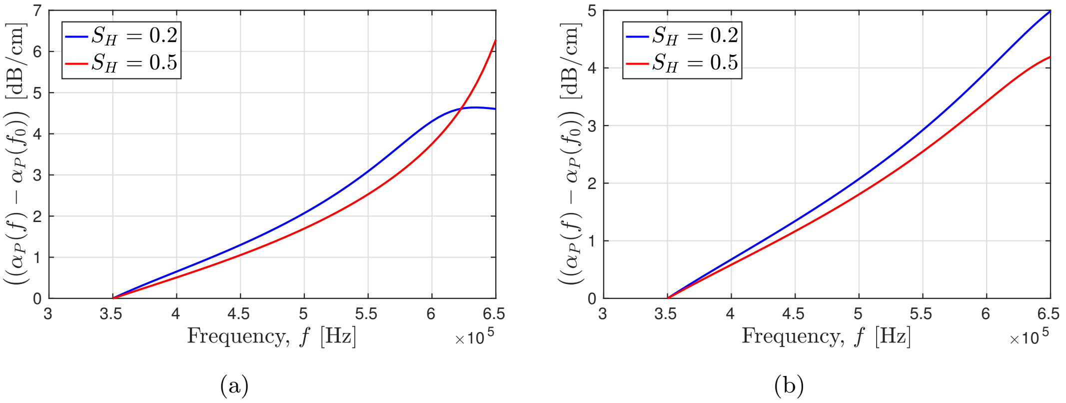

(a) (b)

Figure 7.30: Measured α_P relative to α_P at frequency $f_0 = 350$ kHz for S_H 0.2 and 0.5 for **a)** experiment 3, $S_{w0} = 0.65$ and **b)** experiment 4, $S_{w0} = 0.69$.

The dispersion curves relative to c_P at 350 kHz for S_H 0.2 and 0.5 for experiment 3 and 4 are presented in Fig. 7.31. The dispersion curves are steeper at S_H 0.2 compared with S_H 0.5 in both experiment 3 and 4. As high attenuation is known to give a frequency dependent c_P, the measurements indicate that α_P is higher for S_H 0.2 compared with S_H 0.5.

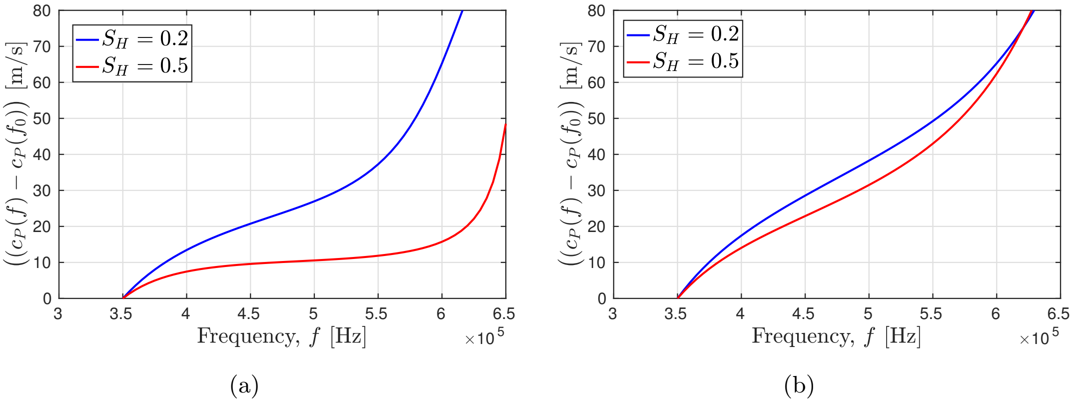

(a) (b)

Figure 7.31: Measured c_P relative to c_P at frequency $f_0 = 350$ kHz for S_H 0.2 and 0.5 for **a)** experiment 3, $S_{w0} = 0.65$ and **b)** experiment 4, $S_{w0} = 0.69$.

Experiment 5 and 7

As for experiment 3 and 4, the difference in α_P and α_P at frequency $f_0 = 350$ kHz is measured for experiment 5 and 7. The results are presented in Fig. 7.32. For experiment 5, the increase in α_P from $f_0 = 350$ kHz to $f_1 = 600$ kHz is 4.9 dB/ cm and 3.0 dB/cm at $S_H = 0.2$ and $S_H = 0.5$, respectively. For experiment 7, the increase in α_P from $f_0 = 350$ kHz to $f_1 = 600$ kHz is 3.5 dB/ cm and 2.5 dB/cm at $S_H = 0.2$ and $S_H = 0.5$, respectively.

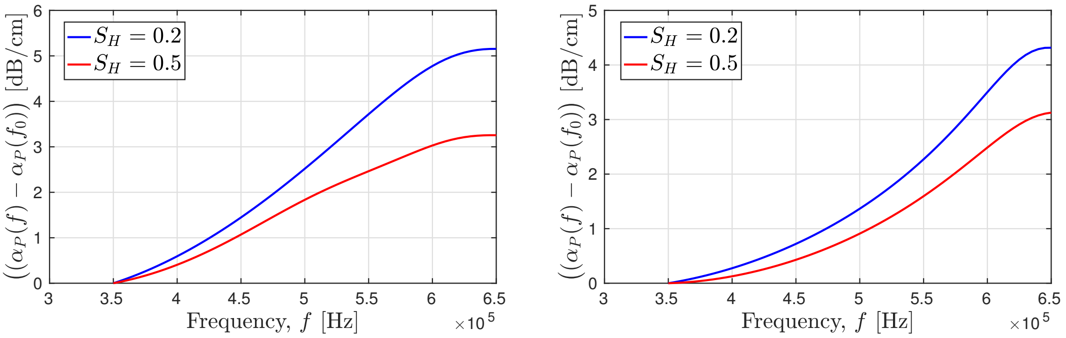

Figure 7.32: Measured α_P relative to α_P at frequency $f_0 = 350$ kHz for S_H 0.2 and 0.5 for **a)** experiment 5, $S_{w0} = 0.73$ and **b)** experiment 7, $S_{w0} = 0.78$.

Experiment 8-10

In experiment 8-10, S_{w0} of the sandstones are above 0.9. By comparing Fig. 7.33 with Fig. 7.32 and Fig. 7.30, the attenuation spectrum is seen to increase more moderately compared with the other experiments.

For experiment 8, the increase in α_P from $f_0 = 350$ kHz to $f_1 = 600$ kHz is 1.3 dB/ cm and 0.4 dB/cm at $S_H = 0.2$ and $S_H = 0.5$, respectively. For experiment 9, this increase is 1.8 dB/ cm and 0.3 dB/cm and for experiment 10 the increase is 1.8 dB/ cm and 0.8 dB/cm at $S_H = 0.2$ and $S_H = 0.5$, respectively.

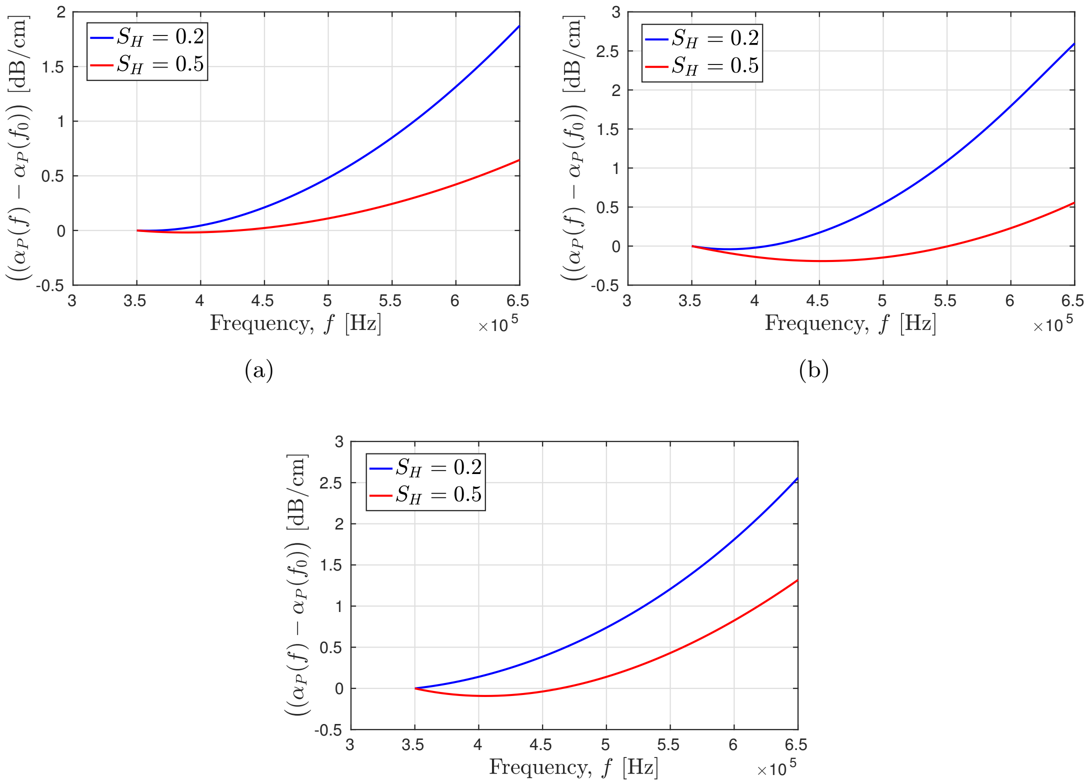

(a)

(b)

(c)

Figure 7.33: Measured α_P relative to α_P at frequency $f_0 = 350$ kHz for S_H 0.2 and 0.5 for **a)** experiment 8, $S_{w0} = 0.92$, **b)** experiment 9, $S_{w0} = 0.94$ and **b)** experiment 10, $S_{w0} = 0.95$.

Attenuation spectrum measurements for fixed S_H for experiment 1-10

To further investigate how water in the pores affect the difference in α_P between $f_0 = 350$ kHz and $f_0 = 600$ kHz is plotted for all experiments (except 1, 2 and 6). $(\alpha_P(f_1) - \alpha_P(f_0))$ is presented for $S_H = 0.2$ in Fig. 7.34 a) and for $S_H = 0.5$ in Fig. 7.34 b). $(\alpha_P(f_1) - \alpha_P(f_0))$ seem to generally be lower when measuring at $S_H = 0.5$ compared with measurement at $S_H = 0.2$. $(\alpha_P(f_1) - \alpha_P(f_0))$ is highest for low S_{w0}. If S_{w0} is known, the measurements indicates that low values of $(\alpha_P(f_1) - \alpha_P(f_0))$ means a high hydrate content and a high value of $(\alpha_P(f_1) - \alpha_P(f_0))$ indicates a low hydrate content.

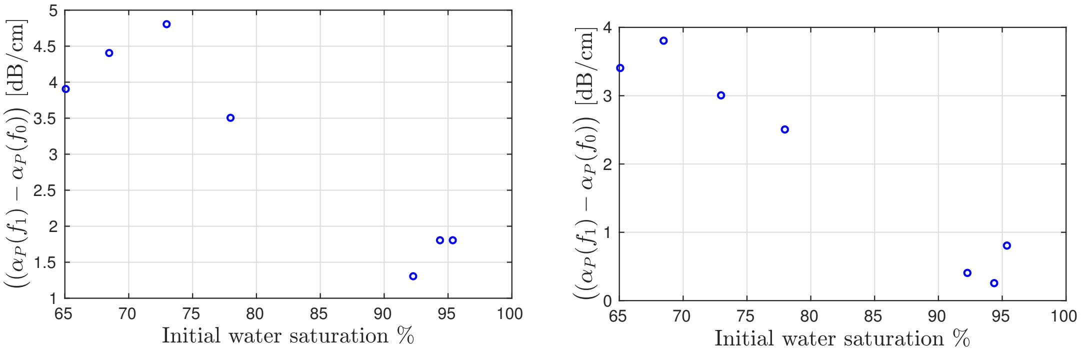

(a)

(b)

Figure 7.34: Difference between the measured α_P at 350 kHz and 600 kHz $(\alpha_P(f_1) - \alpha_P(f_0))$ at **a)** $S_H = 0.2$ and **b)** $S_H = 0.5$.

7.4 Discussion

In this section a discussion of the results in this chapter is provided. The relation between S_H, c_S and c_P in respect to the hydrate growth pattern is discussed in Sec. 7.4.1. The choice of signal processing method and the influence of frequency on the measured c_P is discussed in Sec. 7.4.2. In Sec. 7.4.3 the measured c_S and c_P is compared with literature studies. Attenuation mechanisms and the measured $\Delta\alpha_P$ during hydrate growth is discussed in Sec. 7.4.4. In Sec. 7.4.5, the relevance of comparing the results from this work with data from well logs is discussed briefly.

7.4.1 Relating S_H to the measured c_P and c_S in experiment 1-10 and identifying hydrate growth patterns with numerical models

In Figs. 7.2, 7.3, 7.5 and 7.6 the measured c_P and c_S are seen to increase for increasing S_H. The highest absolute c_P and c_S are measured in the sandstones reaching the highest S_H. This is a well-known results found also in previous studies on hydrate bearing sediments [22, 21, 30, 31, 32, 33, 34, 35].

The increase in c_P from $S_H = 0$ to $S_H = 0.5$ during hydrate growth is measured to be largest for the sandstones having the lowest S_{w0} (Fig. 7.7 b)). Sandstones having low S_{w0} are also seen to have the largest increase in c_S from $S_H = 0$ to $S_H = 0.5$ (Fig. 7.8 b)), however, this trend is not so clear as seen for the P-waves. The absolute value of c_P and c_S at $S_H = 0.5$ seem in general to be highest for the sandstone specimen having lowest S_{w0} (Fig. 7.7 a) and (Fig. 7.8 a))). S_{w0} has previously been related to the maximum reached S_H in hydrate growth experiments [30]. No studies have been found by this author linking S_{w0} and c_P or c_S in different sandstone specimen at the same fixed S_H.

As seen in the experiments (Figs. 7.2, 7.3, 7.5 and 7.6) a high c_P or c_S does not necessarily mean a high hydrate content. Different hydrate growth patterns are known to affect c_P and c_S in sandstones differently [22, 30, 24]. Numerical models (with no loss) are thus used to investigate whether hydrates are forming in the pore fluid, forming and acting as a second type of grain, becoming a load-bearing member of the dry frame, or forming around grain contacts, acting as cement and stiffening the dry frame. These numerical models may aid in identifying the hydrate growth pattern and thus determine the hydrate content. Models including loss are discussed in Sec. 7.4.4.

When hydrates are forming inside the pore fluid, the HFlU-model predicts no change in c_P or c_S during hydrate growth in Fig. 7.9 a) and 7.10 a). By zooming in on the figures, even a small drop is seen in c_P and c_S from $S_H = 0 \sim 0.2$. This is because the density increases while K_{eff} only slightly increase in Eq. (2.21). Only a moderate increase is seen using the HFlP-model (Fig. 7.9 a) and 7.10 a)).

The models treating hydrates as a second load-bearing grain (HFrU and HFrP) predict a 700-800 m/s increase in c_P from $S_H = 0$ to $S_H = 0.5$ (Fig. 7.11 a) and 7.12 a)). The models treating hydrate as cementing material around the quartz-grains (the HCU and HCP-models), predict a very rapid increase in c_P and c_S for low S_H, seen in Figs. 7.13 a) and 7.14 a). The HCU and HCP-models are implementations of Avseth's cementation model [27], wich is developed for unconsolidated sand-packs. One could argue that the change in stiffness due to cementation is larger for sand-packs that for consolidated sandstones, where the grains are initially slightly cemented. However, even if the HCU and HCP-models are not directly comparable to a consolidated sandstone, it is assumed that the dramatic increase in c_P and c_S predicted by the models (Figs. 7.13 a) and 7.14 a)) are also partly true if hydrates act as cement inside the Bentheim sandstone.

For sandstones having the the four lowest S_{w0} (Figs. 7.2 and 7.3), there is an increase in c_P at low S_H. The increase in c_P for $S_H < 0.2$ in experiment 1-4 is largest for experiment 1 and lowest for experiment 4. The increase in c_P seem to be more profound in the experiments having lowest S_{w0}. In experiment 1 ($S_{w0} = 0.48$), the increase is higher than the frame building models (HFrP or HFrU) can explain. This indicates that hydrate cementing processes occur. In experiment 2 ($S_{w0} = 0.55$) the increase in c_P is also clear, however not as clear as for experiment 1. This is also the case for experiment 3 (S_{w0}=0.65). For experiment 4 (S_{w0}=0.69) the increase in c_P is small and similar to the increase seen in experiment 5-7.

In experiment 8-10, where the sandstones have $S_{w0} > 0.9$, there are no measured increase in c_P or c_S for S_H below 0.2 (Fig. 7.6). A small decrease is measured for c_P from $S_H = 0$ to $S_H = 0.2$. The only hydrate growth model to explain this, is the HFlU-model (Fig. 7.9 a) and 7.10 a)), which indicates that the hydrates are forming in the pore fluid for these sandstones at these S_H. Hydrates located in the pore space without appreciable grain-contact are already identified as a possible growth pattern for specimen having high S_{w0} and $S_H < 0.2$ in unconsolidated sediments [46, 34]. For the sandstones having S_{w0} 0.73-0.78 (experiment 5-7, Fig. 7.5), a slight increase is seen during hydrate growth in both c_P and c_S for $S_H < 0.2$. This increase is too low to be explained by the frame building model presented in Fig. 7.12 a). Hydrates forming at low S_H are believed to mostly be placed in the pore fluid for experiment 5-7 as well. After this zero-growth period at low S_H, c_P is seen to steadily increase until maximum S_H is reached for experiment 5-10 (Figs.7.5 and 7.6). By comparing the results with the numerical models, the hydrates in frame-models, HFrU or HFrP give the best fit (Fig. 7.17). Overall for experiment 1-10, for $S_H < 0.2$, there is a clear trend towards hydrates forming in the pore fluid for high S_{w0} and growing into the frame for lower S_{w0}.

7.4.2 Choice of signal processing method and the influence of frequency on the measured c_P for hydrate bearing Bentheim sandstone

In many studies, the first arrival of the signal is used when measuring the compressional and shear wave velocity in hydrate bearing sediments [22, 21, 35]. The use of the first arrival of the signal in c_P-measurements is shown in Fig. 7.3 and gives a higher measured value for c_P compared with the Fourier spectrum method. As the measurement frequency is undefined and the accuracy of measurements using the first arrival is debated [49, 50], more confidence is given to results presented with the Fourier spectrum method.

As seen in experiment 1-4 (Figs. 7.2 and 7.3), c_P is measured to be highest for 600 kHz and lowest for 350 kHz, indicating that dispersion should be detectable. As the accuracy for the S-wave transducers are given to be 60-65 m/s, dispersion is not detectable with these. Dispersion and attenuation mechanisms are closely related. Thus the attenuation mechanisms discussed in Sec. 7.4.4 are believed to cause the measured dispersion.

Due to few data-points, dispersion curves at fixed S_H are only obtained for experiment 3-4 (Fig. 7.31). From these two experiments it seems like a high value for $c_P(f) - c_P(f_0)$ is measured for low S_H and a low value of $c_P(f) - c_P(f_0)$ is measured for high S_H. Investigating dispersion curves from well-logs may thus potentially aid in detecting hydrate-rich regions.

7.4.3 Comparing the c_P and c_S measurements with other studies on hydrate bearing sediments

As discussed in Sec. 1.5, the measured c_P and c_S in almost all studies found by this author on hydrate-bearing sediments are conducted on unconsolidated specimen. In general, the reported c_P and c_S on hydrate-bearing unconsolidated sediments found by this author [22, 32, 164, 33, 35] are lower than c_P and c_S measured in this work. The relative change in c_P and c_S for unconsolidated sediments from zero to maximum S_H are reported to be higher (typically an increase in c_P of approximately 2000 m/s) than found in this work for consolidated Bentheim sandstones. One early laboratory study growing THF-hydrates (tetrahydrofuran hydrate formation, synthetic hydrate growing at atmospheric conditions) in consolidated Berea sandstone was found [36]. Exact measures on S_{w0} or S_H was not given, but c_P was reported to be 4700 m/s at full hydrate growth. In another study, Hu et al. measured c_P and c_S in an unidentified porous consolidated rock. Hu et. al [35] reported an increase in c_P from 4240 m/s at baseline condition to 4660 m/s at $S_H = 0.65$ in the consolidated sediment they used in their study. For the same specimen c_S was reported to increase from 2530 m/s to 2725 m/s at maximum S_H. S_{w0} was given as 40 %. This give an increase in c_P of approximately 400 m/s and for c_S approximately 200 m/s. This increase is comparable to some of the Bentheim sandstones having high S_{w0}, for example experiment 8 (Fig. 7.6 a)), which has an increase of approximately 450 m/s in c_P from $S_H = 0$ to 0.65. Hu et al.'s results is not comparable to experiment 1 (Fig. 7.2), which has more similar S_{w0} (0.48).

The hydrate growth pattern has been subject to discussion in studies relating S_H to c_P and c_S in unconsolidated sediments [22, 32, 164, 33, 35, 34]. Waite et al. [22] used sediment with $S_{w0} = 0.31$ and found a hydrate cementing regime to best fit their measurements. Nakagawa et al. [33] used sediment with $S_{w0} = 0.2$ and also believed a hydrate cementing regime to best explain their measurements. Zhang et al. [34] used sandy sediments with $S_{w0} =0.52$. The hydrate cementing regime was not able to describe the measured increase in c_P and c_S and they concluded that some hydrates were also forming in the pore fluid and some hydrates acting as load-bearing grains.

Priest et al. [164] used the "excess water" and "excess gas" method to manufacture hydrate-bearing unconsolidated sediment specimen. In the "excess gas" method, water is first injected into the specimen, then gas is injected. The amount of water is limiting the amount of hydrate growth. In the "excess water" method, gas is first injected into the specimen, then water is injected. Now, the amount of gas is limiting the amount of hydrate growth. By comparing theoretical models with the measured c_P and c_S, Priest et al. [164] suggested that for the excess gas specimens, the hydrate exhibited a cementing behavior. For the excess water specimens, they suggested hydrate exhibiting a frame supporting behavior. In addition, hydrates formed using the excess water method were found to have no apparent effect on the measured velocities of the sand for $S_H < 0.2$.

Tohidi et al. [209] showed that methane hydrate forms primarily in the center of pores in "water-rich" systems initially containing bubbles of gas. Stern et al. [210] and Waite et al. [211] found that hydrate cements sediment grains in "gas-rich" systems initially containing discrete units of water.

For experiment 5-10 ($S_{w0} > 0.70$, Figs. 7.5 and 7.6), little or no change in c_P or c_S is found for $S_H < 0.2$. This is a similar behavior to the "water-rich" system described by Tohidi et al. [209], where hydrates form in the pore fluid. For $S_H > 0.2$, c_P and c_S increase and the HFrU or HFrP give the best fit for experiment 5-10. Experiment 1, where $S_{w0} < 0.5$, show similarities to the gas-rich system described by Stern et al. [210] and Waite et al. [211] where cementing occurs for even low hydrate concentrations. In Experiment 2-4, the development in c_P can not be solely described with HFl or the HFr- model. This indicates that a combination of hydrates growing in the pore fluid and hydrates acting as load bearing grains is likely. In experiment 2-4, for $S_H > 0.2$, the HFr-model shows the best fit.

Zhang et al. [34] offers an explanation of the analogue experiment on unconsolidated sediments: Because hydrate is hydrophilic, hydrates may suspend in water when the hydrate concentration in the liquid phase is low. However, when the concentration of hydrate in the liquid phase is high, it will adhere to the sand surface, consolidate the sand grain and the c_P will increase. Zhang et al. [34] found that hydrates only form in the fluid for $S_H < 0.3$. These considerations seem to be consistent with the results in experiment 1-10 as well.

A sudden drop in the c_P/c_S-ratio has previously been used to identify hydrates cementing unconsolidated sediments [32] in laboratory studies. Another laboratory study using THF-hydrates showed that the c_P/c_S-ratio can decrease also when hydrates act as load bearing grains [212]. Comparing the study of Priest et al. [32] and Yun et al. [212], the decrease in the c_P/c_S-ratio was found to be much clearer when hydrates are acting as cement. This agrees well with the theoretical c_P/c_S-ratio calculated with the HC-model (Fig. 7.13 b)) and the HFr-model (Fig. 7.12 b)).

In Figs. 7.6 b), d) and e) a clear drop in the measured c_P/c_S is seen. However, no absolute conclusion is reached on whether this is a cementing process. Since the HFrU or HFrP-models (Fig. 7.17) are fairly well predicting the increase in both c_P and c_S, thus hydrates growing in the frame are believed to be the main source of the measured increase in c_P and c_S. Due to the more rapid increase in c_P for experiment 1, cementation of grains is believed to occur. Unfortunately, c_S-measurements are not available for this experiment and thus no c_P/c_S-ratio.

7.4.4 Attenuation mechanisms and measured $\Delta\alpha_P$ during hydrate growth

In the same way as for the wave velocities, the change in α_P is measured during hydrate growth (Figs. 7.19, 7.20, 7.21 and 7.22). Due to possible non-linear effects and the uncertainities described in Sec. 6.1.3, the compressional wave attenuation is presented as α_P relative to α_P at $S_H = 0.2$: $\Delta\alpha_P = \alpha_P - \alpha_P(S_H = 0.2)$.

The attenuation measurements in experiment 1-10 (Figs. 7.19, 7.20, 7.21 and 7.22) show a clear trend: α_P is decreasing for higher S_H. Only one laboratory-study on α_P-measurements of hydrate bearing sediments have been found by this author. Nakagawa et al. [33] measaured Q_P and Q_S in hydrate bearing Ottawa-sand during hydrate growth. In this study, some unexpected results are reported on the α_P - measurements. In the very start of the hydrate growth (low but undefined S_H) α_P is increasing rapidly to a maximum value. From this low (but nonzero) S_H to maximum S_H, α_P decreases 3.5 dB/cm. This decrease in α_P is similar to the measured $\Delta\alpha_P$ in Fig. 7.23. This laboratory study is seen to be consistent with the measurements conducted in this work.

Guerin et al. [39] did not perform laboratory measurements, but analyzed data from the Mallik well and found that the attenuation increased with increasing S_H. Guerin et al. do not clearly give the frequency interval other than "sonic frequencies" are used. From the model Guerin et al. used, squirting flow was given as the explanation for the increasing α_P with increasing S_H. However, this is a contradiction to the laboratory results presented by Nakagawa et al. [33] who also used "sonic frequencies" (frequencies below 10 kHz). No explanation is given here for the differing results from these two studies.

For experiment 3 and 4 shown in Figs. 7.20 a) and c), respectively, there are dips in $\Delta\alpha_P$ at $S_H \approx 0.6$. In experiment 3, there is a peak around $S_H = 0.4$, especially for measurement frequency 600 kHz. There is also a peak at $S_H = 0.4$ for measurement frequency 350 kHz in experiment 8 (Fig. 7.22 a)). There is a general trend that the sandstones having the highest S_{w0} (experiment 8-10 shown in Fig. 7.22) only show a small decrease in $\Delta\alpha_P$ up to $S_H \approx 0.4$. The sandstones having the lowest S_{w0} (experiment 1-2 shown in Fig. 7.19) show a rapid decrease in $\Delta\alpha_P$ for low S_H.

In Fig. 7.23 a) and b), the decrease in α_P from $S_H = 0.2$ to $S_H = 0.0.5$ for experiment 1-10 using 350 kHz and 500 kHz are shown, respectively. It is clear that the drop in

α_P from $S_H = 0.2$ to $S_H = 0.5$ are largest for the sandstones having the lowest S_{w0}. If this is true for a reservoir containing hydrates, it may be argued that hydrates are more easily detected in reservoirs with low water content. However, it also implies that if the water content is known to be high in a certain reservoir, a detected decrease in $\Delta\alpha_P$ might suggest a higher S_H than if the water content is known to be low. It is not further investigated by this author if these laboratory findings can be used to analyze real data from well logs. Because the contrast in $\Delta\alpha_P$ is bigger using 500 kHz compared with 350 kHz (Fig. 7.23 a) and b)), hydrates might be easier to detect using higher frequencies. However, acoustic meausrements from sonic well-logs, typically use frequencies below 20 kHz [213, 39, 57].

To identify some of the attenuation mechanisms present in the sandstone, several numerical models are implemented. The BiotHFrU-model (see Sec. 2.5.4), which takes into account the attenuation at macroscopic levels due to fluid flow, is presented in Fig. 7.24. The BiotHFrU-model is based on the Biot model, which is known to underestimate the attenuation [55, 105, 112]. This underestimation is also seen comparing the BiotHFrU-model (Fig. 7.24) with the measurements in this work (Figs. 7.19, 7.20, 7.21 and 7.22). By taking attenuation due to squirting flow into account, more attenuation is predicted. In this work, squirt flow is included in the BiSqHFrU-model (Sec. 2.5.5, based on Dvorkin and Nur [55]). This model takes both the Biot flow and squirting flow into account and is shown in Fig. 7.25. The BiSqHFrU-model does not predict enough attenuation to explain the measurements either. The squirt-flow model of Dvorkin et al. [55] use a parameter called squirt-length to describe the dimensions of the pores or cracks in which the squirting flow may flow. Widely used [214, 105], however, Dvorkin's Biot-Squirt model has been critizised for not being consistent with Gassmann's equations [170]. Another way of implementing the squirt flow is to relate the squirting flow to cracks and their aspect ratios inside the porous rock [128, 106, 215]. In these models the attenuation is highly dependent on the crack aspect ratio and the aspect ratios may be adjusted to fit the observed atenuation. By using a range of different crack-aspect ratios, porous rocks with multiple attenuation modes due to squirt flow have been modeled [170].

It is well-established that both Biot flow and squirting flow affect the measurements at the frequencies used in this work [55]. With no fluid inside the sandstone there is no squirting flow. If attenuation due to pressure induced fluid flow is the only attenuation mechanism, measurements conducted on dry rocks should give no attenuation. No extensive study on the transmission of waves through dry Bentheim specimen is performed in this work. However, signals are not successfully transmitted and recorded through dry Bentheim specimen at 500 kHz in this work. It is concluded that the elastic waves are heavily attenuated through dry Bentheim sandstones, which means that other attenuation mechanisms than the squirting flow exist.

In many studies, attenuation due to scattering is assumed to be negligable [124, 216, 217]. Sams et al. [218] investigate the attenuation in sedimentary rocks and find that intrinsic loss dominates the scattering loss in their VSP logs (30-280 Hz) and sonic logs (8-24 kHz). Gist et al. [219] report the attenuation in dry Berea sandstone specimen to be lower than the attenuation in water-saturated Berea sandstone specimen at 1 MHz. They conclude that the attenuation due to scattering effects are small compared with the attenuation due to pressure-induced fluid flow. Only a few studies on the attenuation of elastic waves in Bentheim sandstones are found by this author. Mayr et al. [165] discuss whether scattering of elastic waves in Bentheim sandstones may be present and whether the fluid content affect the amount of scattering. They reach no absolute conclusion. However, attenuation due to scattering of elastic waves are seen as a possible attenuation mechanism in porous rocks [124, 220, 137], especially for ultrasonic frequencies.

By using WaTrHFrU-model (based on Watermann and Truell [56]), pore-sized heterogenities are seen to give no significant attenuation in Fig. 7.27. To describe the attenuation seen in the measurement with scattering, larger heterogeneities than the pores must be present. Such heterogeneities may be cracks or patches of fluid [44, 137, 136, 43, 221]. Circular fluid inclusions with radii 500-1000 µm are capable of explaining the attenuation seen in the measurements (Fig. 7.27). However, no measurements are conducted to back this hypothesis. Another attenuation mechanism discussed in the literature is friction between grain contacts. However, this attenuation mechanisms is typically neglected [124].

In Fig 7.28, the WaTrBiSqHFrU-model (Sec. 2.5.7, combination of The Biot-squirt model [55] and scattering model [56]) is plotted for different squirting flow lengths and water inclusion-radii. The model is able to explain the general decrease in α_P seen in the attenuation measurements (Figs. 7.19, 7.20, 7.21 and 7.22). It can also qualitatively explain some of the dips and jumps seen for $\Delta\alpha_P$ during hydrate growth. No absolute conclusion is reached whether the attenuation seen in the measurements are due to scattering or pressure induced fluid-flow. It is believed that both mechanisms are present for frequencies around 500 kHz in partly saturated hydrate bearing Bentheim sandstones.

In Fig. 7.34, $\alpha_P(f) - \alpha_P(f_0)$, where $f_0 = 500$ kHz is shown for experiment 1-10. The difference in $\alpha_P(f) - \alpha_P(f_0)$ between $S_H = 0.2$ and 0.5 is clearly bigger for lower S_{w0}, indicating that hydrates are easier to detect for sandstones having low S_{w0}. This agrees with the c_P-measurements (Fig. 7.7) where the change in c_P during hydrate growth is also higher for lower S_{w0}. The measurements conducted in this work indicate that hydrates are more easily detected in sediments having low S_{w0}. However, if a sediment is known to have high water content, a measured change from baseline in $\alpha_P(f) - \alpha_P(f_0)$, $\Delta\alpha_P$, c_P, $c_P(f) - c_P(f_0)$ and c_S may indicate a high hydrate content.

For industries trying to extract methane gas from methane-hydrate bearing reservoirs, it may not be interesting to know whether the measured attenuation is due to scattering or fluid flow mechanisms. It is important to know the hydrate growth pattern so a proper numerical model may be used to estimate the hydrate content. The attenuation measurements conducted in this work are related to S_{w0} and thus the hydrate growth growth pattern. By fitting parameters, the WaTrBiSqHFrU-model containing both squirting flow and scattering mechanisms gives a fair fit with the some of the measurements. This gives however no proof that this model is correct. More work must be done before such a model could be used to quantitatively predict S_H in a reservoir based on attenuation measurements.

7.4.5 Relevance of comparing the results with data from well logs

Vertical seismic profile (VSP) logs and sonic logs have been used to identify hydrate rich regions from bore-holes [21, 57, 213, 39]. When drilling down in a well, c_P and c_S are typically constant or increasing very slowly with depth due to the increasing pressure in the sediments. This is called the baseline. Sudden increases in c_P and c_S indicate zones of hydrate [57, 213, 39]. Guerin et al. [39] present raw-data from the Mallik-well. Clear jumps in c_P and c_S are seen in the raw data. Estimation of S_H in the sediments relies on using an appropriate numerical model and determining the hydrate growth pattern to relate S_H with c_P and c_S. Knowledge from laboratory studies of the same sediment type as found in the field may aid in understanding well-logs and thus estimate the hydrate content [21]. As mentioned, many laboratory studies are performed on unconsolidated sediments which are present in wells such as the Black Ridge and he Mallik-well [21]. In this work, c_P, c_S and $\Delta\alpha_P$ have been measured for consolidated sediments. As mentioned above, both the relative and the absolute changes in c_P and c_S due to hydrate growth for Bentheim sandstones are found to be differing from measurements conducted on unconsolidated sediments [22, 32, 164, 33, 35, 34]. The attenuation measurements conducted in this work are also relative to α_P at $S_H = 0.2$. Thus. the results presented in this work is not suited to be directly compared with field data from wells such as the Black Ridge and he Mallik-well. No effort is done here to list potential wells containing more consolidated sediments. However, such wells might be more relevant to compare with the measurement results from this work.

Chapter 8

Conclusions and outlook

In this chapter the conclusions and main findings in this work are presented in Sec. 8.1. Potential further work is discussed in Sec. 8.2.

8.1 Conclusions

Due to the potential for using methane hydrates as an energy source, localizing, monitoring and describing hydrate deposit areas are of interest. This has previously been attempted by using acoustic methods and thus information on the relation between the hydrate saturation, S_H, and acoustic properties, such as c_P, c_S and α_P is needed.

The overall aim of this PhD thesis is to measure and discuss c_P, c_S and the change in α_P ($\Delta\alpha_P$) in ten Bentheim sandstone specimen having different initial water saturations, S_{w0} as a function of S_H, during hydrate growth. To the best of this author's knowledge, no laboratory studies on the elastic properties of methane hydrate bearing Bentheim sandstones have been published.

A pressure-cell is modified so that acoustic measurements may be conducted inside the cell during hydrate growth. As specific dimensions are required for experimental equipment to fit inside the pressure cell, transmitting and receiving piezoelectric P-wave and S-wave transducers are designed and constructed. A pressure tight electrical feedthrough is designed and constructed for use with the transducers inside the pressure cell. A robust Matlab logging algorithm able to log the acoustic signal through the Bentheim sandstone every 15 minutes for weeks is developed and used in the measurements.

Because of the limited space inside the pressure cell, unwanted acoustic reflections from sidewalls will affect acoustic measurements, even when short pulses are used. Another source of uncertainty is diffraction effects in the buffers and specimen. The solid buffer method used on plexiglas specimen having approximately the same dimensions as the Bentheim sandstone specimen is simulated using finite element simulations and Fourier synthesis.

The effect of sound diffraction and sidewall-reflections on the simulated c_P using the P-wave transducers are seen to be approximately 4 m/s and 1 m/s, respectively. c_P typically increases approximately 500 m/s in the sandstone during hydrate growth. If the sound diffraction effects and the sidewall-reflections are approximately the same for the plexiglas simulations and the solid buffer method measurements, these effects will not affect the hydrate experiments critically. The effect of sound diffraction and sidewall-reflections on the simulated α_P are approximately 0.1 dB/cm and 0.3 dB/cm, respectively. In this work it is assumed that the effects of the sidewall-reflections and the sound diffraction on the measured α_P stays approximately the same during hydrate growth. Thus $\Delta\alpha_P$ should not be critically affected.

The measured c_P and c_S are seen to increase for increasing S_H in experiment 1-10. The highest absolute c_P and c_S are measured in the sandstones reaching the highest S_H. The increase in c_P and c_S from $S_H = 0$ to $S_H = 0.5$ during hydrate growth is measured to be largest for the sandstones having the lowest S_{w0}.

Because the hydrates may form in different ways inside the sandstone, a high measured c_P or c_S does not necessarily mean a high hydrate content.

Numerical models based on the work of Dvorkin et al. [26] and Helgerud et al. [24] are used to model three different hydrate growth scenarios. In the first scenario, hydrates are forming in the pore fluid of a sandstone (HFl-model), not affecting the dry frame. In the second scenario, all hydrates are forming and acting as a second type of grain, becoming load-bearing members of the dry frame (HFr-model). In the third scenario, hydrates are forming around grain contacts, acting as cement and stiffening the dry frame (HC-model). The HFr-model suggests an increase in c_P and c_S of approximately 400-500 m/s and 200-300 m/s, respectively from $S_H = 0.2-0.5$. The HFl model suggests little or no increase in c_P and c_S during hydrate growth. The HC-model suggests c_P and c_S to increase more than for the HFr-model.

These models simplify the complex nature of a sandstone and do not consider loss of acoustic energy or dispersion effects. A thorough analysis on the accuracy of these models on describing the three different hydrate growth scenarios is not performed in this work. However, models based on the same principles as the HFl, HFr and HC - models are widely used to model c_P and c_S in hydrate bearing sediments for both low measurement frequencies (<20 kHz) [164] and for higher measurement frequencies (approximately 500 kHz) [22, 21, 34].

By comparing these models with the measurements, it is indicated that for experiments 4-10, where $S_{w0} > 0.69$, for $S_H > 0.2$, hydrates act as a second type of grain, becoming a load-bearing member of the dry frame. For $S_H < 0.2$, it is indicated that hydrates are forming primarily in the pore fluid.

For experiment 1, where $S_{w0} = 0.48$, a rapid increase is measured in c_P during hydrate growth, indicating that, at least partly, the hydrates are cementing the quartz grains. For experiments 2-3 ($S_{w0} = 0.55 - 0.65$), it seems like hydrates mainly act as load-bearing members of the dry frame. However, the numerical models indicate that some cementing of the quartz grains occur for $S_H > 0.2$.

Overall, for experiment 1-10, for $S_H < 0.2$, there is a clear trend towards hydrates forming in the pore fluid for high S_{w0} and growing into the frame for lower S_{w0}. For $S_H > 0.2$ there is a trend towards hydrates forming in the frame for high S_{w0} and acting more as cement for lower S_{w0}. This finding has also been reported in the literature [164, 210, 34, 209].

A drop in the c_P/c_S-ratio is indicated in the measurements for $S_{w0} > 0.9$ around $S_H = 0.4$. Of the three hydrate mentioned above, only the HC-model may explain such a drop in the c_P/c_S-ratio. However, no absolute conclusion is given in this work of the mechanism behind the drop.

In the literature, laboratory studies typically focus on measuring c_P and c_S in unconsolidated hydrate bearing sediments using the "first arrival of the pulse," which means that the measurement frequency of the elastic wave is not defined [22, 21, 31]. Only a few laboratory studies are found by this author to measure acoustic properties for hydrate bearing sediments for defined frequencies [35, 32]. The Fourier spectrum method is able to determine the frequency content of short measured signals and is used as the main signal processing method in this work (for frequencies 350 kHz-600 kHz). To the best of this author's knowledge, no laboratory studies have measured the dispersion or the attenuation spectrum in porous rocks or sediments during hydrate growth.

In this work, "the first arrival of the pulse method" gives a higher measured c_P compared with the Fourier spectrum method. c_P is measured to be highest for 600 kHz and lowest for 350 kHz, indicating that dispersion should be detectable. Due to the measurement uncertainty in this work, only the P-wave transducers are able to detect dispersion. From these experiments it seems like a high value for $c_P(f) - c_P(f_0)$ is measured for low S_H and a low value of $c_P(f) - c_P(f_0)$ is measured for high S_H. $f_0 = 350$ kHz.

Pressure induced fluid flow is known to affect α_P-measurements in sandstones for the frequencies used in this work. This attenuation mechanism is not present in dry sandstones. In dry Bentheim sandstone specimen used in this work, signals are not successfully transmitted and recorded at 500 kHz, giving a strong indication that other attenuation mechanisms than pressure induced fluid flow are present. Also the numerical models used in this work including pressure induced fluid flow, are not able to explain the levels of attenuation seen in the measurements.

Multiple scattering of elastic waves is also known to be an attenuation mechanism inside porous rocks, especially for higher frequencies. The numerical models used in this work show some resemblance between the simulations and the measurements of $\Delta\alpha_P$ when multiple scattering (Waterman and Truell's multiple scattering theory) is included in the model.

For the attenuation measurements in experiment 1-10, α_P is decreasing during hydrate growth. α_P is decreasing more for frequency 500 kHz compared with 350 kHz. Also, there is a clear trend towards α_P decreasing more for the sandstone specimen having low S_{w0}. A decreasing α_P during hydrate growth in hydrate bearing sediments has also been found in another laboratory study [33]. However, data from well-logs have also indicated a increase in α_P for higher hydrate saturations [39]. No discussion is provided in this work regarding this apparent inconsistency.

The attenuation spectrum, $\alpha_P(f) - \alpha_P(f_0)$, where $f_0 = 350$ kHz is measured for experiment 1-10. The difference in $\alpha_P(f) - \alpha_P(f_0)$ between the two distinct hydrate saturations $S_H = 0.2$ and $S_H = 0.5$ is clearly bigger for lower S_{w0}. This agrees with the c_P-measurements, where the change in c_P during hydrate growth is also higher for lower S_{w0}.

In this work, the measured acoustic parameters c_P, c_S, $\Delta\alpha_P$, $\alpha_P(f) - \alpha_P(f_0)$ and $c_P(f) - c_P(f_0)$ are more sensitive to changes in S_H at lower S_{w0}. This might indicate that hydrates are more easily detected in sediments having low S_{w0}. Whether these laboratory findings may be used to aid in analyzing field data from well-logs is not discussed further in this work.

From previous measurement on hydrate bearing unconsolidated sediments, c_P and c_S are known to increase for increasing S_H [22, 34, 32, 33]. The change in c_P and c_S during hydrate growth is also found to be higher for lower S_{w0}. One laboratory study is also report a decrease in α_P for increasing S_H [33]. Previous studies in unconsolidated sandy sediments have reported that for $S_H < 0.2$, there is a trend towards hydrates forming in the pore fluid for high S_{w0} and growing into the frame for lower S_{w0}. For $S_H > 0.2$ there is a trend towards hydrates forming in the frame for high S_{w0} and acting more as cement for lower S_{w0}. [164, 210, 34, 209].

In this study, it is shown that these findings are also true for consolidated Bentheim sandstones. However, the increase in c_P and c_S during hydrate growth for Bentheim sandstone is not so high as for the unconsolidated sediment measurements reported in the literature [22, 34, 32, 33].

By using the Fourier spectrum method, P-wave dispersion seems to be detectable in the experiments conducted in this work ($c_P(f) - c_P(f_0)$). Use of the basic pulse method and "the first arrival of the pulse" give a systematic higher measured c_P compared with the Fourier spectrum method. The relative compressional wave attenuation spectrum ($\alpha_P(f) - \alpha_P(f_0)$) is increasing for higher frequencies. As for c_P, and c_S, the measured parameters $\Delta\alpha_P$, $\alpha_P(f) - \alpha_P(f_0)$ and $c_P(f) - c_P(f_0)$ seem to be more sensitive to changes in S_H at lower S_{w0}.

8.2 Further work

There are several improvements that may be addressed for future work. In addition to c_P and c_S, absolute values of α_P and α_S can be measured in Bentheim sandstones during hydrate growth for a wider range of S_{w0}.

Better control over the uncertainty of the shear wave measurements may be achieved. Especially uncertainities due to the the shear wave diffraction correction, rotation of the transducers and uncertainites due to the couplant between the buffers and specimen should be investigated further. With less uncertainty in the measurements, shear wave dispersion may be measured and the measured c_P/c_S-ratio may be more reliable. To be able to compare experiments having different S_{w0} better, more control over the confining pressure of the sandstone and the applied torque is needed.

In this project, the limited space inside the available pressure cell gave rise to unwanted sidewall reflections, interfering with the measurement signal. Such unwanted reflections may be avoided by designing a pressure cell with larger lateral dimensions.

Like c_P and c_S, the attenuation in Bentheim sandstones changes during hydrate growth. However, the numerical models used for discussing the loss mechanisms do not give a precise description of the measurements. A more accurate theoretical model is needed able to describe scattering and pressure induced fluid flow due to cracks of various dimensions, and thus to achieve a better understanding of the attenuation mechanisms.

More information may also be gained on the relations between c_P, c_S, α_P, α_S and S_{w0} and S_H by using lower frequencies (< 50 kHz). Frequencies below 50 kHz are closer to the frequencies typically used in well-logs [218, 32]. To do this, the resonance method may be used [32, 33]. Transducers able to transmit lower frequencies may potentilaay be designed using bender elements [35, 222, 223].

Bibliography

[1] G. J. Moridis, T. S. Collett, R. Boswell, M. Kurihara, M. T. Reagan, C. Koh, and E. Sloan, "Toward production from gas hydrates", SPE Reservoir Evaluation and Engineering **12**(5), pp. 745–771 (2009).

[2] G. Moridis, T. S. Collett, M. Pooladi-Darvish, S. H. Hancock, C. Santamarina, R. Boswell, T. J. Kneafsey, J. Rutqvist, M. B. Kowalsky, and M. T. Reagan, "Challenges, uncertainties, and issues facing gas production from gas-hydrate deposits", SPE Reservoir Evaluation and Engineering **14**(1), pp. 76–112 (2011).

[3] A. V. Milkov, "Global estimates of hydrate-bound gas in marine sediments: how much is really out there?", Earth-Science Reviews **66**(3), pp. 183–197 (2004).

[4] J. B. Klauda and S. I. Sandler, "Global distribution of methane hydrate in ocean sediment", Energy & Fuels **19**(2), pp. 459–470 (2005).

[5] K. A. Kvenvolden, "Gas hydrates -geological perspective and global change", Reviews of geophysics **31**(2), pp. 173–187 (1993).

[6] G. Holder, V. Kamath, and S. Godbole, "The potential of natural gas hydrates as an energy resource", Annual Review of Energy **9**(1), pp. 427–445 (1984).

[7] K. Hayhoe, H. S. Kheshgi, A. K. Jain, and D. J. Wuebbles, "Substitution of natural gas for coal: Climatic effects of utility sector emissions", Climatic Change **54**(1), pp. 107–139 (2002).

[8] M. Nixon and J. L. Grozic, "Submarine slope failure due to gas hydrate dissociation: a preliminary quantification", Canadian Geotechnical Journal **44**(3), pp. 314–325 (2007).

[9] R. E. Kayen, "The mobilization of Arctic Ocean landslides by sea level fall-induced gas hydrate decomposition", Ph.D. thesis, California State University, Hayward, California, 1988.

[10] K. J. Campbell, “Deepwater geohazards: How significant are they?”, The Leading Edge **18**(4), pp. 514–519 (1999).

[11] W. P. Dillon, W. Danforth, D. Hutchinson, R. Drury, M. Taylor, and J. Booth, “Evidence for faulting related to dissociation of gas hydrate and release of methane off the southeastern United States”, Geological Society, London, Special Publications **137**(1), pp. 293–302 (1998).

[12] D. Archer, “Methane hydrate stability and anthropogenic climate change”, Biogeosciences Discussions **4**(2), pp. 993–1057 (2007).

[13] G. R. Dickens, J. R. O’Neil, D. K. Rea, and R. M. Owen, “Dissociation of oceanic methane hydrate as a cause of the carbon isotope excursion at the end of the paleocene”, Paleoceanography **10**(6), pp. 965–971 (1995).

[14] F. McDonal, F. Angona, R. Mills, R. Sengbush, R. Van Nostrand, and J. White, “Attenuation of shear and compressional waves in Pierre shale”, Geophysics **23**(3), pp. 421–439 (1958).

[15] F. N. Tullos and A. C. Reid, “Seismic attenuation of Gulf Coast sediments”, Geophysics **34**(4), pp. 516–528 (1969).

[16] A. M. Trehu, P. E. Long, M. Torres, G. Bohrmann, F. Rack, T. Collett, D. Goldberg, A. Milkov, M. Riedel, P. Schultheiss, *et al.*, “Three-dimensional distribution of gas hydrate beneath southern Hydrate Ridge: constraints from ODP Leg 204”, Earth and Planetary Science Letters **222**(3), pp. 845–862 (2004).

[17] G. Ersland, J. Husebø, A. Graue, and B. Kvamme, “Transport and storage of CO2 in natural gas hydrate reservoirs”, Energy Procedia **1**(1), pp. 3477–3484 (2009).

[18] J. Husebø, G. Ersland, A. Graue, and B. Kvamme, “Effects of salinity on hydrate stability and implications for storage of CO2 in natural gas hydrate reservoirs”, Energy Procedia **1**(1), pp. 3731–3738 (2009).

[19] T. Xu, J. A. Apps, and K. Pruess, “Numerical simulation of CO2 disposal by mineral trapping in deep aquifers”, Applied geochemistry **19**(6), pp. 917–936 (2004).

[20] R. Korbøl and A. Kaddour, “Sleipner vest CO2 disposal-injection of removed CO2 into the Utsira formation”, Energy Conversion and Management **36**(6), pp. 509–512 (1995).

[21] W. J. Winters, I. A. Pecher, W. F. Waite, and D. H. Mason, “Physical properties and rock physics models of sediment containing natural and laboratory-formed methane gas hydrate”, American Mineralogist **89**(8-9), pp. 1221–1227 (2004).

[22] W. F. Waite, W. J. Winters, and D. H. Mason, “Methane hydrate formation in partially water-saturated ottawa sand”, American Mineralogist **89**(8-9), pp. 1202–1207 (2004).

[23] M. A. Biot, “Theory of propagation of elastic waves in a fluid-saturated porous solid. I. Low-frequency range”, The Journal of the Acoustical Society of America **28**(2), pp. 168–178 (1956).

[24] M. Helgerud, J. Dvorkin, A. Nur, A. Sakai, and T. Collett, “Elastic-wave velocity in marine sediments with gas hydrates: Effective medium modeling”, Geophysical Research Letters **26**(13), pp. 2021–2024 (1999).

[25] J. Dvorkin, A. Nur, and H. Yin, “Effective properties of cemented granular materials”, Mechanics of materials **18**(4), pp. 351–366 (1994).

[26] J. Dvorkin and A. Nur, “Elasticity of high-porosity sandstones: Theory for two North Sea data sets”, Geophysics **61**(5), pp. 1363–1370 (1996).

[27] P. Avseth, J. Dvorkin, G. Mavko, and J. Rykkje, “Rock physics diagnostic of North Sea sands: Link between microstructure and seismic properties”, Geophysical Research Letters **27**(17), pp. 2761–2764 (2000).

[28] P. Avseth, T. Mukerji, G. Mavko, and J. Dvorkin, “Rock-physics diagnostics of depositional texture, diagenetic alterations, and reservoir heterogeneity in high-porosity siliciclastic sediments and rocks—a review of selected models and suggested work flows”, Geophysics **75**(5), pp. 75A31–75A47 (2010).

[29] M. Helgerud, W. F. Waite, S. Kirby, and A. Nur, “Elastic wave speeds and moduli in polycrystalline ice IH, SI methane hydrate, and SII methane-ethane hydrate”, Journal of Geophysical Research: Solid Earth **114**, pp. B02212 (2009).

[30] W. J. Winters, W. F. Waite, D. H. Mason, L. Y. Gilbert, and I. A. Pecher, “Methane gas hydrate effect on sediment acoustic and strength properties”, Journal of Petroleum Science and Engineering **56**(1), pp. 127–135 (2007).

[31] M. B. Rydzy and M. L. Batzle, “Ultrasonic velocities in laboratory-formed gas hydrate-bearing sediments”, in *23rd EEGS Symposium on the Application of Geophysics to Engineering and Environmental Problems*, Society of Exploration Geo-

physicists and Environment and Engineering Geophysical Society, Keystone, Colerado, (2010).

[32] J. A. Priest, A. I. Best, and C. R. Clayton, “A laboratory investigation into the seismic velocities of methane gas hydrate-bearing sand”, Journal of Geophysical Research: Solid Earth **110**(B4), pp. B04102 (2005).

[33] S. Nakagawa, T. Kneafsey, *et al.*, “Split Hopkinson Resonant Bar test and its application for seismic property characterization of geological media”, in *Proceedings of the 44th US Rock Mechanics Symposium and 5th US-Canada Rock Mechanics Symposium*, American Rock Mechanics Association, Salt Lake City, Utah, (2010).

[34] Q. Zhang, F.-G. Li, C.-Y. Sun, Q.-P. Li, X.-Y. Wu, B. Liu, and G.-J. Chen, “Compressional wave velocity measurements through sandy sediments containing methane hydrate”, American Mineralogist **96**(10), pp. 1425–1432 (2011).

[35] G. Hu and Y. Ye, *Ultrasonic Waves on Gas Hydrates Experiments*, INTECH Open Access Publisher, (2012).

[36] C. Pearson, J. Murphy, and R. Hermes, “Acoustic and resistivity measurements on rock samples containing tetrahydrofuran hydrates: laboratory analogues to natural gas hydrate deposits”, Journal of Geophysical Research: Solid Earth **91**(B14), pp. 14132–14138 (1986).

[37] A. E. Peksa, K.-H. A. Wolf, and P. L. Zitha, “Bentheimer sandstone revisited for experimental purposes”, Marine and Petroleum Geology **67**, pp. 701–719 (2015).

[38] J. M. Carcione and U. Tinivella, “Bottom-simulating reflectors: Seismic velocities and AVO effects”, Geophysics **65**(1), pp. 54–67 (2000).

[39] G. Guerin and D. Goldberg, “Modeling of acoustic wave dissipation in gas hydrate–bearing sediments”, Geochemistry, Geophysics, Geosystems **6**(7), pp. 2005GC000918 (2005).

[40] M. Lee and T. Collett, “Gas hydrate saturations estimated from fractured reservoir at site NGHP-01-10, Krishna-Godavari basin, India”, Journal of Geophysical Research: Solid Earth **114**(B7), pp. B07102 (2009).

[41] K. W. Winkler and W. F. Murphy III, “Acoustic velocity and attenuation in porous rocks”, Rock physics and phase relations: A Handbook of physical constants (collection of articles) , pp. 20–34 (1995).

[42] F. Gassmann, “Elastic waves through a packing of spheres”, Geophysics **16**(4), pp. 673–685 (1951).

[43] R. Galvin and B. Gurevich, “Effective properties of a poroelastic medium containing a distribution of aligned cracks”, Journal of Geophysical Research: Solid Earth **114**(B7), pp. B07305 (2009).

[44] J. Hudson, “Attenuation due to second-order scattering in material containing cracks”, Geophysical Journal International **102**(2), pp. 485–490 (1990).

[45] S. Crampin, “Effective anisotropic elastic constants for wave propagation through cracked solids”, Geophysical Journal International **76**(1), pp. 135–145 (1984).

[46] M. Jakobsen, J. A. Hudson, T. A. Minshull, and S. C. Singh, “Elastic properties of hydrate-bearing sediments using effective medium theory”, Journal of Geophysical Research: Solid Earth **105**(B1), pp. 561–577 (2000).

[47] M. Sæther, P. Lunde, and G. Ersland, “Sound velocity measurement methods for porous sandstone. measurements, finite element modelling, and diffraction correction”, in *Proceedings of the 39th Scandinavian Symposium on Physical Acoustics, Geilo, Norway*, , (2016).

[48] W. I. Futterman, “Dispersive body waves”, Journal of Geophysical Research **67**(13), pp. 5279–5291 (1962).

[49] J. B. Molyneux and D. R. Schmitt, “First-break timing: Arrival onset times by direct correlation”, Geophysics **64**(5), pp. 1492–1501 (1999).

[50] J. B. Molyneux and D. R. Schmitt, “Compressional-wave velocities in attenuating media: A laboratory physical model study”, Geophysics **65**(4), pp. 1162–1167 (2000).

[51] K. W. Winkler and T. J. Plona, “Technique for measuring ultrasonic velocity and attenuation spectra in rocks under pressure”, Journal of Geophysical Research: Solid Earth **87**(B13), pp. 10776–10780 (1982).

[52] E. P. Papadakis, K. A. Fowler, and L. C. Lynnworth, “Ultrasonic attenuation by spectrum analysis of pulses in buffer rods: Method and diffraction corrections”, The Journal of the Acoustical Society of America **53**(5), pp. 1336–1343 (1973).

[53] J. Wu, “Determination of velocity and attenuation of shear waves using ultrasonic spectroscopy”, The Journal of the Acoustical Society of America **99**(5), pp. 2871–2875 (1996).

[54] D. H. Green and H. F. Wang, “Shear wave diffraction loss for circular plane-polarized source and receiver”, The Journal of the Acoustical Society of America **90**(5), pp. 2697–2704 (1991).

[55] J. Dvorkin and A. Nur, “Dynamic poroelasticity: A unified model with the squirt and the biot mechanisms”, Geophysics **58**(4), pp. 524–533 (1993).

[56] P. C. Waterman and R. Truell, “Multiple scattering of waves”, Journal of Mathematical Physics **2**(4), pp. 512–537 (1961).

[57] S. Chand, T. A. Minshull, D. Gei, C., and M. José, “Elastic velocity models for gas-hydrate-bearing sediments-A comparison”, Geophysical Journal International **159**(2), pp. 573–590 (2004).

[58] F. D. Adams and E. G. Coker, *An Investigation Into the Elastic Constants of Rocks: More Especially with Reference to Cubic Compressibility*, Carnegie Institution of Washington, (1906).

[59] W. Zisman, “Young’s modulus and Poisson’s ratio with reference to geophysical applications”, Proceedings of the National Academy of Sciences **19**(7), pp. 653–665 (1933).

[60] J. M. Ide, “Comparison of statically and dynamically determined Young’s modulus of rocks”, Proceedings of the National Academy of Sciences **22**(2), pp. 81–92 (1936).

[61] F. Birch and D. Bancroft, “The effect of pressure on the rigidity of rocks. I”, The Journal of Geology **46**(1), pp. 59–87 (1938).

[62] A. Kimball and D. Lovell, “Internal friction in solids”, Physical Review **30**(6), pp. 948 (1927).

[63] R. Wegel and H. Walther, “Internal dissipation in solids for small cyclic strains”, Physics **6**(4), pp. 141–157 (1935).

[64] W. Born, “The attenuation constant of earth materials”, Geophysics **6**(2), pp. 132–148 (1941).

[65] H. J. McSkimin, “Ultrasonic methods for measuring the mechanical properties of liquids and solids”, Physical Acoustics **1**(part A), pp. 271–334 (1964).

[66] D. S. Hughes and H. J. Jones, “Variation of elastic moduli of igneous rocks with pressure and temperature”, Geological Society of America Bulletin **61**(8), pp. 843–856 (1950).

[67] D. S. Hughes and J. H. Cross, "Elastic wave velocities in rocks at high pressures and temperatures", Geophysics **16**(4), pp. 577–593 (1951).

[68] D. S. Hughes and C. Maurette, "Variation of elastic wave velocities in basic igneous rocks with pressure and temperature", Geophysics **22**(1), pp. 23–31 (1957).

[69] M. R. J. Wyllie, A. R. Gregory, and L. W. Gardner, "Elastic wave velocities in heterogeneous and porous media", Geophysics **21**(1), pp. 41–70 (1956).

[70] F. Birch, "The velocity of compressional waves in rocks to 10 kilobars", Journal of Geophysical Research **65**(4), pp. 1083–1102 (1960).

[71] W. Sachse and Y. Pao, "On the determination of phase and group velocities of dispersive waves in solids", Journal of Applied Physics **49**(8), pp. 4320–4327 (1978).

[72] P. He and J. Zheng, "Acoustic dispersion and attenuation measurement using both transmitted and reflected pulses", Ultrasonics **39**(1), pp. 27–32 (2001).

[73] R. A. Kline, "Measurement of attenuation and dispersion using an ultrasonic spectroscopy technique", The Journal of the Acoustical Society of America **76**(2), pp. 498–504 (1984).

[74] M. R. Ayling, P. G. Meredith, and S. A. F. Murrell, "Microcracking during triaxial deformation of porous rocks monitored by changes in rock physical properties, I. Elastic-wave propagation measurements on dry rocks", Tectonophysics **245**(3), pp. 205–221 (1995).

[75] G. Simmons, "Velocity of shear waves in rocks to 10 kilobars, 1", Journal of Geophysical Research **69**(6), pp. 1123–1130 (1964).

[76] A. Williams Jr, "The piston source at high frequencies", The Journal of the Acoustical Society of America **23**(1), pp. 1–6 (1951).

[77] A. Khimunin, "Numerical calculation of the diffraction corrections for the precise measurement of ultrasound absorption", Acta Acustica united with Acustica **27**(4), pp. 173–181 (1972).

[78] A. Khimunin, "Numerical calculation of the diffraction corrections for the precise measurement of ultrasound phase velocity", Acta Acustica united with Acustica **32**(3), pp. 192–200 (1975).

[79] P. H. Rogers and A. L. Van Buren, “An exact expression for the Lommel-diffraction correction integral”, The Journal of the Acoustical Society of America **55**(4), pp. 724–728 (1974).

[80] R. Bass, “Diffraction effects in the ultrasonic field of a piston source”, The Journal of the Acoustical Society of America **30**(7), pp. 602–605 (1958).

[81] R. Chivers, L. Bosselaar, and P. Filmore, “Effective area to be used in diffraction corrections”, The Journal of the Acoustical Society of America **68**(1), pp. 80–84 (1980).

[82] T. Lerch, L. Schmerr, and A. Sedov, “Characterization of spherically focused transducers using an ultrasonic measurement model approach”, Journal of Research in Nondestructive Evaluation **8**(1), pp. 1–21 (1996).

[83] E. Klein and T. Reuschlé, “A model for the mechanical behaviour of Bentheim sandstone in the brittle regime”, Pure and Applied Geophysics **160**(5-6), pp. 833–849 (2003).

[84] L. E. Kinsler, A. R. Frey, A. B. Coppens, and J. V. Sanders, *Fundamentals of Acoustics, 4th Edition*, Wiley, New Tork, (1999).

[85] B. I. Pandit and M. S. King, “Elastic wave propagation in propane gas hydrates”, in *Proceedings of the 4th Canadian Permafrost Conference*, pp. 335–342, International Permafrost Association, Calgery, Alberta, (1982).

[86] W. F. Waite, M. B. Helgerud, A. Nur, J. C. Pinkston, L. A. Stern, S. H. Kirby, and W. B. Durham, “Laboratory measurements of compressional and shear wave speeds through methane hydrate”, Annals of the New York Academy of Sciences **912**(1), pp. 1003–1010 (2000).

[87] D. H. Johnston and M. N. Toksöz, “Ultrasonic P and S wave attenuation in dry and saturated rocks under pressure”, Journal of Geophysical Research: Solid Earth **85**(B2), pp. 925–936 (1980).

[88] A. Nur and G. Simmons, “The effect of saturation on velocity in low porosity rocks”, Earth and Planetary Science Letters **7**(2), pp. 183–193 (1969).

[89] J. Wang, S. Wu, J. Geng, and P. Jaiswal, “Acoustic wave attenuation in the gas hydrate-bearing sediments of Well GC955H, Gulf of Mexico”, Marine Geophysical Research **1**, pp. 1–14 (2017).

[90] A. Timur, “Velocity of compressional waves in porous media at permafrost temperatures”, Geophysics **33**(4), pp. 584–595 (1968).

[91] R. W. Zimmerman and M. S. King, “The effect of the extent of freezing on seismic velocities in unconsolidated permafrost”, Geophysics **51**(6), pp. 1285–1290 (1986).

[92] T. Minshull, S. Singh, and G. Westbrook, “Seismic velocity structure at a gas hydrate reflector, offshore western Colombia, from full waveform inversion”, Journal of Geophysical Research: Solid Earth **99**(B3), pp. 4715–4734 (1994).

[93] P. Leclaire, F. Cohen-Ténoudji, and J. Aguirre-Puente, “Extension of Biot’s theory of wave propagation to frozen porous media”, The Journal of the Acoustical Society of America **96**(6), pp. 3753–3768 (1994).

[94] Kuster and Toksöz, “Velocity and attenuation of seismic waves in two phase media: part 1: Theoretical formulation”, Geophysics **39**, pp. 587–606 (1974).

[95] Z. Hashin and S. Shtrikman, “A variational approach to the theory of the elastic behaviour of multiphase materials”, Journal of the Mechanics and Physics of Solids **11**(2), pp. 127–140 (1963).

[96] W. Voigt, *Lehrbuch der Kristallphysik*, B. G. Terbner, Leipzig, (1928).

[97] A. Ruess, “Berechnung der Fleissgrenze von Mischkristallen auf Grund der Plastizitats bedingung fur Einkrisalle”, Zeitschrift für Angewandte Mathematics aus Mechanik **9**, pp. 49–58 (1929).

[98] M. Wyllie, G. Gardner, and A. Gregory, “Studies of elastic wave attenuation in porous media”, Geophysics **27**(5), pp. 569–589 (1962).

[99] A. B. Wood, *A Textbook of Sound*, G. Bell and Sons, Ltd, London, (1941).

[100] R. Hill, “The elastic behaviour of a crystalline aggregate”, Proceedings of the Physical Society. Section A **65**(5), pp. 349 (1952).

[101] A. Norris, “A differential scheme for the effective moduli of composites”, Mechanics of materials **4**(1), pp. 1–16 (1985).

[102] R. W. Zimmerman, “Elastic moduli of a solid containing spherical inclusions”, Mechanics of Materials **12**(1), pp. 17–24 (1991).

[103] Z. Liu and S. Z. Sun, “The differential Kuster–Toksöz rock physics model for predicting S-wave velocity”, Journal of Geophysics and Engineering **12**(5), pp. 839 (2015).

[104] P. Digby, "The effective elastic moduli of porous granular rocks", Journal of Applied Mechanics **48**(4), pp. 803–808 (1981).

[105] X. Tang, "A unified theory for elastic wave propagation through porous media containing cracks—An extension of Biot's poroelastic wave theory", Science China Earth Sciences **54**(9), pp. 1441–1452 (2011).

[106] I. Palmer and M. Traviolia, "Attenuation by squirt flow in undersaturated gas sands", Geophysics **45**(12), pp. 1780–1792 (1980).

[107] M. W. Lee, *Proposed moduli of dry rock and their application to predicting elastic velocities of sandstones*, US Department of the Interior, US Geological Survey, (2005).

[108] M. A. Biot and D. G. Willis, "The elastic coefficients of the theory of consolidation", Journal of Applied Mechanics **24**, pp. 594–601 (1957).

[109] W. Murphy, A. Reischer, and K. Hsu, "Modulus decomposition of compressional and shear velocities in sand bodies", Geophysics **58**(2), pp. 227–239 (1993).

[110] K. W. Winkler, "Contact stiffness in granular porous materials: Comparison between theory and experiment", Geophysical Research Letters **10**(11), pp. 1073–1076 (1983).

[111] R. J. O'Connell and B. Budiansky, "Seismic velocities in dry and saturated cracked solids", Journal of Geophysical Research **79**(35), pp. 5412–5426 (1974).

[112] B. Budiansky and R. J. O'Connell, "Elastic moduli of a cracked solid", International Journal of Solids and Structures **12**(2), pp. 81–97 (1976).

[113] R. J. O'Connell and B. Budiansky, "Viscoelastic properties of fluid-saturated cracked solids", Journal of Geophysical Research **82**(36), pp. 5719–5735 (1977).

[114] S. Xu and R. E. White, "A new velocity model for clay-sand mixtures", Geophysical prospecting **43**(1), pp. 91–118 (1995).

[115] R. D. Stoll and E. O. Bautista, "Using the Biot theory to establish a baseline geoacoustic model for seafloor sediments", Continental Shelf Research **18**(14), pp. 1839–1857 (1998).

[116] T. J. Plona, "Observation of a second bulk compressional wave in a porous medium at ultrasonic frequencies", Applied Physics Letters **36**(4), pp. 259–261 (1980).

[117] U. Shankar and M. Riedel, “Gas hydrate saturation in the Krishna–Godavari basin from P-wave velocity and electrical resistivity logs”, Marine and Petroleum Geology **28**(10), pp. 1768–1778 (2011).

[118] M. I. Ehsan, N. Ahmed, P. Khalid, L. X. Wei, and M. Naeem, “An application of rock physics modeling to quantify the seismic response of gas hydrate-bearing sediments in Makran accretionary prism, offshore, Pakistan”, Geosciences Journal **20**(3), pp. 321–330 (2016).

[119] J. Dvorkin, M. Prasad, A. Sakai, and D. Lavoie, “Elasticity of marine sediments: Rock physics modeling”, Geophysical Research Letters **26**(12), pp. 1781–1784 (1999).

[120] R. Mindlin, “Compliance of elastic bodies in contact”, J. Appl. Mech. Trans. ASME **16**, pp. 259–268 (1949).

[121] A. Nur, G. Mavko, J. Dvorkin, and D. Galmudi, “Critical porosity: A key to relating physical properties to porosity in rocks”, The Leading Edge **17**(3), pp. 357–362 (1998).

[122] P. Avseth, N. Skjei, and G. Mavko, “Rock-physics modeling of stress sensitivity and 4D time shifts in patchy cemented sandstones—Application to the Visund Field, North Sea”, The Leading Edge **35**(10), pp. 868–878 (2016).

[123] J. Sarout, “Impact of pore space topology on permeability, cut-off frequencies and validity of wave propagation theories”, Geophysical Journal International **189**(1), pp. 481–492 (2012).

[124] K. W. Winkler, “Dispersion analysis of velocity and attenuation in Berea sandstone”, Journal of Geophysical Research: Solid Earth **90**(B8), pp. 6793–6800 (1985).

[125] K. W. Winkler, “Estimates of velocity dispersion between seismic and ultrasonic frequencies”, Geophysics **51**(1), pp. 183–189 (1986).

[126] A.-M. Wulff, S. Raab, and E. Huenges, “Alteration of seismic wave properties and fluid permeability in sandstones due to microfracturing”, Physics and Chemistry of the Earth, Part A: Solid Earth and Geodesy **25**(2), pp. 141–147 (2000).

[127] A. Best, C. McCann, and J. Sothcott, “The relationships between the velocities, attenuations and petrophysical properties of reservoir sedimentary rocks”, Geophysical Prospecting **42**(2), pp. 151–178 (1994).

[128] W. F. Murphy III, K. W. Winkler, and R. L. Kleinberg, “Acoustic relaxation in sedimentary rocks: Dependence on grain contacts and fluid saturation”, Geophysics **51**(3), pp. 757–766 (1986).

[129] J. White, “Computed seismic speeds and attenuation in rocks with partial gas saturation”, Geophysics **40**(2), pp. 224–232 (1975).

[130] D. L. Johnson, “Theory of frequency dependent acoustics in patchy-saturated porous media”, The Journal of the Acoustical Society of America **110**(2), pp. 682–694 (2001).

[131] J. A. Hudson, “Wave speeds and attenuation of elastic waves in material containing cracks”, Geophysical Journal International **64**(1), pp. 133–150 (1981).

[132] K. W. Winkler, “Frequency dependent ultrasonic properties of high-porosity sandstones”, Journal of Geophysical Research: Solid Earth **88**(B11), pp. 9493–9499 (1983).

[133] W. W. Wepfer and N. I. Christensen, “Compressional wave attenuation in oceanic basalts”, Journal of Geophysical Research: Solid Earth **95**(B11), pp. 17431–17439 (1990).

[134] R. Galvin and B. Gurevich, “Scattering of a longitudinal wave by a circular crack in a fluid-saturated porous medium”, International Journal of Solids and Structures **44**(22), pp. 7389–7398 (2007).

[135] C. Sayers and R. Smith, “The propagation of ultrasound in porous media”, Ultrasonics **20**(5), pp. 201–205 (1982).

[136] R. Ciz, B. Gurevich, and M. Markov, “Seismic attenuation due to wave-induced fluid flow in a porous rock with spherical heterogeneities”, Geophysical Journal International **165**(3), pp. 957–968 (2006).

[137] T. M. Müller, B. Gurevich, and M. Lebedev, “Seismic wave attenuation and dispersion resulting from wave-induced flow in porous rocks — A review”, Geophysics **75**(5), pp. 75A147–75A164 (2010).

[138] J.-M. Conoir and A. N. Norris, “Effective wavenumbers and reflection coefficients for an elastic medium containing random configurations of cylindrical scatterers”, Wave motion **47**(3), pp. 183–197 (2010).

[139] C. Ying and R. Truell, “Scattering of a plane longitudinal wave by a spherical obstacle in an isotropically elastic solid”, Journal of Applied Physics **27**(9), pp. 1086–1097 (1956).

[140] Y.-H. Pao and C. Mow, “Scattering of plane compressional waves by a spherical obstacle”, Journal of Applied Physics **34**(3), pp. 493–499 (1963).

[141] K. Winkler, A. Nur, and M. Gladwin, “Friction and seismic attenuation in rocks”, Nature **277**(5697), pp. 528–531 (1979).

[142] Y.-H. Wang and J. Santamarina, “Attenuation in sand: an exploratory study on the small-strain behavior and the influence of moisture condensation”, Granular Matter **9**(6), pp. 365–376 (2007).

[143] M. W. Knuth, H. J. Tobin, and C. Marone, “Evolution of ultrasonic velocity and dynamic elastic moduli with shear strain in granular layers”, Granular Matter **15**(5), pp. 499–515 (2013).

[144] K. W. Winkler and A. Nur, “Seismic attenuation: Effects of pore fluids and frictional-sliding”, Geophysics **47**(1), pp. 1–15 (1982).

[145] G. M. Mavko, “Frictional attenuation: An inherent amplitude dependence”, Journal of Geophysical Research: Solid Earth **84**(B9), pp. 4769–4775 (1979).

[146] M. W. Lee, “Velocities and attenuations of gas hydrate-bearing sediments”, Geological Survey and Dept. of the Interior, Scientific Investigations Report 2007–5264, Reston, Virginia (2007).

[147] D. Gei and J. M. Carcione, “Acoustic properties of sediments saturated with gas hydrate, free gas and water”, Geophysical Prospecting **51**(2), pp. 141–158 (2003).

[148] N. H. Pham, J. M. Carcione, H. B. Helle, and B. Ursin, “Wave velocities and attenuation of shaley sandstones as a function of pore pressure and partial saturation”, Geophysical Prospecting **50**(6), pp. 615–627 (2002).

[149] J.-X. Nie, J. Ba, D.-H. Yang, X.-F. Yan, Z.-Y. Yuan, and H.-P. Qiao, “BISQ model based on a Kelvin-Voigt viscoelastic frame in a partially saturated porous medium”, Applied Geophysics **9**(2), pp. 213–222 (2012).

[150] R. D. Stoll, “Acoustic waves in ocean sediments”, Geophysics **42**(4), pp. 715–725 (1977).

[151] E. D. Sloan, “Fundamental principles and applications of natural gas hydrates”, Nature **426**(6964), pp. 353–363 (2003).

[152] S. Almenningen, “An experimental study of methane hydrates in sandstone cores”, Master thesis, University of Bergen, Dept. of Physics and Technology, Bergen, Norway (2015).

[153] S. Circone, S. H. Kirby, and L. A. Stern, “Direct measurement of methane hydrate composition along the hydrate equilibrium boundary”, The Journal of Physical Chemistry B **109**(19), pp. 9468–9475 (2005).

[154] J. Husebø, “Monitoring depressurization and CO2-CH4 exchange production scenarios for natural gas hydrates”, University of Bergen, Dept. of Physics and Technology, Bergen, Norway (2008).

[155] E. O. Brigham and E. O. Brigham, *The Fast Fourier Transform and its applications*, Prentice Hall Englewood Cliffs, (1988).

[156] Mathworks Inc., “MATLAB, R2016b”, Natick, Massachusetts, USA.

[157] M. Treiber, J.-Y. Kim, L. J. Jacobs, and J. Qu, “Correction for partial reflection in ultrasonic attenuation measurements using contact transducers”, The Journal of the Acoustical Society of America **125**(5), pp. 2946–2953 (2009).

[158] COMSOL Inc., “Comsol Multiphysics, Version 4.2, Acoustic Module User’s Guide”, Stockholm, Sweden.

[159] COMSOL Inc., “Comsol Multiphysics, Version 4.2, Structural Mechanics User’s Guide”, Stockholm, Sweden.

[160] P. Lunde, “Phys374 - Theoretical Acoustics”, University of Bergen, Dept. of Physics and Technology, Bergen, Norway (2008).

[161] M. A. Biot, “Theory of propagation of elastic waves in a fluid-saturated porous solid. II. Higher frequency range”, The Journal of the Acoustical Society of America **28**(2), pp. 179–191 (1956).

[162] E. Klein, P. Baud, T. Reuschlé, and T. Wong, “Mechanical behaviour and failure mode of Bentheim sandstone under triaxial compression”, Physics and Chemistry of the Earth, Part A: Solid Earth and Geodesy **26**(1-2), pp. 21–25 (2001).

[163] Peace Software, `http://www.peacesoftware.de/einigewerte/methan_e.html`, [Online; accessed 02-June-2018].

[164] J. A. Priest, E. V. Rees, and C. R. Clayton, “Influence of gas hydrate morphology on the seismic velocities of sands”, Journal of Geophysical Research: Solid earth **114**(pp. B11) (2009).

[165] S. I. Mayr and H. Burkhardt, “Ultrasonic properties of sedimentary rocks: Effect of pressure, saturation, frequency and microcracks”, Geophysical Journal International **164**(1), pp. 246–258 (2006).

[166] Y. Masuda, “Numerical calculation of gas-production performance from reservoirs containing natural gas hydrates”, in *Proceedingsof Western Regional Meeting*, Society of Petroleum Engineers Inc., Long Beach, California, (1997).

[167] R. Kleinberg, C. Flaum, D. Griffin, P. Brewer, G. Malby, E. Peltzer, and J. Yesinowski, “Deep sea NMR: Methane hydrate growth habit in porous media and its relationship to hydraulic permeability, deposit accumulation, and submarine slope stability”, Journal of Geophysical Research: Solid Earth **108**(B10) (2003).

[168] E. Spangenberg, “Modeling of the influence of gas hydrate content on the electrical properties of porous sediments”, Journal of Geophysical Research: Solid Earth **106**(B4), pp. 6535–6548 (2001).

[169] D. L. Johnson and T. J. Plona, “Acoustic slow waves and the consolidation transition”, The Journal of the Acoustical Society of America **72**(2), pp. 556–565 (1982).

[170] M. Jakobsen and M. Chapman, “Unified theory of global flow and squirt flow in cracked porous media”, Geophysics **74**(2), pp. WA65–WA76 (2009).

[171] C. Yuan-Feng, Y. Ding-Hui, and Y. Hui-Zhu, “Biot/squirt model in viscoelastic porous media”, Chinese Physics Letters **19**(3), pp. 445 (2002).

[172] ENI, “Product Data: Type ENI 240L RF power amplifier”, `http://www.testequipmenthq.com/datasheets/ENI-2100L-Datasheet.pdf`, [Online; accessed 02-June-2018].

[173] Agilent, “Product Data: Type 33220A signal generator”, `https://www.keysight.com/upload/cmc_upload/All/6C0633120A_USERSGUIDE_ENGLISH.pdf`, [Online; accessed 02-June-2018].

[174] A. J. Niklasson, “Ultrasonic 2-D SH probe modeling in anisotropic solids”, The Journal of the Acoustical Society of America **100**(4), pp. 2132–2138 (1996).

[175] A. Boström and H. Wirdelius, “Ultrasonic probe modeling and nondestructive crack detection”, The Journal of the Acoustical Society of America **97**(5), pp. 2836–2848 (1995).

[176] A. Eriksson, J. Mattsson, and A. Niklasson, “Modelling of ultrasonic crack detection in anisotropic materials”, NDT & E International **33**(7), pp. 441–451 (2000).

[177] L. Schmerr and J.-S. Song, *Ultrasonic nondestructive evaluation systems*, Springer, (2007).

[178] E. P. Papadakis, “Diffraction of ultrasound radiating into an elastically anisotropic medium”, The Journal of the Acoustical Society of America **36**(3), pp. 414–422 (1964).

[179] R. Morrison, *Grounding and shielding techniques in instrumentation*, J. Wiley and Sons, (1967).

[180] Olympus, “Product Data: Type Olympus Panametrics-NDT- V302 1.0 MHz”, `https://www.olympus-ims.com/en/ultrasonic-transducers/immersion/`, [Online; accessed 02-June-2018].

[181] C. Dang, L. Schmerr Jr, and A. Sedov, “Modeling and measuring all the elements of an ultrasonic nondestructive evaluation system I: modeling foundations”, Journal of Research in Nondestructive Evaluation **14**(3), pp. 141–176 (2002).

[182] K. K. Andersen, “Reciprocity calibration of ultrasonic piezoelectric disks in air”, Master thesis, University of Bergen, Dept. of Physics and Technology, Bergen, Norway (2015).

[183] R. Hauge, “Finite element modeling of ultrasound measurement systems for gas. comparison with experiments in air”, Master thesis, University of Bergen, Dept. of Physics and Technology, Bergen, Norway (2013).

[184] P. Droin, G. Berger, and P. Laugier, “Velocity dispersion of acoustic waves in cancellous bone”, IEEE Transactions on Ultrasonics, Ferroelectrics, and Frequency Control **45**(3), pp. 581–592 (1998).

[185] H. Fosså, “Ultrasound phantom for myocardium”, Master thesis, University of Bergen, Dept. of Physics and Technology, Bergen, Norway (2011).

[186] Y. Kuwahara, H. Ito, and T. Kiguchi, “Comparison between natural fractures and fracture parameters derived from vsp”, Geophysical journal international **107**(3), pp. 475–483 (1991).

[187] H. Packard, "Product Data: Type Operation and Service Manual, Model 4192A LF Impedance Analyzer", .

[188] M. Aanes, "Undersøkelser av piezokeramiske skiver . Målinger og endelig element analyser", Master thesis, University of Bergen, Dept. of Physics and Technology, Bergen, Norway (2009), (In Norwegian).

[189] A. R. Selfridge, "Approximate material properties in isotropic materials", IEEE Transactions on Sonics and Ultrasonics **32**(3), pp. 381–394 (1985).

[190] C. Sayers and C. Tait, "Ultrasonic properties of transducer backings", Ultrasonics **22**(2), pp. 57–60 (1984).

[191] M. G. Grewe, T. Gururaja, T. R. Shrout, and R. E. Newnham, "Acoustic properties of particle/polymer composites for ultrasonic transducer backing applications", IEEE Transactions on Ultrasonics, Ferroelectrics, and Frequency Control **37**(6), pp. 506–514 (1990).

[192] Meggitt, "Product Data: Type Pz37", `https://www.meggittferroperm.com/`, [Online; accessed 02-June-2018].

[193] M. Aanes, "Interaction of piezoelectric transducer excited ultrasonic pulsed beam with fluid-embedded viscoelastic plate. Finite element modeling, angular spectrum modeling and measurements", PhD thesis, Department of Physics and Technology, University of Bergen, Bergen, Norway (2014).

[194] ANSI/IEEE standard 176-1987, *IEEE Standard on Piezoelectricity*, Institute of Electrical and Electronics Engineers Inc., New York, (1987).

[195] Mitutoyo Europe, "Product Data: Type Mitutoyo High accuracy digimatic micrometer", `https://www.mitutoyo.com`, [Online; accessed 02-June-2018].

[196] Ted Pella Inc., "Product Data: Type Pelco Conductive Liquid Silver Paint", `https://www.tedpella.com`, [Online; accessed 02-June-2018].

[197] Struers, "Product Data: Type Epofix kit", `https://e-shop.struers.com`, [Online; accessed 02-June-2018].

[198] 3M, "Product Data: Type 3M Scotch-Weld 2216", `https://www.3m.com/`, [Online; accessed 02-June-2018].

[199] Scorpion Oceanic, "Product Data: Type Solres-01", `http://www.scorpionoceanics.co.uk/polyurethane-resin`, [Online; accessed 02-June-2018].

[200] M. Vestrheim, “Phys373 - Acoustic Measurement Systems”, University of Bergen, Dept. of Physics, Bergen, Norway (2007).

[201] J. Kocbach, “Finite element modeling of ultrasonic piezoelectric transducers”, Ph.D. thesis, University of Bergen, Norway (2000).

[202] A and D LTD, “Product Data: Type A and D Ltd GF-3000”, `https://www.aandd.jp/products/manual/balances/gf.pdf`, [Online; accessed 02-June-2018].

[203] L. Hauge, J. Gauteplass, M. Høyland, G. Ersland, A. Kovscek, and M. Fernø, “Pore-level hydrate formation mechanisms using realistic rock structures in high-pressure silicon micromodels”, International Journal of Greenhouse Gas Control **53**, pp. 178–186 (2016).

[204] S. Almenningen, E. Iden, M. A. Fernø, and G. Ersland, “Salinity effects on pore-scale methane gas hydrate dissociation”, Journal of Geophysical Research: Solid Earth (2018).

[205] W. F. Waite, J. C. Santamarina, D. D. Cortes, B. Dugan, D. Espinoza, J. Germaine, J. Jang, J. Jung, T. J. Kneafsey, H. Shin, *et al.*, “Physical properties of hydrate-bearing sediments”, Reviews of Geophysics **47**(4), pp. RG4003 (2009).

[206] T. Chen, D. C. Lawton, and F. Peterson, “Physical parameter estimation for sandstone reservoirs”, Consortium for Research in Elastic Wave Exploration Seismology Research Report **1991**, pp. 291–305 (1991).

[207] C. Ecker, J. Dvorkin, and A. Nur, “Sediments with gas hydrates: Internal structure from seismic AVO”, Geophysics **63**(5), pp. 1659–1669 (1998).

[208] S. Almenningen and G. Ersland, “Water permeability measurements on hydrate-saturated sandstone cores with immobile gas”, in *31th International Symposium of the Society of Core Analysts*, The Society of Core Analysts, Vienna, Austria, (2017).

[209] B. Tohidi, R. Anderson, M. B. Clennell, R. W. Burgass, and A. B. Biderkab, “Visual observation of gas-hydrate formation and dissociation in synthetic porous media by means of glass micromodels”, Geology **29**(9), pp. 867–870 (2001).

[210] L. A. Stern, S. H. Kirby, W. B. Durham, S. Circone, and W. F. Waite, “Laboratory synthesis of pure methane hydrate suitable for measurement of physical properties and decomposition behavior”, in *Natural Gas Hydrate*, pp. 323–348, Springer, (2000).

[211] W. Waite, B. DeMartin, S. Kirby, J. Pinkston, and C. Ruppel, "Thermal conductivity measurements in porous mixtures of methane hydrate and quartz sand", Geophysical Research Letters **29**(24) (2002).

[212] T. S. Yun, F. Francisca, J. C. Santamarina, and C. Ruppel, "Compressional and shear wave velocities in uncemented sediment containing gas hydrate", Geophysical Research Letters **32**(10), pp. L10609 (2005).

[213] G. Guerin, D. Goldberg, and A. Meltser, "Characterization of in situ elastic properties of gas hydrate-bearing sediments on the Blake Ridge", Journal of Geophysical Research: Solid Earth **104**(B8), pp. 17781–17795 (1999).

[214] M. S. Diallo and E. Appel, "Acoustic wave propagation in saturated porous media: reformulation of the Biot/Squirt flow theory", Journal of Applied Geophysics **44**(4), pp. 313–325 (2000).

[215] T. D. Jones, "Pore fluids and frequency-dependent wave propagation in rocks", Geophysics **51**(10), pp. 1939–1953 (1986).

[216] S. R. Pride, J. G. Berryman, and J. M. Harris, "Seismic attenuation due to wave-induced flow", Journal of Geophysical Research: Solid Earth **109**(B1), pp. B01201 (2004).

[217] J. Ba, J. Carcione, and J. Nie, "Biot-Rayleigh theory of wave propagation in double-porosity media", Journal of Geophysical Research: Solid Earth **116**(B6), pp. B06202 (2011).

[218] M. Sams, J. Neep, M. Worthington, and M. King, "The measurement of velocity dispersion and frequency-dependent intrinsic attenuation in sedimentary rocks", Geophysics **62**(5), pp. 1456–1464 (1997).

[219] G. A. Gist, "Fluid effects on velocity and attenuation in sandstones", The Journal of the Acoustical Society of America **96**(2), pp. 1158–1173 (1994).

[220] J. Dvorkin and R. Uden, "Seismic wave attenuation in a methane hydrate reservoir", The Leading Edge **23**(8), pp. 730–732 (2004).

[221] B. Gurevich, M. Brajanovski, R. J. Galvin, T. M. Müller, and J. Toms-Stewart, "P-wave dispersion and attenuation in fractured and porous reservoirs–poroelasticity approach", Geophysical Prospecting **57**(2), pp. 225–237 (2009).

[222] L. P. Suwal and R. Kuwano, “Disk shaped piezo-ceramic transducer for P and S wave measurement in a laboratory soil specimen”, Soils and Foundations **53**(4), pp. 510–524 (2013).

[223] R. O. Deniz, “Bender elements and bending disks for measurement of shear and compressional wave velocities in large sand specimens”, Ph.D. thesis, Northeastern University, Boston, Massachusetts (2008).

Appendix A

Matlab logging scripts

In this appendix the logging scripts used during the hydrate experiments are presented. LoggingScript.m is the main program.

LoggingScript.m

```
vinfo = instrhwinfo('visa','agilent');
vinfo.ObjectConstructorName

%%%% SCOPPE and Sig gen initialize %%%%
samples = 100e3;
ch=1; % Lese fra kanal 1 på skop
measWaitPause = 5;
SkopString = 'USB0::0x0699::0x0410::C024017::0::INSTR'
ud_skop = visa('agilent',SkopString,...
'InputBufferSize',samples,'OutputBufferSize',samples);
fopen(ud_skop);
fprintf(ud_skop, 'DATA:ENCDG RIBINARY;WIDTH 1');  % reset command
fclose(ud_skop);

ud_signal = visa('agilent', 'GPIB0::6::INSTR');

%%%%%%%%%%%%%%%%%% 3: Measurement Series %%%%%%%%%%%%%%%%%%%%

fopen(ud_signal);fopen(ud_skop);
```

```
burst_rate = 50; % Tid(i Hz) mellom hver burst
voltinn_var = [100e-3 100e-3];
ScalingDistinct = [50e-3 50e-3];

SigGenMinMaxSafety = [1e-3 100e-3];
ScopeSafety = [1e-3 10];

ScalingTreshTooLowAmplitude = [2e-3 2e-3];

nonLinPercentTresh = 8;
nonLinearNumberOfCyclesTest = 2;

Gen_or_Scope_or_ScopeNonlinear_Scaling = 1;

measWaitPause = 0.1;
measWaitPauseFinal = 15;
average = 256;
cycles = [1];

freq = [500e3];
MeasuringDays = 40;
minutes_between_meas = 15;

periods_in_excess = 3;
AdjustAmplitude{1} = [1 0 2 500e3];
AdjustAmplitude{2} = [0 55e-6 8];
AdjustAmplitude{3} = [0 50e-6 105e-6];

%%%%%%%%%%%%%%%%%%%%%%%%%%%%%%%%%%%%%%%%%%%%%%%%%%%%%%%%%%%%%%%%

fprintf(ud_signal,'BM:STATe ON')
fprintf(ud_signal,['BM:INT:RATE ' num2str(burst_rate)]);
fprintf(ud_skop,['ACQ:NUMAV ' num2str(average)]);
fprintf(ud_skop,['HOR:RECO ' num2str(samples)]);
fprintf(ud_skop,'TRIGGER:A:EDGE:SOURCE AUX');
fprintf(ud_skop,'TRIGGER:A:EDGE:SLOPE rise');
```

```
fprintf(ud_skop,':TRIGGER:A:LEVel 1.1000E+00');
fprintf(ud_skop,'TRIGGER:A:EDGE:COUPLING AC');


voltinn_init_save = voltinn_var; % Spenning på innsignal fra generatoren


go = 1;
MeasNr = 0;
PickWinMethod = AdjustAmplitude{2};

while go && toc< MeasuringDays*24*60*60
  if minutes_between_meas*MeasNr < toc/60;
    MeasurementTime = clock;

    for ii = 1:length(cycles)
      if PickWinMethod(1) == 1;
PickWinMethod(3)= cycles(ii)+periods_in_excess;
      elseif PickWinMethod(1) == 3;
PickWinMethod(3)= cycles(ii)+periods_in_excess;
    end

    AdjustAmplitude{2} = PickWinMethod;

    for jj = 1:length(freq)
      disp(['Freq' int2str(jj)])
      fprintf(ud_signal,['BM:NCYC ', num2str(cycles(ii))]);
      fprintf(ud_signal,['FREQ ', num2str(freq(jj))]);
      voltinn = voltinn_var(jj);
      fprintf(ud_signal,['VOLT ' num2str(voltinn)]);
      Scaling = ScalingDistinct(jj);
      fprintf(ud_skop,['CH',num2str(ch),':SCA ',num2str(Scaling)]);

      if Gen_or_Scope_or_ScopeNonlinear_Scaling == 1
Volt_Scale = ScaleLimitSigGenRev02(ud_skop,ud_signal,ch,...
measWaitPauseFinal,SigGenMinMaxSafety,ScalingDistinct(jj),...
```

```
voltinn,AdjustAmplitude{1},ScopeSafety);
        voltinn = Volt_Scale(1);Scaling = Volt_Scale(2);
      end
      [x,wf,tidsskala] = DPOLes_egenRev02(ud_skop,ch,measWaitPauseFinal);

      Meas{ii}{jj}{1} = x;    % {cycles}{freq}{variable}
      Meas{ii}{jj}{2} = wf;
      Meas{ii}{jj}{3} = voltinn;
      Meas{ii}{jj}{4} = clock;
      disp('One meas taken')
      voltinn_var(jj) = voltinn;
      ScalingDistinct(jj) = Scaling;
      if voltinn  == SigGenMinMaxSafety(1); disp('on low volt limit');
      end
    end
end

name = ['measurements/Meas_' num2str(MeasNr) '.mat'];
save(name,'Meas','MeasurementTime','cycles','freq')
MeasNr = MeasNr+1;
disp('Finished')
```

DPOLes_egenRev02.m

```
function [x,wf,tidsskala] = DPOLes_egenRev02(ud_skop,ch,measWaitPause)
fprintf(ud_skop,['DAT:SOU CH' num2str(ch)]);   % chose ch 1

fprintf(ud_skop, 'DATA:ENCDG RIBINARY;WIDTH 1');
pause(.1); % Wait to ensure that the scope wipes its memory.
fprintf(ud_skop,'ACQ:STATE STOP');% stop old midling
pause(.1); % Wait to ensure that the scope wipes its memory.
fprintf(ud_skop,'ACQ:STATE RUN');% Start new midling aquisition.
pause(measWaitPause);
fprintf(ud_skop,'CURV?');

pause(.1)
```

```
ydata = binblockread(ud_skop,'int8'); % reading data curve

pause(.1)
fscanf(ud_skop);
fprintf(ud_skop,'HOR:SCA?');  %ask for tidsskala/div
tidsskala = str2num(fscanf(ud_skop));  %save tidssakal  /div

fprintf(ud_skop,'WFMO:XZE?'); % time coordinate of the first point
xze = str2num(fscanf(ud_skop));
%save time coordinate of the first point

fprintf(ud_skop,'WFMO:XIN?'); % time between points (fs)
xin = str2num(fscanf(ud_skop)); % save fs

fprintf(ud_skop,'WFMO:YMU?');
% vertical scale factor per digitizing level in units
YMU = str2num(fscanf(ud_skop)); %read volts/div

fprintf(ud_skop,'WFMO:YZE?'); % vertical offset
YZE = str2num(fscanf(ud_skop)); % read ofset

x = xze:xin:(xze+(length(ydata)-1)*xin); % time vector
wf = (ydata*YMU) + YZE; % scaling the waveform (wf)
wf = wf';
```

adjustAmplitude_egenrev02.m

```
function out = adjustAmplitude_egenrev02(ud_skop,ch,measWaitPause...
,SignalForm,...
AdjustAmplitude,ScalingTresh)

%%%% PROGRAM STARTS %%%%%%

offSetmethodAdjustAmplitude = AdjustAmplitude{1};
PickWin =AdjustAmplitude{2};
PickWinSafety = AdjustAmplitude{3};
```

```
Scaling = str2num(query(ud_skop,['CH',num2str(ch),':SCA?']));
verticalScalings = [1e-3 10];

screenRows = 4;
HaveBeenTooBig = false;
go = 1;
goCounter = 1;
while go
  if offSetmethodAdjustAmplitude(1) == 1 || ...
  offSetmethodAdjustAmplitude(1) == 2

    fprintf(ud_skop,[['CH' num2str(ch)] ':POS ' '0']);
    [x,wf,timeDiv] = DPOLes_egenRev02(ud_skop,ch,measWaitPause);
    deleteOffset_tmp = delete_offset(x,wf,offSetmethodAdjustAmplitude);
    offset = deleteOffset_tmp{2}/Scaling;
    fprintf(ud_skop,['CH1:POS ' num2str(-offset)]);
    [x,wf,timeDiv] = DPOLes_egenRev02(ud_skop,ch,measWaitPause);
    deleteOffsetSafety_tmp  = fourier_transform(x,wf,0);
    if abs(deleteOffsetSafety_tmp{2}(1)) > 0.5*Scaling;
      offSetmethodAdjustAmplitude(1) = 3;
    end
  end

  if offSetmethodAdjustAmplitude(1) == 3
    fprintf(ud_skop,[['CH' num2str(ch)] ':POS ' '0']);
    [x,wf,timeDiv] = DPOLes_egenRev02(ud_skop,ch,measWaitPause);
    deleteOffset_tmp  = fourier_transform(x,wf,0);
    offset = deleteOffset_tmp{2}(1)/Scaling;
    fprintf(ud_skop,[['CH' num2str(ch)] ':POS ' num2str(-offset)]);
  end

  if offSetmethodAdjustAmplitude(1) == 4
    fprintf(ud_skop,[['CH' num2str(ch)] ':POS ' '0']);
  end
```

```
  [x,wf,timeDiv] = DPOLes_egenRev02(ud_skop,ch,measWaitPause);
  SignalForm{1}= x;
  SignalForm{2}= wf;
  fs = 1/(x(2)-x(1));
  freq = SignalForm{3};
  samplesInPeriod = round(1/freq * fs);

  %%%%%%%%%%%%%%%%%%%%% picking window samples %%%%%%%%%%%%%%%%%%
    if PickWinSafety(1) == 0 ;
      RelevantSamplesStartSafety = 1;
      RelevantSamplesStopSafety = length(wf);
    end
    if PickWin(1) == 0
      RelevantSamplesStart = 1;
      RelevantSamplesStop = length(wf);
      absV = max(abs(wf));
    elseif PickWin(1) == 1    % input periods
      onset_tmp = findOnsetRelZerolineRev02(SignalForm);
      onset = onset_tmp{1};

      if PickWinSafety(1) == 1     % times safety
RelevantSamplesStartSafety_tmp = find(x>PickWinSafety(2));
        if isempty(RelevantSamplesStartSafety_tmp);
  RelevantSamplesStartSafety = 1;
else RelevantSamplesStartSafety = RelevantSamplesStartSafety_tmp(1);
      end

      RelevantSamplesStopSafety_tmp = find(x>PickWinSafety(3));
      if isempty(RelevantSamplesStopSafety_tmp);
RelevantSamplesStopSafety = length(wf);
      else RelevantSamplesStopSafety = RelevantSamplesStopSafety_tmp(1);
      end

      elseif PickWinSafety(1) == 2    % time and periods after
RelevantSamplesStartSafety_tmp = find(x>PickWinSafety(2));
        if isempty(RelevantSamplesStartSafety_tmp);
```

```
  RelevantSamplesStartSafety = 1;
        else
  RelevantSamplesStartSafety = RelevantSamplesStartSafety_tmp(1);
        end
        RelevantSamplesStopSafety = RelevantSamplesStartSafety...
        + round(PickWinSafety(3) *samplesInPeriod);

        if RelevantSamplesStartSafety == 1 ...
        || RelevantSamplesStopSafety > length(wf);
  RelevantSamplesStopSafety =  length(wf);
end
      end

    RelevantSamplesStart = onset + round( PickWin(2)*samplesInPeriod);
    RelevantSamplesStop = RelevantSamplesStart + ...
    round(PickWin(3) *samplesInPeriod);

    if RelevantSamplesStart > length(wf) || RelevantSamplesStart < 1 ...
    || RelevantSamplesStop > length(wf) || onset< RelevantSamplesStartSafety ...
    || onset > RelevantSamplesStopSafety ;
      absV = max(abs(wf(RelevantSamplesStartSafety:RelevantSamplesStopSafety)));
    else
      absV = max(abs(wf(RelevantSamplesStart:RelevantSamplesStop)));
    end
    elseif PickWin(1) == 2    % input times
      RelevantSamplesStart_tmp = find(x>PickWin(2));

      if isempty(RelevantSamplesStart_tmp);
RelevantSamplesStart = 1;
      else
RelevantSamplesStart = RelevantSamplesStart_tmp(1);
      end
      RelevantSamplesStop_tmp = find(x>PickWin(3));
      if isempty(RelevantSamplesStop_tmp);
RelevantSamplesStop  = length(wf);
      else
```

```
RelevantSamplesStop = RelevantSamplesStop_tmp (1);
      end
      if RelevantSamplesStart > length(wf) ...
      || RelevantSamplesStop > length(wf);
absV = max(abs(wf));
      else
absV = max(abs(wf(RelevantSamplesStart:RelevantSamplesStop)));
      end

    elseif PickWin(1)   == 3    % INPUT START TIME AND PERIODS AFTER
      RelevantSamplesStart_tmp = find(x>PickWin(2));
    elseif isempty(RelevantSamplesStart_tmp) ;
      RelevantSamplesStart = 1;
    else
      RelevantSamplesStart = RelevantSamplesStart_tmp(1);
    end

    RelevantSamplesStop =...
    RelevantSamplesStart + round(PickWin(3) *samplesInPeriod);
    if RelevantSamplesStart == 1 || RelevantSamplesStop > length(wf);
      RelevantSamplesStop =  length(wf);
    end

    absV = max(abs(wf(RelevantSamplesStart:RelevantSamplesStop)));

    end
  if RelevantSamplesStart > length(wf) || RelevantSamplesStart < 1 ...
  || RelevantSamplesStop > length(wf) ...
  || RelevantSamplesStop < RelevantSamplesStart

    RelevantSamplesStart = 1;  RelevantSamplesStop = length(wf);
  end
  %%%%%%%%%%%%%%%%%%%%%%%%%%%%%%%%%%%%%%%%%%%%%%%%%%%%%%%%%%%
  Scaling = str2num(query(ud_skop,['CH',num2str(ch),':SCA?']));
  if absV > screenRows*Scaling
    if Scaling <= verticalScalings(2)/2
```

```
      Scaling = Scaling*2;
      fprintf(ud_skop,['CH',num2str(ch),':SCA ',num2str(Scaling)]);
      HaveBeenTooBig = true;
    end
    if Scaling > verticalScalings(2)/2
      fprintf(ud_skop,['CH',num2str(ch),':SCA ',num2str(verticalScalings(2))]);
      HaveBeenTooBig = true;
    end

    elseif absV < screenRows*Scaling  && ~HaveBeenTooBig
      if (screenRows*Scaling/2 < max(abs(wf)))
go = 0;
elseif Scaling >= verticalScalings(1)*2
        Scaling = Scaling/2;
        fprintf(ud_skop,['CH',num2str(ch),':SCA ',num2str(Scaling)]);
        HaveBeenTooWeak = true;
      elseif Scaling < verticalScalings(1)*2
Scaling = verticalScalings(1);
        fprintf(ud_skop,['CH',num2str(ch),':SCA ',num2str(Scaling)]);
        HaveBeenTooWeak = true;
      end
    else
      go = 0;
    end
    goCounter = goCounter+1;
end

if (absV > screenRows*Scaling ) ; AmplitudeOK = 3;   % clipping
elseif absV < screenRows* ScalingTresh; AmplitudeOK = 2;   % very low amplitude
else AmplitudeOK = 1;
end
out{1} = AmplitudeOK;
out{2} = x;
out{3} = wf;
out{4} = [RelevantSamplesStart RelevantSamplesStop];
out{5} = Scaling;
```

Appendix B

Matlab scripts for the numerical models

In this appendix the matlab-codes for the numerical models are presented. For FirableSand.m, the HFr and HFl-models are implemented (Secs. 2.5.1 and 2.5.2). For Dvorkin_Nur_BISQ_rev the BiSqHFr-model (Sec. 2.5.5) is implemented and for WaterMannWithSayers_rev03_fun.m, the WaTrHFr-model (Sec. 2.5.6) is implemented.

FirableSand.m

```
function out = FriableSand_Egen_fun(S_H,S_w0,...
Reuss_Hill_Patchy,Hydrate_Fluid_or_Frame_orSolid)

mu_q = 39.6e9;
K_q = 38.7e9;
rho_q = 2650;
K_w = 2.25e9;
rho_w = 1000;
K_H = 7.7e9;
mu_H = 3.2e9;
rho_H = 850;
BetaQ = 0.24;
K_dry0 = 11e9;
mu_dry0 = 8e9;
```

```
phi_w0 = S_w0*BetaQ;
K_g = 11e6;
rho_g = 70;
phi_g0 = BetaQ-phi_w0;

%%%%%%%%% phi %%%%%%%%%%%%%%%
phi_H = S_H * BetaQ;
phi_q = 1-BetaQ;

if Hydrate_Fluid_or_Frame_orSolid == 1
    phi_s = 1-BetaQ;
    phi_f = 1-phi_s;
%     phi_Hf = phi_H;
    xi_H = phi_H/(phi_f);
    w_H = 0;
    w_H_end = 0;
    w_q = 1;
    BetaS = BetaQ;
elseif Hydrate_Fluid_or_Frame_orSolid == 2 ...
|| Hydrate_Fluid_or_Frame_orSolid == 3
    phi_s = phi_q+phi_H;
    phi_f = 1-phi_s;
%     phi_Hf = 0;
    xi_H = 0;
    w_H = phi_H/phi_s;
    w_H_end = 1-phi_q;
    w_q = phi_q/phi_s;
    BetaS = 1-phi_s;
end


phi_LossWaterToHydrate = S_H/1.26*BetaQ;
phi_w_TOT = phi_w0 - phi_LossWaterToHydrate;

phi_tot = phi_q + phi_H + phi_w_TOT + phi_g0;
if phi_tot - phi_g0 > 1
```

```
    phi_g = 0;
    phi_w = 1- phi_q -phi_H -phi_g;
else
    phi_w = phi_w_TOT;
    phi_g = 1- phi_q -phi_H - phi_w;
end

xi_w = phi_w/(phi_f);
xi_g = phi_g/(phi_f);

%%%%%%%%%%%%%%%% Solid Elastic parameters %%%%%%%%%%%%%%%%%%

K_s = 0.5*(w_q*K_q^-1 + w_H*K_H^-1)^-1 + 0.5 * (w_q*K_q + w_H*K_H);
mu_s = 0.5*(w_q*mu_q^-1 + w_H*mu_H^-1)^-1 + 0.5 * (w_q*mu_q + w_H*mu_H);
rho_s = w_q*rho_q + w_H*rho_H;

K_s_EndPoint = 0.5*((1-w_H_end)*K_q^-1 +...
w_H_end*K_H^-1)^-1 + 0.5 * ((1-w_H_end)*K_q + w_H_end*K_H);
mu_s_EndPoint = 0.5*((1-w_H_end)*mu_q^-1 +...
w_H_end*mu_H^-1)^-1 + 0.5 * ((1-w_H_end)*mu_q + w_H_end*mu_H);
%%%%%%%%%%%%%% Hashin strikman Solid frame %%%%%%%%%%%%%

BetaEnd = BetaQ;
% porosity_s = 0.24
z = mu_dry0/6 *(9*K_dry0 + 8*mu_dry0)/(K_dry0 + 2*mu_dry0);

K_dry = (BetaS/BetaEnd /(K_dry0 + 4/3*mu_dry0) +...
(1-BetaS/BetaEnd) /(K_s_EndPoint + 4/3*mu_dry0) )^-1 - 4/3 *mu_dry0;
mu_dry = (BetaS/BetaEnd /(mu_dry0 + z) +...
(1-BetaS/BetaEnd) /(mu_s_EndPoint + z) )^-1 - z;
if Hydrate_Fluid_or_Frame_orSolid == 3
    K_dry = K_dry0;
    mu_dry = mu_dry0;
end

%%%%%%%%%%%%%%%%%%% Fluid Effect Reuss or Patchy %%%%%%%%%%%%%%
```

```
rho_f = xi_w*rho_w + xi_g*rho_g+xi_H*rho_H ;
rho_tot = rho_s*phi_s + rho_f*phi_f;

if Reuss_Hill_Patchy == 1
    K_f = (xi_w*K_w^-1 + xi_g*K_g^-1 + xi_H*K_H^-1)^-1;
    K_sat = K_s * (BetaS*K_dry - (1+BetaS)*K_f*K_dry/K_s +... K_f ) /...
    ( (1-BetaS)*K_f + BetaS*K_s -K_f*K_dry/K_s );
    mu_sat = mu_dry;
    if isnan(K_sat)
        K_sat = K_dry;
        rho_tot = rho_s;
    end
elseif Reuss_Hill_Patchy == 2
    disp('Error:: Hill not implemented')
elseif Reuss_Hill_Patchy == 3
    K_WH_Reuss = (xi_w/(xi_w+xi_H)*K_w^-1 +   xi_H/(xi_w+xi_H)*K_H^-1)^-1;
    Kg_sat = K_s * (BetaS*K_dry - (1+BetaS)*K_g*K_dry/K_s + K_g ) ...
    / ( (1-BetaS)*K_g + BetaS*K_s -K_g*K_dry/K_s );
    KwH_sat = K_s * (BetaS*K_dry -(1+BetaS)*K_WH_Reuss*K_dry/K_s + K_WH_Reuss)...
    / ( (1-BetaS)*K_WH_Reuss + BetaS*K_s -K_WH_Reuss*K_dry/K_s );
    mu_sat = mu_dry;
    M_pathcy = (xi_g/(Kg_sat+4/3*mu_sat) + (xi_w+xi_H)/(KwH_sat+4/3*mu_sat))^-1;
    mu_patchy = mu_dry;
    K_sat = M_pathcy-4/3*mu_patchy;
end


Vp = sqrt((K_sat + 4/3*mu_sat)/rho_tot);
Vs = sqrt((mu_sat)/rho_tot);

Vp_dry = sqrt((K_dry + 4/3*mu_dry)/(rho_s*phi_s));
Vs_dry = sqrt((mu_dry)/(rho_s*phi_s));
%%%%%%%%%%%%%%%% OUT %%%%%%%%%%%%%%%%%%%%%%%%

out{1} = Vp;
out{2} = Vs;
```

```
out{3} = K_sat;
out{4} = mu_sat;
out{5} = K_dry;
out{6} = mu_dry;
out{7} = [phi_s phi_H phi_w phi_g];
out{8} = [rho_s rho_f rho_w rho_g];
out{9} = [K_s mu_s K_f];
out{10} = [Vp_dry Vs_dry];
% out{9} = V_p_patchy;
```

Dvorkin_Nur_BISQ_rev02_fun.m

```
 function out = Dvorkin_Nur_BISQ_rev02_fun(S_H,S_w0,freq,R_sq)

mu_q = 39.6e9;
K_q = 38.7e9;
rho_q = 2650;
porosity_0 = 0.24;
K_w = 2.25e9;
rho_w = 1000;
K_H = 7.7e9;
mu_H = 3.2e9;
rho_H = 850;
phi_w0 = S_w0*porosity_0;
K_g = 11e6;
% K_g = 2.5e9;
rho_g = 70;

kappa_s0 = 1.1.*  1e-12;
N_perm = 14;
% r_s = 70e-6;
r_s = R_sq/2;
eta_w = 1.8e-3;
eta_g = 0.021e-3;
% eta_g = 1.8e-3;
```

```
Reuss_Hill_Patchy = 1;
Hydrate_Fluid_or_Frame_orSolid = 2 ;
% 1; Fluid, 2; Frame 3; solid
BISQ = 1;
%%%%%%%%% phi %%%%%%%%%%%%%%%%

out2 = FriableSand_Egen_fun(S_H,S_w0,...
Reuss_Hill_Patchy,Hydrate_Fluid_or_Frame_orSolid);
porosity_s = 1-out2{7}(1);
rho_s = out2{8}(1);
rho_f = out2{8}(2);
phi_s = out2{7}(1);
phi_H = out2{7}(2);
phi_w = out2{7}(3);
phi_g = out2{7}(4);
phi_f = 1-phi_s;
K_s = out2{9}(1);
K_f = out2{9}(3);
mu_s = out2{9}(2);
K_sm = out2{5};
mu_sm = out2{6};
Vp_gas = out2{1};
Vs_gas = out2{2};
Vp_dry = out2{10}(1);
Vs_dry = out2{10}(2);

%%%%%%%%%%%%%%%%%% Program starts %%%%%%%%%%%
rho1 = (1-porosity_s).*rho_s;
rho2 = porosity_s.*rho_f;
rho = rho1 + rho2;       % effective density

w = 2.*pi.*freq;
% eta_f0 = f_w*eta_w + f_g*eta_g;
eta_f0 = phi_w/(phi_w+phi_g)*eta_w + phi_g/(phi_w+phi_g)*eta_g;
if isnan(eta_f0)
    eta_f0 = 0;
```

```
end

h = r_s *((1+phi_f/phi_s)^(1/3)-1);
xi = h/2*sqrt(w*rho_f/eta_f0);
% xi
if xi < 3.2
    F = 1+1/0.7178*exp(0.7178*(xi-3.2))/12 + xi/6*i;
elseif xi >= 3.2
    F = 1/2 + 2*xi/12 + exp(-0.7178*(xi-3.2))/12 + xi/6*i;
end
% F
eta_f = eta_f0*F;
% eta_f = eta_f0

% kappa_i0 = 5e-4;
% kappa_s = kappa_s0*(phi_f/porosity_0)^3;
% kappa_i = kappa_i0*(porosity_0/phi_H)^2*(phi_f/phi_s)^3;

% k_rw = (1-S_H)^15;
k_rw = (1-S_H)^N_perm;
prmblty = k_rw*kappa_s0;
% prmblty = 1e-12
% prmblty = kappa_s0*(phi_f/porosity_0)^3;

% prmblty = ((porosity_s-0.0)/(porosity_0-0.1))^10 * kappa_s0;

% prmblty =(1/kappa_s + 1/kappa_i)^-1;
% prmblty =kappa_s0*(phi_f/porosity_s)^3;
% prmblty = 5e-3.*  9.869233e-13;

w_c = eta_f.*porosity_s./prmblty./rho_f;

% R = 500e-6;
% R = 70e-6;
% porosity_s = 0.15
% c1 = K_sm./phi_s./K_s;
```

```
% K_av = ((1-c1).*phi_s./K_s + phi_f./K_f).^-1;
% R12 = (1-c1).*phi_s .* phi_f.*K_av;

r12 = 0.5;
Geom= phi_s/phi_f*r12+1;
rho_12 = -(Geom-1)*porosity_s*rho_f;
rho_a = -rho_12;
% rho_a = 500;



% BIOT HIGH FREQ:
% v=eta_f0/rho_f
% kappa1 = a1*sqrt(alfa/v)
% a1 = radius duct
% alfa = omega;
%%%%%%%%%%%%%%%%%%%%%%%%%%%%%%%%%%%%%%%%%%%%%%%%%%%%%%%%
% c1 = K_sm/(phi_s*K_s);
% K_av = ((1-c1).*phi_s./K_s + phi_f./K_f).^-1;
Q = K_s./(1-porosity_s-K_sm/K_s);
F_biot = (1./K_f + 1./porosity_s./Q).^-1;
% F = K_av*phi_f

  lambda = sqrt(rho_f.*w.^2./...
  F_biot.*((porosity_s+rho_a./rho_f)./porosity_s + i .* w_c./w));
if BISQ == 1
    F_sq = F_biot.*(1-2.*besselj(1,lambda.*R_sq)./...
    lambda./R_sq./besselj(0,lambda.*R_sq));
else
    F_sq = F_biot;
end

if isnan(F_sq)
    F_sq = F_biot;
%     rho_sat = rho_s;
end
```

```
alfa = 1-K_sm./K_s;
poisson_frame = (3*K_sm-2*mu_sm)./(2*(3*K_sm+mu_sm));

A = porosity_s.*F_sq.*M_sm./rho2.^2;
B = ( F_sq.*(2.*alfa - porosity_s - porosity_s.*rho1./rho2)...
-(M_sm+F_sq.*alfa.^2./porosity_s).* ( 1+rho_a./rho2+i.*w_c./w))./rho2;
C = rho1./rho2+(1+rho1./rho2).*(rho_a./rho2+i.*w_c./w);

Y_1 = -B./2./A + sqrt((B./2./A).^2 - C./A);
Y_2 = -B./2./A - sqrt((B./2./A).^2 - C./A);
k1_number = sqrt(Y_1)*w;
k2_number = sqrt(Y_2)*w;
k_number = [k1_number k2_number];

%%%%%%%%%%%%%%%%%%%%%%
V = w./(k_number);
[a,b] = max(V);

Vp_fast = V(b);     % Vp
dB_cm_fast = imag(k_number(b))*8.7/100;
% dB_cm1 = imag(k_number(1))*8.7/100;
% dB_cm2 = imag(k_number(2))*8.7/100;

out{1} = Vp_fast;
out{2} = dB_cm_fast;
out{3} = k_number;
out{4} = porosity_s;
out{5} = K_s;
out{6} = mu_s;
out{7} = rho_s;
out{8} = K_f;
out{9} = rho_f;
out{10} = Vp_gas;
out{11} = Vs_gas;
out{12} = rho;
```

```
out{13} = [Vp_dry Vs_dry];
out{14} = [phi_s phi_f];
```

WaterMannWithSayers_rev03_fun.m

```
function out2 = WaterMannWithSayers_rev03_fun(S_H,S_w0,...
freq,a_rad,CavityElasticFluid)
% clear
%
% a_rad = 200e-6;
% S_H = 0.2;
% S_w0 = 0.8;
% freq = 500e3;
% CavityElasticFluid = 2;

%%%%%%%%%%%%%%%%%%%%%%%%%%%%%%%%%%%%%%%%%%%%%%
R_sq = 170e-6;
% R_sq = 50e-6;
out = Dvorkin_Nur_BISQ_rev02_fun(S_H,S_w0,freq,R_sq);
porosity_s = out{4};
K_s = out{5};
mu_s = out{6};
rho_s = out{7};
K_f = out{8};
rho_f = out{9};
c_f = sqrt(K_f/rho_f);
w = 2*pi*freq;

%%%%%%%%%%%%%%%%%%%%%%%%%%%%%%%%%%%%

c_long1 = out{1};  % BISQ
c_shear1 = out{11};
rho1 = out{12}; % rho total porous medium

c_long2 = c_f;
c_shear2 = 2000;
```

```
rho2 = rho_f;

%%%%%%%%%%%%%% Pao %%%%%%%%%%%%%%%%%
mu1 = c_shear1^2*rho1;
mu2 = c_shear2^2*rho2;
p = mu2/mu1;
eta = rho1/rho2;
k_long2 = w/c_long2;
k_shear2 = w/c_shear2;
k_long1 = w/c_long1;
k_shear1 = w/c_shear1;
ka = k_long1*a_rad;
n0 = porosity_s / (4/3*pi*a_rad^3);

A_0k = myFun_n(0,a_rad,k_long1,k_shear1,...
k_long2,k_shear2,p,eta,CavityElasticFluid);
A_1k = myFun_n(1,a_rad,k_long1,k_shear1,...
k_long2,k_shear2,p,eta,CavityElasticFluid);
A_2k = myFun_n(2,a_rad,k_long1,k_shear1,k_long2,...
k_shear2,p,eta,CavityElasticFluid);
A_3k = myFun_n(3,a_rad,k_long1,k_shear1,k_long2,...
k_shear2,p,eta,CavityElasticFluid);
A_4k = myFun_n(4,a_rad,k_long1,k_shear1,k_long2,...
k_shear2,p,eta,CavityElasticFluid);

%%%%%%%%%%%%%%%%% Multiple scatt WaterMann Truell %%%%%%%%%%%%%%%%%%
X0 = [1 3 5 7]/i/k_long1;
Xpi = [1 -3 5 -7]/i/k_long1;
Tok = [A_0k A_1k A_2k A_3k];

f_0 = X0*  conj(Tok)';
f_pi = Xpi*conj(Tok)';

c1 = w/K_eff1;
c2 = w/real(K_eff1);
alfa1_dbcm = imag(K_eff1)/100*8.68;
```

```
out2{1} = c2;
out2{2} = alfa1_dbcm;

%%%%%%%%%%%%%%% END %%%%%%%%%%%%%%%%%%%%%%%%%%%%%

function out = myFun_n(n,a,k_long1,...
k_shear1,k_long2,k_shear2,p,eta,CavityElasticFluid)
% p = mu2/mu1;
% eta = rho1/rho2;

phi_0 = 1/((2*n+1)*i^n);
a1 = k_long1;
B1 = k_shear1;
a2 = k_long2;
B2 = k_shear2;
r = a;

j_nz = @(n,z)  sqrt(pi/2/z)*besselj(n+.5,z);
y_nz = @(n,z)  sqrt(pi/2/z)*bessely(n+.5,z);
h_nz = @(n,z) j_nz(n,z) +    i*y_nz(n,z);

E_31 = (n^2 - n - 1/2*B1^2*r^2) * h_nz(n,a1*r) + 2*a1*r*h_nz(n+1,a1*r);
E_32 = -n*(n+1)*((n-1)*h_nz(n,B1*r)-B1*r*h_nz(n+1,B1*r));
E_41 = (n-1)*h_nz(n,a1*r)-a1*r*h_nz(n+1,a1*r);
E_42 = -(n^2 - 1 - 1/2*B1^2*r^2) * h_nz(n,B1*r) - B1*r*h_nz(n+1,B1*r);
E_3 = -i^n*(2*n+1)*((n^2 - n - ...
1/2*B1^2*r^2) * j_nz(n,a1*r) + 2*a1*r*j_nz(n+1,a1*r));
E_4 = -i^n*(2*n+1)*( (n-1)*j_nz(n,a1*r)-a1*r*j_nz(n+1,a1*r) );

E_11 = n*h_nz(n,a1*r)-a1*r*h_nz(n+1,a1*r);
E_21 = h_nz(n,a1*r);
E_12 = -n*(n+1)*h_nz(n,B1*r);
E_22 = -(n+1)*h_nz(n,B1*r)+B1*r*h_nz(n+1,B1*r);
E_13 = n*j_nz(n,a2*r) - a2*r*j_nz(n+1,a2*r);
E_23 = j_nz(n,a2*r);
```

```
E_33 = (n^2 - n - 1/2*B2^2*r^2) * j_nz(n,a2*r) + 2*a2*r*j_nz(n+1,a2*r);
E_43 = (n-1)*j_nz(n,a2*r)-a2*r*j_nz(n+1,a2*r);
E_14 = -n*(n+1)*j_nz(n,B2*r);
E_24 = -(n+1)*j_nz(n,B2*r)+B2*r*j_nz(n+1,B2*r);
E_34 = -n*(n+1)*((n-1)*j_nz(n,B2*r)-B2*r*j_nz(n+1,B2*r));
E_44 = -(n^2 - 1 - 1/2*B2^2*r^2) ...
* j_nz(n,B2*r) - B2*r*j_nz(n+1,B2*r);
E_1 = -i^n*(2*n+1)*(n*j_nz(n,a1*r)-a1*r*j_nz(n+1,a1*r) );
E_2 = -i^n*(2*n+1)*j_nz(n,a1*r);

E_33f = -1/2/eta*B1^2*r^2*j_nz(n,a2*r);

if CavityElasticFluid ==1
Matrix_n = [E_31 E_32; E_41 E_42];
b_vec = phi_0*[E_3;E_4];
elseif CavityElasticFluid ==2
Matrix_n = [E_11 E_12 E_13 E_14;...
    E_21 E_22 E_23 E_24;...
    E_31 E_32 E_33*p E_34*p;...
    E_41 E_42 E_43*p E_44*p] ;
b_vec = phi_0*[E_1;E_2;E_3;E_4];

elseif CavityElasticFluid ==3
Matrix_n = [E_11 E_12 E_13;...
    E_31 E_32 E_33f;...
    E_41 E_42 0] ;
b_vec = phi_0*[E_1;E_3;E_4];
end
XX_n = linsolve(Matrix_n,b_vec);
out = (XX_n(1));
end
end
```

Graphic design: Communication Division, UIB / Print: Skipnes Kommunikasjon AS

uib.no

ISBN: 978-82-308-3594-4